THE FRACTURE PROPERTIES OF HIGH STRENGTH ALUMINIUM CASTING ALLOYS

BY

PHILIP EDWARD HOLDEN

FOR THE AWARD OF

DOCTOR OF PHILOSOPHY

1979

SUMMARY

The fracture properties of a range of high strength aluminium casting alloys, in various heat treated conditions, have been investigated in three point bending.

Sharp cracks, necessary for fracture toughness testing, were produced by both fatigue cracking and spark machining and the compatibility of the two methods has been discussed. Stress intensity factors were determined for the curve crack fronts from experimental compliance data and a practical method of dealing with crack front curvature, has been proposed.

The five available methods for determining the critical stress intensity factor (K_{1c}) have been evaluated and their accuracies and limitations discussed. In order to measure the load-point displacements of the specimens, a rig, considered to be an improvement on existing rigs, has been developed. Initiation of the cracks was detected using an electrical potential technique, which could also be used to determine crack growth rates and predict crack lengths. Geometrical effects on the stress intensity factor, such as blunt notches and short cracks emanating from the roots of blunt notches, have been assessed and are compared with the theoretical solutions. Structural influences on the stress intensity factor, such as material condition and porosity, have also been investigated.

The data collected from the majority of the specimens was tabulated, punched and fed into a computer programme designed to calculate the fracture toughness parameters. The results have been presented graphically and analysed statistically using standard analysis of variance packages. Optical and electron microscopy has been used to examine the fracture surfaces and an explanation of the mechanism of fracture has been suggested for each alloy.

Key words: Aluminium, fracture, toughness, crack, castings.

CONTENTS

PAGE

LIST OF FIGURES

DETAILS Figure No.

1. INTRODUCTION.

Aluminium alloys are becoming increasingly important in applications requiring high strength and toughness, particularly where a saving in weight is involved. Today, it is possible to cast to close dimensional tolerances and subsequent heat treatment can produce a structure with mechanical properties equivalent to those attained by mechanical working processes, but at a percentage of the cost. These high strength aluminium castings often fail in a manner exhibiting low ductility (i.e. self propagating crack growth in elastically stressed material) but as yet little systematic work has been carried out in investigating the fracture behaviour of these materials. The determination of the yield strength (or 0.2% proof stress) still remains the principal method of evaluating these high strength alloys, even though stresses in service may be limited by fracture rather than yield.

The concepts of fracture mechanics recognises that the majority of structural components will contain minute cracks or defects. The fracture toughness of a material is the quantity measured which relates these defects to the applied stress to cause fracture. Castings frequently contain a degree of porosity which effectively contributes to the overall size and proportion of defects present and thus to the greater likelihood of failure.

In a practical sense, fracture toughness is generally expressed in the form of the critical stress intensity factor, K_{1c} (where subscript 1. refers to the opening mode where the in-plane loading is symmetric with respect to the crack plane). This is a material property which is independent of crack length, applied stress, or specimen geometry. Although fabrication of a structure may have been based on fracture theory, its eventual failure could be due to poor design; this is often

the case where there is an involvement of large sections.

The techniques used for the determination of K_{1c} under linear elastic conditions (L.E.F.M.) are now well established (1, 2)*. To obtain valid K_{1c} data for relatively tough materials, however, necessitates the use of such large specimens that actual sections used in service may not be truly represented. One approach to the fracture analysis of these tough materials is the application of elastic-plastic fracture mechanics (E.P.F.M.). This development interrelates applied stress, crack length and material toughness for a condition which is dependent on structural geometry when fracture has occurred after general yielding.

Although there are numerous specimen geometries available for fracture toughness testing, little variation can be found in the configurations of the notches machined into these specimens. In structural components, fatigue cracks often initiate from relatively blunt areas (such as rivet holes, corrosion pits, weld repairs etc.). The stress distribution is considerably effected by the root radius of one of these blunt areas, coupled with the depth and shape of any fatigue cracks that may be emanating from these said areas.

The detection of cracks and discontinuities by non-destructive methods are forever improving, with the result of stricter inspection procedures. The fact remains, however, that discontinuities are present regardless of detection or not. Fracture mechanics is the best available tool for determining acceptable stress levels, discontinuity sizes and material properties and is, therefore, directly applicable to structural design.

* References are given in a general reference section at the end of this thesis.

2. DEVELOPMENTS IN FRACTURE MECHANICS.

2.1 The energy balance approach.

The fracture properties of materials were first investigated by Griffith (3) who found an inverse square relationship between crack size and fracture stress in several hard glass spheres. His theory was based on the assumption that unstable crack growth would occur when the "strain energy release rate" exceeded the rate of absorbtion of energy as new fracture surfaces were formed. By considering an ellipsoidal crack of unit thickness, Griffith proposed that the total energy in the system U may be given by:

$$U = U_o + U_\gamma - U_a \quad . \quad . \quad . \quad . \quad . \quad (1)$$

Where U_o = elastic energy of an infinite body.

$U\gamma$ = increase in elastic surface energy.

U_a = reduction in elastic energy due to the introduction of a crack.

U_γ the elastic surface energy term, is given by:

$$U_\gamma = 4a\gamma_e \quad . \quad . \quad . \quad . \quad . \quad . \quad (2)$$

Where 4a = the surface area of the crack faces.

γ_e = the surface energy of the material.

According to Griffith:

$$U_a = \frac{\pi\sigma^2 a^2}{E} \quad . \quad . \quad . \quad . \quad . \quad (3)$$

Therefore: (see fig.1)

$$U = U_o + 4a\gamma_e - \frac{\pi\sigma^2 a^2}{E} \quad . \quad . \quad . \quad (4)$$

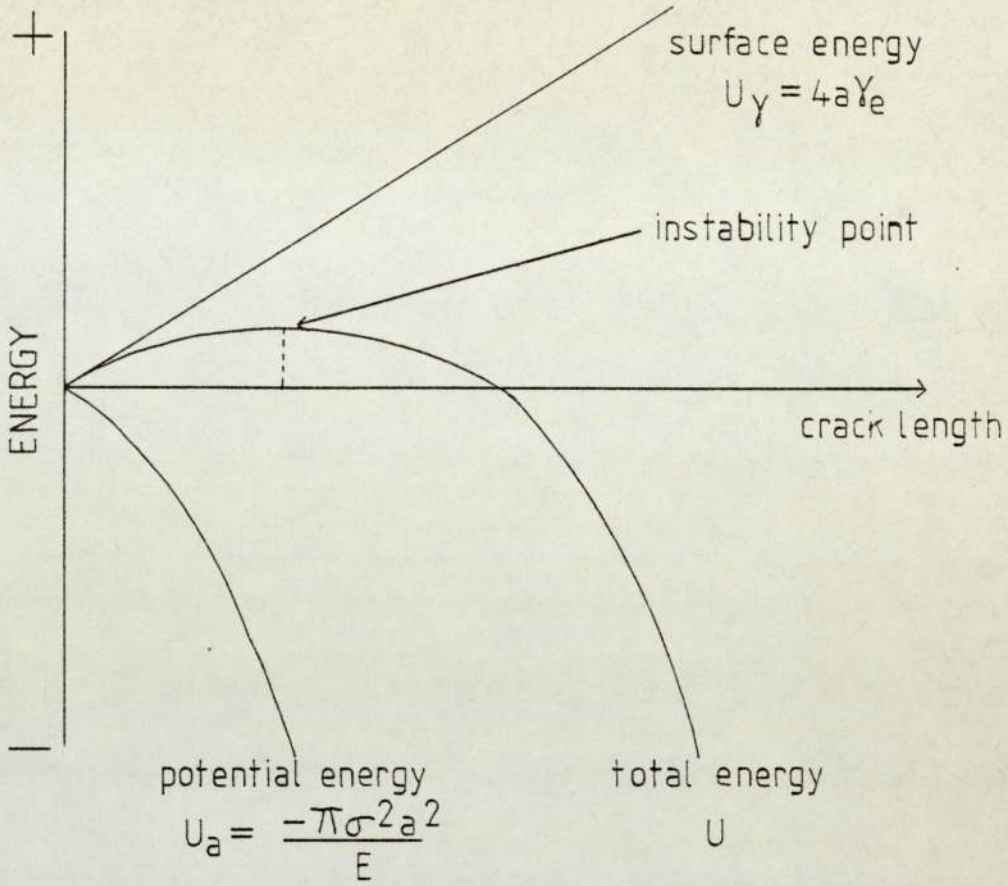

Fig.1. The effect of energy on crack length

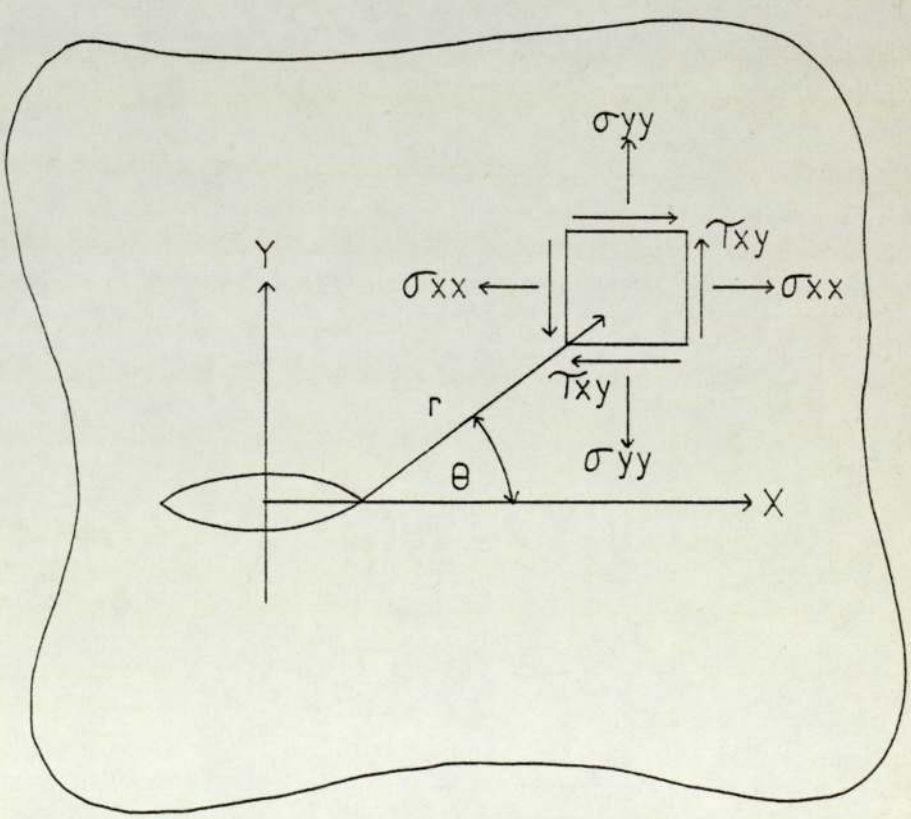

Fig. 2. Stresses near a crack tip.

The condition for energy balance occurs when:

$$\frac{d}{da}\left(\frac{\pi\sigma^2 a^2}{E}\right) = \frac{d}{da}\left(4a\gamma_e\right) \quad \cdots \quad (5)$$

which leads to the Griffith equation:

$$\sigma\sqrt{a} = \left(\frac{2\gamma_e E}{\pi}\right)^{1/2} \quad \cdots \quad (6)$$

and rearranging equation (6) gives:

$$G = \frac{\pi\sigma^2 a}{E} = 2\gamma_e \quad \cdots \quad (7)$$

Where G represents the strain energy release rate.

Most materials do not behave in an entirely elastic manner and there is usually some plastic deformation at the crack tip. If this region is small relative to the containing body then G may be calculated according to theory. Irwin (4) suggested a modification to the Griffith fracture criteria so that plastic deformation at the crack tip may be accounted for. i.e.

$$\frac{\pi\sigma^2 a}{E} = 2\gamma_e + 2\gamma_p \quad \cdots \quad (8)$$

Orowan (5) re-wrote the Griffith equation in the form:

$$\sigma = \sqrt{\frac{2(\gamma_e+\gamma_p)E}{\pi a}} \quad \cdots \quad (9)$$

and as γ_p the plastic deformation term is considerably larger than γ_e, the elastic surface energy term, this approximates to:

$$\sigma = \sqrt{\frac{2\gamma_p E}{\pi a}} \quad \cdots \quad (10)$$

The major limitation of the energy balance approach is that although the instability of sharp cracks may be defined this analysis cannot be

used to examine stable crack extension.

2.2 The stress intensity factor approach.

A smooth notch in an elastically stressed body causes an increase in stress at the crack tip. The magnitude of this stress is measured by the stress concentration factor, K_T, which is defined as the ratio of stresses at the crack tip to the applied stress. As the notch root radius tends to zero, the notch becomes a crack and the stress concentration factor becomes inappropriate. Irwin (6) focused his attention on the stress distribution near the tip of a crack and by using an analysis originally developed by Westergaard (7) was able to represent the stresses in the following manner.*

$$\sigma_x = \frac{K_I}{(2\pi r)^{1/2}} \cos\frac{\theta}{2}\left[1 - \sin\frac{\theta}{2}\sin\frac{3\theta}{2}\right]$$

$$\sigma_y = \frac{K_I}{(2\pi r)^{1/2}} \cos\frac{\theta}{2}\left[1 + \sin\frac{\theta}{2}\sin\frac{3\theta}{2}\right]$$

$$\tau_{xy} = \frac{K_I}{(2\pi r)^{1/2}} \sin\frac{\theta}{2}\cos\frac{\theta}{2}\cos\frac{3\theta}{2} \quad . \qquad (11)$$

$$\sigma_z = \nu(\sigma_x + \sigma_y), \qquad \tau_{xz} = \tau_{yz} = 0$$

$$U = \frac{K_I}{G}\left(\frac{r}{2\pi}\right)^{1/2} \cos\frac{\theta}{2}\left[1 - 2\nu + \sin^2\frac{\theta}{2}\right]$$

$$V = \frac{K_I}{G}\left(\frac{r}{2\pi}\right)^{1/2} \sin\frac{\theta}{2}\left[2 - 2\nu - \cos^2\frac{\theta}{2}\right]$$

$$W = 0$$

* Although Irwin (6) presented the stresses in the vicinity of a crack tip for all three modes of deformation (see fig.3) only the first or opening mode is generally considered in fracture theory.

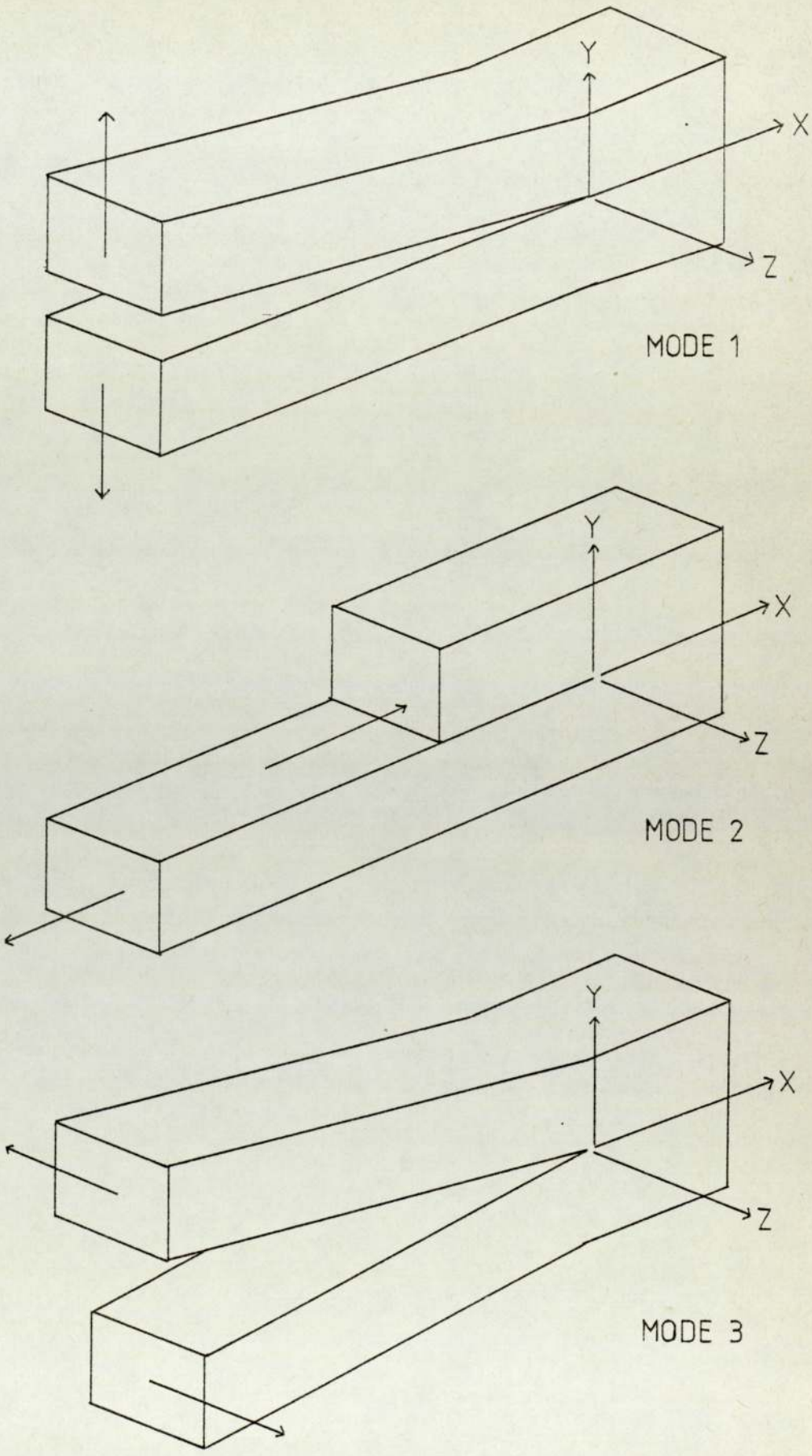

Fig. 3. The three basic modes of crack surface displacements.

Where r and θ are cylindrical polar ordinates of a point with respect to the crack tip. (see fig.2). As r approaches zero and neglecting the higher order terms of r, Westergaard's equations are a good approximation to the stress distribution at the tip of a crack. Providing that the distance, x, ahead of the crack tip is small, then the local stress σ_y, may be given by:

$$\sigma_y = K/\sqrt{2\pi x} \quad . \quad . \quad . \quad . \quad (12)$$

Where K is the stress intensity factor, and describes the level of local stress distribution (see fig.4).

Dimensional analysis of Westergaard's equations show that the stress intensity factor is proportional to the applied stress σ and the crack length a. The general form being:

$$K_1 = \sigma\sqrt{a}.\ Y.\left(\frac{a}{w}\right). \quad . \quad . \quad . \quad (13)$$

Here Y $(\frac{a}{w})$ is a geometrical constant which for a specific geometry is dependent only on the crack length to gross width ratio. For standard specimens the variation of K_1 with $(\frac{a}{w})$ is usually expressed as a polynomial series. K - calibrations constructed in this way, for bend specimens, are shown in fig.5. Y values for three important configurations are illustrated in fig.6.

As the strain energy release rate G is equivalent to the stress intensity factor K in elastic conditions, the following relationship exists:

$$G_1 = \frac{1+k}{8\mu} K_1^2 \quad . \quad . \quad . \quad (14)$$

Where μ is the shear modulus and k is a function of Poisson's ratio (v). A materials resistance to fracture may be represented by either G_{1c} or K_{1c}. Generally, however, K_{1c} is prefered as it is independent

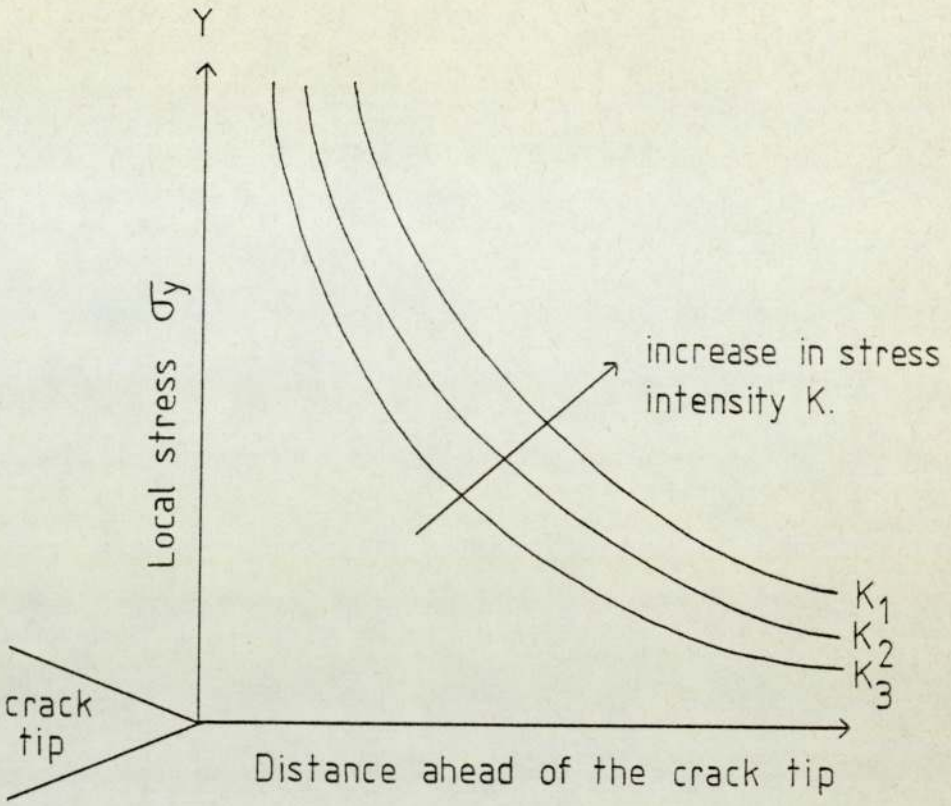

Fig. 4. Distribution of stress at a crack tip.

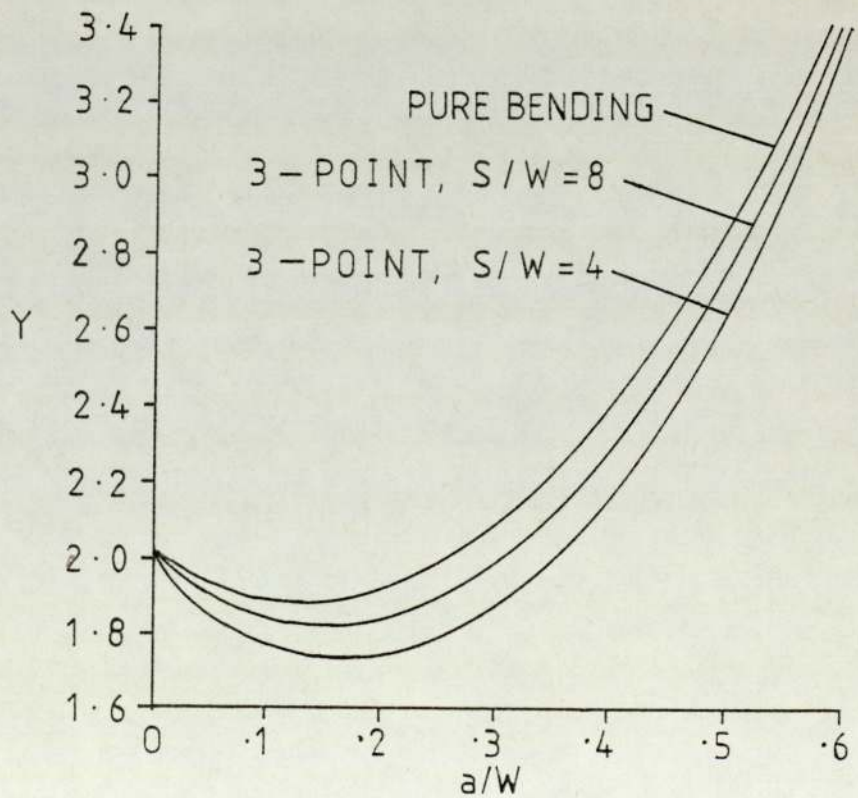

Fig. 5. K calibrations for bend specimens

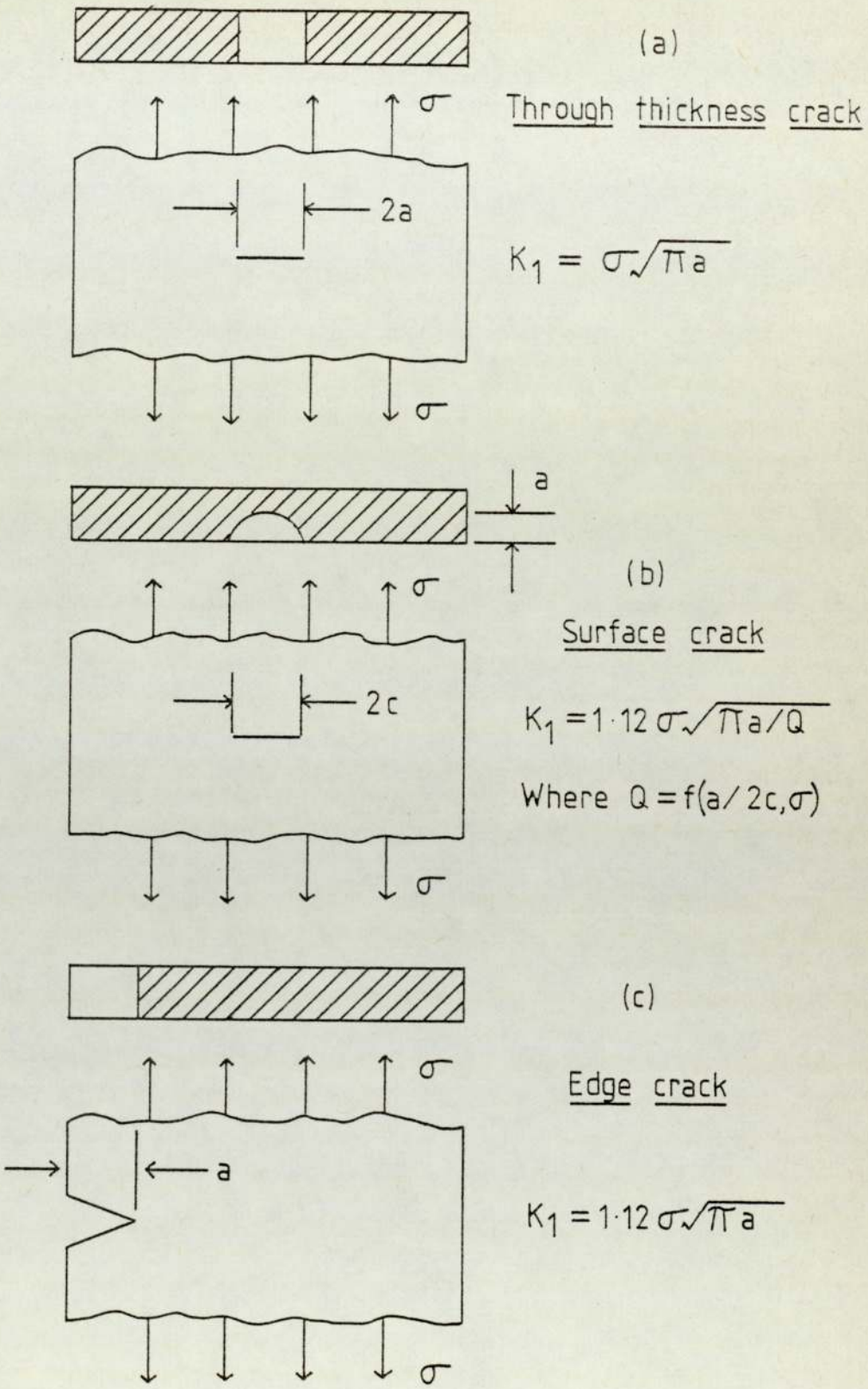

Fig. 6. K_1 values for three important geometries

of material modulus.

2.3 Linear elastic fracture mechanics.

2.3.1 Plastic zones.

The result of high elastic stresses in the vicinity of a crack tip is the formation of a plastic zone, where microscopic yielding has taken place. The size of this plastic zone varies according to whether the stresses are developed in "plane stress" or "plane strain" conditions. In a relatively thick section the plastic regions near the surface are almost entirely in a condition of plane stress, whilst those in the centre portion are in a condition of plane strain (see fig.7). Assuming that the stresses ahead of the crack tip are always less than the yield stress σ_{ys}, the radius of the plastic zone may be given by:

$$r_y = \frac{1}{2\pi}\left(\frac{K_{Ic}}{\sigma_{ys}}\right)^2 \quad \cdots \quad (15a)$$

for plane stress

or

$$r_y = \frac{1}{5{\cdot}6\pi}\left(\frac{K_{Ic}}{\sigma_{ys}}\right)^2 \quad \cdots \quad (15b)$$

for plane strain

2.3.2 Dimensional effects.

If the theories of linear elastic fracture mechanics are to apply, the thickness of a body must be of sufficient size in order to completely contain the plastic zone. (i.e. plane strain conditions). The decrease of stress intensity with increase in specimen thickness, B, is shown in fig.8. Here it may be seen that the stress intensity levels out after attaining a certain minimum thickness B_{min}. In practice, to

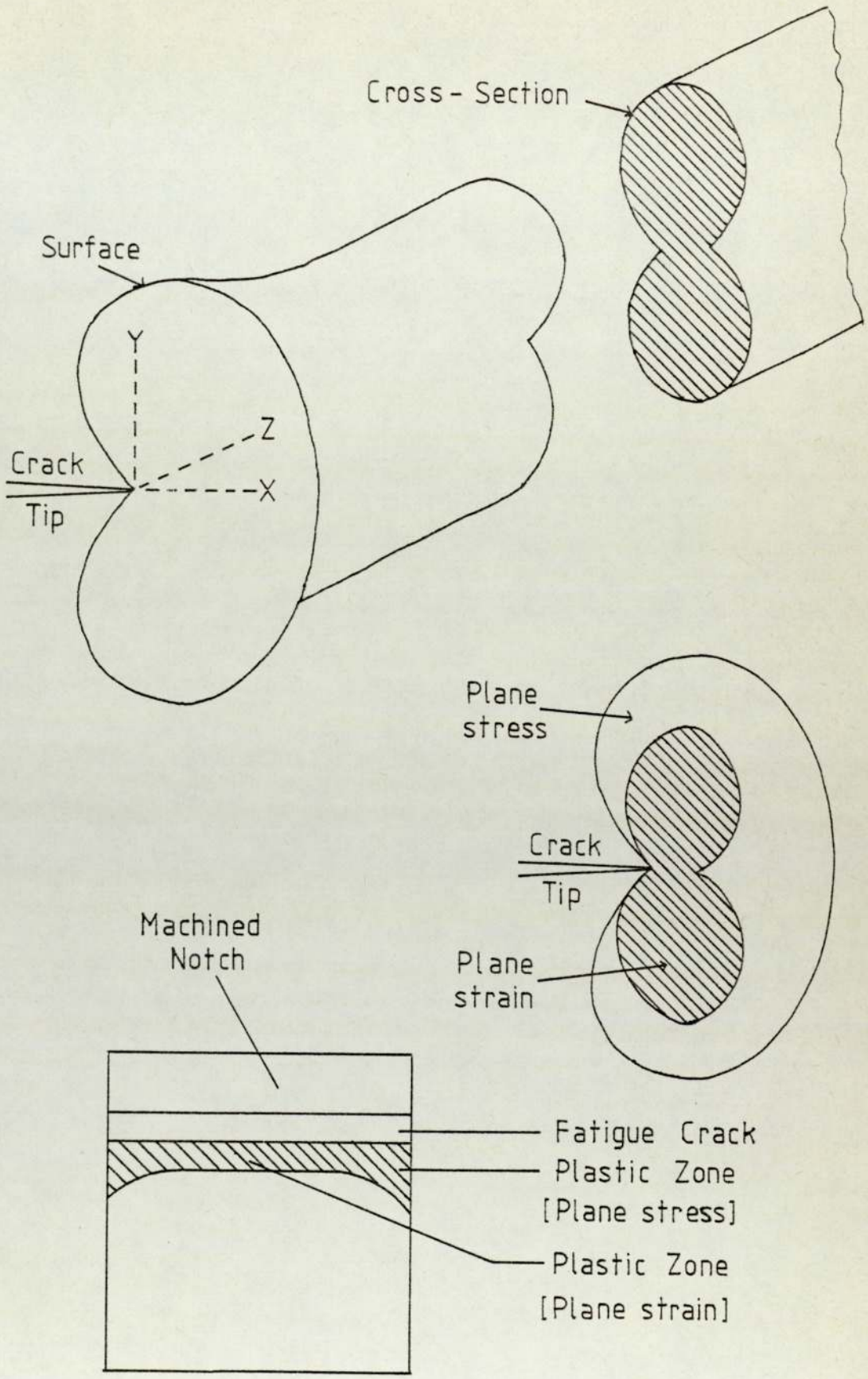

Fig.7. The plastic zone ahead of a crack tip.

ensure that the stress intensity factor is obtained in plane strain conditions, the standards (1,2) specify that the value of B should be greater than:

$$4{\cdot}0\left(\frac{K_{1c}}{\sigma_{ys}}\right)^2 \quad \cdots \quad (16)$$

although an earlier draft (8) recommends that the thickness should be greater than:

$$2{\cdot}5\left(\frac{K_{1c}}{\sigma_{ys}}\right)^2 \quad \cdots \quad (16a)$$

This value is often conservative and valid K_{1c} data may be obtained at thicknesses less than B_{min}. (see fig.8).

Plane strain conditions do not always guarantee that the stress intensity will be the critical value, K_{1c} as measured under linear elastic conditions. Errors can arise in the value of K_1 at distances ahead of the crack tip and these errors will increase with distance. Modification of the stress intensity factor to include some extent of plastic deformation ahead of the crack tip in an infinite body has been accomplished by both Irwin (4) and Orowan (5) i.e.

$$K = \sigma\sqrt{\pi(a + r_y)} \quad \cdots \quad (17)$$

Where r_y is the plastic zone size given in equations (15a) and (15b). The greater the ductility of a material, the larger its plastic zone; therefore, with reference to equation (17) the greater will be the correction made to the stress intensity factor, K_1. For this reason, standard specimen requirements recommend that in order for elastic analysis to be applicable, the plane strain plastic zone size should be less than 0.02a (where a is the crack length). Fig.9 illustrates this point.

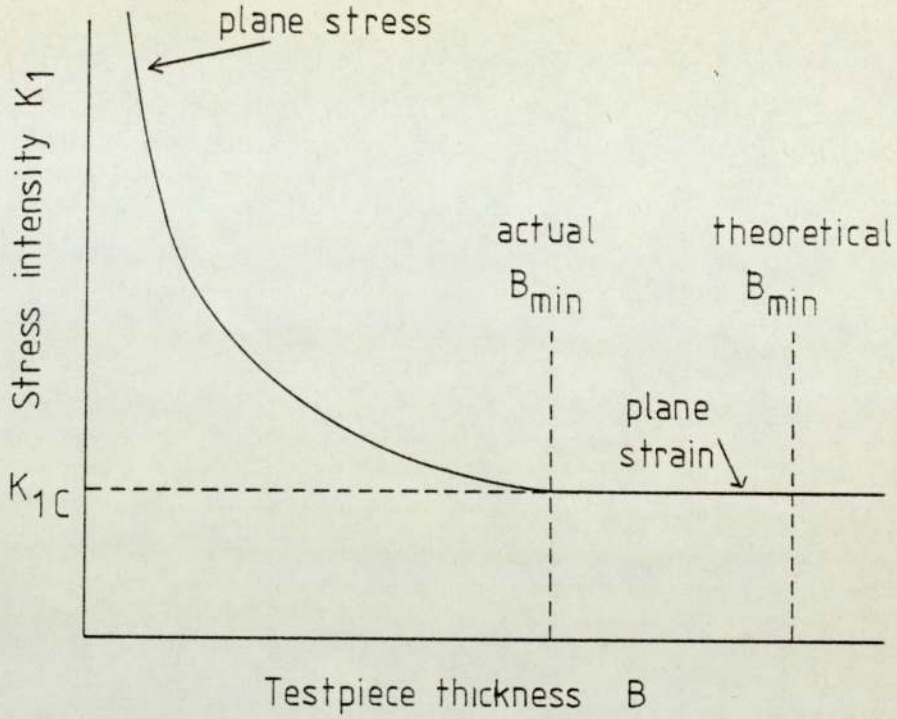

Fig. 8. The effect of thickness on K_1.

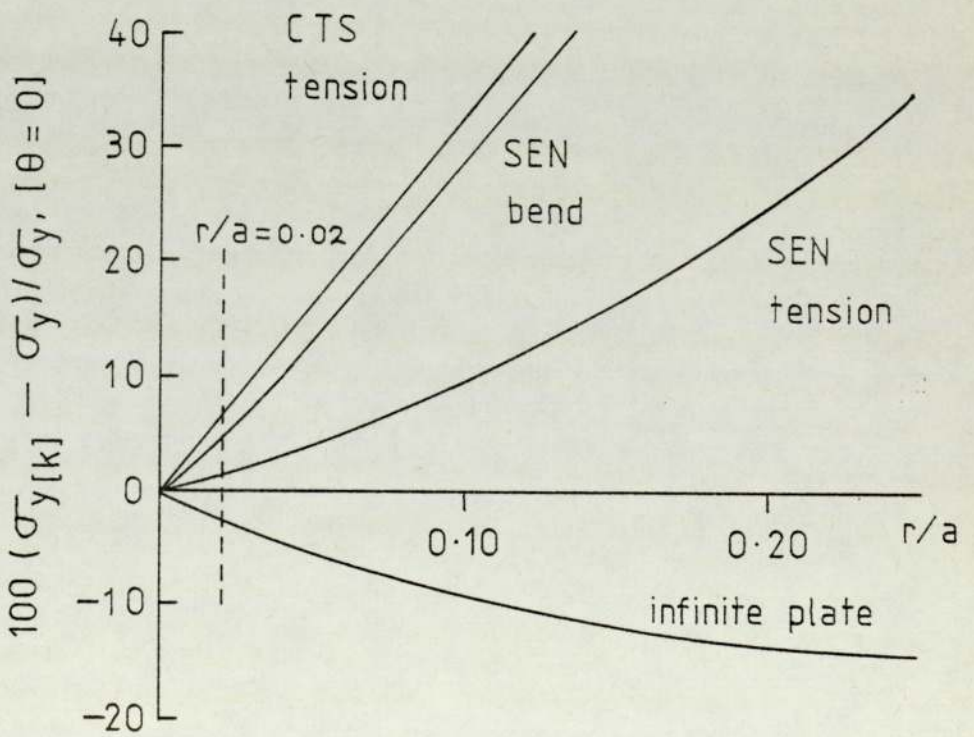

Fig. 9. Deviation of $\sigma_{y[k]}$ on $\theta = 0$ plane

2.3.3 Critical defect sizes.

2.3.3.1 General.

One of the major advantages in knowing the fracture toughness of a material is the ability to accurately predict the critical defect size for a certain level of applied stress. If we consider the case of a through crack in an infinite plate (as shown in fig.6a) where $Y = \sqrt{\pi}$, then by substituting for Y in equation (13) and rearranging, we obtain:

$$\sigma = \frac{K_{Ic}}{\sqrt{(\pi a)}} \quad . \quad . \quad . \quad . \quad . \quad . \quad (18)$$

The critical defect size for a certain level of applied stress or working stress, σ_w, may then be given by:

$$a_c = \frac{K_{Ic}^2}{\pi \sigma_w^2} \quad . \quad . \quad . \quad . \quad . \quad . \quad (19)$$

Equation (19) represents the critical defect size for purely elastic fracture conditions. If we now take a step further to include plastic yielding at the crack tip (see section 2.3.2) then by substituting σ_w for σ and by combining equations (15a) and (17) we may write:

$$K_{Ic} = \sigma_w (\pi a)^{\frac{1}{2}} \left[1 + \tfrac{1}{2}\left(\sigma_w/\sigma_{ys}\right)^2\right]^{\frac{1}{2}} . \quad (20)$$

where the term in the square brackets represents the plane stress plastic zone correction factor.

Consider the following example where the gross stress to fracture σ_w, was equal to half of the yield stress, σ_{ys}. From equation (20) the critical defect size a_c may be given by:

$$a_c = \frac{K_{Ic}^2}{\sigma_w^2 \pi} (0.88) \quad . \quad . \quad . \quad (21)$$

This means that in plane stress conditions the critical defect size is reduced by approximately 12 percent. Similarly, the critical defect size for plane strain conditions (where r_y is given in equation 15b) may be written as:

$$a_c = \frac{K_{Ic}^2}{\sigma_w^2 \pi} \left(0.97\right) \quad . \quad . \quad . \quad . \quad (22)$$

or the plane strain condition reduces the critical defect size by about 3 percent.

2.3.3.2 Totally embedded defects.

According to Irwin (9) the stress intensity at any point on the front of a totally embedded crack (see fig.10a) can be given by:

$$K_I = \sigma_w \Phi^{-1} \sqrt{\pi (a + r_y)} \quad . \quad . \quad . \quad (23)$$

where, assuming that the cross section of the crack is elliptical Φ is the shape factor dependent on the ratio of the minor axis to the major axis (values of Φ are given in table.1 from Barnby (10))

Table.1 Values of Φ for elliptical embedded flaws.

(a = length of minor axis, b = length of major axis)

a/b	0	0.2	0.4	0.6	0.8	1.0
Φ	1	1.05	1.15	1.28	1.42	$\pi/2$

In plane strain conditions a_c may therefore be written as:

$$a_c = \frac{K_{Ic}^2}{\sigma_w^2 \pi} \left[\Phi^2 - \frac{\sigma_w^2}{4(2)^{\frac{1}{2}} \sigma_{ys}^2} \right] \quad . \quad . \quad (24)$$

where the term in brackets corresponds to the plane strain plastic zone correction factor and shape factor combined.

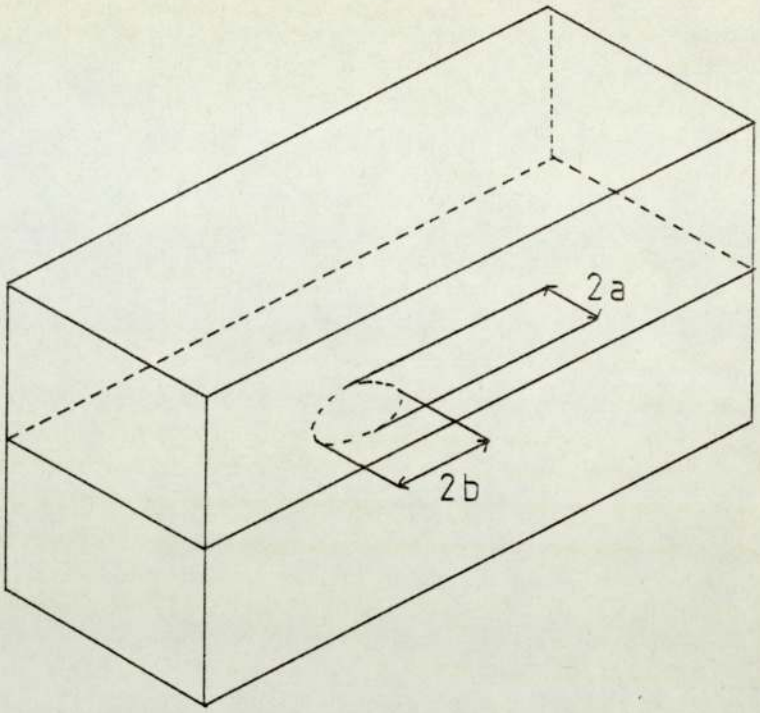

Fig.10a. Totally embedded crack

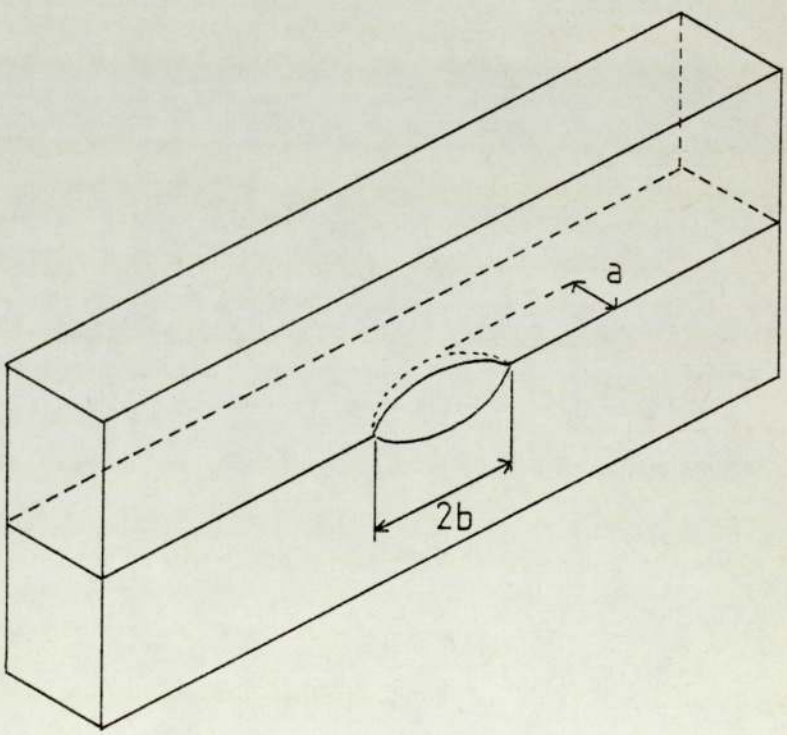

Fig.10b. Semi-elliptical surface crack

2.3.3.3 Surface defects.

Fig.10b illustrates a semi-elliptical surface crack (thumb nail crack) of depth a and surface length 2b extending into an infinite block. This type of defect is essentially half of the totally embedded elliptical crack shown in fig.10a, with the exception that this surface crack has a free surface. This free surface (or front surface) tends to increase the magnitude of the stress intensity owing to the greater generation of stress at the crack tip. The stress intensity for this type of crack may therefore be given by:

$$K_1^2 = \frac{\sigma_w^2 \pi (a + r_y)}{\Phi} \quad . \quad . \quad . \quad . \quad (25)$$

By combining equations (15b) and (25) and rearranging, a_c for plane strain conditions may be given by:

$$a_c = \frac{K_{1c}^2}{\pi \sigma_w^2} \left[\frac{\Phi^2 - 0{\cdot}212 \sigma_w^2 / \sigma_{ys}^2}{1{\cdot}2} \right] \quad (26)$$

Where in this case the bracketed term is a combination of the plane strain plastic zone correction factor, the front face correction factor and the shape factor. More generally, equation (26) is written:

$$\left(\frac{a}{Q}\right)_c = \frac{K_{1c}^2}{1{\cdot}2 \pi \sigma_w^2} \quad . \quad . \quad . \quad . \quad (27)$$

Where Q, the defect shape factor, is equivalent to:

$$Q = \Phi^2 - 0{\cdot}212 \sigma_w^2 / \sigma_{ys}^2 \quad . \quad . \quad (28)$$

Fig.11 shows the effect that the depth/surface length has on the defect shape parameter, with increasing values of plastic zone correction factor.

2.3.3.4 Irregular shaped defects.

The critical sizes for irregular shaped defects has been

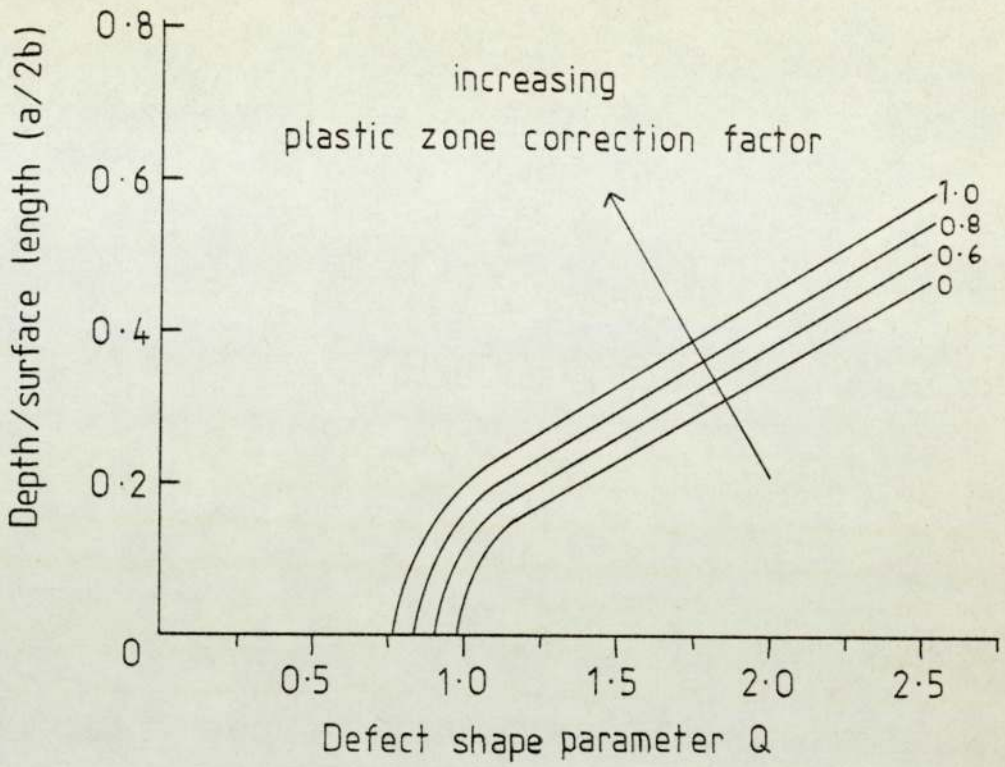

Fig.11. The effect of the depth/surface length on Q.

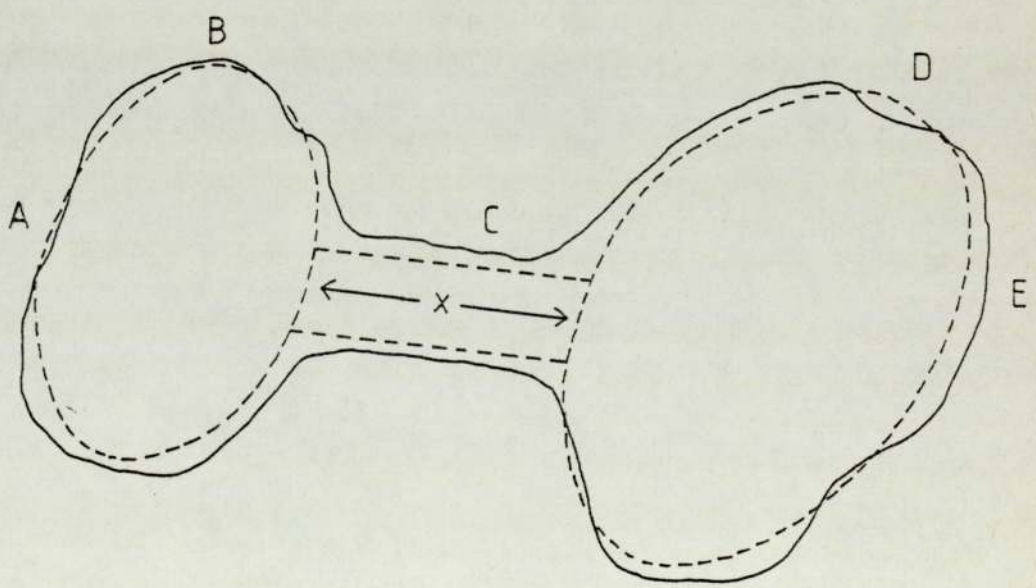

Fig.12. An irregular shaped defect

described by Barnby (10). Consider the irregular defect shown diagrammatically in fig.12, which represents the cross section of two flat cracks inter-connected by a narrow neck. To estimate the critical defect size of this shape we first need to know the stress intensities at various points on this shape, say A, B, C, D and E. The stress intensity at positions A and C may be determined from the combination of an isolated elliptical crack and a half ellipse. Point C is similar to a through crack of length x. At points B and D we could assume isolated ellipses and the K_1 values here would depend on the shape factors of these ellipses. Practically, the accuracy to which the critical defect size, for an irregular shape, needs to be determined depends upon its overall size. If the irregular shape is small enough to be completely engulfed by an elliptical shape, which itself is critical then, the determination of the critical defect size for this elliptical shape is purely academic. If, however, the apparent size of the irregular shape is much larger than the overall critical defect size then, the irregular shape's critical defect size must be accurately determined.

2.3.3.5 Crack or defect coalescence.

The coalescence of cracks or defects in a material to form a larger single defect depends upon the separation of adjacent defects. If we consider the simple case of two co-planar circular cracks of diameter D and radius a, the distance between the cracks may be given by, W. Where W = na (see fig.13a). The coalescence conditions for various groups of circular embedded cracks are shown in fig.13b. This figure is best explained by use of the following example:
Consider two defects both of which have defect sizes of half the critical size (i.e. $D/D_{crit} = 0.5$). The point of intersection of curve No.3 and the dotted line representing $D/D_{crit} = 0.5$ corresponds to the minimum defect separation in order for two cracks to coalesce at their

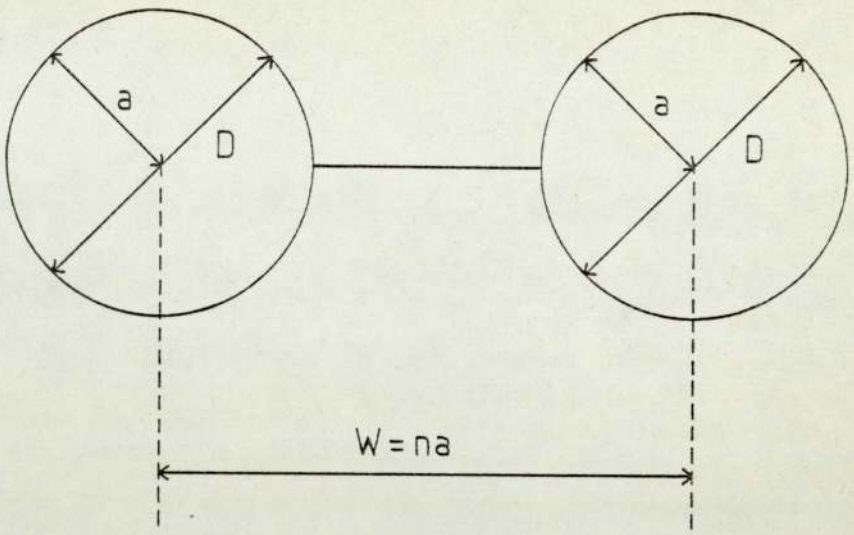

Fig.13a. Two adjacent co-planar circular cracks

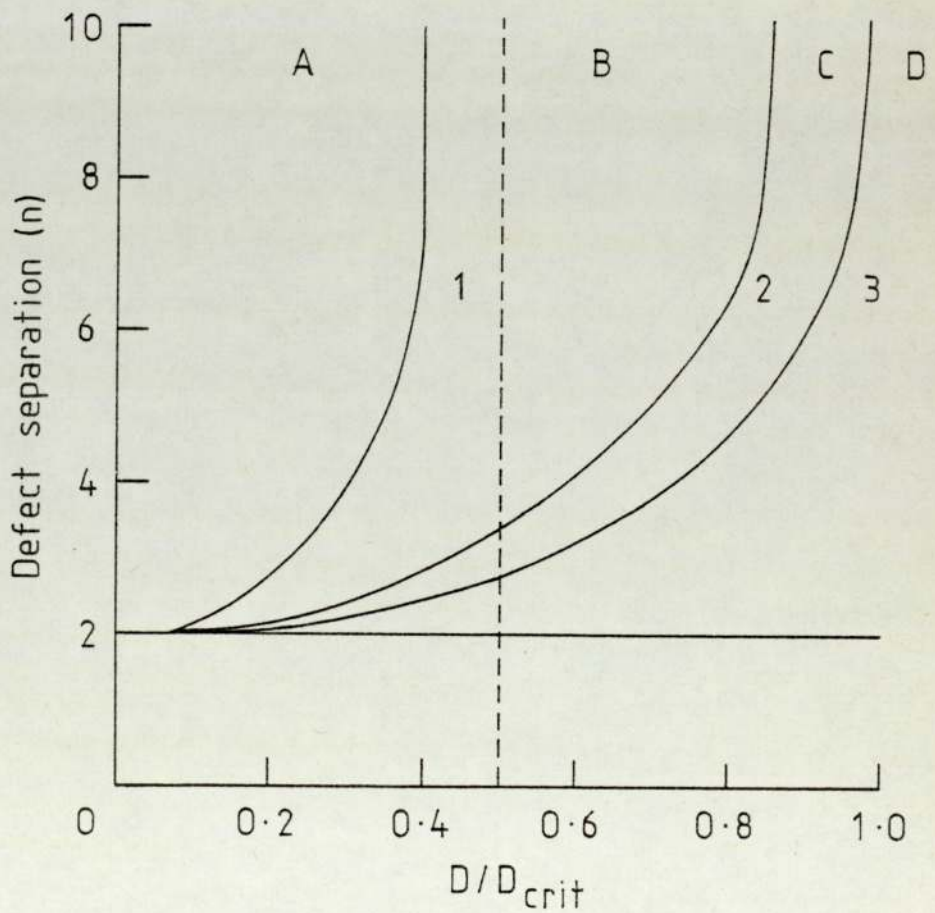

Fig.13b. Coalescence conditions for circular embedded cracks.

crack tips. Thus in the area A no cracks will join, in region B only an infinite number of cracks would join, in region C three or more cracks would join, and finally in area D all cracks will join together. Although it is understood that this diagram only gives coalescence conditions for two dimensional situations, it is nevertheless a good approximation to the real problem.

2.4 Elastic - plastic (yielding) fracture mechanics.

2.4.1 General.

The limitations of linear elastic fracture mechanics as a method for evaluating the fracture properties of materials has brought about the development of yielding fracture mechanics. The concepts of yielding fracture mechanics enables the fracture toughness of a material to be assessed after gross plastic deformation has taken place. Three main procedures are currently in use for extending the available linear elastic fracture mechanics into elastic-plastic conditions, namely:

a) Crack opening displacement (C.O.D)

b) J-integral analysis (J)

c) R-curve analysis

2.4.2 Crack opening displacement.

2.4.2.1 Analytical models of C.O.D.

The original model representing plastic deformation at the tip of a crack was presented by Vitvitskii and Leonov (11) which was modified using dislocation theory by Bilby, Cottrell and Swindon (12). Dugdale (13) and at about the same time Barenblatt (14) used the model to represent the extent of yielding of a slit contained in an infinitely large plate (see fig.14). A uniform stress, σ, is applied perpendicularly to the faces of the crack which causes the crack of

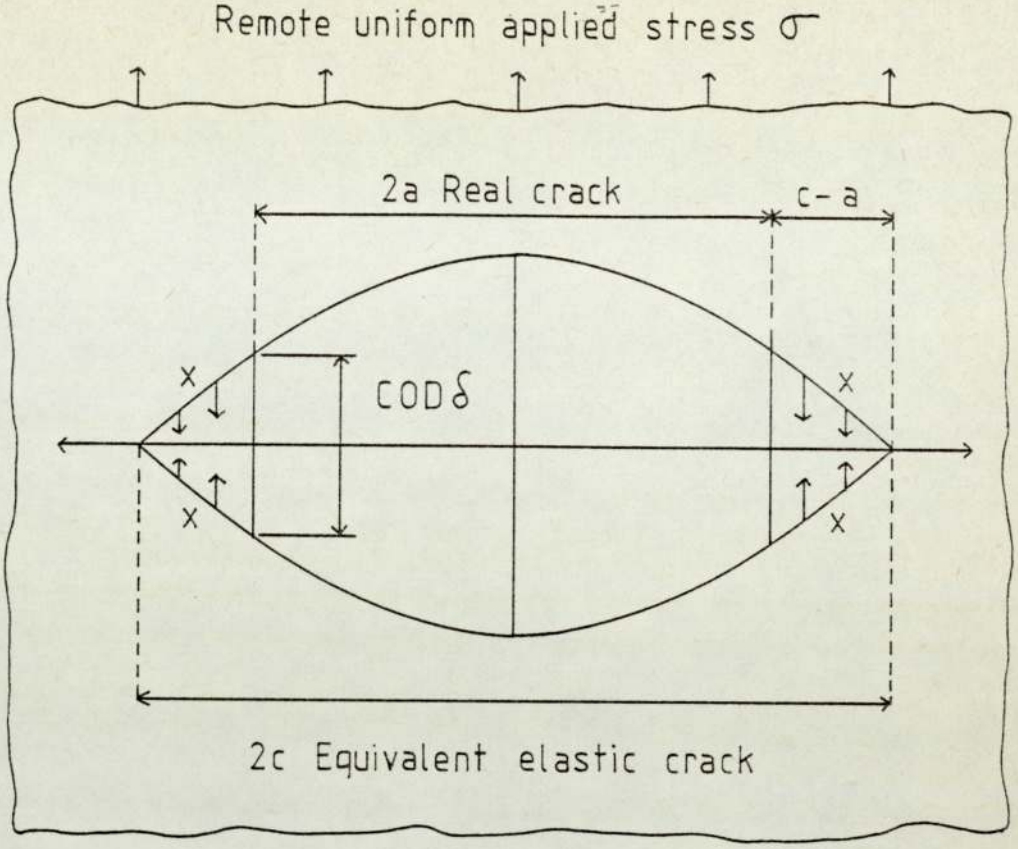

Fig.14. Dugdale's strip-yield model for crack tip plasticity

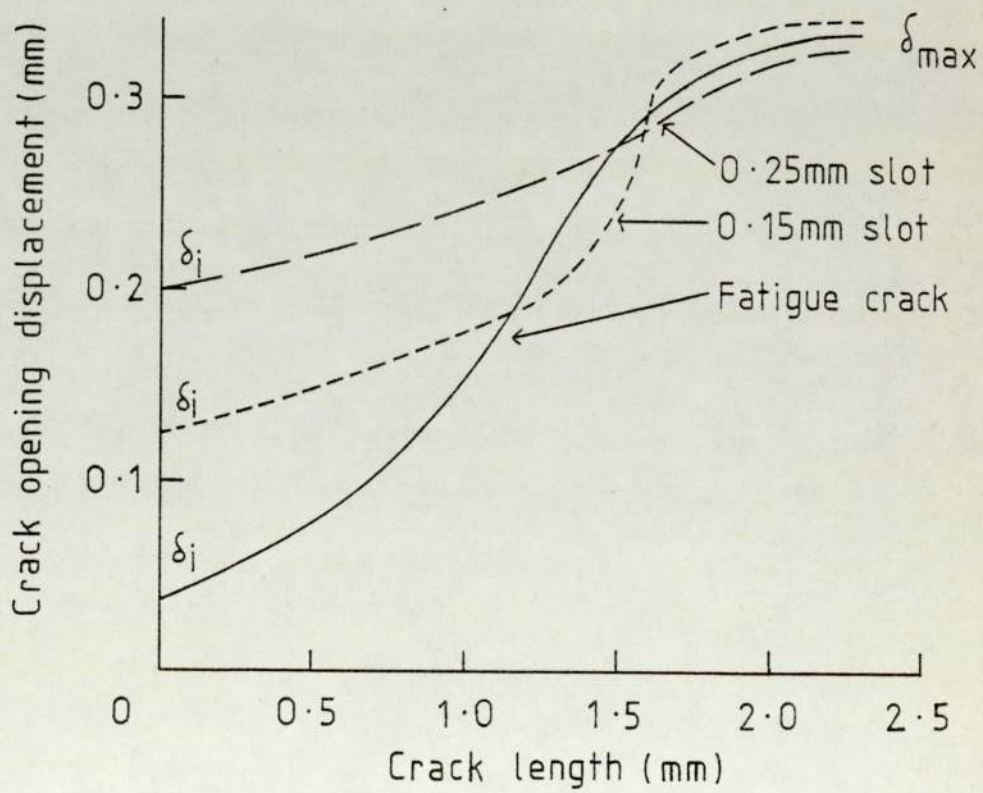

Fig.15. The effect of notch width on COD and crack growth

length 2a to increase to a new length 2c. The difference between the original and new crack lengths (2c - 2a) corresponds to plastically deformed areas at the crack tip. A restraining stress 'x' acts at the regions of plasticity, thus preventing the crack from opening.

Wells (15) by applying the Dugdale model to fracture observed that the tip of the slit opened with a near square ended contour. From this he proposed that the fracture behaviour in the vicinity of a crack could be represented by the " crack surfaces opening displacement " (C.O.D.). Furthermore, fracture would occur at a critical value of crack opening displacement, δ_c. In fig.14 if the restraining stress 'x' = σ_y and the length of the new crack 2c is replaced in terms of 'a', then:

$$\frac{a}{c} = \frac{\cos\pi}{2} \cdot \frac{\sigma}{\sigma_y} \quad \ldots\ldots \quad (29)$$

Where σ is a uniform applied stress. From this the crack opening displacement δ is given by:

$$\delta = \frac{8\sigma_y a}{\pi E} \cdot \log \sec \frac{\pi\sigma}{2\sigma_y} \quad \ldots\ldots \quad (30)$$

Using a series expansion for $\log \sec \left[\left(\frac{\pi}{2}\right)\left(\frac{\sigma}{\sigma_y}\right)\right]$ it was found that:

$$\delta = \frac{8\sigma_y a}{\pi E}\left[\frac{1}{2}\left(\frac{\pi}{2}\cdot\frac{\sigma}{\sigma_y}\right)^2 + \frac{1}{12}\left(\frac{\pi}{2}\cdot\frac{\sigma}{\sigma_y}\right)^4 + \frac{1}{45}\left(\frac{\pi}{2}\cdot\frac{\sigma}{\sigma_y}\right)^6 + \ldots\right] \quad (31)$$

If the applied stress σ is less than about $\frac{3}{4}$ σ_y then equation (31) approximates to:

$$\delta = \frac{\pi\sigma^2 a}{E\sigma_y} \quad \ldots\ldots \quad (32)$$

2.4.2.2 Correlation between C.O.D., G and K.

With reference to equations (7) and (22) it can be shown that the strain energy release rate for a centre crack, in an infinite plate may

be given by:

$$G = \frac{\pi\sigma^2 a}{E} = \sigma_y \delta \quad . \quad . \quad . \quad . \quad (33)$$

If the correction factor, r_y, for plane stress is incorporated in equation (33) such that $2c = 2\,(a + r_y)$ then the modified expression for G will be:

$$G = \sigma_y \delta \left[1 + \frac{1}{2}\left(\frac{\sigma}{\sigma_y}\right)^2\right] \quad . \quad . \quad . \quad (34)$$

Which represents an extension of L.E.F.M. into plane stress conditions. For plane strain conditions G has been represented by:

$$G = M\sigma_y \delta \quad . \quad . \quad . \quad . \quad . \quad . \quad (35)$$

Where M at the present is the subject of much controversy, owing to the discrepancies between theoretical and practical values. M values available from the literature, together with their corresponding references are listed below:

$M = \frac{\pi}{4}$	Wells. (15) plane stress.
$M = 1$	Bilby, Cottrell and Swindon (12) anti-plane strain.
$M = \frac{2}{3}(1 - \nu^2)$	Hahn and Rosenfield. (16) plane strain.
$M = 2.2\,(1 - \nu^2)$	Finite element analysis (17, 18 and 19) plane strain.
$M = 2 \pm 0.5$	Wells (18) plane strain (experimental).

Generally, M is taken as 1 in plane stress and 2 in plane strain.

An equivalent form of equation (14) in section 2.2 may be written as:

$$K_{1c}^2 = G_{1c} E / (1 - \nu^2) \quad . \quad . \quad (36)$$

By combining equations (34) and (35) it can at once be seen that

$$K_{1c} = \sqrt{\frac{M.E.\sigma_y \delta}{(1 - \nu^2)}} \qquad (37)$$

2.4.2.3 Crack opening displacement at initiation δ_i.

The crack opening displacement δ in many materials is difficult to physically define, since the crack profiles may not be 'square ended' owing to material effects such as micro structure, grain size, inclusions, porosity etcetera. Wells and Burdekin (20) have suggested that the crack opening displacement should be taken at the elastic - plastic boundary. Large scale yielding, however, would tend to move the boundary so far along the crack flanks that the C.O.D. would depend on the crack length. Dawes (21) has proposed that owing to stretching of the crack tip from its original position, the C.O.D. should be defined as the displacement at the original crack tip position. According to Dawes this definition will be independent of crack tip profile and position of the elastic - plastic boundary.

δ_i, the value at which initiation from an existing crack occurs, is at present the parameter which comes nearest to being a material property. Work of this nature has been carried out by Smith and Knott (22). They took several specimens, containing either fatigue cracks or slots of various widths and loaded them to stages on a load - crack opening displacement curve. By then breaking the specimens open in liquid nitrogen it was possible to measure the fibrous crack length in each case. Fig.15 shows these fibrous crack lengths as a function of C.O.D. From these graphs δ_i was then estimated by extrapolating the curves to zero.

Subsequent work on the crack opening displacement at initiation shows that the value δ_i can be detected using the potential drop technique (detailed in Draft for Development 19 (23)). Here δ_i may be characterised by the first change in potential between two probes spot welded on opposite faces of a crack mouth. Whilst this technique may be used with some aluminium alloys and steels, crack extension is often so gradual that no sharp change in potential may be observed. δ_i does

appear to be a promising parameter for characterising fracture after general yielding, since the problem of stable crack growth and its interpretation is not relevant at initiation.

2.4.3 J - Integral analysis.

2.4.3.1 Definition.

The Rice (24) J contour integral parameter is a method of characterising stress - strain fields near a crack tip by an integration path remote from the crack tip. This integration path may then by substituted for a path closer to the crack tip region, since any integral taken in an anticlockwise sense from the lower crack face to the upper crack face will be path independent (see fig.16). By adopting this approach fracture may be examined at plastically deformed crack tips, possibly with limited amounts of stable crack propagation. For two dimensional elastic - plastic conditions J is defined as:

$$J = \int_R W dy - T_i \frac{du_i}{dx} ds \quad \cdot \quad \cdot \quad \cdot \quad (38)$$

Where: R is the contour surrounding the crack tip.

W is the strain energy density given by:

$$W = W(\varepsilon) = \int_0^{\varepsilon} \sigma_{ij} \, d\varepsilon_{ij} \quad \cdot \quad \cdot \quad (39)$$

$T_i dU_i$ are work terms when components of surface tractions on the contour path R move through displacements dU_i.

S is the arc length along the contour path R.

Rice has proved path independence by considering <u>any</u> closed path R' which encloses an area A' (providing the path does not cross the crack). From Rice's integral the contribution to J along any crack surface = 0, since dy = 0 and T_i = 0, therefore:

$J_R + J_{R'} = J_{\text{closed path}} = 0$ <u>or</u> $J_R = J_{R'}$ (see fig.16).

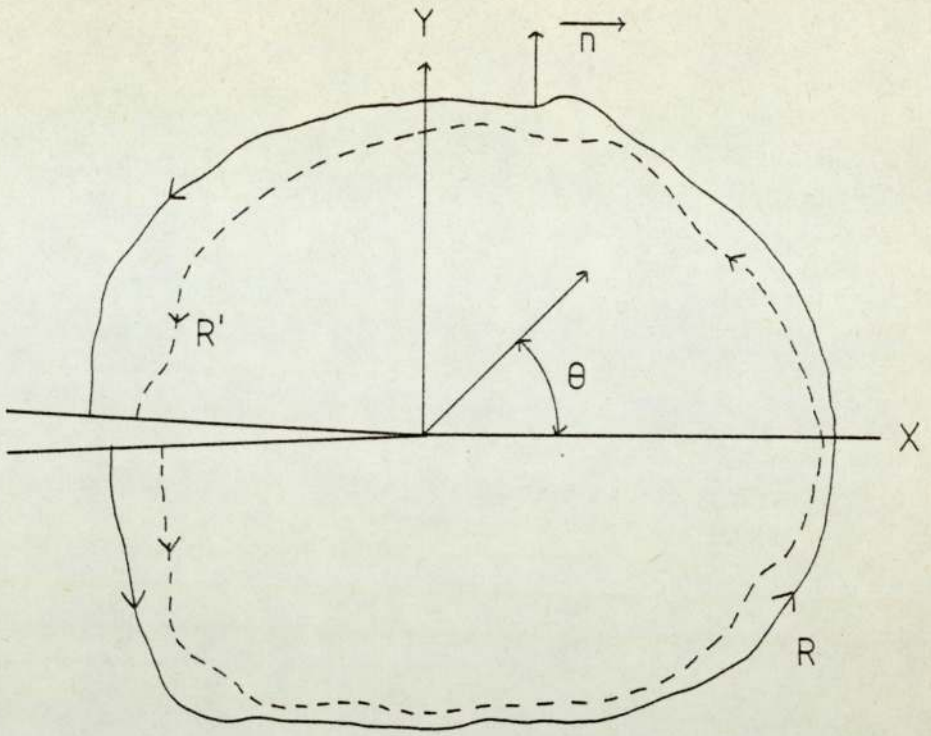

Fig. 16. Arbitrary line integral contours at a crack tip

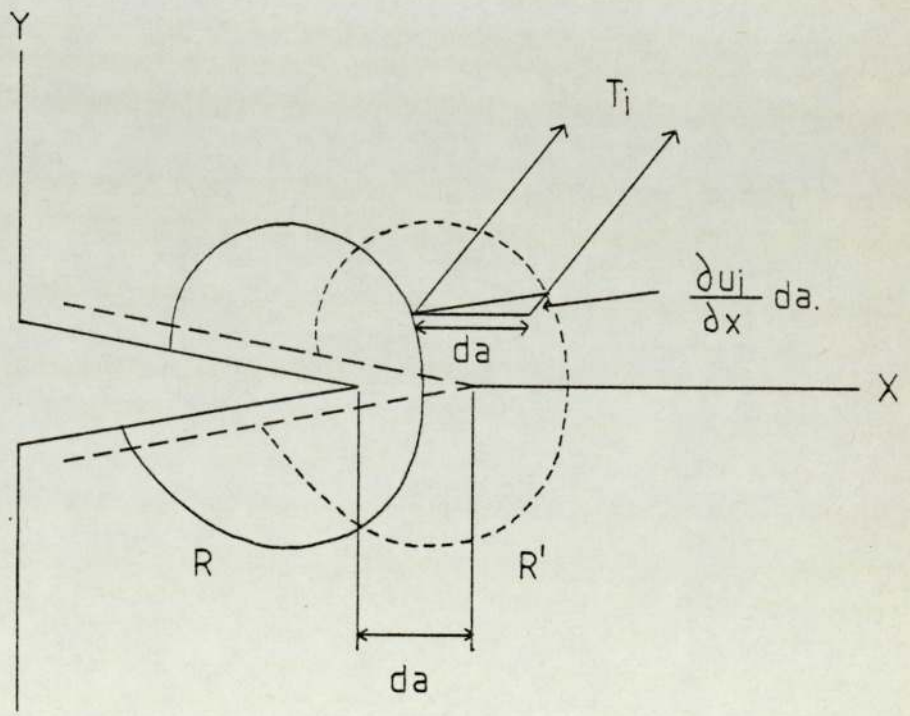

Fig. 17. The J integral applied to crack extension

2.4.3.2 Interpretation of the J integral parameter.

Consider fig.17 where da represents some crack extension. The original contour position R is shown as the full line whilst the new contour R', a distance da away, is shown as the dotted line.

$$\text{IF } J = \int_R W dy - \int_R T_i \frac{du_i}{dx} ds \qquad (40)$$

Then by multiplying each term by da we obtain:

$$Jda = \int W dy da - \int T_i \frac{du_i}{dx} ds da \qquad (41)$$

Where Jda represents the total amount of energy available for crack extension da. Jda is identical for all contour paths, including the one very close to the crack tip, because of the path independence of J. Rice (25) has shown that as the J integral parameter corresponds to crack tip deformation, it must be related to energy balance conditions. J may therefore, be represented as the difference in potential energy between two, identically loaded bodies, having crack lengths of a and a + da respectively (as shown in fig.18) for unit thickness B:

$$J = -\lim_{\Delta a \to 0} \frac{U(a+\Delta a) - U(a)}{\Delta a} = -\frac{\partial U}{\partial a} \qquad (42)$$

2.4.3.3 Applicability of the J integral parameter.

The application of the J integral to fracture analysis comes from viewing the stress and strain fields surrounding a crack tip. In fig. 19a three distinct areas around a crack tip are shown diagrammatically namely:

a) elastic b) plastic c) intensely deformed zone

The elastic approach to the problem is only appropriate when the crack tip plastic zone size r_y is small compared with the other dimensions of the body. L.E.F.M. is therefore, only applicable for

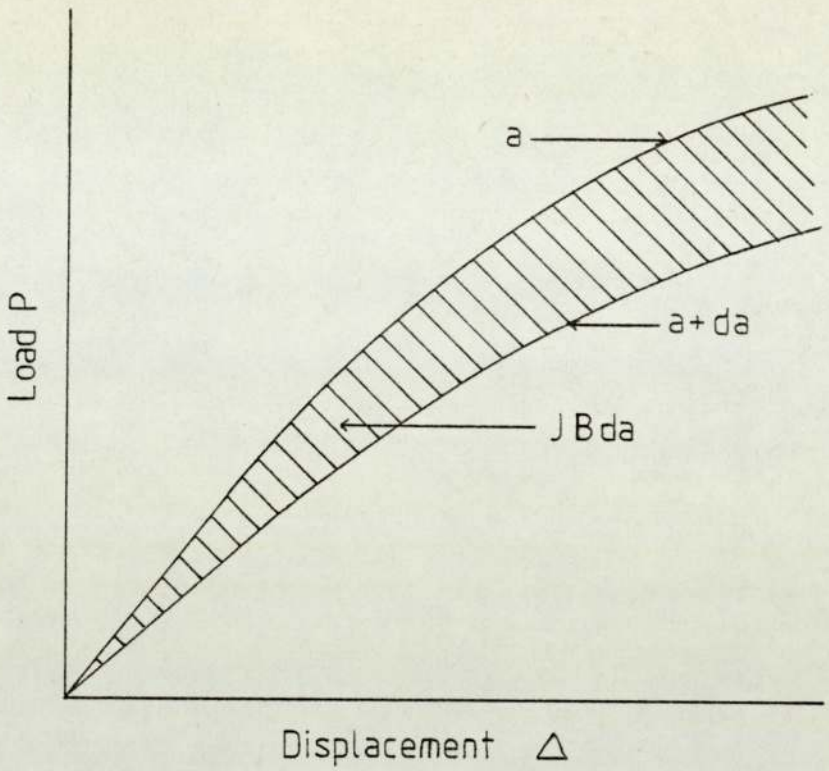

Fig.18. Evaluation of the J integral.

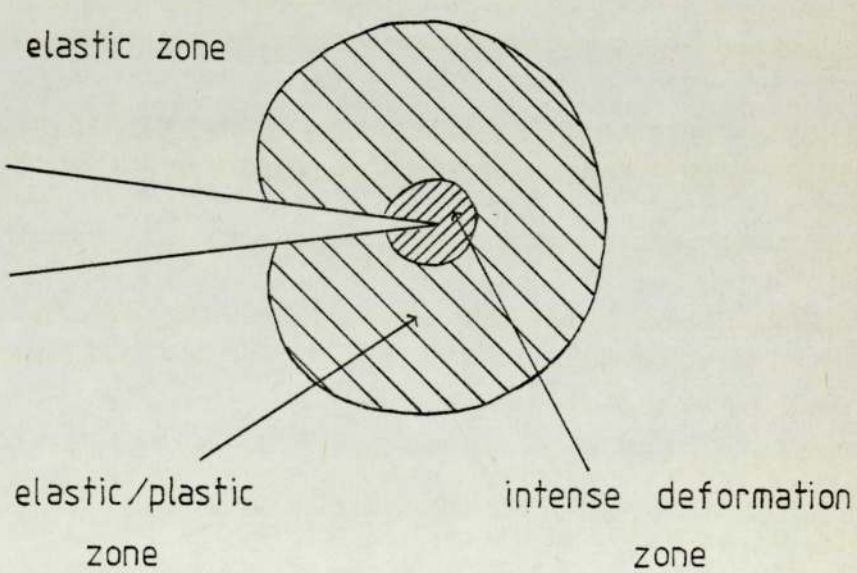

Fig.19a. Areas surrounding a crack tip.

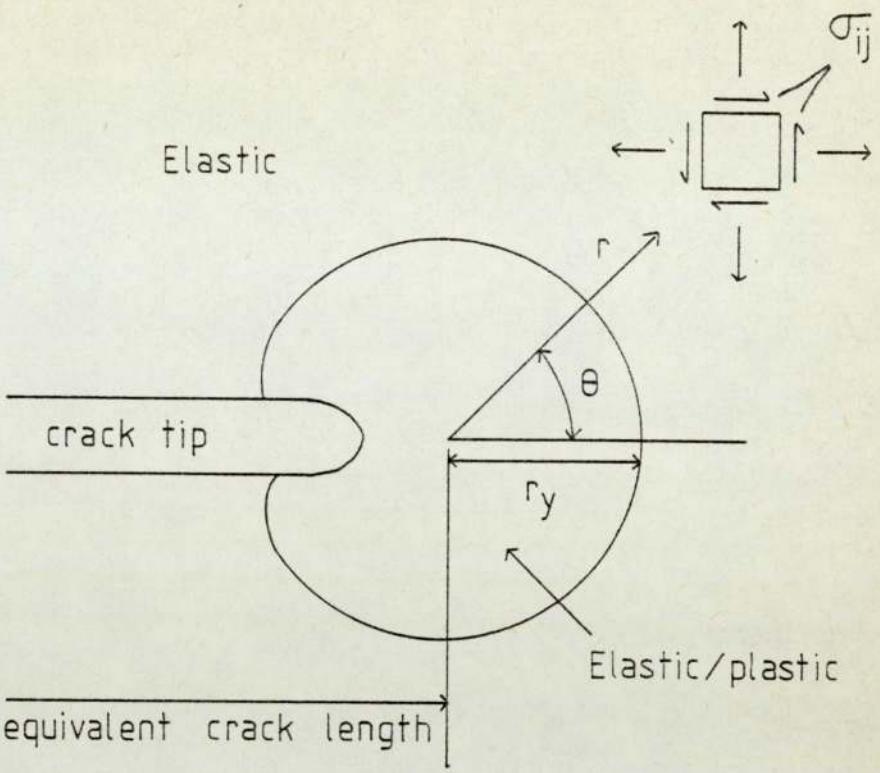

Fig.19b. The elastic condition at a crack tip

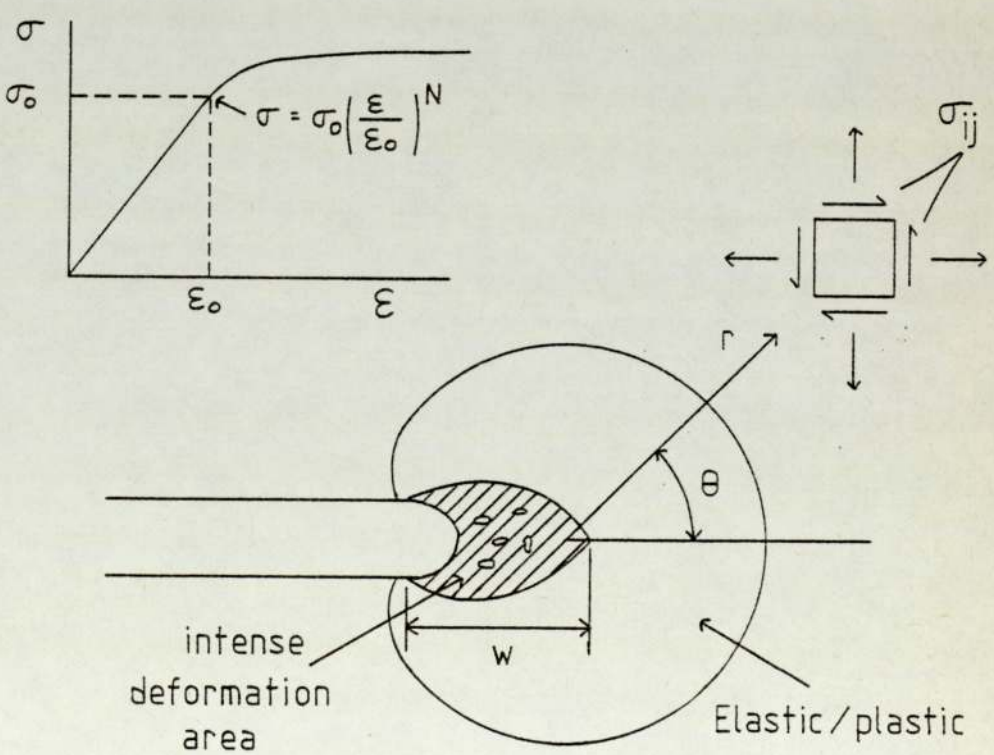

Fig. 19c. The elastic/plastic condition at a crack tip

small scale yielding. The distribution of the stresses for the elastic condition may be given in terms of σ_{ij} (see fig.19b) where:

$$\sigma_{ij} = \frac{K}{\sqrt{r}} \Sigma f(\theta) \quad . \quad . \quad . \quad (43)$$

for $2r_y < r << $ body planar dimensions (r_y is given in equation (15)).

The elastic - plastic condition around a crack tip is illustrated in fig.19c. The stress and strain intensity factors at the tip of a crack have been derived independently by Hutchinson (26) and Rice and Rosengren (27). The dependence of distance r from the crack tip may be given in the form:

$$\sigma \propto \frac{1}{r^{1/N+1}} \sigma(\theta) \quad . \quad . \quad . \quad . \quad (44a)$$

$$\varepsilon^p \propto \frac{1}{r^{N/N+1}} \varepsilon(\theta) \quad . \quad . \quad . \quad . \quad (44b)$$

$$\text{displacements } U \propto r^{1/(N+1)} U(\theta) \quad . \quad . \quad (44c)$$

where N is the strain hardening exponent. Note that for the linear elastic condition N = 1, therefore the elastic - plastic equation (44a) reduces to the L.E.F.M. equation (43). The methods used by Hutchinson and Rice and Rosengren are thus similar to the derivation of the L.E.F.M. factor described by Hayes (28).

In linear elastic fracture mechanics the recommended minimum specimen thickness, in order to obtain valid K_{1c} results, is given by: (see also section 2.3.2)

$$B \geq 4{\cdot}0\left(\frac{K_{1c}}{\sigma_{ys}}\right)^2 \quad . \quad . \quad . \quad . \quad (45)$$

Similarly, in elastic - plastic fracture mechanics there will be thickness limitations, as the size of the intense deformation zone must be

small compared with the planar dimensions, in order for the J integral analysis to be appropriate. Begley and Landes (29) have suggested from their results on bend specimens that the thickness B should be greater than:

$$B > 25 \cdot 0 \frac{J_{1c}}{\sigma_{ys}} \quad \cdot \quad \cdot \quad \cdot \quad \cdot \quad \cdot \quad (46)$$

since, at thicknesses less than this value they found some variation in the value of J_{1c}.

Experimental evidence in support of the J integral as a parameter for describing fracture, has been produced by Landes and Begley (30). They obtained several load - displacement records for various specimens with differing crack lengths (see fig.20a). By then evaluating the area under each individual curve, up to a specific displacement, they were able to construct graphs of energy per unit thickness against crack length for a variety of displacements (see fig.20b). The gradients of these curves, shown in fig.20b, represent the change in potential energy per unit thickness per change in crack length and are therefore equivalent to J. To estimate the critical value of J (J_{1c}) J was plotted against displacement. J_{1c} then corresponded to the point at which the average displacement at failure cut the curve, as shown in fig.20c.

The suggested procedure for the determination of J_{1c} proposed by Landes and Begley has highlighted the advantages and limitations of using the J integral as a characterising parameter for fracture. One of the possible limitations could be the difference in slip line fields for dissimilar configurations. This would mean that J would have to be restricted to contained plasticity. Begley and Landes (29) have shown, however, that for two independent geometries the difference in slip line was of no consequence and both geometries gave the same value of J_{1c}. This supports their theories on crack tip "blunting"

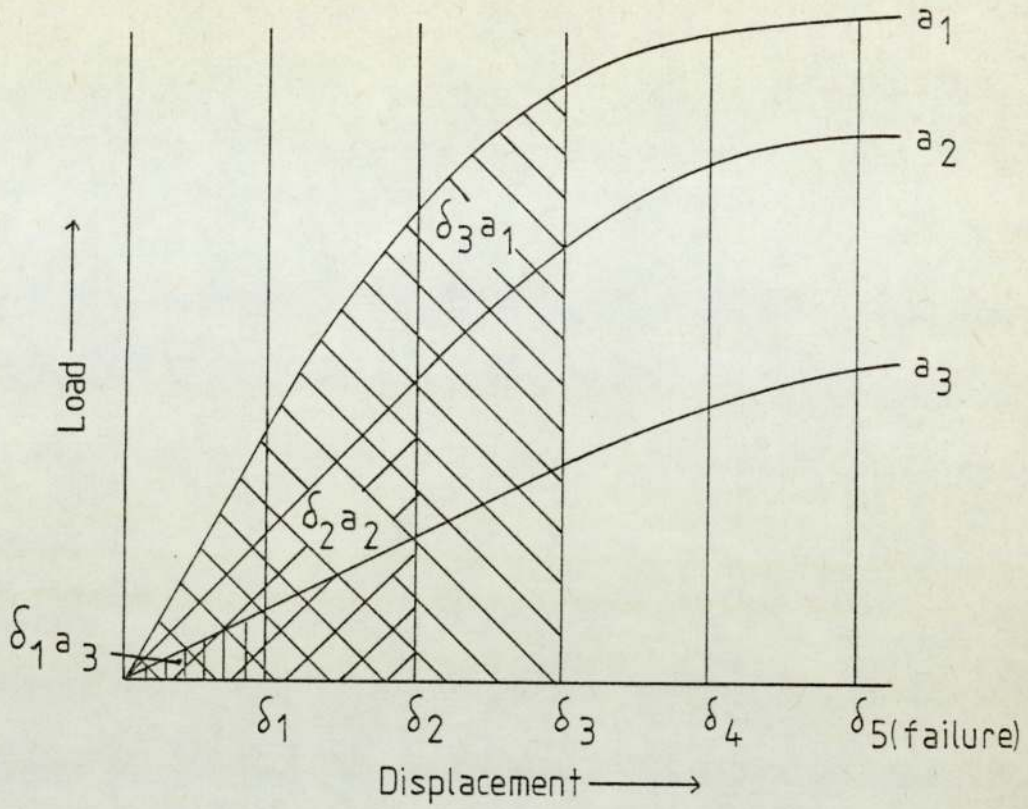

Fig.20a. Compliance curves for various crack lengths with the areas up to specific displacements

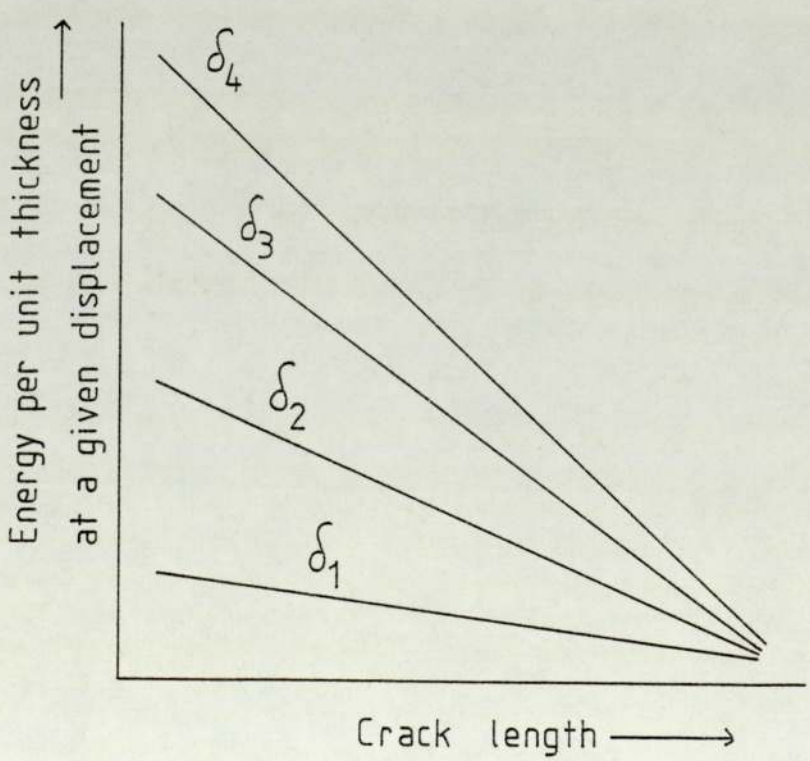

Fig. 20b. Energy absorbed versus crack length for specific displacements

overriding the effect of slip line field formation.

The advantage of the J integral approach is that it may be used to describe conditions at the crack tip, where analysis by existing methods are most subject to error. In linear elastic conditions J is equivalent to G and as J is a field parameter it may be related to the crack opening displacement in the same manner as G (see section 2.4.2.2). The J integral approach potentially offers promising applications in elastic - plastic fracture analysis of complex structures.

2.4.4 R - Curve analysis.

The concept of describing fracture by resistance (R) curves was introduced by Irwin and Kies (31). They found that "the strain energy release rate and the fracturing work rate must be equal at the onset of instability and that they are unlikely to differ widely in magnitude as fracturing continues" (see fig.21). Krafft et al (32) have represented the Irwin and Kies concept in the form of relative crack extension, illustrated in fig.22. Here the critical value of G, G_c, is given by the tangent of the G curve to the R curve, where G is the crack driving force and R is the crack growth resistance.

An R curve is a plot of crack growth resistance against slow stable crack extension. Although K_R (the driving force for stable crack extension) is calculated from the effective crack length, it is usually plotted against actual crack extension. At the point of instability (given as the point of tangency between the K_R and K curves) K_R is equivalent to K_c (the plane stress critical stress intensity factor). K_c, however, is not a material property and depends on: temperature, strain rate, body thickness and initial crack length. Whereas, K_{1c} (the plane strain critical stress intensity factor) only depends on temperature and strain rate.

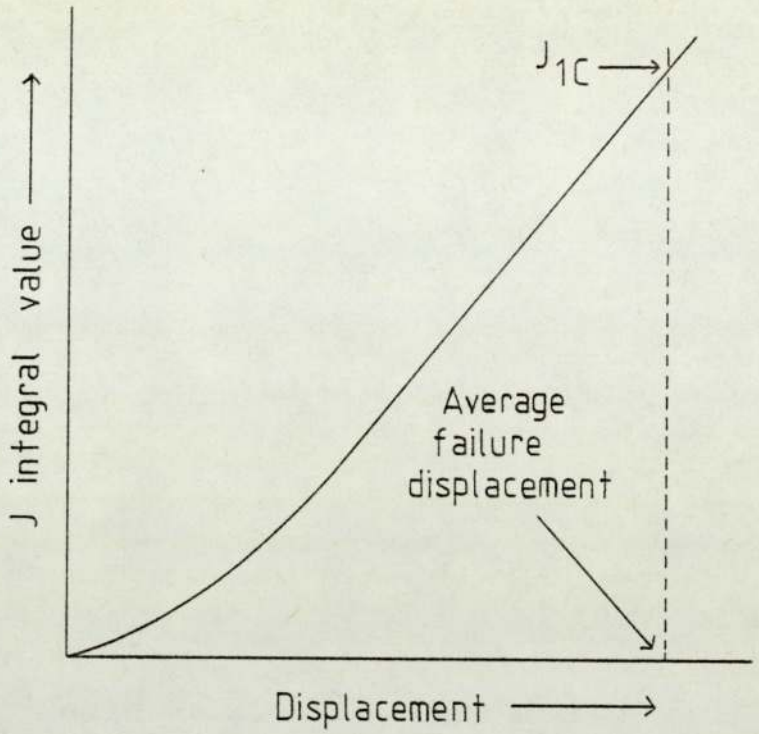

Fig. 20c. The J integral as a function of displacement

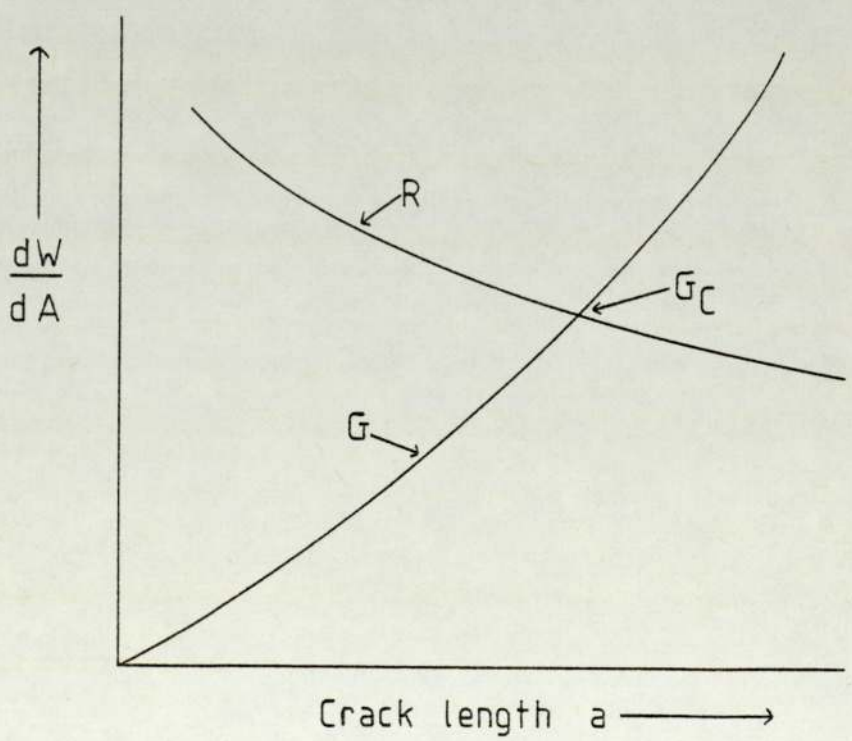

Fig. 21. The original Irwin and Kies R-curve concept

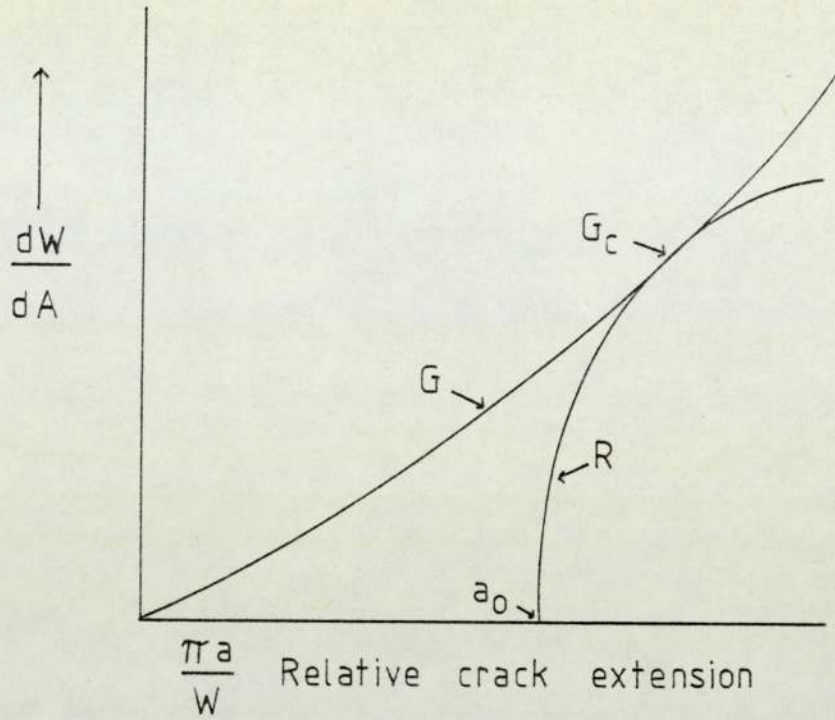

Fig. 22. G and R as functions of relative crack extension

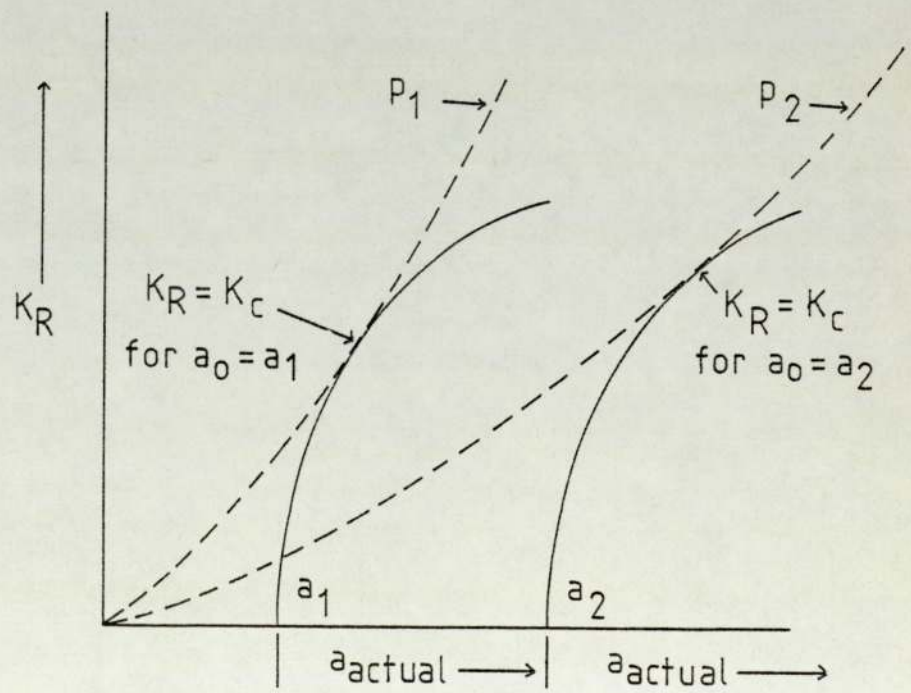

Fig. 23. K_c determination from R curves

The effect of initial crack length on K_c for a specific thickness is shown in fig.23 (35). Here a_1 and a_2 are two different initial crack lengths and the curves p_1 and p_2 represent the K lines for loads of P_1 and P_2 respectively, where $P_1 > P_2$. As an R curve gives the variation of K_c with change in initial crack length, it is only dependent on three variables namely: temperature, strain rate, and thickness. R curves, therefore, may be used to characterise plane stress or mixed plane stress and plane strain fracture behaviour.

The methods available for R curve determination are given in A.S.T.M. 527 (33) and more recently in the A.S.T.M. standards (34). R curves may be obtained experimentally by either "load control" or "displacement control" methods. Generally displacement control is preferred as it allows the R curve to be obtained after the point of instability where $K_R = K_c$. The relationship between the two methods has been investigated by Heyler and Mc cabe (35 and 36) but only for L.E.F.M. conditions.

An alternative method for R curve determination has been suggested by Judy and Goode (37). They took several specimens of differing widths and thicknesses and found the total energy to failure for each case. By then dividing the fracture energy by the remaining ligament area and plotting this against crack extension, the fracture energy could be given by:

$$U = R_\rho (\Delta a)^2 B^{\frac{1}{2}} \quad . \quad . \quad . \quad . \quad (47)$$

where R_ρ is a constant dependent on the resistance of the material to fracture. As R_ρ and B are known quantities, the slope of the R curve U/B.(B - a) versus Δ a may be determined.

R curve analysis may be used to describe the fracture behaviour of specific thin sections and in some cases where ductile tearing is

prevalent. In the majority of structural components, however, it is not a practicable method, because:

a) The R curves obtained may not be relevant to the structure.

b) Construction of the driving force curves is only, as yet, possible by elastic - plastic finite element analysis.

c) Although an allowance was made for the plastic zone size in estimating the effective crack length for producing R curves, the shape of the crack front was assumed to remain constant, during slow stable crack growth.

Neale (38) has proposed, using finite element analysis, that as a crack propagates there will be an increase in load as the crack becomes more bowed. At the attainment of the maximum load the crack will have arrested into a thumbnail crack shape*. According to Neale this shape will be a consequence of specimen thickness and mixed plane stress and plane strain states. The assumption that a crack advances with a constant front shape, in R curve analysis, may therefore be an over simplification.

For these reasons the majority of research in yielding fracture mechanics has concentrated on the techniques of crack opening displacement and J integral analysis.

* The effect of curved crack fronts is dealt with in detail in section 3.

3. THEORETICAL CONSIDERATIONS.

3.1 Finite element analysis.

3.1.1 Introduction.

Analytical solutions are mathematical expressions which describe the value of desired, unknown quantities at any point within a body, consequently they must be valid for an infinite number of points within that body. Analytical solutions are therefore, limited to certain simplified situations. For the more complex engineering problem it is necessary to resort to numerical methods (39 and 40) which give approximate, but acceptable solutions. Numerical methods usually involve the dividing of a structure into a discrete number of points or units. This process is known as discretization and is the basis of finite element analysis (41 and 42).

Finite element analysis is the representation of a structure by an assemblance of numerous sub - divisions, called elements. These elements (which may be triangles or quadrilaterals, for two dimensional analysis, or tetrahedra, hexahedra and rectangular prisms, for three dimensional analysis) interconnect at nodal points or nodes. Fig.24 shows a two dimensional representation of a finite element mesh. In order to analyse a finite element mesh any one of the following procedures may be employed:

a) The displacement method; where the displacements are the primary unknown quantities.

b) The equilibrium method; where the stresses are the primary unknown quantities.

c) The mixed method; where both displacements and stresses are the primary unknown quantities.

In subsequent sections the "stiffness matrix" of a basic element,

using the equilibrium method, will be determined as this is the basic unit for solving problems by finite element analysis.

3.1.2 Displacements.

Consider the triangular element of unit thickness illustrated in fig.25. This element has, at each corner, nodes (given by i, j and k with co-ordinates in the form (x,y)). The displacements of the element are represented in terms of (u,v) for each node. Assuming that the displacement components u and v va ry linearly with x and y we may write:

$$\begin{aligned} u &= C_1 + C_2x + C_3y \\ v &= C_4 + C_5x + C_6y \end{aligned} \qquad \ldots\ldots (48)$$

where the constants C_1 to C_6 are chosen so that:

at node i $u = u_i$, at node j $u = u_j$, and at node k $u = u_k$

$v = v_i$, $v = v_j$, $v = v_k$

Therefore 6 equations result, namely:

$$\begin{aligned} u_i &= C_1 + C_2x_i + C_3y_i \\ u_j &= C_1 + C_2x_j + C_3y_j \\ u_k &= C_1 + C_2x_k + C_3y_k \end{aligned} \qquad \ldots\ldots (49)$$

$$\begin{aligned} v_i &= C_4 + C_5x_i + C_6y_i \\ v_j &= C_4 + C_5x_j + C_6y_j \\ v_k &= C_4 + C_5x_k + C_6y_k \end{aligned} \qquad \ldots\ldots (50)$$

As iteration is the only method of evaluating the constants in the equation above, high speed digital computers are normally used in finite element analysis.

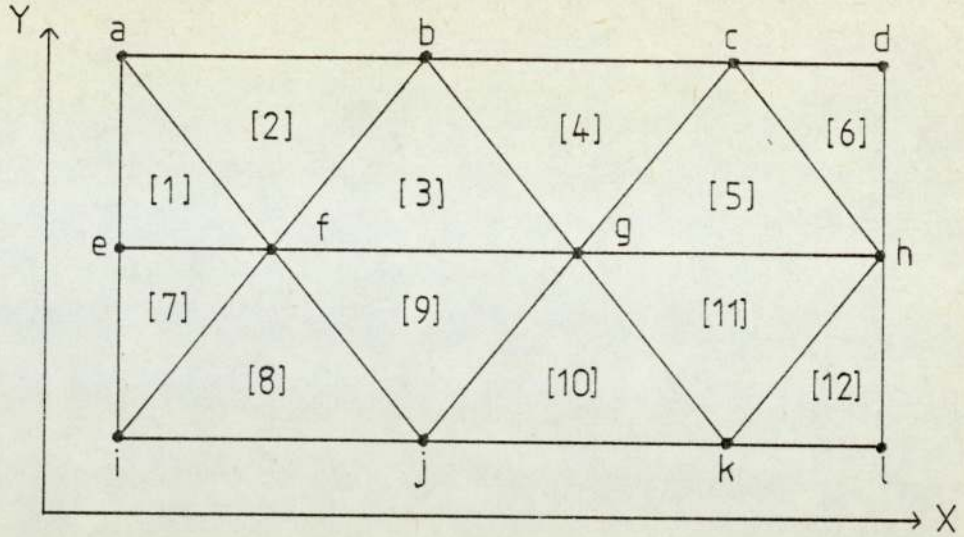

Element numbers [1], [2], [3]---------

Node numbers a,b,c---------------

Fig. 24. Finite element idealisation of a continuum
12 elements and 12 nodes

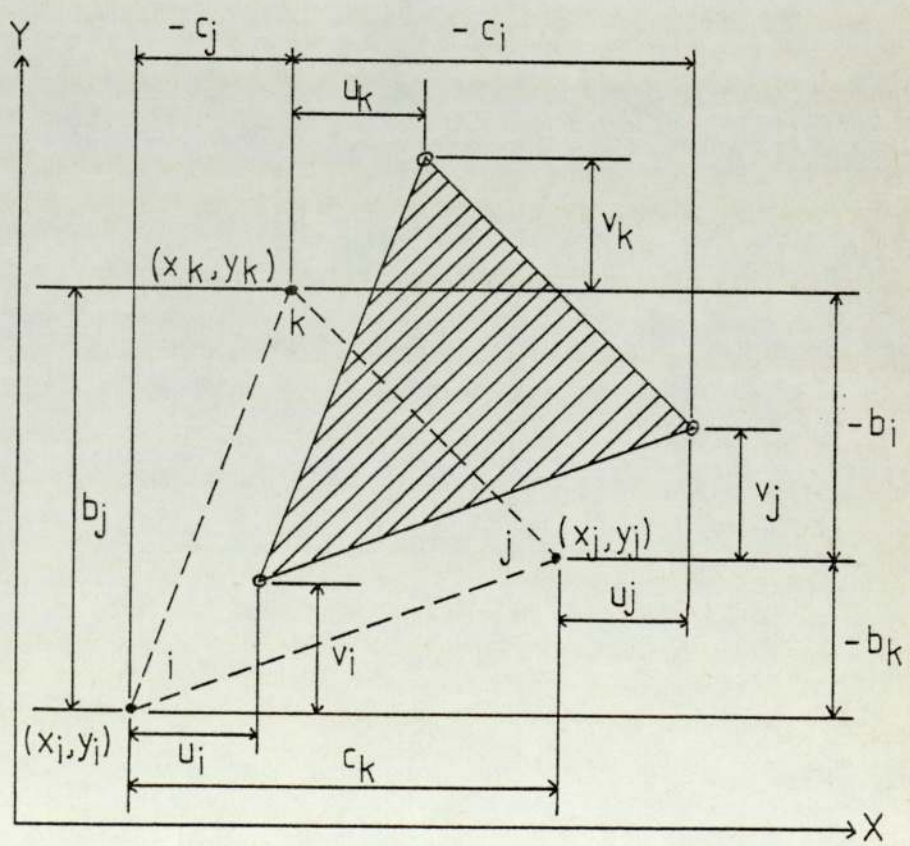

Fig. 25. Dimensions and displacements of a triangular element

Equation (49) can now be written in matrix form. i.e.

$$\begin{bmatrix} 1 & x_i & y_i \\ 1 & x_j & y_j \\ 1 & x_k & y_j \end{bmatrix} \begin{Bmatrix} C_1 \\ C_2 \\ C_3 \end{Bmatrix} = \begin{Bmatrix} u_i \\ u_j \\ u_k \end{Bmatrix} \quad . \quad . \quad (51)$$

By dividing by Δ , where Δ =

$$\begin{bmatrix} 1 & x_i & y_i \\ 1 & x_j & y_j \\ 1 & x_k & y_k \end{bmatrix}$$

= twice the area of the triangular element.

and by applying Cramer's rule

$$C_1 = \frac{1}{\Delta} \begin{bmatrix} u_i & x_i & y_i \\ u_j & x_j & y_j \\ u_k & x_k & y_k \end{bmatrix} = \frac{1}{\Delta} (u_i a_i + u_j a_j + u_k a_k) \quad (52)$$

Where the values a_i, a_j, and a_k have been obtained by multiplying out the Δ matrix with respect to the first column.

$$\begin{aligned} a_i &= x_j y_k - x_k y_i \\ a_j &= x_k y_i - x_i y_k \\ a_k &= x_i y_j - x_j y_i \end{aligned} \quad . \quad . \quad . \quad . \quad . \quad . \quad (53)$$

A similar procedure is followed for the other constants, which may be combined to form a single matrix. i.e.

$$\begin{Bmatrix} C_1 \\ C_2 \\ C_3 \\ C_4 \\ C_5 \\ C_6 \end{Bmatrix} = \frac{1}{\Delta} \begin{bmatrix} a_i & 0 & a_j & 0 & a_k & 0 \\ b_i & 0 & b_j & 0 & b_k & 0 \\ c_i & 0 & c_j & 0 & c_k & 0 \\ 0 & a_i & 0 & a_j & 0 & a_k \\ 0 & b_i & 0 & b_j & 0 & b_k \\ 0 & c_i & 0 & c_j & 0 & c_k \end{bmatrix} \begin{Bmatrix} u_i \\ v_i \\ u_j \\ v_j \\ u_k \\ v_k \end{Bmatrix} \quad (54)$$

3.1.3 Strains.

In plane stress for a thin body:

$$\sigma_{zz} \approx \sigma_{yz} \approx \sigma_{zx} = 0 \quad . \quad . \quad . \quad (55)$$

Consider the strain/displacement equations.i.e.

$$\varepsilon_{xx} = \frac{\partial u}{\partial x}\cdot, \quad \varepsilon_{yy} = \frac{\partial v}{\partial y}\cdot, \quad \varepsilon_{zz} = \frac{\partial w}{\partial z}\cdot,$$

$$\varepsilon_{yz} = \frac{1}{2}\left[\frac{\partial v}{\partial z} + \frac{\partial w}{\partial y}\right]\cdot, \quad \varepsilon_{zx} = \frac{1}{2}\left[\frac{\partial w}{\partial x} + \frac{\partial u}{\partial z}\right]\cdot, \quad \varepsilon_{xy} = \frac{1}{2}\left[\frac{\partial u}{\partial y} + \frac{\partial v}{\partial x}\right]. \quad (56)$$

For plane stress these simplify to:

$$\varepsilon_{xx} = \frac{\partial u}{\partial x}\cdot, \quad \varepsilon_{yy} = \frac{\partial v}{\partial y}\cdot, \quad \varepsilon_{xy} = \frac{1}{2}\left(\frac{\partial u}{\partial y} + \frac{\partial v}{\partial x}\right) \quad (57)$$

and from equations (48) and (57) we may write in matrix form:

$$\begin{matrix}\varepsilon_{xx}\\ \varepsilon_{yy}\\ \varepsilon_{xy}\end{matrix} = \frac{1}{\Delta}\begin{bmatrix} b_i & 0 & b_j & 0 & b_k & 0 \\ 0 & c_i & 0 & c_j & 0 & c_k \\ c_i & b_i & c_j & b_j & c_k & b_k \end{bmatrix}\begin{Bmatrix} u_i \\ v_i \\ u_j \\ v_j \\ u_k \\ v_k \end{Bmatrix} \quad (58)$$

or $$\{\varepsilon\} = [B]\{\delta\}^e \quad . \quad . \quad . \quad . \quad . \quad . \quad . \quad . \quad (59)$$

where B is the square bracketed matrix term in equation (58) and lists the nodal displacements. A relationship between strain and displacements has now been formed.

3.1.4 Stress/strain relationships.

The stress/strain relationships for isotropic materials, according to Hooke's law, may be given in a simplified form as:

$$\varepsilon_{xx} = \frac{1}{E}\left(\sigma_{xx} - \nu\sigma_{yy}\right)$$

$$\varepsilon_{yy} = \frac{1}{E}\left(\sigma_{yy} - \nu\sigma_{xx}\right) \quad \cdots \quad (60a)$$

$$\varepsilon_{xy} = \frac{2}{E}\left(1+\nu\right)\sigma_{xy} \qquad \text{for plane stress}$$

$$\varepsilon_{xx} = \frac{1}{E}\left[\sigma_{xx} - \nu\left(\sigma_{yy} + \sigma_{zz}\right)\right]$$

$$\varepsilon_{yy} = \frac{1}{E}\left[\sigma_{yy} - \nu\left(\sigma_{zz} + \sigma_{xx}\right)\right] \quad \cdots \quad (60b)$$

$$\varepsilon_{xy} = \frac{2}{E}\left(1+\nu\right)\sigma_{xy} = \frac{1}{G}\sigma_{xy} \qquad \text{for plane strain}$$

Writing these equations in matrix form we obtain:

$$\{\varepsilon\} = [C]\{\sigma\} \quad \cdots \quad (61)$$

where:

$$\{\varepsilon\} = \begin{Bmatrix} \varepsilon_{xx} \\ \varepsilon_{yy} \\ \varepsilon_{xy} \end{Bmatrix}, \quad \{\sigma\} = \begin{Bmatrix} \sigma_{xx} \\ \sigma_{yy} \\ \sigma_{xy} \end{Bmatrix}$$

$[C]$ is known as the elastic compliance matrix and is inverted to give the "elastic stiffness matrix" $[S]$, where:

$$[S] = \frac{E}{(1-\nu^2)}\begin{bmatrix} 1 & \nu & 0 \\ \nu & 1 & 0 \\ 0 & 0 & (1-\nu)/2 \end{bmatrix} \quad \cdots \quad (62a)$$

for plane stress

or

$$[S] = \frac{E}{(1+\nu)(1-2\nu)} \begin{bmatrix} 1-\nu & \nu & 0 \\ \nu & 1-\nu & 0 \\ 0 & 0 & (1-2\nu)/2 \end{bmatrix} \cdot \quad (62b)$$

for plane strain.

Although the compatability equations are not directly involved with the equilibrium method in finite element analysis they must be satisfied by the strain distributions within the elements if the analysis is to be acceptable. Now that the elastic stiffness matrix has been determined for each individual element, the strain energy stored in each element may be given by:

$$U_e = \frac{1}{2}\int_e \{\varepsilon\}^t [S] \{\varepsilon\} \, d\,vol \quad \cdot \quad \cdot \quad (63)$$

from which the total strain energy in the body can be determined by summing all the individual element values. The potential energy in the system is then found and since this must remain constant at equilibrium:

$$\delta V = 0 = \{\delta q\}^t \left([K]\{q\} - \{Q\} \right) \quad \cdot \quad (64)$$

where $\{q\}$, $\{Q\}$ are the generalised co-ordinates and forces.
The variations in (δq) are taken arbitrary, therefore equation (64) reduces to the stiffness equilibrium equation.

$$[K]\{q\} = \{Q\} \cdot \quad \cdot \quad \cdot \quad \cdot \quad \cdot \quad (65)$$

where K is the assembled stiffness matrix.

Equation (65) may then be solved for q, after imposing certain displacement boundary conditions on the system, hence the element strains and stresses may be determined. (47).

3.2 Stress concentration factors.

The stress concentration factor at the root of a notch is given by the ratio of the maximum and nominal stresses at that notch root. i.e.

$$K_T = \frac{\sigma_{maximum}}{\sigma_{nominal}} \quad . \quad . \quad . \quad . \quad (66)$$

A compedium of stress concentration factors for numerous configurations has been published by Peterson (43) and some of the more important configurations are illustrated in Faupel (44). Stress concentration factors for flat bars containing single notches subjected to pure bending have been determined using a photoelastic technique by Leven and Frocht (45). Fig.26 shows the results of their work where K_T was plotted versus notch root radius divided by remaining ligament length for several notch depths. Providing that the notch root radius is fairly large and the notch is of an intermediate depth, Leven and Frocht's work offers a basis for the description of stresses at notch roots.

Neuber (46) has suggested that the stress concentration factor for a notch of arbitrary depth a, and root radius ρ, subjected to pure bending, may be estimated by combining the equations obtained for deep and shallow notches. i.e.

$$K_{DEEP} = \frac{2\left(\frac{a}{\rho}+1\right) - \alpha_1\sqrt{\frac{a}{\rho}+1}}{\frac{4}{\alpha_2}\left(\frac{a}{\rho}+1\right) - 3\alpha_1} \quad . \quad (67)$$

where $$\alpha_1 = \frac{2\left(\frac{a}{\rho}+1\right)\sqrt{\frac{a}{\rho}}}{\left(\frac{a}{\rho}+1\right)\arctan\left(\sqrt{\frac{a}{\rho}}\right)+\sqrt{\frac{a}{\rho}}}$$

$$\alpha_2 = \frac{4\left(\frac{a}{\rho}\right)\sqrt{\frac{a}{\rho}}}{3\left[\sqrt{\frac{a}{\rho}} + \left(\frac{a}{\rho}-1\right)\arctan\sqrt{\frac{a}{\rho}}\right.}$$

and $K_{shallow} = 1 + 2\sqrt{\frac{a}{\rho}}$ . . . . . (68)

and, therefore by Neuber $K_T = \frac{\left[(K_s - 1)(K_d - 1)\right]}{\left[(K_s - 1)^2 + (K_d - 1)^2\right]}$ . . (69)

Although Neuber's equation is a good approximate for K_T values of arbitrary notch lengths, errors will occur in the value of K_T when the notch is in between the deep and shallow depths. Currently, the most reliable method for determining stress concentration factors in engineering situations is by finite element analysis. (see the previous section). Richards and Wood (47) have evaluated stress concentration factors for a number of single edge notch specimens subjected to both pure and three point bending. Comparison of their results for K_T, obtained by finite element procedures, and data generated by both Leven and Frocht's and Neuber's solutions is given in fig. 27 and detailed in table 2. To obtain K_T values for three point bending was a comparatively simple task of moving the loading points from four to three locations, whilst maintaining the same element mesh size. Richards and Wood have shown that there was excellent agreement between their results, for pure bending, and the data generated by existing methods. It was reasonable to assume, therefore, that the K_T values produced for three point bending were of a similar accuracy to those obtained for pure bending. Although most of the results for three point bending, obtained by Richards and Wood, were for a span length to width ratio of 4 to 1, two results were estimated for an 8 to 1 ratio. The stress concentration factor results for the 8 to 1 ratio, shown in fig.27, fell in between those results for pure bending and 4 to 1 three point bending. It is interesting to note that Brown and Srawley (48) obtained a similar trend for Y, the geometric factor, for stress intensity calculations of sharp cracks (see fig.5).

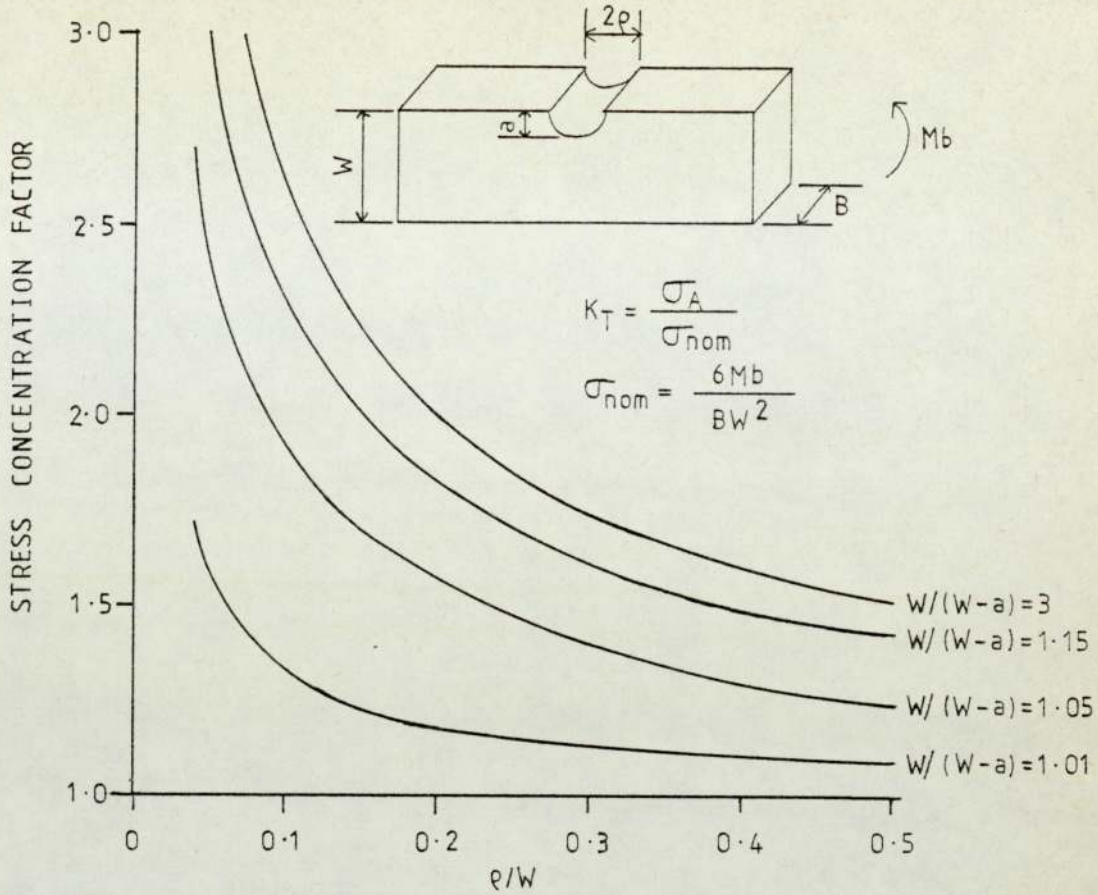

Fig. 26. K_T factors for single notched flat bars in pure bend.

Notch details depth (mm)	root rad (mm)	Stress concentration factors Neuber (pure bend)	Leven & Frocht (pure bend)	F.E.A. (4 pt bend)	F.E.A. (3 pt bend)
20	0.13	10.40	-	10.24	9.61
5	0.13	8.39	-	8.67	8.03
5	0.13	7.97	-	8.20	7.59
5	0.51	4.31	-	4.40	4.09
5	0.76	3.64	-	3.68	3.42
5	6.35	1.70	-	1.60	1.51
10	0.13	7.47	-	7.28	6.84
10	0.76	3.36	3.3	3.22	3.06
10	1.52	2.54	2.38	2.37	2.26
10	3.17	1.94	1.79	1.74	1.69

Table 2. Stress concentration factors.

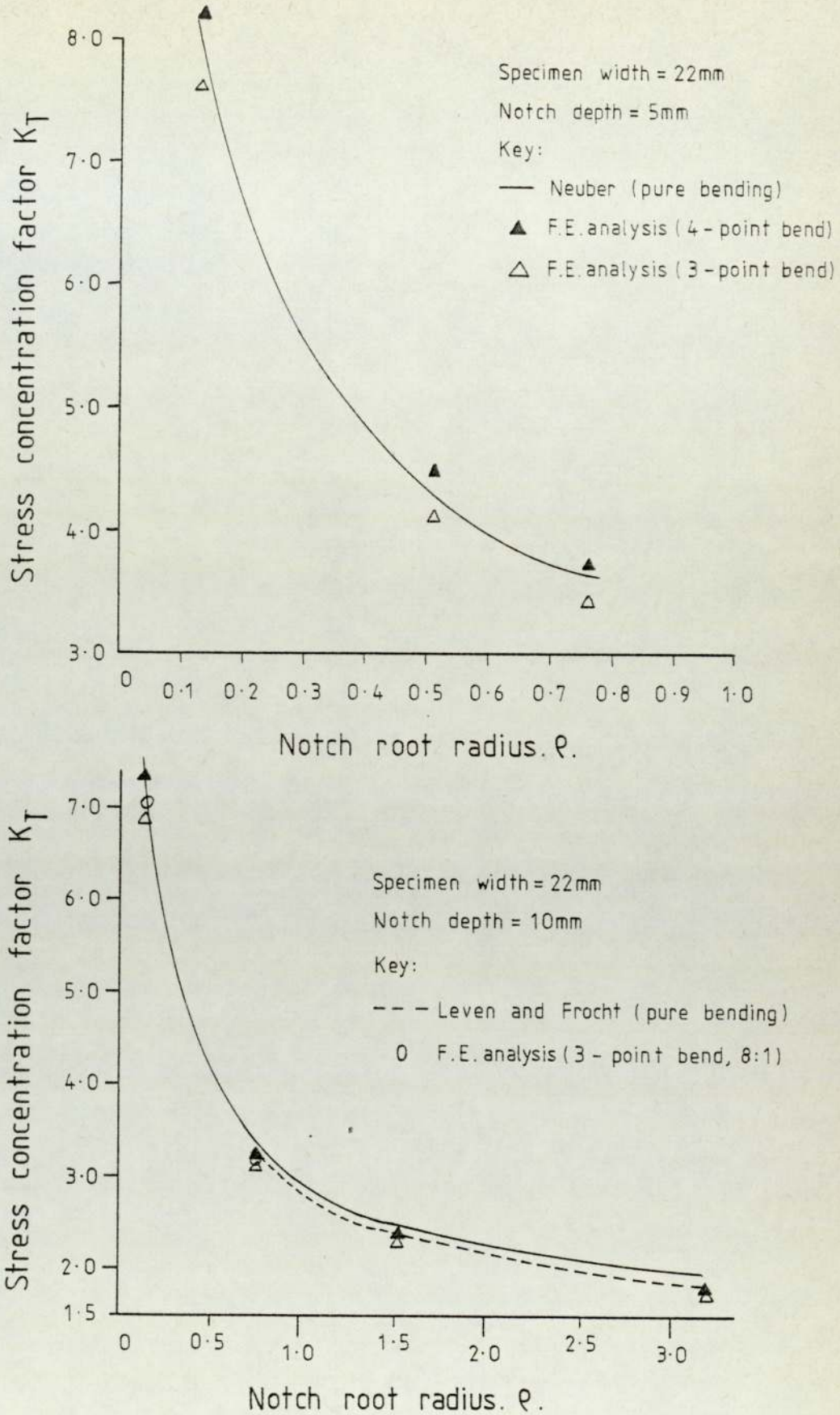

Fig. 27. Stress concentration factors as a function of notch root radius

3.3 Stress intensity factors of sharp cracks emanating from notches.

There are numerous methods available for determining stress intensity factors of sharp cracks in different body configurations. Some of the more widely used methods, together with their accuracy and usefulness, are summarised in a paper by Rooke and Cartright (49). A "Compendium of Stress Intensity Factors" has also been published by Rooke and Cartright (50). The majority of sharp cracks occurring in service, however, initiate and grow from stress concentration sites such as notches, defects or sharp changes in section. The descriptions of stress intensity factors for these conditions are complicated and the methods available for their determination become considerably limited. Finite element analysis offers the greatest potential for solving these types of problems.

Yamamoto et al (51, 52 and 53) have derived stress intensity factor equations, for sharp cracks emanating from semi-elliptical notches, by combining analytical and numerical solutions. By using Koiter's formula (54) Yamamoto and Ao (51) were able to obtain an empirical expression for K_1 for fine cracks emanating from a notch, given by:

$$K_1 = \left[1{\cdot}122(\alpha\sigma_b) + 0{\cdot}683(1{\cdot}19\beta\sigma_b/\rho)c\right]\sqrt{(\pi c)} \quad (70)$$

where $\alpha\sigma_b$ is the stress at the notch root

$\beta\sigma_b/\rho$ is the stress gradient at the notch root

and $\alpha = \gamma\left[1 + 2\sqrt{(a/\rho)}\right]$

$$\beta = -\gamma\left[3 + 4\sqrt{(a/\rho)}\right]$$

$$\gamma = F\left(\frac{a}{\rho}\right)h\left(\frac{a}{w}\right)/1{\cdot}122$$

$$F\left(\frac{a}{\rho}\right) = 1{\cdot}122 - \left[0{\cdot}383\sqrt{\frac{a}{\rho}} - 0{\cdot}102\right]\left[2a/\rho + \sqrt{\frac{a}{\rho}}\right]$$

$$h\left(\frac{a}{w}\right) = 1{\cdot}107 - 1{\cdot}552\,a/w + 7{\cdot}71\left(\frac{a}{w}\right)^2 - 13{\cdot}55\left(\frac{a}{w}\right)^3 + 14{\cdot}25\left(\frac{a}{w}\right)^4$$

where: a is the notch depth, c is the crack length, ρ is the notch root radius, P is the midpoint load, W is the specimen width and L is the specimen span length.

For crack lengths which were greater than a critical value of c, c_o, where c_o is given by:

$$c_o = \xi(W-a)$$

and

$$\xi_o = 1 - \exp\left[-0.5\sqrt{(a\rho)}/(W-a)\right]$$

$K_{1\ deep}$ could be estimated from an "equivalent crack length" (a + c) see fig.28. According to Yamamoto and Ao this value of K_1 also corresponded to the limiting value of K_1 for notch root cracks of length c, as a/ρ tended to infinity. For cracks less than c_o, Yamamoto and Ao have produced an empirical formula for three point bending by combining their numerical solution and equation (70). This formula conforms with equation (70) and is continuous at the condition $c = c_o$. The formula is as follows:

$$K_{1\ shallow} = \sigma_b\left(a_o + a_1\xi + a_2\xi^2 + a_3\xi^3\right)\sqrt{\left[\pi(W-a)\xi\right]} \quad (71)$$

$$K_{1\ deep} = \sigma_b h(\eta)\sqrt{(\pi W \eta)} \quad (72)$$

where: $\xi = c/(W-a)$, $\xi_o = c_o/(W-a)$

$\eta = (a+c)/W$, $\eta_o = (a+c_o)/W$

$a_o = 1.122\alpha$

$a_1 = 0.683 \times 1.19\left(\beta/\rho\right)(W-a)$

$a_2 = -3(a_o - b_o)/\xi_o^2 - (2a_1 + b_1)/\xi_o$

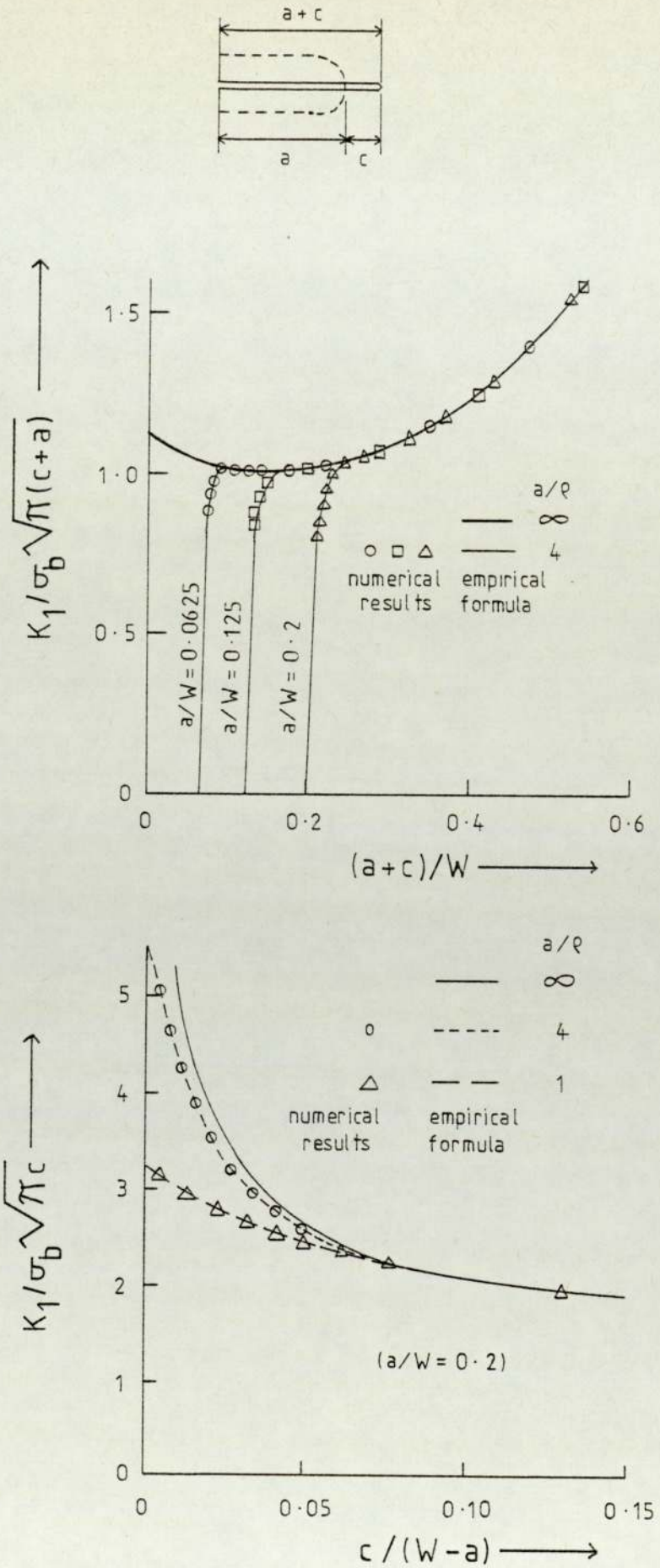

Fig. 28. Dimensionless K_1 values versus functions of c and a+c

$$a_3 = 2(a_0 - b_0)/\xi_0^3 + (a_1 + b_1)\xi_0^2$$

$$b_0 = h(\eta_0)/\sqrt{[(\eta_0 - a/w)/\eta_0]}$$

$$b_1 = 0.5(1 - a/w)[-h(\eta_0)a/w\eta_0^2 + 2d(\eta_0) \times (\eta_0 - a/w)/\eta_0]/\sqrt{[(\eta_0 - a/w)/\eta_0]^3}$$

$$h(\eta) = 1.107 - 1.552\eta + 7.71\eta^2 - 13.55\eta^3 + 14.25\eta^4$$

$$d(\eta_0) = -1.552 + 15.42\eta_0 - 40.65\eta_0^2 + 57\eta_0^3.$$

The results of Yamamoto and Ao's analysis for three point bending is illustrated in fig.28 where it may be seen that there was good agreement between their empirical equation and their numerical solution. An extension of Yamamoto, Ao and Sumi's work (52) on single edge notch tension specimens has been proposed by Jergeus (55). By expressing the width and depth of a notch in elliptical form, so that the semi-minor axis $b = \sqrt{ap}$ and the semi-major axis = a, Jergeus has derived an equation for an equivalent crack length based on earlier work produced by Smith et al (56, 57 and 58) i.e.

$$l = e + c \quad \cdots \quad (73)$$

Where l is the equivalent crack length
e is the contribution due to the notch } see fig.29.
c is the crack length

and (from Jergeus):

$$\frac{e}{a} = \left(1 - \exp\left[-4\left(1 + \frac{a}{b}\right)\frac{c}{b}\right]\right) \quad \cdots \quad (74)$$

values for e/a, obtained by:

a) Jergeus's equation

b) Finite element analysis

are shown as a function of c/b in fig.30. Here, Jergeus's solution

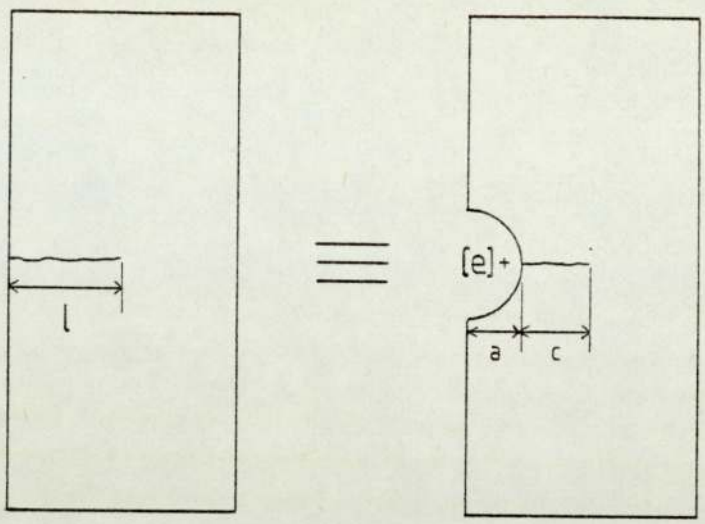

Fig. 29. The equivalent crack length of a notch and crack combined

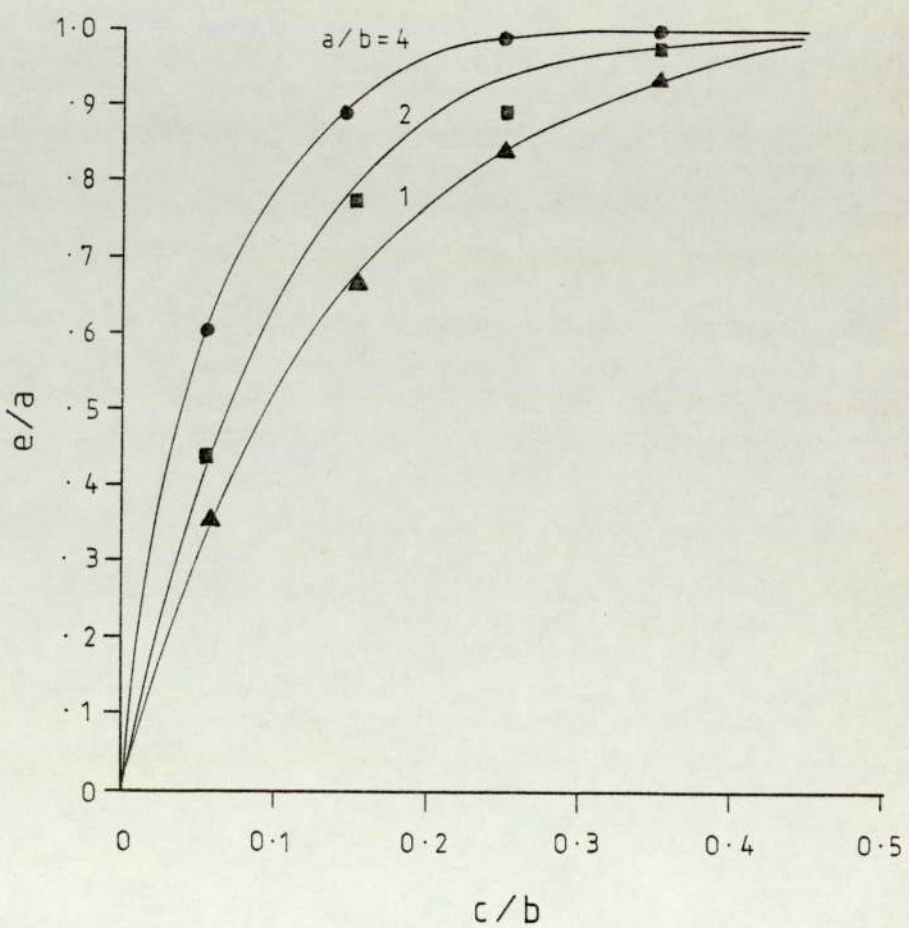

Fig. 30. The notch contribution factor as a function of c.

agreed favourably with both finite element analysis and Nisitani's analysis, in the range of interest (i.e. $0 < c/b < 0.5$). Several workers have recognized the presence of a zone of influence in front of a notch tip. The depth of this zone, given by a critical crack length c_o, however, appears to be the subject of much controversy. Some of the values obtained from the literature and their corresponding references are listed below:

a) $c_o = \xi_o(W - a)$ (given in equation (82); Yamamoto et al (52)

b) $c_o = 0.13\sqrt{a\rho}$; Smith (58)

c) $c_o = 0.25\sqrt{a\rho}$; Novak and Barsom (59)

d) $c_o = 0.5\sqrt{a\rho}$; Smith and Miller (57)

Critical crack lengths for all these conditions are shown as a function of ρ for notch depths of 5 and 10 mm in fig.31. Examination of these curves in fig.31, together with those shown in fig.30 tends to indicate that the zone of influence extends up to a value of about $0.5 - 0.6\sqrt{a\rho}$. Outside this zone the effective crack length may simply be given as the addition of the notch depth and the crack length.

3.4 The effect of notch root radius in fracture mechanics.

3.4.1 Relationships between stress concentration and stress intensity factors.

Stress intensity factors may be estimated from stress concentration factors as the root radius of a notch tends to zero. Irwin (60) has shown that:

$$K_I = \lim_{\rho \to 0} K_T \frac{\sigma_o \sqrt{\pi \rho}}{2} \quad \ldots \quad (75)$$

where $K_T = \dfrac{\sigma_{max}}{\sigma_o}$ and $K_{II} = K_{III} = 0$

The case for a semi-elliptical notch, of depth a, and root radius ρ subjected to a uniform tensile stress, σ_o has recently been examined

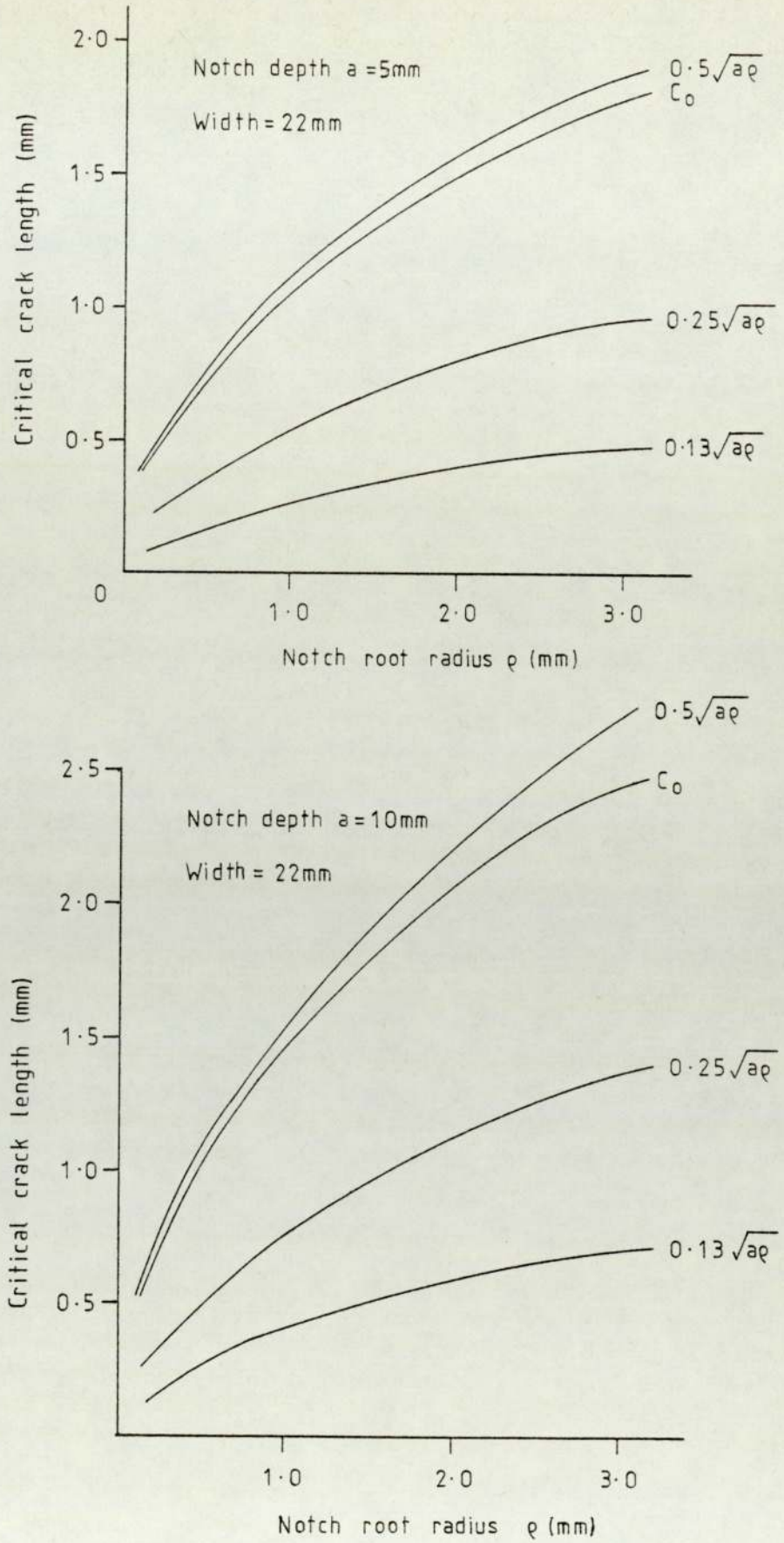

Fig. 31. Critical values of cracks emanating from notches

by Hasebe and Kutunda (61). As the formula for the stress concentration factor, K_T, may be given by:

$$K_T = \sum_{j=1}^{\infty} C_j \left(\frac{\rho}{a}\right)^{0.5j-1} \quad \cdots \quad (76)$$

where C_j = coefficient determined from boundary conditions, and shape,

ρ = notch root radius,

j = (1, 2, 3 - - - - -)

by combining equations (75) and (76) they obtained:

$$K_I = \frac{1}{2} C_j \sigma_o \sqrt{\pi a} \quad \cdots \quad (77)$$

where coefficient C_j could be determined by the following methods.

Method 1

Considering only the first term of the coefficient C_j:

$$K_T = C_1 \left(\frac{\rho}{a}\right)^{-0.5} \quad \cdots \quad (78)$$

where C_1 could be calculated by substituting the appropriate values for ρ/a and K_T.

Method 2

As the ρ/a ratio becomes large the linear relationship between K_T and $\sqrt{\rho/a}$ may not always hold and it becomes necessary to consider the other terms of C_j i.e.

$$K_T = C_1 \sqrt{\frac{a}{\rho}} + C_2$$

$$K_T = C_1 \sqrt{\frac{a}{\rho}} + C_2 + C_3 \sqrt{\frac{\rho}{a}} \quad \cdots \quad (79)$$

$$K_T = C_1 \sqrt{\frac{a}{\rho}} + C_2 + C_3 \sqrt{\frac{\rho}{a}} + C_4 \left(\frac{\rho}{a}\right)$$

$$K_T = C_1 \sqrt{\frac{a}{\rho}} + C_2 + C_3 \sqrt{\frac{\rho}{a}} + C_4 \left(\frac{\rho}{a}\right) + C_5 \left(\frac{\rho}{a}\right)^{1.5}$$

The coefficients above were determined by a least squares of errors

method.

Method 3

In order to obtain K_T values when ρ/a becomes very small, Hasebe and Kutunda have extrapolated their curves, produced from equations (79) to zero. These extrapolated results were then used to determine new coefficients in the equations (79). New values of K_T could then again be determined by extrapolation and by repeating this operation several times, the accuracy of the expression for K_T was improved. Although Hasebe and Kutunda have derived an empirical relationship between K_1 and K_T, their analysis is not appropriate for determining stress intensity factors of short, sharp cracks emanating from blunt notches. It is also thought that as ρ/a approaches zero (i.e. the notch becomes a crack) their extrapolation technique will not be of sufficient accuracy for predicting reliable stress intensity factor values.

3.4.2 Plastic deformation at the tip of a blunt crack.

The situation of blunt cracks, of finite root radius, loaded in uniform tension has been studied by Smith (62). His solution, obtained for anti-plane strain has been regarded as a good approximation to plane strain conditions. More recently Vitek (63 and 64) has produced equations which characterise the plastic deformation ahead of a blunt crack in plane strain conditions. Vitek's work, based on earlier work by Bilby, Cottrell and Swindon (12) and Dugdale (13) was the representation of the plastic zone by an array of edge dislocations. The distribution of these dislocations were then solved numerically as a function of crack root opening displacement and plastic zone size. The results obtained by Vitek are shown in fig.32 and the equations he derived are shown below:

$$\sigma/\sigma_1 = \frac{(\rho/a)}{2+(\rho/a)^{\frac{1}{2}}} + \frac{4}{\pi\left(2+(\rho/a)^{\frac{1}{2}}\right)} \times \arccos \qquad (80)$$

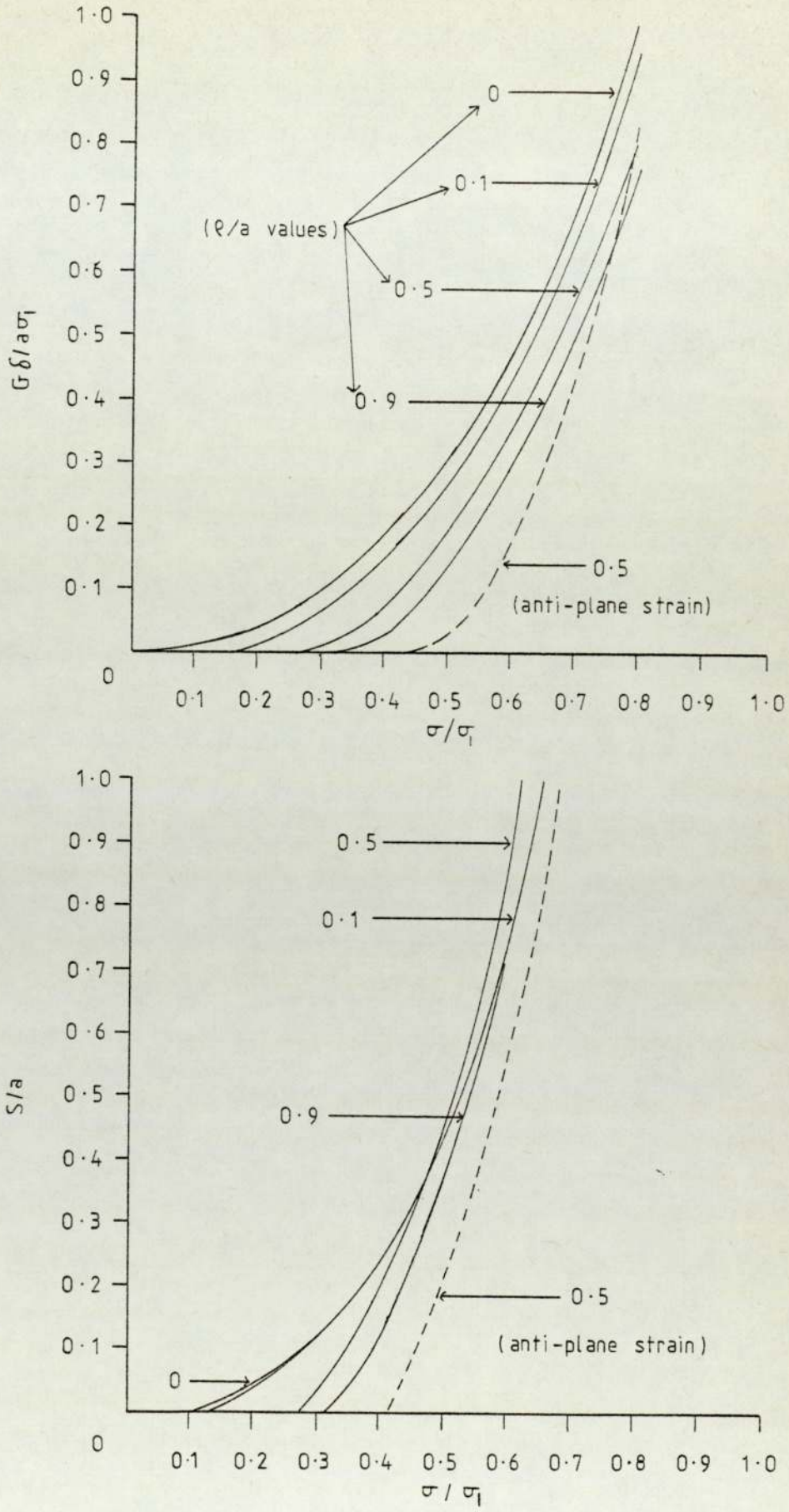

Fig. 32. Dependence of σ/σ_1 on C.O.D. and plastic zone

$$\left[\frac{1-\rho/a}{1+s/a-(\rho/a)^{\frac{1}{2}}\left\{\left[(1+s/a)^2-1+\frac{\rho}{a}\right]^{\frac{1}{2}}-\chi\left(\frac{\rho}{a}\right)s/a\left(1+(s/a)^{\frac{1}{2}}\right)\right\}}\right] \quad (80)$$

where σ = applied uniaxial stress a = crack depth

σ_1 = yield stress s = plastic zone size

ρ = crack root radius $\chi\left(\frac{\rho}{a}\right)$ is a function of $\frac{\rho}{a}$ given in table 3.

Table 3. Numerical values of $\chi(\rho/a)$

$\frac{\rho}{a}$	10^{-4}	5×10^{-4}	10^{-3}	5×10^{-3}	10^{-2}	5×10^{-2}
$\chi\left(\frac{\rho}{a}\right)$	2.20	2.10	2.00	1.70	0.80	0.32
$\frac{\rho}{a}$	0.1	0.2	0.3	0.4	0.5	0.6
$\chi\left(\frac{\rho}{a}\right)$	0.21	0.11	0.08	0.055	0.040	0.032
$\frac{\rho}{a}$	0.7	0.8	0.9	1.0		
$\chi\left(\frac{\rho}{a}\right)$	0.024	0.016	0.008	0		

and

$$\frac{G\delta}{\sigma_1 a} = \frac{4(1-\nu)}{\pi} \times \ln \left\{\sec \frac{1}{2}\pi \left[\frac{\sigma}{\sigma_1}+\left(\frac{\rho}{a}\right)^{\frac{1}{2}}\left(1-\frac{\sigma}{\sigma_1}\right)\left\{2\left(1-\frac{\sigma}{\sigma_1}\right)\left(\frac{\sigma}{\sigma_1}-\frac{(\rho/a)}{2+(\rho/a)^{\frac{1}{2}}}\right)-\frac{1}{2}\right\}\right]\right\} \quad (81)$$

where G = the shear modulus given by: $E/(2(1+\nu))$

δ = the crack opening displacement

σ_1 is identified with the ultimate tensile strength σ_u

(see Heald, Spink and Worthington 1972 (65))

According to Vitek (63) a blunt crack will require a stress greater than:

$$\sigma_1 \left(\frac{\rho}{a}\right)^{\frac{1}{2}} \Big/ \left(2+\left(\frac{\rho}{a}\right)^{\frac{1}{2}}\right) \quad (82)$$

in order to initiate plastic deformation. Consequently at low stress levels both δ and s have values less than those for sharp cracks. As the level of stress is increased, δ increases, but δ is always smaller for larger root radii (see fig.32a). The plastic zone size, however, may be larger for a blunt crack than for a sharp crack, providing the stress level is high enough (see fig.32b). Vitek's results may be applied to the examination of crack initiation and propagation from blunt notches and/or holes. His analysis therefore covers apparent fracture toughness testing.

3.4.3 Apparent stress intensity factors ($K_{A(\rho)}$).

The stress required to propagate fracture from a semi-elliptical notch of semi-major axis c and semi-minor axis b (root radius ρ where $\rho = b^2/c$) contained in an infinite body, has been given for anti-plane strain conditions by Smith (62) i.e.

$$\frac{\sigma_f}{\sigma_u} = \frac{1}{\left[1+\left(\frac{\rho}{c}\right)^{\frac{1}{2}}\right]} \left\{ \frac{2}{\pi} \sec\left[\exp\left(\frac{\pi K_{1c}^{\,2}}{8\sigma_u^{\,2} c}\right)\right] + \left(\frac{\rho}{c}\right)^{\frac{1}{2}} \right\}. \quad (83)$$

Where σ_f = the fracture stress

σ_u = the ultimate tensile stress

By assuming that Smith's solution for anti-plane strain deformation was approximately equal to that of plane strain deformation, Spink et al (66) have derived an expression for the "apparent fracture toughness" $K_{A(\rho)}$ where: $(K_{1c}/\sigma_u) << 1$ (i.e. small scale yielding) and:

$$\sigma_f = \frac{K_{1c} + \sigma_u (\pi\rho)^{\frac{1}{2}}}{(\pi c)^{\frac{1}{2}} \left[1+\left(\frac{\rho}{c}\right)^{\frac{1}{2}}\right]} \quad . \quad . \quad . \quad (84)$$

$K_{A(\rho)}$ may now be given as:

$$K_{A(\rho)} = \frac{K_{1c} + \sigma_u (\pi\rho)^{\frac{1}{2}}}{\left[1+\left(\frac{\rho}{c}\right)^{\frac{1}{2}}\right]} \quad . \quad . \quad . \quad . \quad (85)$$

Fig.33 shows $K_{A(\rho)}$ results, obtained by Spink et al, (66), plotted as a function of $\sqrt{\frac{\rho}{a}}$. For small values of ρ a small change in ρ will result in a large change in $K_{A(\rho)}$; also the lower the fracture toughness of a material, the greater the initial change in $K_{A(\rho)}$. Discrepancies between experimental and predicted fracture toughness values have been observed by Spink et al (66) for low toughness materials as the root radius approached zero. Vitek (62 and 63) has suggested that Spink, Worthington and Heald's analysis, based on anti-plane strain, gave an under estimate of the true fracture toughness. By taking an example where $\frac{\rho}{a} = 0.5$ he has shown from his own equations (see section 3.4.2) that the corresponding values of $K_{1c} / \sigma u a^{\frac{1}{2}} = 0.75$ when $\frac{\sigma_f}{\sigma_y} = 0.5$ and 1.285 when $\frac{\sigma_f}{\sigma_y} = 0.7$; whereas Spink's equation (85) gave values of 0.26 and 0.91 respectively.

One of the less apparent conclusions of Spink, Worthington and Heald's work (66) is that it was difficult to accurately mechanically machine notches with sharp root radii. Mechanical machining may also result in residual deformation at a notch tip, which would have to be overcome before a crack could initiate and grow. Electron discharge machining (spark machining) does not leave a deformed layer at a notch tip and has been used by Pickens and Curland (67) for producing sharp notches in cemented carbide specimens. Their work (after similar work by Chermant et al (68)) was to spark machine notches of various root radii, using a work hardened copper foil as a former. Chermant et al had previously noticed that spark machined notches gave consistantly lower K_Q values than mechanically machined notches of the same root radii. They concluded that spark machining gave regions of sharper local curvature at the notch root, and this, together with thermal cracking resulted in an apparently lower fracture toughness value. To account for the difference in experimental and actual K_{1c} values, Pickens and Curland have formulated a correction factor based on Novak

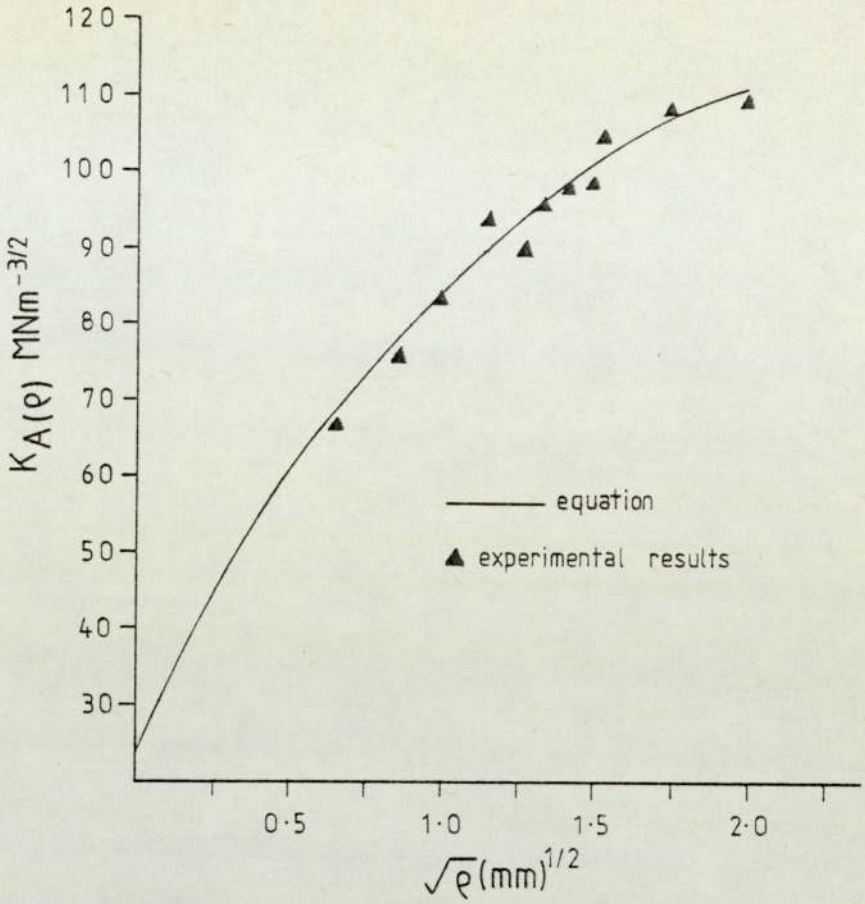

Fig. 33. Dependence of root radius on $K_{apparent}$

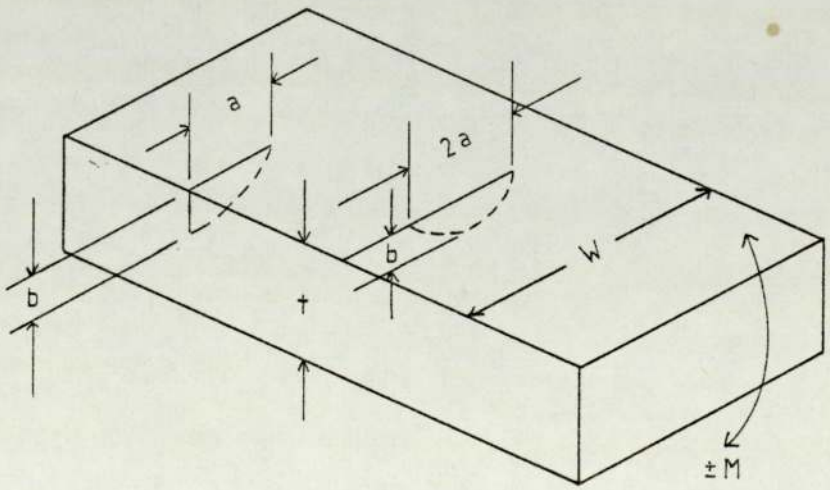

Fig. 34. Semielliptical surface cracks in bending fatigue

and Barsom's equation for cracks emanating from blunt notches (59) and Tada's work on stress fields at blunt notches (69) i.e.

Correction factor = actual K_{1c} / experimental K_{1c}

$$= \frac{1}{\pi}\left[\pi + \frac{\rho}{c+\rho/2}\cot\left(\sin^{-1}\sqrt{\frac{\rho/2}{\rho/2+c}}\right) - 2\sin^{-1}\sqrt{\frac{\rho/2}{\rho/2+c}}\right] \quad (86)$$

Where c is the crack length and ρ is the crack root radius.

3.5 Crack front curvature.

The majority of analytical data used for constructing K calibration curves is obtained on the assumption that a crack front always remains straight. This is often not the case for physical situations such as those encountered in service and the laboratory. Swedlow and Ritter (70) have recognised that errors will occur in fracture toughness testing if the original fatigue cracks are curved or bowed. According to their analysis for elliptical cracks in infinite bodies, the magnitude of the stress intensity varies at different points along the crack perimeter.

Burck's work (71) on the propagation rates from various positions along the perimeter of a semi-elliptical crack in bending, supports Swedlow and Ritter's findings. By assuming that the Paris relationship (72) was obeyed independently at each point on the crack front. i.e.

$$\delta = A(\Delta K)^n \quad . \quad . \quad . \quad . \quad . \quad . \quad (87)$$

Where δ is an increment in crack growth normal to the crack front.

ΔK is the range of stress intensity

A and n are material constants

Burck describes the stress intensity range, Δ K as:

$$\Delta K = \Delta\sigma\sqrt{b}\, f(b/a, b/c, \phi) \quad . \quad . \quad . \quad . \quad (88)$$

where $\Delta\sigma$ is the surface bending stress range

ϕ is the position on the crack front

b, t and a are shown in fig.34

As the crack profiles are approximated to ellipses only the growth rates of the major and minor axes need to be considered. i.e.

$$\frac{da}{dN} = A(\Delta K_A)^n \quad \cdots \quad (89a)$$

$$\frac{db}{dN} = A(\Delta K_B)^n \quad \cdots \quad (89b)$$

Where ΔK_A and ΔK_B correspond to the range of stress intensities at the tips of the major and minor axes respectively. The number of cycles required for crack propagation from an initial crack length, a_o, to the final crack length, a_f, can be given by the integral of equation (89a). This was achieved by Burck numerically - the solution being:

$$N = \int_{a_o}^{a_F} da/A\left[\Delta K_A\left(b, b/a, b/c\right)\right]^n \quad \cdots \quad (90)$$

and when the crack depth 'b' corresponded to the crack length a:

$$b = \int_{a_o}^{a} \left(\Delta K_B/\Delta K_A\right)^n + da + b_o \quad \cdots \quad (91)$$

The results obtained by Burck for K_B/K_A plotted as a function of b/t are shown in fig.35 for decreasing values of the exponent n. It is apparent from Burck's work that crack fronts are unlikely to remain geometrically similar when a crack advances. The assumption that the stress intensity remains constant along a crack front is, therefore, an over simplification. Geometrical changes in crack fronts during slow stable crack propagation have been investigated by Neale (38). His assumption is that, after initiation, a crack will arrest into a thumb nail shape which is capable of sustaining a higher load than the

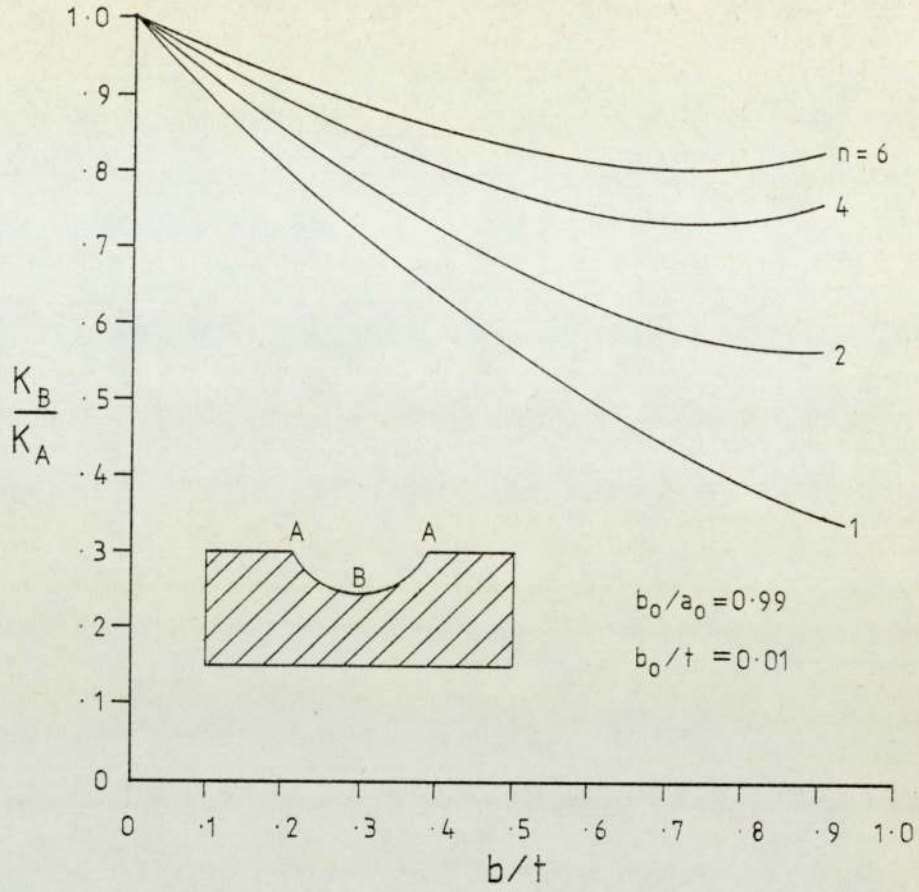

Fig. 35. Ratios of interior-to-surface stress intensity factors for propagating fatigue cracks

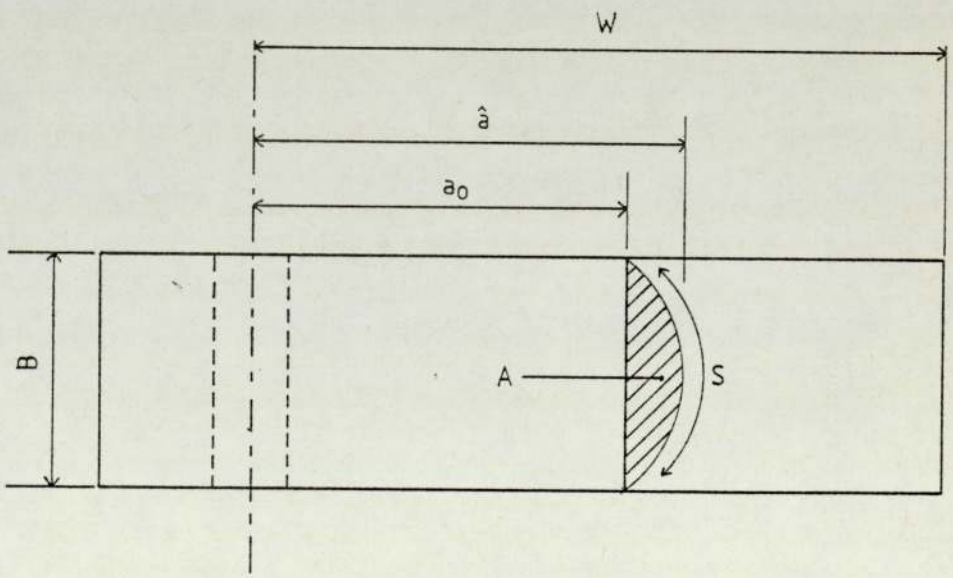

Fig. 36. Diagrammatic representation of a section through a parabolic crack front

original straight crack front. Consider the section through a compact tension specimen illustrated in fig.36. Here W is the specimen width, B is the specimen thickness, a_o is the original straight crack length, $\hat{a}$ is the final parabolic crack length and A is the area indicated. According to Neale, as a crack initiates and arrests into a thumbnail shape there will be a corresponding increase in crack front length. As this increase in crack front length is equivalent to an increase in specimen thickness, the stress intensity factor will be reduced. During this period of crack advance, since the load will be increasing, the strain energy release rate $-\frac{\partial U}{\partial a}$, will also be increasing, therefore, the stress intensity factor becomes larger. The net result proposed by Neale is that although a crack front may alter its shape by advancing, the stress intensity factor will remain constant. Consider the equation used for obtaining K_{1c} (2)

$$K_1 = \left(\frac{P}{BW}\right)\sqrt{a}\left(\frac{a}{W}\right) \quad \cdot \quad \cdot \quad \cdot \quad \cdot \quad (92)$$

and the formula used for converting G_1 to K_1 given in equation (36)

$$K = \sqrt{\left[\left(E/B\right) - \left(-\frac{\partial U}{\partial a}\right)\right]} \quad \cdot \quad \cdot \quad \cdot \quad (93)$$

where $G = -\frac{\partial U}{\partial a}$

Combining equations (92) and (93) Neale showed that the stress intensity factor of a parabolic crack could be given by:

$$f\left(\frac{\hat{a}}{W}\right) = \sqrt{\left[E\left(-\frac{\partial U}{\partial a}\right)\right]} \times BW/P\sqrt{a} \quad \cdot \quad \cdot \quad (94)$$

Neale's finite element results for parabolic crack fronts, together with Wessel's solution (73) for a straight crack front are shown in fig.37. From these curves it can be seen that as a crack arrests into a thumbnail shape the stress intensity factor decreases. As finite element analysis is both costly and time consuming, Neale (74) has

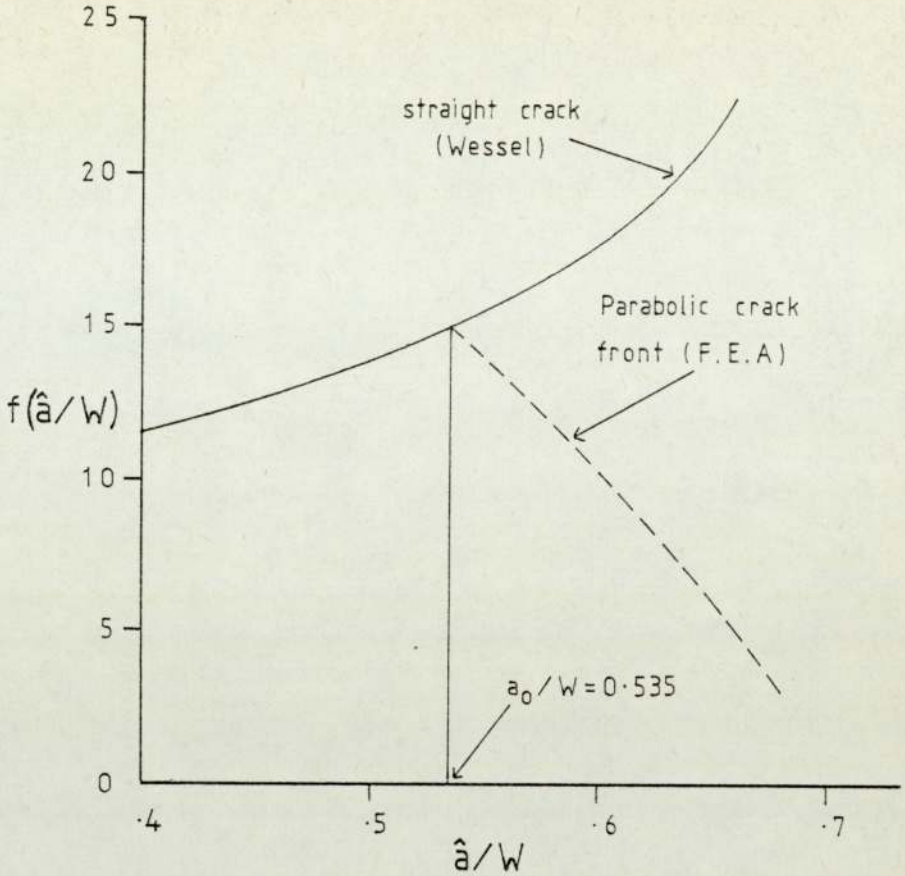

Fig. 37. Stress intensity coefficients of straight and parabolic crack fronts

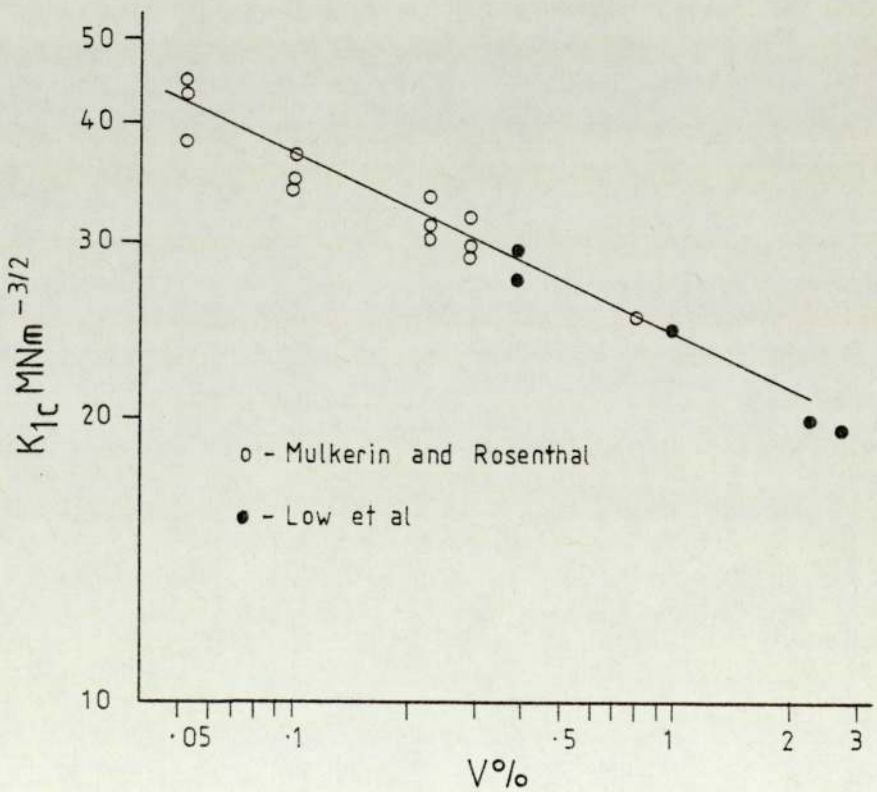

Fig. 38. K_{1c} versus volume fraction of inclusions

proposed a simple model in order to derive stress intensity factors for parabolic crack fronts. The equation from his model is given by:

$$K = \frac{P}{BW} \cdot \frac{B}{S} \sqrt{a'} f(a'/w) \quad \cdot \quad \cdot \quad (95)$$

where S is the length of the thumbnail crack and a' is the crack length given by: (see fig. 36.)

$$a' = a + \frac{A}{B} \quad \cdot \quad \cdot \quad \cdot \quad \cdot \quad \cdot \quad \cdot \quad (96)$$

Equation (95) is of interest as it appears that Neale has combined the effects of increase in crack front length with decrease in remaining ligament area in order to describe the stress intensity factor of a parabolic crack front.

3.6 Effects of microstructure on fracture properties.

The fracture toughness of a material is dependent upon its microstructure. The relationship between fracture and microstructure, however, is difficult to establish because of the number of variables involved and, the problems encountered in accurately describing microstructures. For the simple case of evenly distributed particles contained in a homogeneous matrix, the mean particle diameter d may be given by (after Edelson and Baldwin (75)):

$$d = D\sqrt{\left(\frac{2}{3v}\right)}(1-v) \quad \cdot \quad \cdot \quad \cdot \quad \cdot \quad (97)$$

where v is the volume fraction of particles

D is the particle diameter

This formula, however, is of limited use since it does not take into consideration the overall shape, size and distribution of the particles.

The influence of inclusion content on the toughness of aluminium alloys has been investigated by Mulkerin and Rosenthal (76) and Low et al (77) (see fig.38). Here it can be seen that fracture toughness

decreases linearly as a function of the log of inclusion content. Ductile material surrounding inclusions directly in front of a crack tip will be subjected to very large plastic strains. The inclusions are fractured by these strains, with the resulting formation of voids. Void formation can alternatively initiate from particle - matrix decohesion. As these voids grow, the matrix between adjacent voids fractures, leaving a characteristic dimple shape.

The influence of the matrix on the fracture behaviour of aluminium alloys has been reviewed by Karl - Heinz Schwalbe (78). For the 7075 aluminium alloy series it has been shown that toughness may be improved by removing the impurities such as iron, silicon and chromium. A certain amount of chromium is, however, desirable as it combines with the aluminium to form chromium rich incoherent particles which tend to restrict the movement of dislocations within a material. Without these particles, the coherent aging precipitates offer little resistance to dislocation movement and slip concentrations result on a few slip bands in relatively soft material. The fracture process occurs, therefore, by slip plane and grain boundary decohesion.

Overaging these aluminium alloys may be used to provide "pinning points" for restricting dislocation movement, but now a denuded, precipitate free, zone occurs at the grain boundary. In this situation, the fracture process is almost entirely intergranular, but with the formation of small dimples at these denuded areas. This tends to suggest that grain size plays an important role in the fracture properties of these alloys. Plane stress fracture toughness data obtained by Thompson and Zinkham (79) is in agreement with this suggestion, as shown in fig.39.

Fracture behaviour in aluminium/silicon/magnesium casting alloys has been investigated, separately, by Saunders (80) and Austen and Williamson (81). According to Saunders, the mechanism of crack

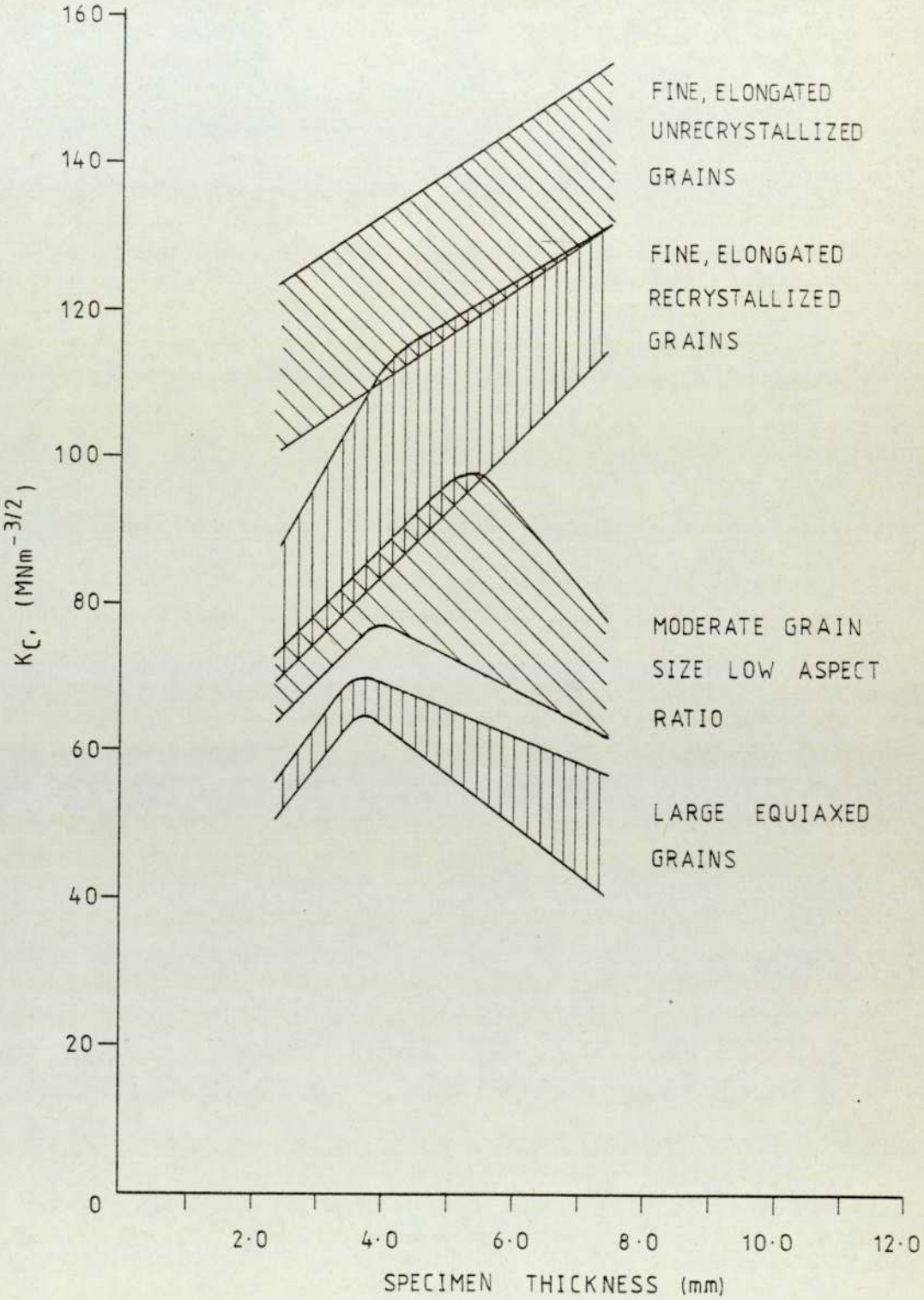

Fig. 39. Effect of thickness on K_c of overaged 7000 series alloys with various grain sizes

propagation in these alloys is by micro void coalescence - the voids being nucleated from cleavage of silicon particles. Further examination of the fracture surfaces revealed that crack propagation followed a path linking these silicon particles. Silicon, therefore, appears to control both the path and mode of fracture in these alloys.

A number of workers have suggested that K_{1c} may be correlated with particle size, spacing and distribution. For cleavage, Hahn and Rosenfield (82) have proposed that:

$$K_{1c} = 0{\cdot}55(\sigma_{cL} - \sigma_y) \quad . \quad . \quad . \quad . \quad (98)$$

where σ_{cl} = cleavage stress

σ_y = yield stress

According to Wilshaw, Rau and Tetelman (83) fracture will occur when σ_y is greater than σ_{cl} within the region of the crack tip. Using slip line theory for finite root radii notches, they obtained:

$$K_{1c} = 2{\cdot}98\,\sigma_y\left[\exp\left(\sigma_u/\sigma_y - 1\right) - 1\right]^{\frac{1}{2}} \times \sqrt{(\rho_{eff})} \quad (99)$$

where ρ_{eff} is the effective root radius. Assuming that the grain size D could be related to ρ_{eff}, Schwalbe has proposed the following formula:

$$K_{1c} = \frac{2\beta}{\sqrt{\pi}} \sqrt{\left(\tfrac{1}{2}\alpha D\right)}\,\sigma_{cL} \quad . \quad . \quad . \quad . \quad (100)$$

where α is the factor relating the size and diameter of a grain.

β is a constant for converting general yielding to small scale yielding.

For ductile crack propagation, the crack tip advance displacement δ_{tx} is equal to half the crack tip opening displacement δ. From the literature when the dimple formation is due to coarse inclusions:

$$\delta_{tx} \approx d \quad . \quad . \quad . \quad . \quad . \quad (101)$$

and when the dimples are formed at fine particles:

$$\delta_{tx} > d \quad . \quad . \quad . \quad . \quad . \quad . \quad . \quad (102)$$

In overaged aluminium alloys, where $\delta_{tx} \approx d$, the fracture toughness may be obtained from the crack tip advance displacement according to equation (37) i.e.

$$K_{Ic} = \sqrt{\left(\frac{M.E.\sigma_y.2\delta_{tx}}{(1-\nu^2)}\right)} \quad . \quad . \quad . \quad (103)$$

Where $M \approx 1$ in plane stress and $M \approx 2$ in plane strain.

3.7 The fracture properties of wrought aluminium alloys.

The toughness of wrought aluminium alloy products is often very much greater than equivalent cast products. There is also far more literature available on the fracture properties of these wrought materials. In this section the fracture properties of wrought aluminium alloys, with similar compositions to the cast alloys under investigation, will be briefly examined so that they may be used at a later stage for comparison.

The appropriate series of wrought aluminium alloys - according to the A.S.T.M. standards (84) - are the 2000 series, where copper is the principle alloying element, and the 4000 and 6000 series, where silicon is the principle alloying element. In general the wrought alloys to be used for comparison were in the T6 condition (i.e. solution treated and artificially aged), although deformation, in the form of stretching, between solution treatment and aging may have taken place. Wrought products tend to exhibit different mechanical properties, depending on whether the specimen is taken in a longitudinal or transverse orientation, therefore it is necessary to quote the values of fracture toughness for both these situations.

The fracture toughnesses of a range of wrought aluminium alloys,

Table.4.

Typical fracture properties of wrought aluminium alloys.

Alloy and condition	Reference	0.2% Proof stress. (MNm^{-2})		K_{1c}. ($MNm^{-3/2}$)	
		long.	tran.	long.	tran.
2014 T651	(86)	437	432	29.4	23.6
2020 T651	(85)	534	540	24.7	22.9
		524	534	26.5	19.1
		526	533	22.9	21.2
2024 T851	(85)	453	448	24.7	20.7
		455	451	25.4	20.7
		452	444	28.0	24.8
6061 T651	(87)	291	286	33.0	29.7
DTD 5020	(88)	440	440	29.1	29.1
S.T. Stretched		440	440	28.2	28.2
and A.A.		440	440	27.3	27.3
DTD 5090	(88)	374	344	46.0	46.0
S.T. Stretched		374	344	43.5	43.5
and A.A.					
BS L77	(88)	440	440	19.2	21.9
S.T. Stretched					
and A.A.					
BS L93	(88)	437	437	25.5	25.5
S.T. Stretched		427	427	22.7	22.7
and A.A.		-	413	-	20.5

S.T. - Solution treated, A.A. - Artificially aged.

including three of the 2000 series have been investigated by Kaufman, Nelson and Marshall Holt (85) using three specimen types. Some of their results are incorporated in table 4., together with values obtained from the following references:

Kaufman and Marshall Holt (86)

Nelson and Kaufman (87)

Liebowitz (88)

The fracture toughness values tabulated in table 4 are for plane strain conditions; there is, however, a great amount of data available for plane stress conditions since a consequence of these high strength wrought alloys is that they often exhibit a great amount of ductility (89 and 90).

4. EXPERIMENTAL CONSIDERATIONS.

4.1 Compliance testing.

Irwin and Kies (91) have developed a method of determining strain energy release rates for a variety of geometries subjected to different loading conditions. By representing the strain energy in a body by:

$$U = \frac{P^2 c}{2} \quad . \quad . \quad . \quad . \quad . \quad (104)$$

where P is the force and c is the compliance of the body, they obtained:

$$\frac{dU}{da} = \frac{1}{2} P^2 \frac{dc}{da} \quad . \quad . \quad . \quad . \quad (105)$$

For plane stress, the stress intensity factor may therefore be given by:

$$K_1 = P\left[\frac{E}{2}\frac{dc}{da}\right]^{1/2} \quad . \quad . \quad . \quad . \quad (106)$$

The experimental determination of K_1 is usually achieved by fitting a least squares polynomial to the compliance versus crack length curve. This polynomial series may then be differentiated with respect to crack length and used to obtain the compliance function Y. K_1 can then be found according to the general formula (see equation (13)):

$$K_1 = \sigma\sqrt{a}\; Y\left(\frac{a}{w}\right) \quad . \quad . \quad . \quad . \quad (107)$$

For W.O.L. (wedge open loading) C.T. (compact tension) (73) and D.C.B. (double cantilever beam) (92) specimens, K can be expressed by:

$$K = \frac{P\sqrt{a}}{Ba}\left[\frac{1}{2}\left(\frac{a}{w}\right)\frac{d(CEB)}{d(a/w)}\right]^{1/2} \quad . \quad . \quad (108)$$

where P is the applied load
W is the specimen width
a is the crack length
c is the compliance
B is the specimen thickness
E is Young's modulus

The dimensionless quantity CEB (normalised compliance) is introduced for simplicity. K is more commonly given by:

$$K = \frac{P\sqrt{a}}{B\,W}\,Y \qquad (109)$$

therefore by combining equations (108) and (109) we obtain:

$$Y = \frac{W}{a}\left[\left\{\frac{1}{2}\left(\frac{a}{W}\right)\frac{d(CEB)}{d(a/W)}\right\}^{1/2}\right] \qquad (110)$$

The term in the square brackets is denoted C_3, and is often expressed as a polynomial. For example C_3 for the W.O.L. specimen has been evaluated by Wilson (93 and 94) i.e.

$$C_3 = 30{\cdot}96\left(\frac{a}{W}\right) - 195{\cdot}8\left(\frac{a}{W}\right)^2 + 730{\cdot}6\left(\frac{a}{W}\right)^3 - 1186{\cdot}3\left(\frac{a}{W}\right)^4 + 754{\cdot}6\left(\frac{a}{W}\right)^5 \qquad (111)$$

C_3 may be obtained from the derivative of the polynomial expression obtained for the CEB versus a/W curve. This procedure, however, tends to give poor results because of the limitations in fitting polynomial expressions to these type of curves and any errors incurred during this stage will be magnified on differentiation. The other limitation of this procedure is that no expression can be obtained for a/W in terms of CEB. By taking logs of CEB, Collipriest (95) has produced two independent polynomial equations for CEB and a/W i.e.

$$\ln(CEB) = K_0 + K_1\left(\frac{a}{W}\right) + K_2\left(\frac{a}{W}\right)^2 + K_3\left(\frac{a}{W}\right)^3 + K_4\left(\frac{a}{W}\right)^4 + K_5\left(\frac{a}{W}\right)^5 \qquad (112a)$$

$$\frac{a}{W} = K_0 + K_1\ln(CEB) + K_2(\ln(CEB))^2 + K_3(\ln(CEB))^3 + K_4(\ln(CEB))^4 + K_5(\ln(CEB))^5 \qquad (112b)$$

but because there are two sets of numerical constants in these equations, they are not directly relatable. From equation (112a) the derivative of CEB could be given by:

$$\frac{dCEB}{d\,a/W} = exp\left[k_0 + k_1\left(\frac{a}{w}\right) + k_2\left(\frac{a}{w}\right)^2 + k_3\left(\frac{a}{w}\right)^3 + k_4\left(\frac{a}{w}\right)^4 + k_5\left(\frac{a}{w}\right)^5 \times \left\{k_1 + 2k_2\left(\frac{a}{w}\right) + 3k_3\left(\frac{a}{w}\right)^2 + 4k_4\left(\frac{a}{w}\right)^3 + 5k_5\left(\frac{a}{w}\right)^4\right\}\right] \quad \cdots \quad (113)$$

This equation, however, does not appear to have any distinct advantage over simply differentiating the polynomial expression for CEB; except that by taking the log of CEB, the curve fitting procedure may be improved since polynomial cycling would be reduced.

The disadvantages of polynomial curve fitting procedures in compliance calibration have been discussed by Ryder et al (96). As a result of their work on W.O.L. (wedge open loaded) specimens, they describe a potentially improved technique for analytically expressing compliance data. Consider the following expression for CEB.

$$CEB = (\exp(\exp(f(a/W))) - \exp(1.0)) \quad \cdots \quad (114)$$

and $$f(a/W) = e + (v - e)(-\ln(1 - a/W))^{1/k} \quad \cdots \quad (115)$$

where e, v and k are numerical parameters. By taking the log of equation (114) and rearranging we obtain:

$$1 - a/W = exp\left[\frac{Ln(ln\ CEB + 1) - e}{V - e}\right]^k \quad \cdots \quad (116)$$

According to Ryder et al, these equations are valid over the entire range $0 < a/W < 1$. Therefore the values for the numerical parameters may be determined at the conditions: $a/W = 0$ and $a/W = 1$. i.e. By setting $a/W = 0$ in equation (116) we obtain:

$$CEB = \exp(\exp(e)) - \exp(1.0) \quad \cdots \quad (117)$$

therefore $$e = \ln(\ln(CEB + \exp(1.0))) \quad \cdots \quad (118)$$

CEB could be determined from the stress analysis of an un-notched

specimen or by experiment. As an a/W value of 1.0 is meaningless it is suspected that Ryder et al have used an iterative method for determining the numerical parameters e, v and k. The results of their work on Ti-6Al-4V W.O.L. specimens, together with Wilson's solution (equation 111) are shown in fig.40 where it can be seen that there was good agreement between both solutions. The advantages of Ryder et al's equations are:

a) Only three parameters are involved in their equation, rather than 10 or 11 used in the polynomial expressions (see equation 113)

b) The functions derived for CEB and a/W are reversible.

c) Their equation is accurate over the entire range $0 < a/W < 1$

Ryder's equation will be incorporated at a later stage in this work for analysing compliance data of straight and curved crack fronts.

4.2 The determination of J from single load-displacement records.

An experimental method for determining the value of J has been presented by Begley and Landes (30). Although their procedure gives accurate results, several specimens are required in order to obtain the critical value of J, J_{1c}. Rice, Merkle and Paris (97) have suggested a method of estimating J_{1c} from single load-displacement records. Consider the strain energy of a cracked specimen, where, following Rice et al:

$$U_{total} = U_{no\ crack} + U_{crack} \qquad \cdot \quad \cdot \qquad (119)$$

By applying Castiliano's theorem (98) we may write:

$$\delta_{total} = \delta_{no\ crack} + \delta_{crack} \qquad \cdot \quad \cdot \qquad (120)$$

According to Rice et al the relationship between J and the uncracked ligament length, for the case of three point bending, may be given by:

$$J = \frac{2}{b} \int^{\delta_{crack}} P d\left(\delta_{crack}\right) \qquad \cdot \quad \cdot \quad \cdot \qquad (121)$$

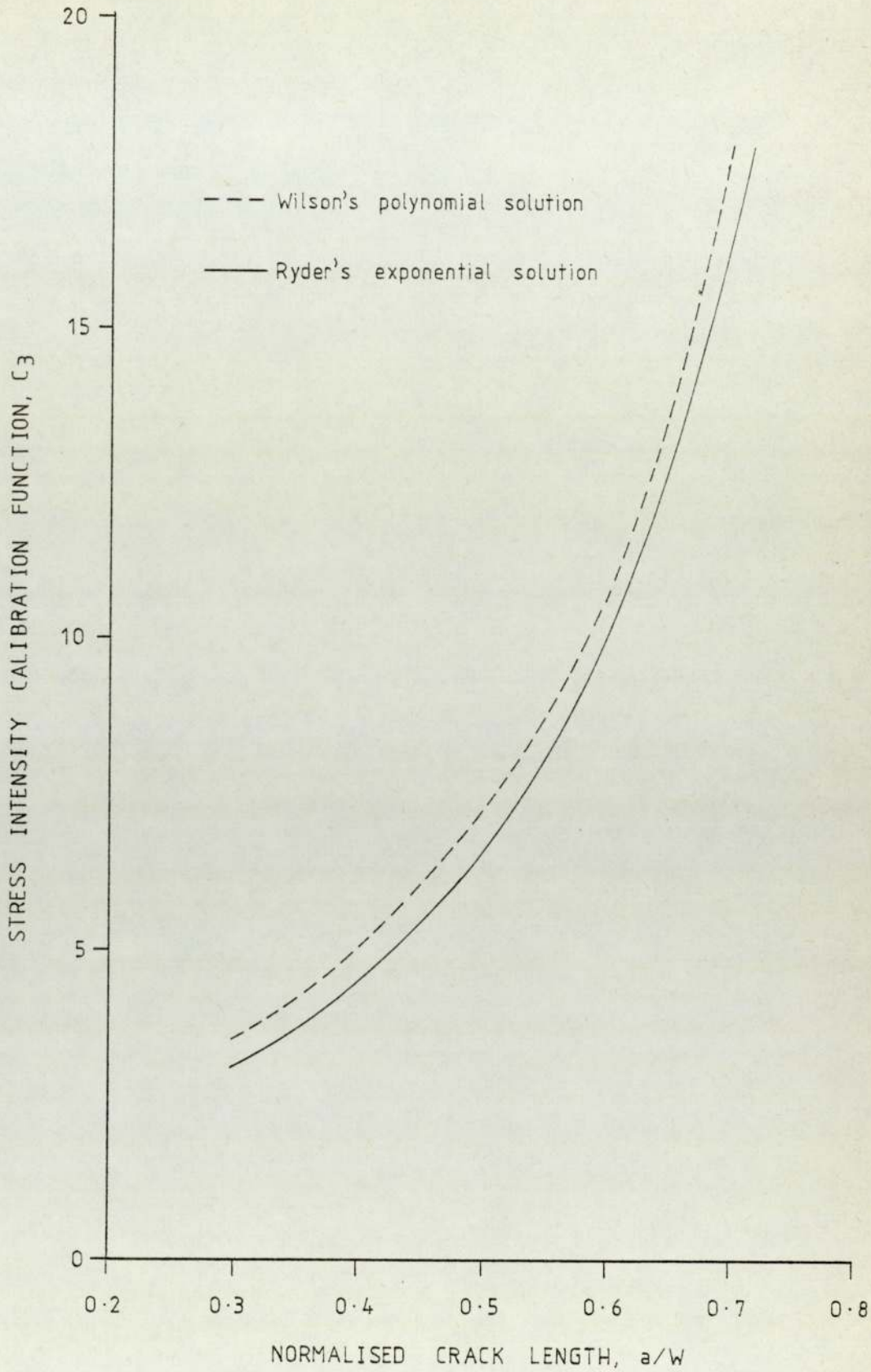

Fig. 40. C_3 versus a/W for Ti-6Al-4V(RA)[after Ryder]

where b, the uncracked ligament length = (W - a) and P is the applied load. The value for δ_{crack} may be directly obtained from equation (120):

$$\delta_{crack} = \delta_{total} - \delta_{no\ crack} \quad \cdot \quad \cdot \quad (122)$$

where δ_{total} is the displacement at crack initiation (from the load-displacement record) of a pre-cracked specimen and $\delta_{no\ crack}$ is the displacement of the uncracked specimen. For three point bending, $\delta_{no\ crack}$ may be given from beam theory. i.e.

$$\delta_{no\ crack} = \frac{PL^3}{48EI} \quad \cdot \quad \cdot \quad \cdot \quad \cdot \quad \cdot \quad (123)$$

Where I, the second moment of area = $\frac{BW^3}{12}$ $\quad \cdot \quad \cdot \quad \cdot \quad \cdot \quad (124)$

therefore $\delta_{no\ crack} = \frac{PL^3}{4EBW^3}$ $\quad \cdot \quad \cdot \quad \cdot \quad \cdot \quad (125)$

An application of Rice, Merkle and Paris' suggestion has been developed by Barnby and Daimalani (99) in determining the fracture toughness of a range of cast steels. Their experimental method was to measure the total mid-point displacement of pre-cracked three point bend specimens using a differential core transducer (see illustration in their paper). By numerically integrating the load-load point displacement curve up to the point of crack initiation they were able to obtain the total energy in the cracked specimens. The energy available for crack extension, and hence J, could then be found by subtracting the energy contributed by the uncracked specimen from the total energy. In order to exclude rig displacements, Barnby and Daimalani mounted their transducer as close as possible to the load application point. It is thought, however, that with small load point displacements the effect of the rollers sinking in during testing may result in errors on the final record.

The elimination of rig displacements and roller sink in, with three point bend specimens, has been achieved by Dawes (21). From his equipment it can be seen that the load point displacement is measured between a 'comparison bar' mounted on pins which are attached to the specimen side faces at the ends of the loading span. The original contact points for the comparison bar lie on the neutral axis directly above the loading points. Dawes has shown that using his apparatus the vertical displacements of the notch mouth represented the true value to within $\pm$ 2%, provided that the total angle of bend did not exceed about 8^{o}. Although Dawes' apparatus may be more accurate than that used by Barnby and Daimalani, it is thought that the Barnby and Daimalani method may be improved by subtracting an experimental value of uncracked specimen energy from the total energy: rather than a theoretical value (see fig.41.).

4.3 The three point bend rotational factor r.

The recommended procedure for calculating crack opening displacements from crack mouth opening displacements is detailed in British Standards Draft for Development 19 (23). In this document the relationship between the forementioned displacements assumes a centre of rotation at a distance of r(W - a) from the crack tip, where r is the rotational factor (see fig.42.). According to Wells (100) the value for r = 0.45. This value is currently adopted in DD 19.

Ingham et al (101) have found that the value of r = 0.33; whereas Sumpter and Turner (102) propose that:

$$r_p = 0.4 \text{ when } a/W > 0.45$$

$$r_p = 0.45 \text{ when } a/W < 0.45$$

where r_p is the rotational factor after net section yielding. Dawes (103) has derived an equation for r_p based on earlier equations

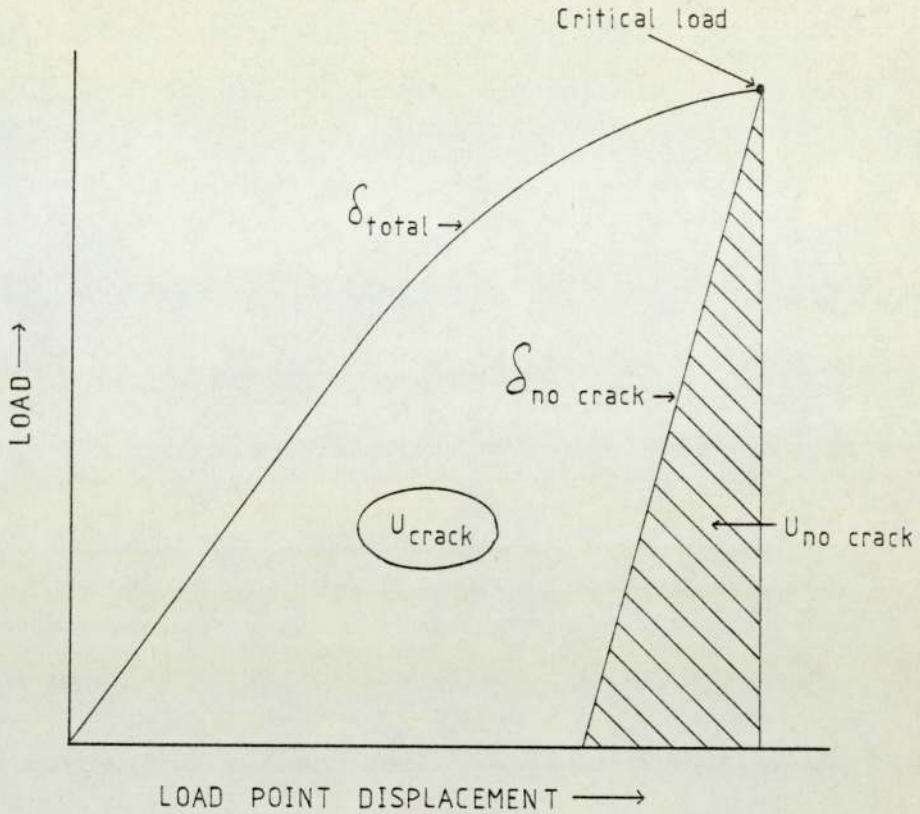

Fig. 41. Diagrammatic representation of specimen energies and displacements

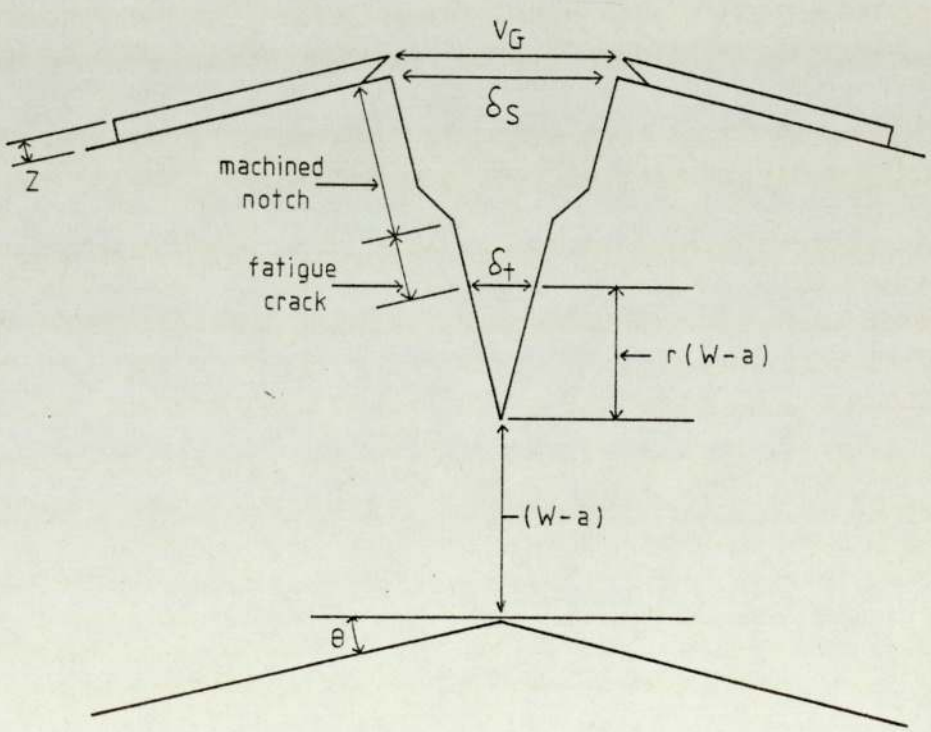

Fig. 42. Diagrammatic representation of a notch, fatigue crack and the centre of rotation.

developed by Sumpter and Turner. i.e.

$$r_p = \frac{1}{(W - a)} \left[\frac{V_p W}{q_p} - (a + z) \right] \quad . \quad . \quad (126)$$

where V_p is the plastic component of crack mouth opening displacement

q_p is the plastic component of load point displacement

z is the knife edge thickness

The value for r_p was then determined by simultaneous measurement of V_p and q_p using the apparatus shown in reference (21) and described in the previous section. Owing to the controversy in the value of r, Dawes has proposed the following equation for determining COD, which is shortly to appear in the new standard for COD testing.

$$\delta = \frac{K^2}{2\sigma_y E'} + \frac{V_p}{\left(1.25 \frac{a + z}{W - a}\right)} \quad . \quad . \quad (127)$$

Where E' = E in plane stress and $\frac{E}{(1 + \nu^2)}$ in plane strain. K is given by the formula:

$$K_1 = \frac{P'}{BW} \sqrt{a} \; f\left(\frac{a}{W}\right) \quad . \quad . \quad . \quad . \quad (128)$$

and, for this case P' is the critical load (i.e. the load at crack initiation). Examination of equation (127) reveals that Dawes has expressed δ by combining the elastic and plastic components. By rearranging equation (126) it follows that:

$$\frac{V_p}{q_p} = \frac{a + z + r_p (W - a)}{W} \quad . \quad . \quad . \quad . \quad (129)$$

Values of V_p/q_p as a function of a/W are shown for r values of 0.33, 0.4 and 0.45 in fig.43. (where the value of z taken was 1.7 mm)

From these graphs it is apparent that there is a relationship between crack mouth, opening and load point displacements, and, this relationship is dependent on r. An extension of this finding could be the interchange of load-load point displacement and load-mouth opening displacement records. This would mean that J could be determined from crack mouth opening displacement records.

4.4 The electrical potential method for determining initiation and propagation of cracks.

The electrical potential technique for determining crack initiation and propagation is now well established and is described in reference (22) appendix A. Basically the technique involves applying a large current to the ends of the specimen, and monitoring the change in electrical potential between two probes attached to each side of the crack or notch.

One of the major problems associated with the electrical potential technique is analysing the resulting data. Johnson (104) has derived the following relationship:

$$\frac{V_a}{V_{ao}} = \frac{\cosh^{-1}\left[\dfrac{\cosh(\pi Y/W)}{\cos(\pi a/W)}\right]}{\cosh^{-1}\left[\dfrac{\cosh(\pi Y/W)}{\cos(\pi a_o/W)}\right]} \qquad (130)$$

where V_a is the reference voltage at crack length a

V_{ao} is the reference voltage at a known crack length a_o

Y is the distance over which the potential is measured

W is the specimen width

According to Cooke and Robinson (105) there was poor agreement between their experimental results and Johnson's equation. An improved analytical solution has been proposed by Gilby and Pearson (106) the equations for which are:

a) Uniform current

$$V = \text{imaginary part of } \left[k_1 \cos^{-1} \left(\frac{\cos(\pi z/2W)}{\cos(\pi a/2W)} \right) \right] \quad (131a)$$

b) Point, current application

$$V = \text{real part of } \left[k_2 \ln \left(\frac{\varepsilon + ic}{\varepsilon - ic} \right) \right] \quad (131b)$$

where V = the potential difference between Q and the cracking plane

W = specimen width

a = x + if

k_1 = proportionality constant (dependent on material, specimen type and electrical test conditions)

$$\varepsilon = \sqrt{\sec^2(\pi z/2W)\cos^2(\pi a/2W) - 1}$$

$$c = \sqrt{1 - \cos^2(\pi a/2W)\,\mathrm{sech}^2(\pi d/2W)}$$

For both Johnson's and Gilby and Pearson's solutions, a calibration curve of V_a/V_{ao} versus a/W will eliminate the proportionality constant. The positioning of the probes, however, still governs the shape of these curves and if the probes are not attached in identical positions for each test, several calibration curves will be required. A limitation of the analytical solutions is that they may not be used to describe 'equivalent' crack lengths of notches + cracks; for these cases, only calibration curves are applicable.

The sensitivity of the electrical potential technique depends on several factors such as; specimen size, crack length, magnitude of the applied current, material properties and probe spacing. Cooke and Robinson (105) have reported that they can detect a 0.01 mm change in crack length for steel specimens at an applied current of 30 amps. This value is typical of the sensitivity of the technique, although some workers quote a better sensitivity (107 and 108).

As crack initiation cannot be truly detected using the electrical

potential technique, it is normally defined as the first point of deviation on either the displacement-potential change or the time-potential change record. For the majority of situations this definition of initiation is acceptable but, as observed by Bachmann and Munz (109) there may be a drop in potential at the beginning of a test. They have attributed this initial drop to 'rough' fatigue crack surfaces which, upon loading may partly form electrical contacts, thus causing a drop in potential.

The electrical potential method, described so far in this section involves the application of a stable, dirrect current supply to the ends of the specimen. Currently an A.C. electrical potential system is under development (110) which appears to have several advantages over the existing D.C. technique. The A.C. system utilises a high frequency alternating current (1-5A and 2-30KH$_z$) applied remotely from the crack or notch mouth. A high frequency is required for concentrating the path of the current to the surface layers, which produces a 'skin effect'. When this skin effect is developed, the total current requirements are very much smaller than with the D.C. system, so the risk of specimen heating is minimised.

The major advantage,proclaimed by the developers of the A.C. system is that the potential difference across a crack mouth does not alter with probe positioning; providing that is, the probes are not too close to the current application points. This advantage, together with the higher voltages produced across a crack, means that the A.C. system could be used to determine the shape of a crack front. The sensitivity of the A.C. technique has yet to be assessed, but it is thought that the equipment has promising applications in fracture mechanics.

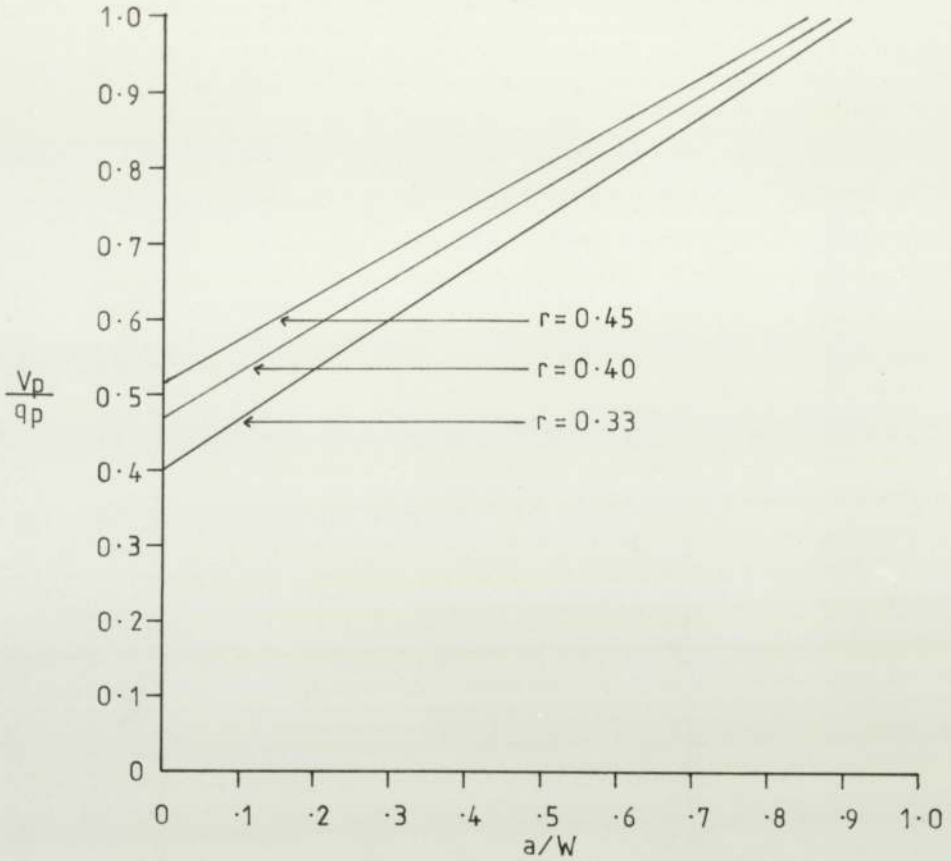

Fig. 43. Mouth opening: load point displacements versus a/W

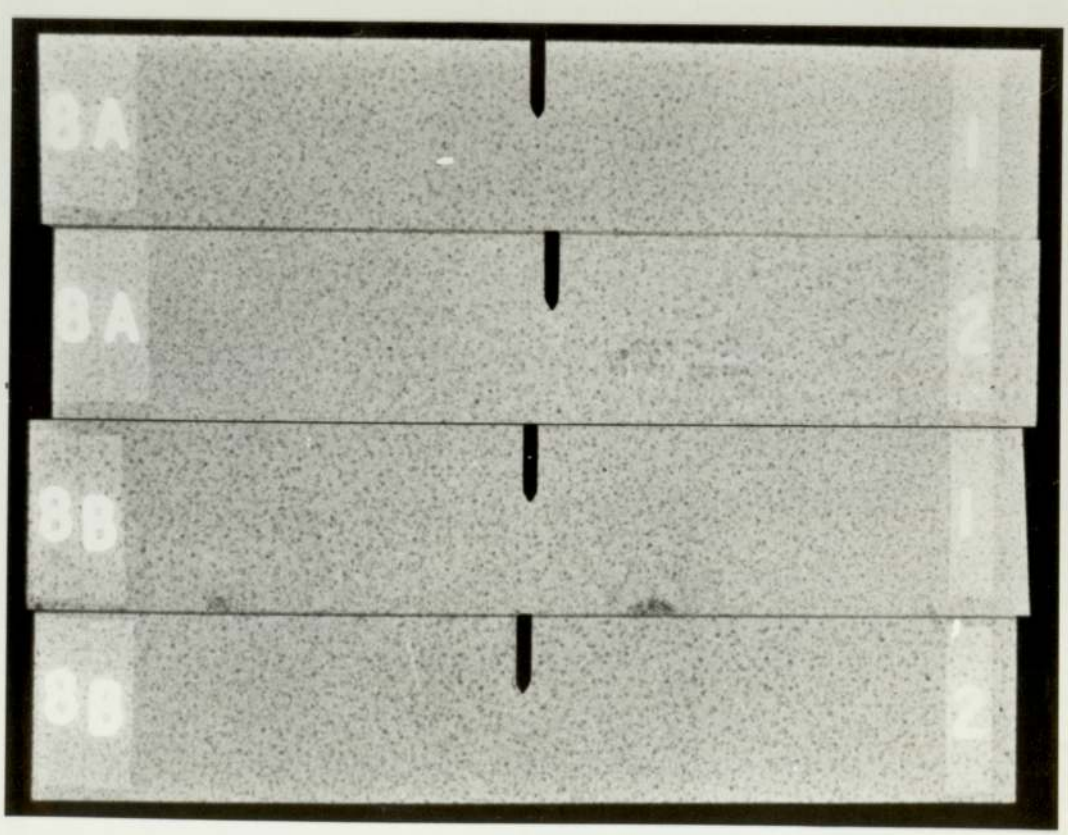

Fig. 44. Typical radiograph, showing porosity, in A 354 specimens

5. EXPERIMENTAL DESIGN AND PROCEDURE.

5.1 Materials and heat treatment.

The high strength aluminium casting alloys to be investigated were:

a) Al - Si - Cu (Alcoa 354)

b) Al - Cu (A.U.W.E. 224)

c) Al - Cu - Ag (A.U.W.E. 224 + Ag)

d) Al - Cu - Ag (K01 or 201.2)

Alcoa 354 is an aluminium company of America specification. A.U.W.E. 224 and 224 + Ag are Admiralty Underwater Weapons Establishment specifications. K01 is an American specification similar to A.M.S. (Aerospace Material specification) 4229.

The analyses of these materials is shown in table.5.

Each of the above materials, with the exception of K01, were sand cast into four block sizes, namely:

a) 280 mm x 200 mm x 50 mm

b) 400 mm x 200 mm x 50 mm

c) 400 mm x 200 mm x 25 mm

d) 400 mm x 200 mm x 14 mm

(The seven K01 specimens were taken from a block, sand cast at British Non-Ferrous). The procedure for casting the aluminium silicon alloys, together with its foundary behaviour, is described in an A.U.W.E. report by Swinyard (111). The 224 and 224 + Ag alloys were cast in a similar manner to this alloy.

After casting, the blocks were radiographed to show up the extent of porosity together with any large defects. A typical radiograph is shown in fig.44. Heat treatment of these alloys was in accordance with the recommended practice incorporated in table.6, and the aging periods were varied in order to produce specimens in differently aged conditions. Both solution, and aging treatments were carried out in air-circulation

Table 5. Chemical analyses of the aluminium alloys.

Element	Alcoa 354	AUWE 224	AUWE 224+Ag	K01
Cu	1.91	4.56	4.69	4.0-5.0
Ag	0.01	0.01	0.42	0.4-1.0
Mg	0.36	0.33	0.37	.18-.35
Si	8.10	0.08	0.08	.05 max
Mn	0.02	0.02	0.02	.20-.30
Ti	0.16	0.11	0.13	.15-.35
Zn	0.02	0.05	0.05	-
Fe	0.16	.10 max	.10 max	.10 max
Sn	0.02	-	-	-
Zr	0.01	0.01	0.01	-
Ni	0.02	-	-	-
V	-	.10 max	.10 max	-
Al	Remainder	Remainder	Remainder	Remainder

furnaces, and as these specimens showed no sign of distortion, it was satisfactory to heat treat them at this stage.

5.2 Specimen details and preparation.

Three point bend specimens (as described in BS 5447 (1) section 6) were machined from the cast blocks, according to the details shown in figs.45, 46, 47 and 48. Dimensions of these specimens including notch depths, root radii and crack length are incorporated in the appendix of this thesis. The specimens taken from the 280 mm x 200 mm x 50 mm blocks were to be used for determining the effect of thickness on fracture toughness and therefore these thicknesses ranged from 4 to 40 mm. The larger specimens, machined from the 400 mm x 200 mm x 50 mm blocks, were to be used for L.E.F.M. testing. The remaining specimens from these 400 mm type blocks were designed so as to assess the effects of crack length, notch and crack root radii, crack front curvature, thickness and aging times, on the fracture process. Specimens were taken in duplicate from the 280 mm x 200 mm x 50 mm blocks and in triplicate from the 400 mm type blocks.

After machining, the specimens were solution treated and aged for the appropriate period of times (details given in appendix). Notching the specimens was achieved by either mechanical or electro-spark machining; the difference being that mechanical machining gave an included angle of 60° at the root of the notch (see BS 5447 (1)) whereas spark maching resulted in a specific root radius only. The advantage of spark machining was that it could be used for producing curved crack fronts using a parabolically shaped copper former. Similarly, fine notches used for simulating sharp fatigue cracks could be produced using a thin copper foil (0.05 mm thick). This was sharpened on 600 wet and dry paper in order to obtain very sharp root radii. Following production, each specimen was to be measured before

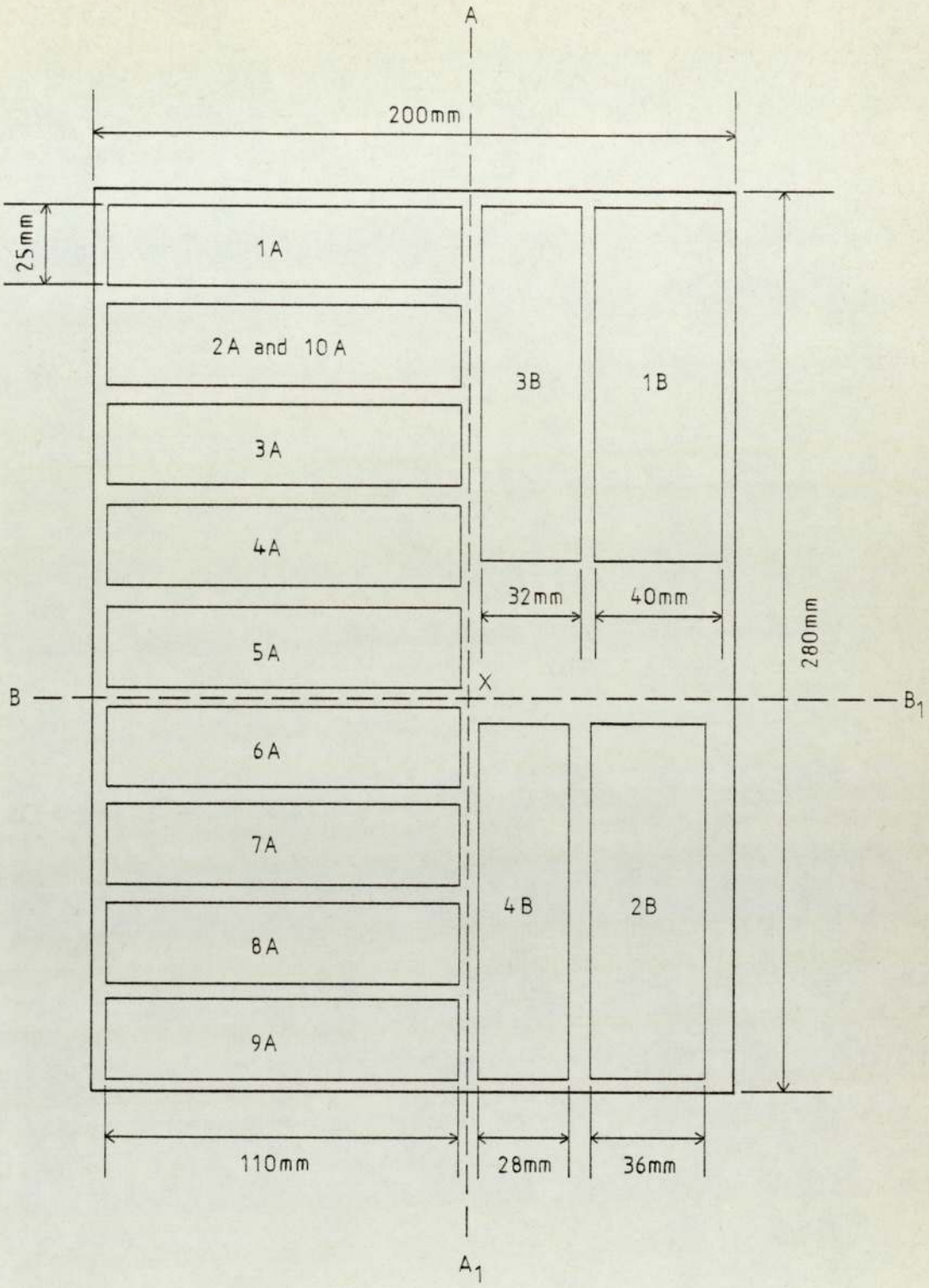

Fig. 45. Details of specimens taken from 280mm x 200mm x 50mm blocks

a) Plan view - half full size

All dimensions given are half full size

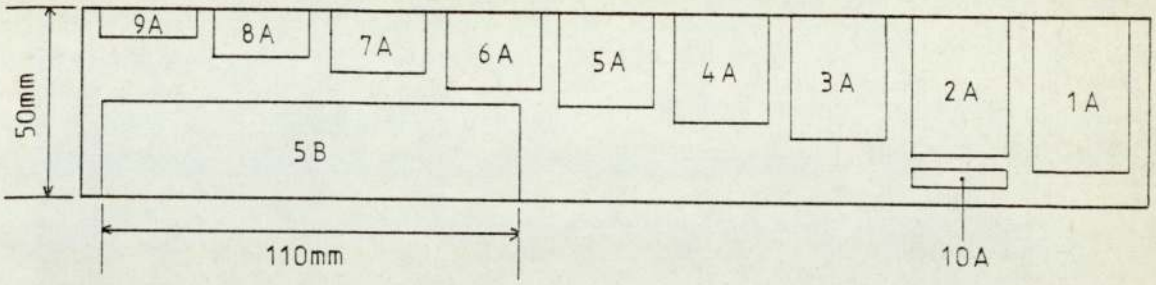

b) Left hand section on $A - A_1$

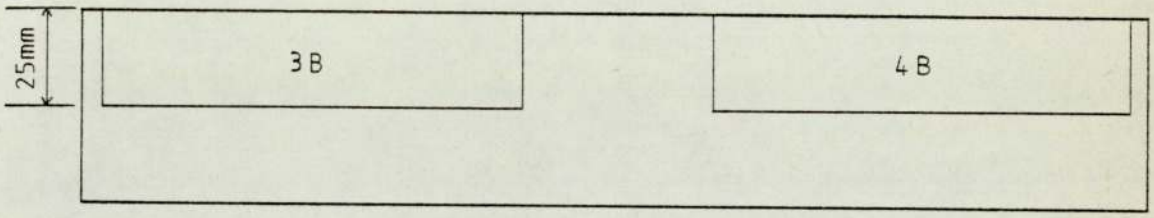

c) Right hand section on $A - A_1$

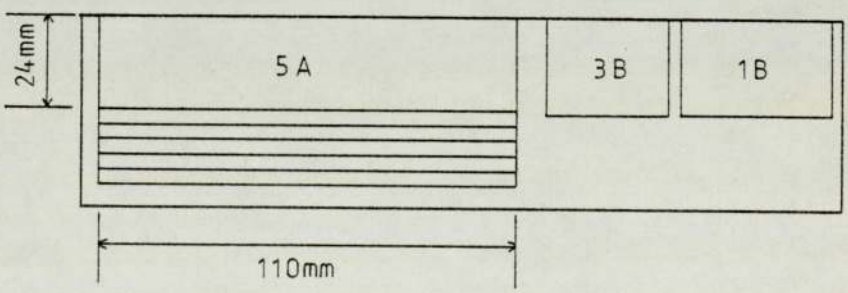

d) Upper section on $B - B_1$

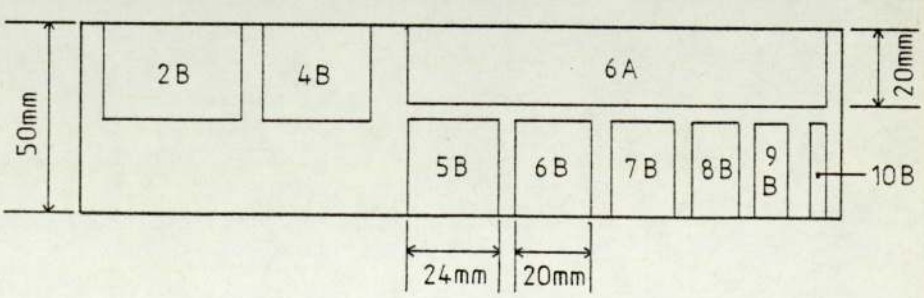

e) Lower section on $B - B_1$

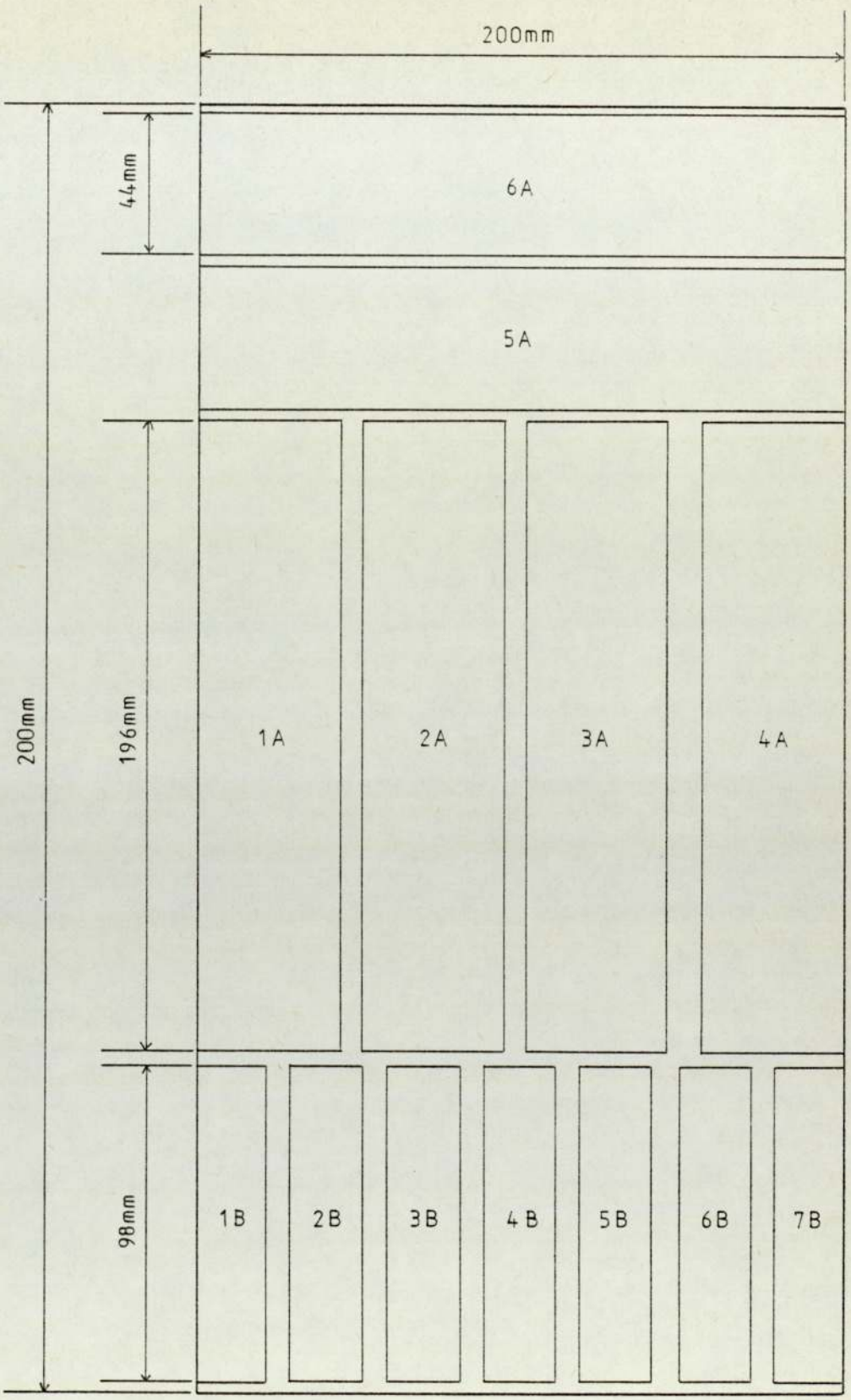

Fig. 46. Details of specimens taken from 400mm x 200mm x 50mm blocks

a) Plan view - half full size

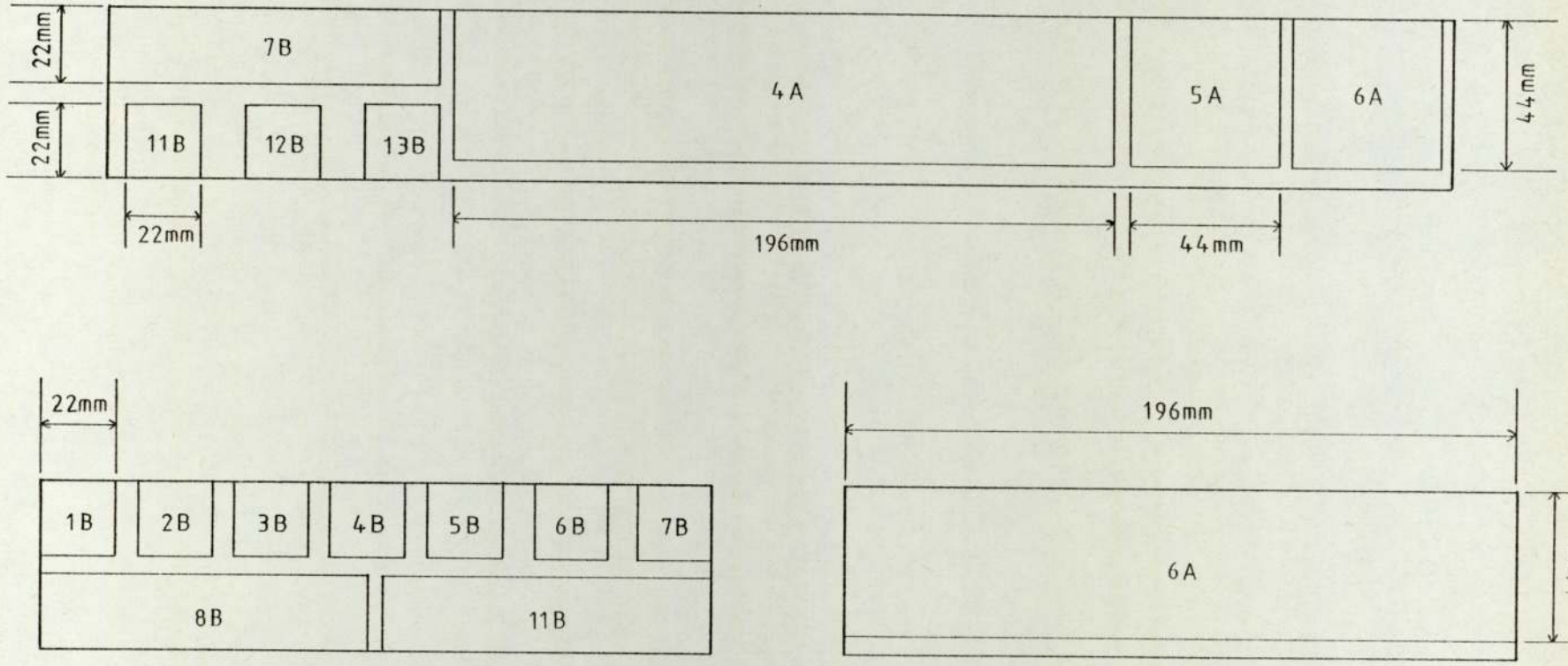

Fig. 46b. Front and end elevations - half full size

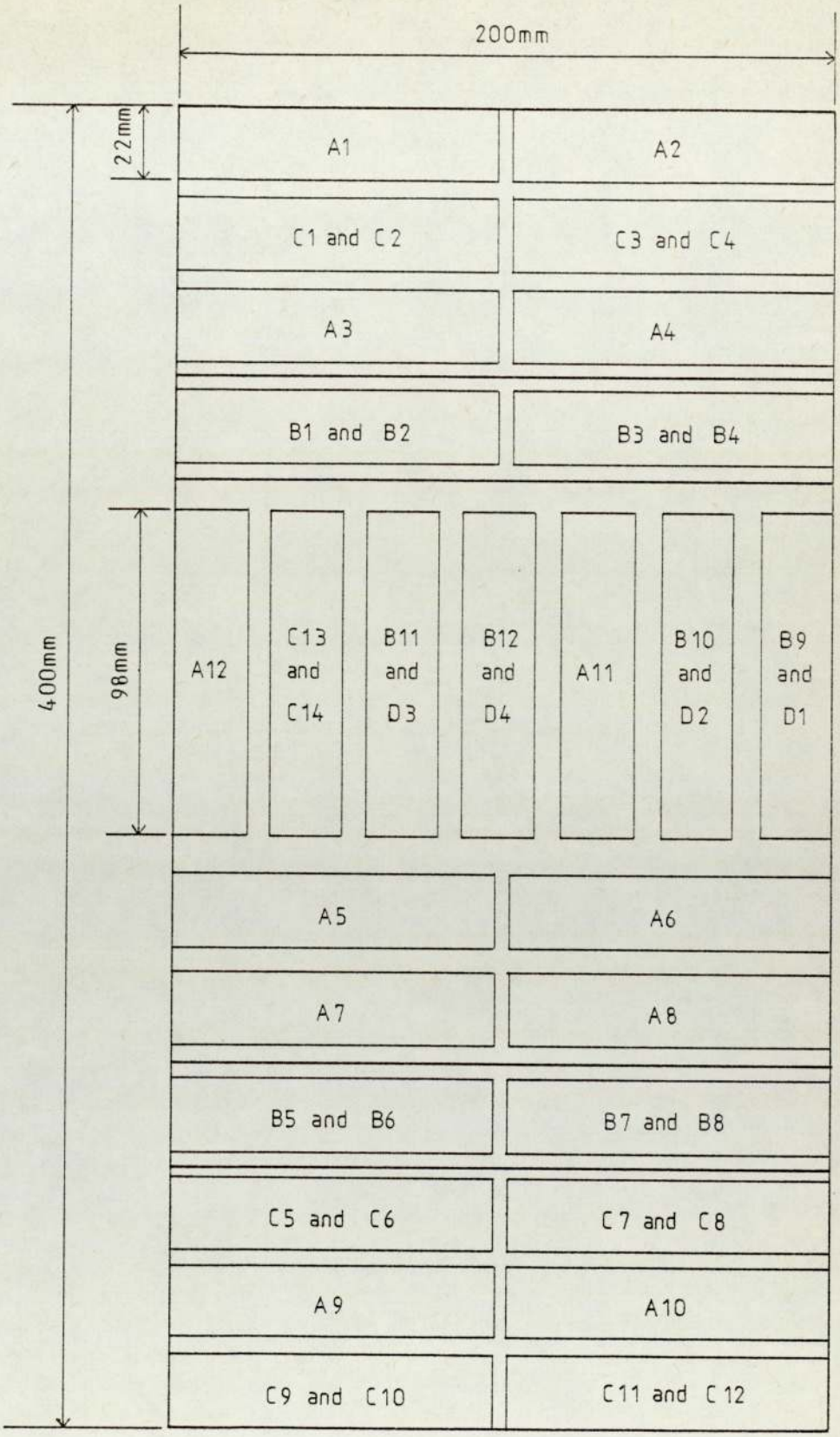

Fig. 47. Details of specimens taken from 400mm x 200mm x 25mm blocks

a) Plan view - half full size

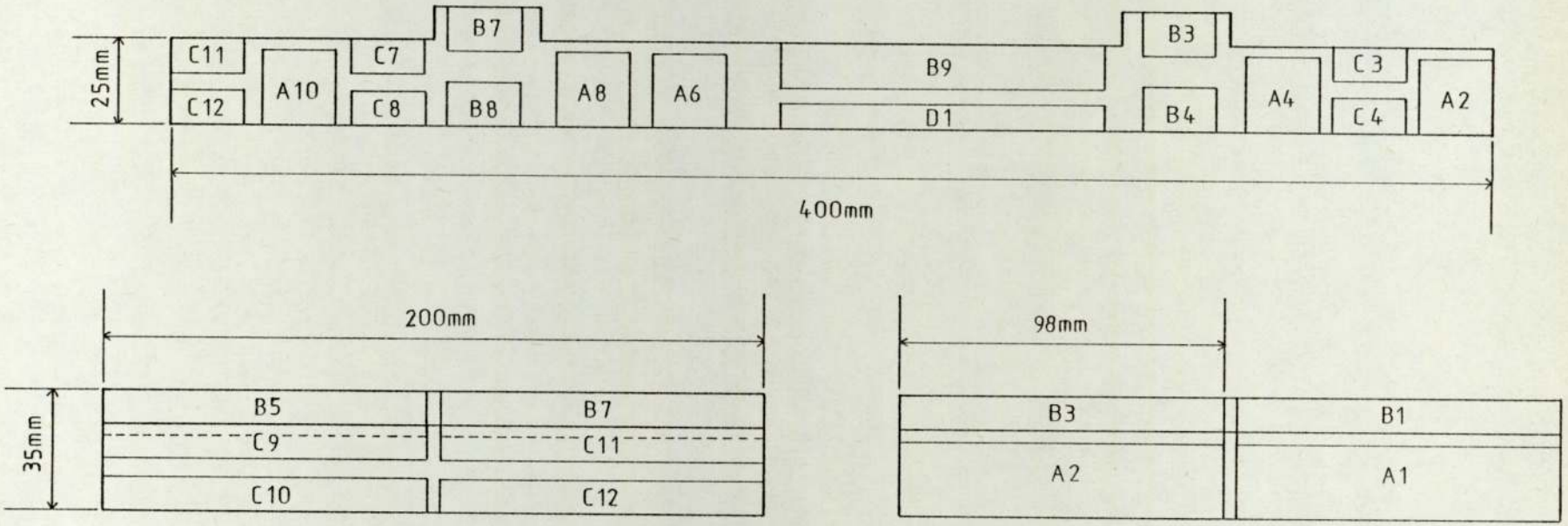

Fig. 47b. Front and end elevations - half full size

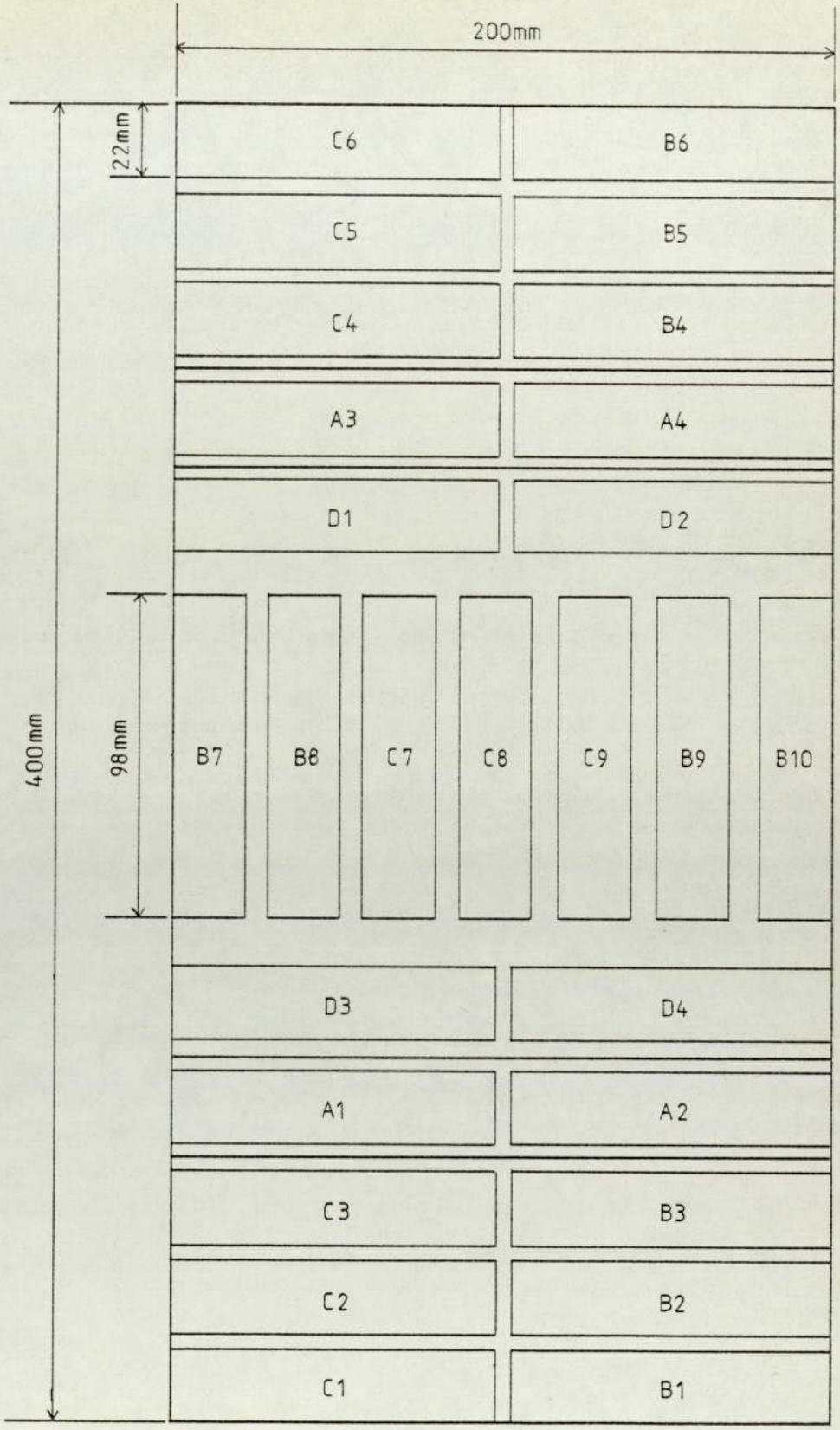

Fig. 48. Details of specimens taken from 400mm x 200mm x 14mm blocks

a) Plan view - half full size

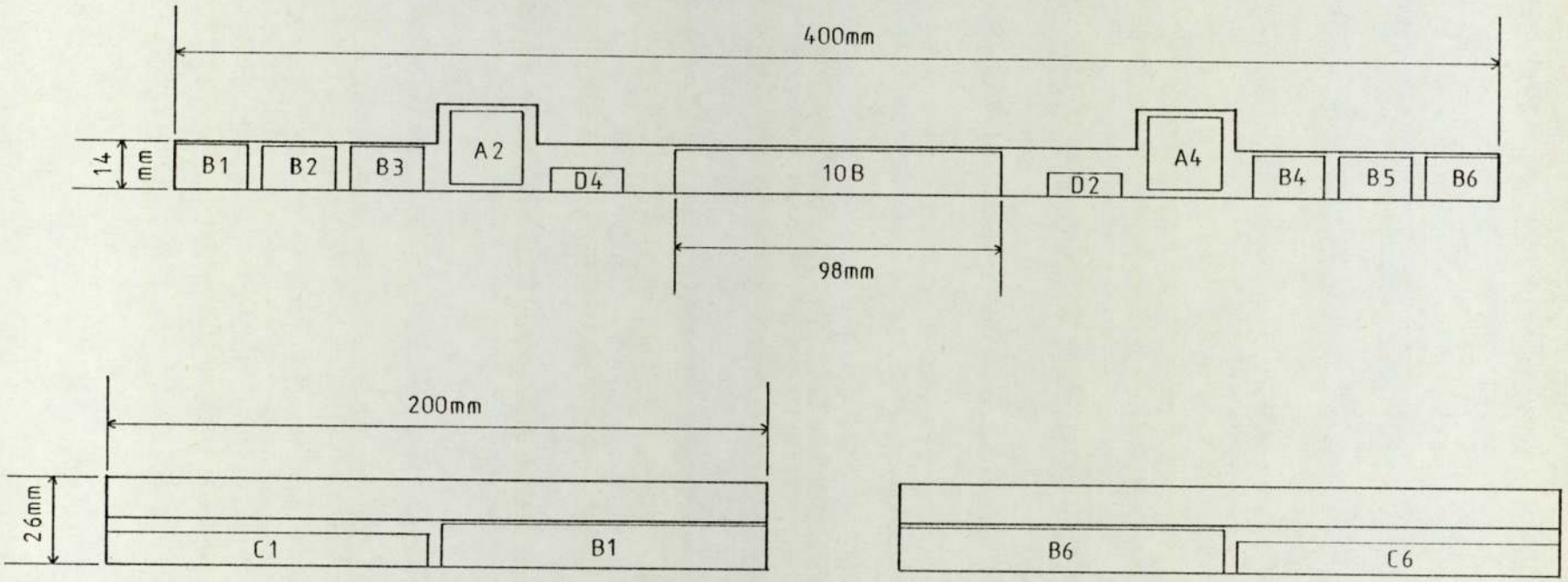

Fig. 48b. Front and end elevations - half full size

being tested. In order to determine the notch width and root radius a "shadowgraph" was used. The tracings obtained from this instrument were then compared with standard root radii circles and the measurements recorded.

5.3 Fatigue pre-cracking.

Fatigue pre-cracking of the specimens was performed on an Amsler Vibrophore; for the specimens taken from the 280 mm type blocks, crack growth rates were measured optically, but this was found to be both tedious and inaccurate. For the majority of the appropriate specimens therefore, fatigue crack growth rates were monitored using the electrical potential technique described in section 4.4.

The construction of the calibration curve was achieved using the 5 mm thick specimens in the following manner. Two probes were spot-welded on to the top face of the specimen on opposite sides of the notch mouth, at a distance of 5 mm apart. A current of 50 amps was then applied to the ends of the specimen at exactly the same position for each individual test. By adopting this procedure, the complex analytical solutions of Johnson and Gilby and Pearson could be avoided. Crack lengths were simulated using very fine saw cuts taken at 1 mm intervals, and for each new "crack" depth the corresponding reference potential was recorded. The data was represented in graphical form and a least squares polynomial was then fitted to this curve. (see fig.49). As the calibration curve corresponded to a specific specimen geometry, the crack length for any alloy could be predicted (for W = 22 mm) by modifying the curve by the combination of thickness and specific resistance factors. i.e.

$$\frac{a}{W} = \frac{I.SP}{10B} \times \left(0{\cdot}218 + 0{\cdot}563\left(\frac{V_a}{V_{ao}}\right) - 0.210\left(\frac{V_a}{V_{ao}}\right)^2 + 0{\cdot}051\left(\frac{V_a}{V_{ao}}\right)^3 - 0{\cdot}005\left(\frac{V_a}{V_{ao}}\right)^4\right) \quad . \quad . \quad . \quad . \quad . \quad . \quad (134)$$

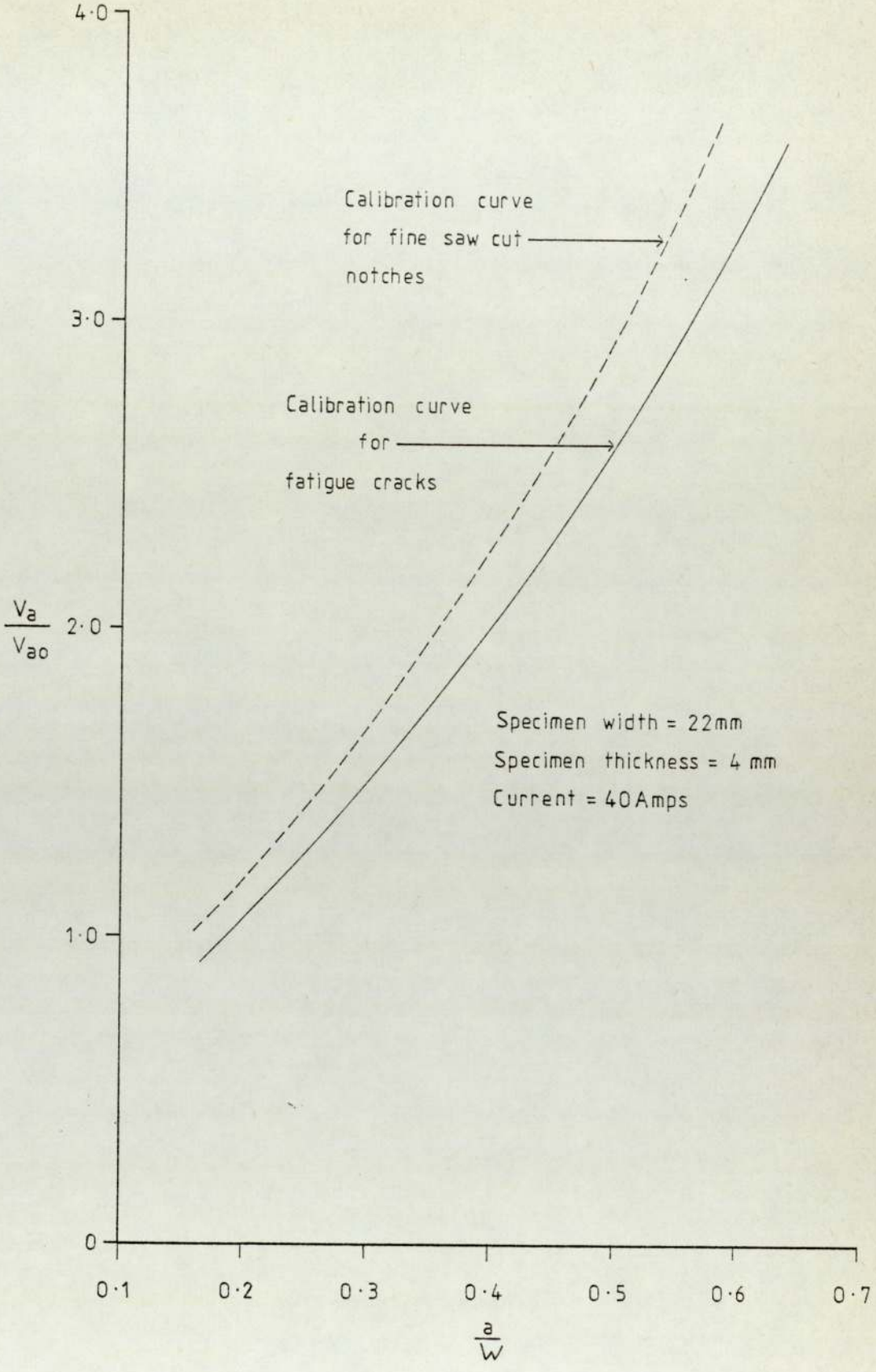

Fig.49. Potential difference calibration curves for Alcoa 354 alloy (artificially aged).

where Va = crack reference potential B = specimen thickness

Vao = original crack reference potential I = current

SP = specific resistance factor.

After breaking some of the specimens open to check the calibration curve, it was discovered that the fatigue cracks were longer than predicted. For this reason, a calibration curve of fatigue crack length versus reference potential was also constructed and is also shown in fig.49. Examination of the two calibration curves (shown in fig.49) suggests a direct relationship between the two curves and that fatigue crack lengths could be predicted by modifying the notch length versus reference potential curve by some factor. This factor was found experimentally to be approximately 1.14. The discrepancy between the two curves was thought to be due to fretting of the fatigue crack surfaces, which provided electrical contact links across the faces of the crack, so decreasing the resistance.

According to the recommendations laid down in British Standards Draft for Development 3 and 19 (8 and 23) the final 1.25 mm of fatigue crack should be grown in more than 50,000 cycles to ensure a sharp crack tip. The fatigue crack could therefore be grown in two stages, initially quite fast and for the final portion, in accordance with the standards. Normally the final portion started at a predicted value of about 0.45 a/W and every effort was made to ensure that the fatigue crack was within the range 0.45 - 0.55 a/W. To ensure that the cracks grew symmetrically, the specimen was located on the centre of the bottom support by means of two clamps which prevented any lateral movement.

5.4 Fracture toughness testing.

Fast fracturing of the specimens was carried out on a 5000 Kg capacity Instron testing machine at a constant cross head displacement rate of 0.1 mm per minute. The three point bend rig used was based on

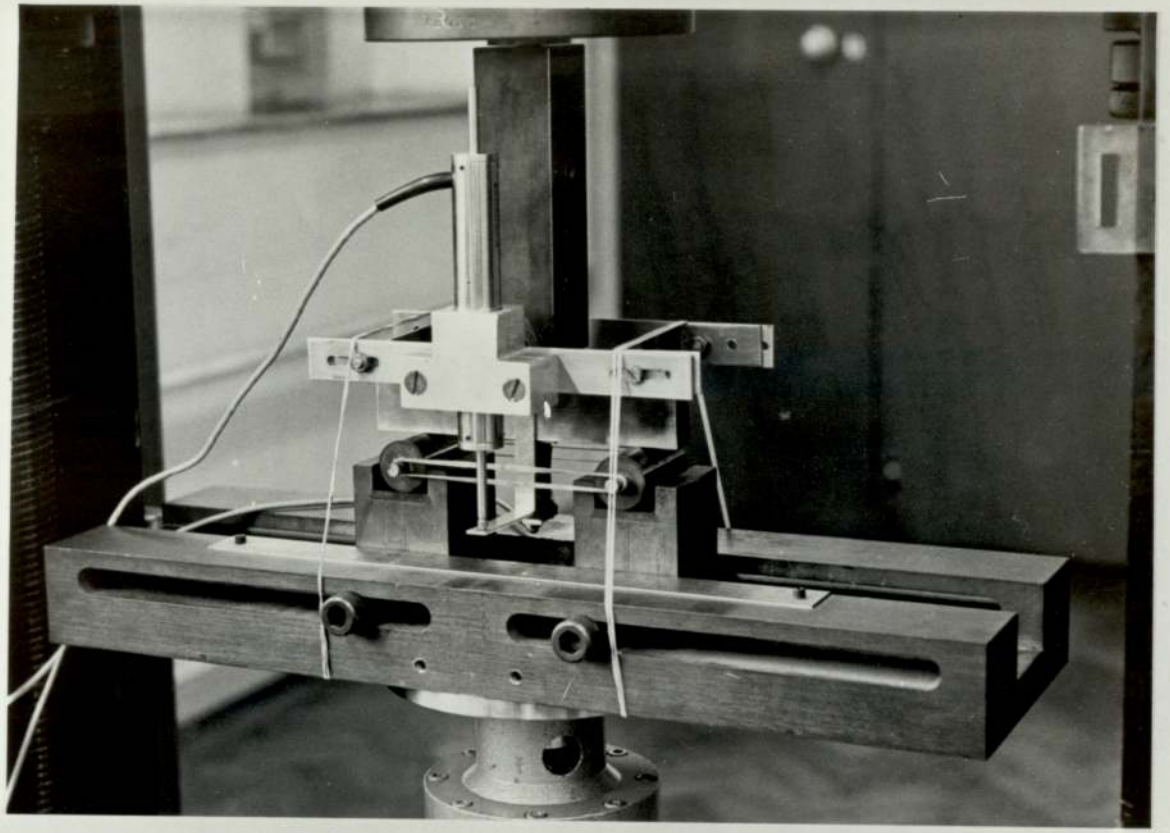

Fig.50. The rig used for measuring the load point displacements for the A.U.W.E. 224 + Ag and KO1 alloys.

the illustrations shown in BS 5447 and Barnby and Daimalani (99). The transducer mounted on the top ram, as developed by Barnby and Daimalani was used for measuring the load point displacements for the A.U.W.E. 224 and A354 alloys. For the A.U.W.E. 224 + Ag and KO1 alloys the improved load point displacement rig illustrated in fig.50 was used.

After a short period of warming up the equipment, the load cell was calibrated with all three flat-bed recorders switched on. These recorders were to be used for producing the following graphical records:

a) Load - clip gauge (crack mouth opening) displacement

b) Load - load point displacement

c) Time - load/potential (i.e. twin pen recorder)

Before the commencement of testing it was necessary to calibrate the clip gauge and transducer, so as to find the magnification given by each and to check over which portion they were linear. The clip gauge could be directly calibrated using a point micrometer and the transducer was calibrated using the constant cross-head displacement of the machine. Now that the linear portion of the clip gauge had been found, a mild steel gauge was made to correspond to this portion so that the knife edges could be attached to the specimen at the correct distance apart each time. In order to measure the load-point displacements from the improved rig, a reference beam was secured to the middle of one of the specimen side faces with an adhesive. Finally two reference probes were spot-welded onto opposite faces of the notch mouth and a current of 60 amps was applied to the ends of the specimen. Testing could now proceed. A diagrammatic illustration of the equipment is shown in fig.51.

During the test the reference potential would increase when the crack initiated. This often corresponded to the point on the other graphs where the load arrested momentarily. All three recorders were

used for notched and cracked specimens, but for blunt notches no electrical potential equipment was necessary, since initiation of the cracks occurred spontaneously at the attainment of the "critical load" (see fig.64b). For the un-notched (beam) specimens, only the load-load point displacement records were required.

5.5 Compliance measurements.

The compliance values of the three point bend specimens were determined from the load-load point displacement records obtained from the rig illustrated in fig.50. Compliance could be given as the reciprocal of stiffness (i.e. compliance = displacement/applied load) For ease of calculation, the dimensionless form of compliance (CEB) was used, where:

C = compliance

E = Young's modulus

B = specimen thickness

The compliance values for the curved and straight crack fronted, compact tension specimens (measured by Crow (113)) were determined from the crack opening displacements at the load line. Since COD was recorded at the crack mouth, an adjustment was made for this effect according to the same procedure used by Ryder, Bowie and Pettit (96) where:

$$COD_{LL} = COD_{M}\left(\frac{a}{a + d}\right)$$

where COD_{LL} is the COD at the load line.

COD_{M} is the COD measured at the crack mouth by the clip gauge.

d is the distance between the load line and the knife edges.

a is the crack length

CEB was found by:

$$CEB = \left(\frac{COD_{LL}}{P}\right) EB$$

5.6 Post-test measurements.

5.6.1 Fatigue crack data records.

A diagrammatic illustration of a typical time-reference potential record is shown in fig.52. By assuming that the fatigue machine developed a constant number of cycles per unit time, the rate of change of potential with respect to the number of cycles could be directly obtained from these records. The reference potentials were then converted to crack lengths using the constructed calibration curve shown in fig.49 and hence the da/dN ratio could be determined for a range of crack lengths.

The range of stress intensity, Δ K, was calculated from the maximum fatigue load (since the minimum fatigue load was conveniently taken as zero) and the instantaneous area of the remaining ligament. As the main objective of this work was to grow sharp fatigue cracks prior to fracture toughness testing, the fatigue crack propagation data was limited to a narrow range of a/W.

5.6.2 Fracture toughness data records.

Diagrammatic illustrations of these test records, together with the measurements to be taken are shown in fig.53. The required graphical measurements are:

a) Maximum load P_{max} (KN).

b) 5% secant load P_Q (KN).

c) Critical load P_c (KN).

d) Critical mouth opening displacement (from clip gauge) CCGD (mm).

e) Critical load point displacement CLPD (mm).

f) Total area under load-LPD record up to P_c (Joules).

g) Area under load-LPD record up to $P_Q/2$ (Joules).

h) 1/gradient of the linear portion of the load-LPD record for uncracked specimens.

i) 1/ gradient of the linear portion of the load-LPD record for the cracked specimens.

j) 1/gradient of the linear portion of the load-CGD record for the cracked specimens.

This data was recorded on data input sheets, together with specimen dimensions and other material properties. The effective crack length was to be determined from three separate measurements a_1, a_2 and a_3, shown diagrammatically in fig.54. Often the crack fronts were difficult to distinguish, although oblique lighting improved the situation. The values for Young's modulus and the yield stresses (0.2% proof stress) were obtained from the literature, or experimentally according to BS 18 on tensile testing. The appropriate areas under the load-load point displacement curve could be determined by representing these areas by equivalent triangles, as shown in fig.53. After completion of the input data sheets, data cards were punched for each specimen. The relevant data is incorporated in the appendix of this thesis.

5.7 Metallography and fractography.

Micro-sections for all the alloys were taken from the remaining specimen halves which had been heat treated to the naturally and artificially aged conditions. For the A.U.W.E. 224 and 224 + Ag alloys, micro-sections were also taken for over-aged conditions. The sections were mounted in conducting bakelite (in order that micro-probe analysis could be carried out), ground and polished in the normal metallurgical

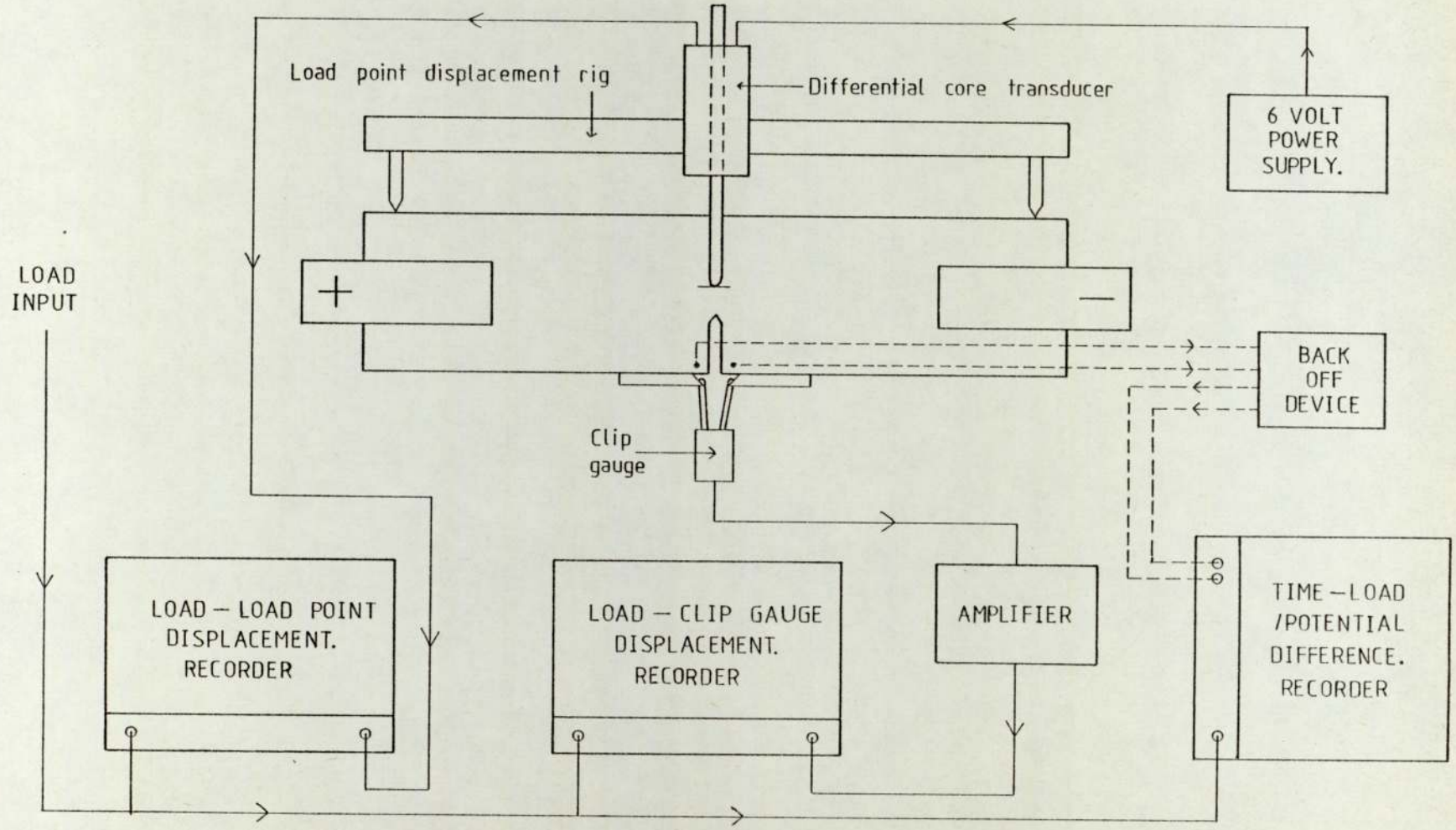

Fig. 51. Diagrammatic illustration of the experimental apparatus

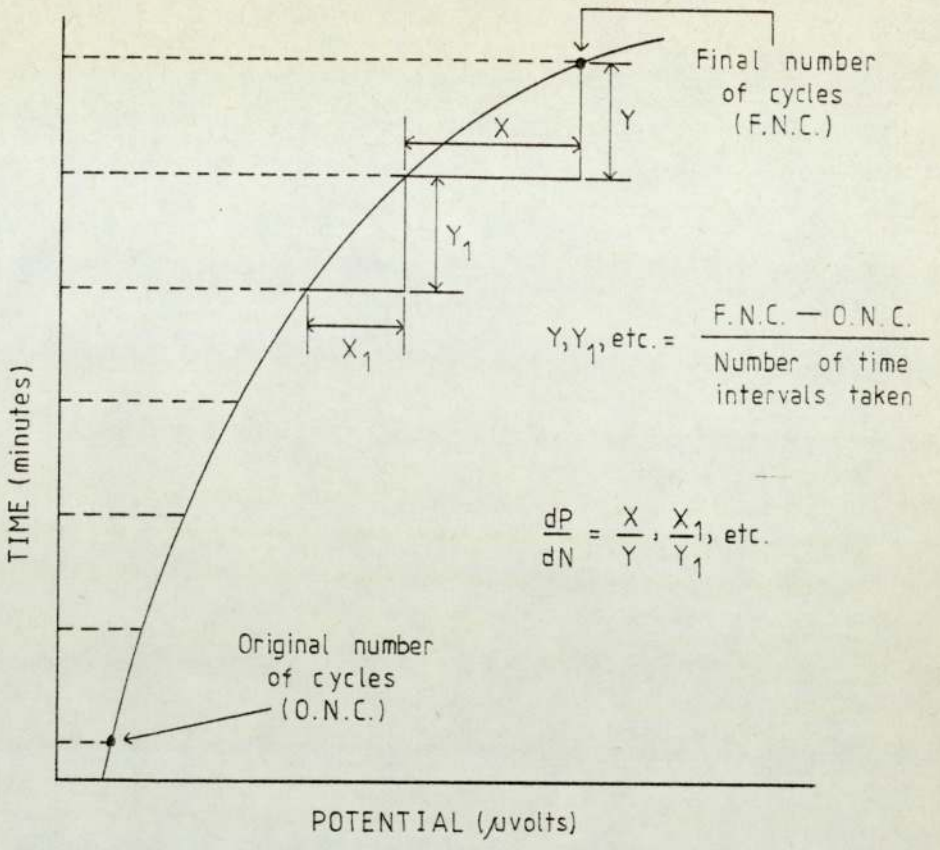

Fig.52. Diagrammatic representation of a time-potential record showing the construction procedure and the required values.

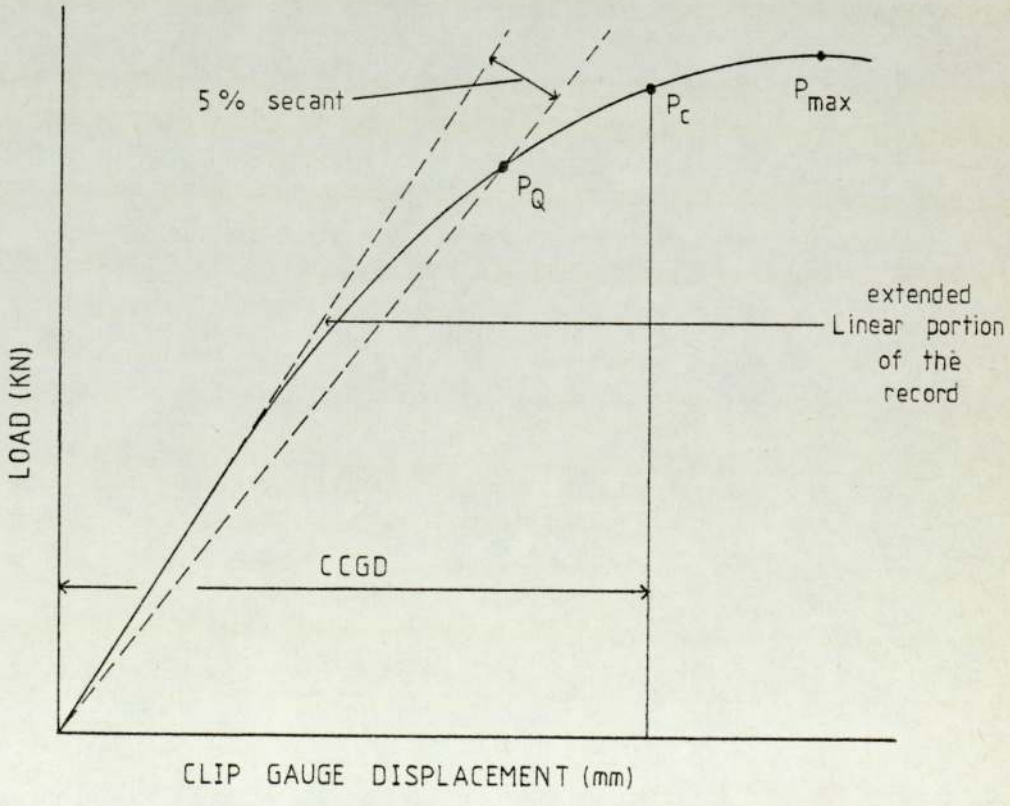

Fig.53a. Diagrammatic representation of a load-CGD record showing the construction procedure and the required data.

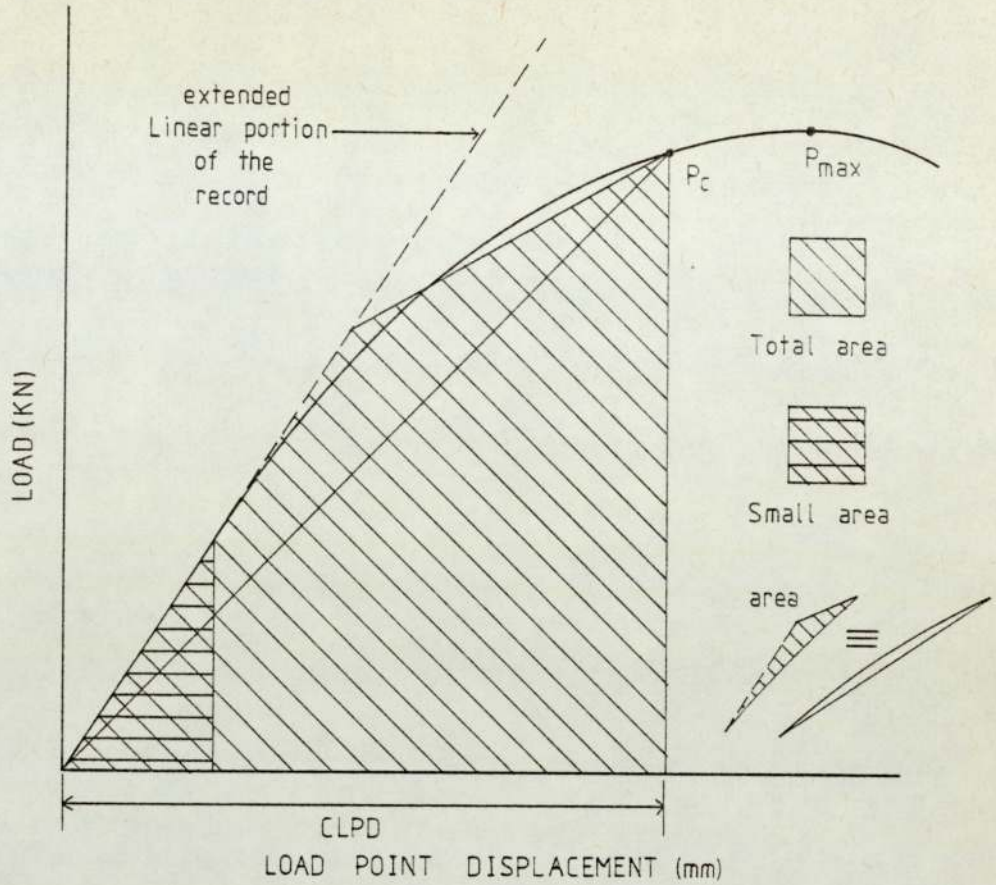

Fig. 53b. Diagrammatic representation of a load-LPD record showing the construction procedure and the required data.

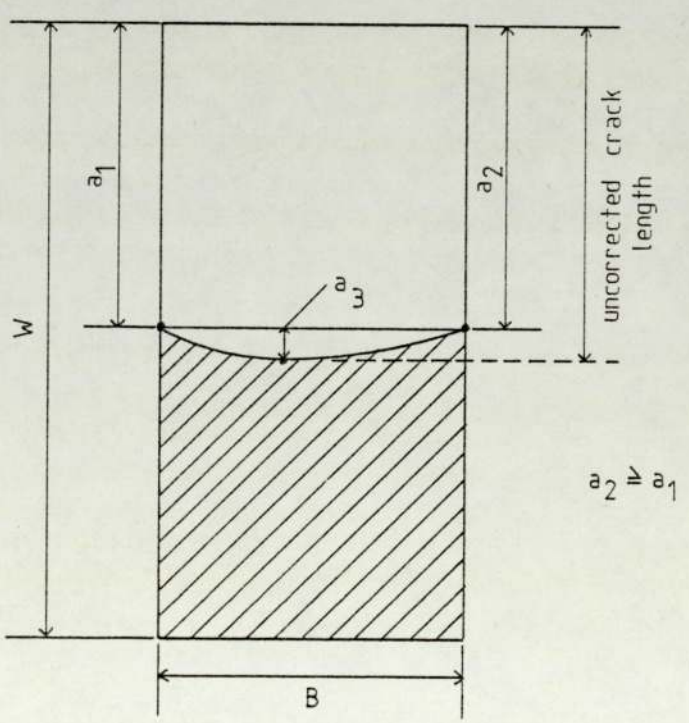

Fig. 54. Diagrammatic representation of a curved crack front, illustrating the required crack length readings.

manner and examined in both the etched and unetched conditions (etchant 0.5% hydrofluoric acid). For the case of the A 354 alloy the volume fraction of the silicon needles was estimated using an image analysing computer, although it was realised that these measurements were very susceptible to the final preparation of the micro-section. The results for the percentage volume fraction are shown in table 11. Hardness and grain size determinations were also carried out on all the micro-sections and are incorporated in table 12.

Photographs taken of the relevant micro structures in the etched condition are illustrated in plates 1 to 10 inclusive. For the as cast A 354 alloy, micro-probe analysis was used to analyse the distribution of elements across some of the silicon needles and an impurity phase. Photographs of these distributions are shown in plates 11 to 14 inclusive.

The fracture surfaces of the alloys were examined using both optical and scanning electron microscopy. Optical photographs for two of the alloys are shown in plates 15 and 16. Scanning electron micrographs of the fracture surfaces, together with spark machined cracks and surfaces are shown in plates 17 to 29 inclusive. A pictorial view of a fatigue crack emanating from a spark machined notch is shown in plate 30.

Table 6. Heat treatments and typical tensile properties.

Material	Heat treatment	Proof stress (MNm -2)	Tensile strength (MNm -2)	Elong-ation. (%)
Alcoa 354	10 hours minimum at 525°C, quench in water at 60 - 80°C, age for 8 hours at 170°C and air cool.	295	324	2
AUWE 224	48 hours at 535°C, quench in water at 70°C, age for 24 hours at 170°C and air cool	470	500	5
AUWE 224 +Ag	48 hours at 535°C, quench in water at 70°C, age for 24 hours at 170°C and air cool.	470	500	5
KO1	2 hours minimum at 513°C, then 14 hours at 525°C, quench in water at 70°C, age at room temp. for 12 - 24 hours, then 5 hours at 170°C and air cool.	345	412	3

Table 11. The volume fraction of the silicon phase in as cast A 354.

(using an image analysing computer)

Block number 1.

Percentage volume fraction

8.0	9.1	5.5	9.5	4.0	11.5	12.0	15.5	7.8	14.0
9.5	7.0	11.0	15.0	5.0	6.5	12.5	7.2	10.0	6.0
6.5	5.5	10.5	6.7	13.5	9.5	9.3	9.5	8.5	8.0
9.3	7.9	12.7	9.0	10.5	10.6	4.9	12.5	8.9	11.8
7.8	9.6	10.3	6.9	8.0	7.9	7.6	11.8	10.3	13.6

mean of 50 results = 9.32 ± 5.4

Block number 2.

Percentage volume fraction

15.0	12.5	10.3	10.8	7.0	8.4	7.6	14.4	12.6	6.8
7.6	15.4	13.0	9.1	10.0	8.5	9.0	15.5	13.5	11.5
12.4	10.2	6.4	10.1	9.0	11.1	13.9	8.4	7.4	7.7
3.2	6.4	7.0	17.1	4.4	15.5	10.5	13.5	11.6	9.8
14.9	9.6	15.0	11.0	11.0	14.3	8.8	4.0	6.0	4.0

mean of 50 results = 10.25 ± 6.9

Table 12. Mechanical properties of the alloys.

Material	Condition	Hardness HV10	0.2% Proof stress (MNm-2)	Grain size (mm)
A 354	AC	82.1 ± 8.3	-	-
	NA	104.7 ± 9.2	190	-
	AA8	121.3 ± 12.5	295	-
A.U.W.E. 224	NA	127.7 ± 11.9	325	0.20
	AA24	141.6 ± 7.7	420	0.25
A.U.W.E. 224 + Ag.	NA	116.6 ± 13.8	210	0.20
	AA1	128.4 ± 11.7	235	0.20
	AA3	129.7 ± 13.3	250	0.20
	AA6	133.0 ± 11.6	253	0.20
	AA12	140.9 ± 20.6	285	0.20
	AA24	150.1 ± 16.2	320	0.20
	AA48	156.5 ± 10.6	310	0.20
	AA96	146.1 ± 11.6	300	0.20
KO1	AC A1	95.8 ± 6.6	200	0.20
	AC A2	95.1 ± 5.8	200	0.20
	AC A3	69.2 ± 27.7	200	0.20
	AC B1	84.8 ± 9.9	200	0.20
	AC B2	90.9 ± 8.7	200	0.20
	AC B3	93.2 ± 6.9	200	0.20
	AC C1	94.1 ± 7.8	200	0.20

6. EXPERIMENTAL RESULTS.

6.1 Fatigue data.

The data obtained from the time-reference potential records was fed into a computer programme which initially converted this data into the form of crack lengths and number of cycles. From this converted data, the programme then proceeded to calculate da/dN by a 'finite difference' method, taking gradients at regular intervals of N (where N = number of cycles). For each instantaneous value of 'a', the range of stress intensity could then be given by:

$$\Delta K = \frac{6 P Y \sqrt{a}}{B W^{\frac{3}{2}}} \quad . \quad . \quad . \quad . \quad . \quad (133)$$

where P is the maximum fatigue load, and Y may be given by: (112)

$$Y = 1{\cdot}93 - 3{\cdot}07\left(\frac{a}{W}\right) + 14{\cdot}53\left(\frac{a}{W}\right)^2 - 25{\cdot}11\left(\frac{a}{W}\right)^3 + 25{\cdot}80\left(\frac{a}{W}\right)^4 \quad (134)$$

The data was finally processed and presented in the form of $\log_{10} da/dN$ versus $\log_{10} \Delta K$. The results for the A.U.W.E. 224 type alloys are shown graphically in fig.55.

The stabilisation period for the electrical potential equipment was only of the order of a few minutes and maximum sensitivity was maintained by repeatingly "backing off" the increasing reference potential, rather than altering the sensitivity range on the recorder. During fatigue cycling, the cracks were observed to grow intermittently, often arresting at the specimen side surfaces. For the aluminium-silicon alloy, micro cracks grew ahead of the main fatigue crack, and then linked up. This, however, was not shown up on the time-reference potential traces. No plastic zones were observed ahead of the crack tips for any of the alloys.

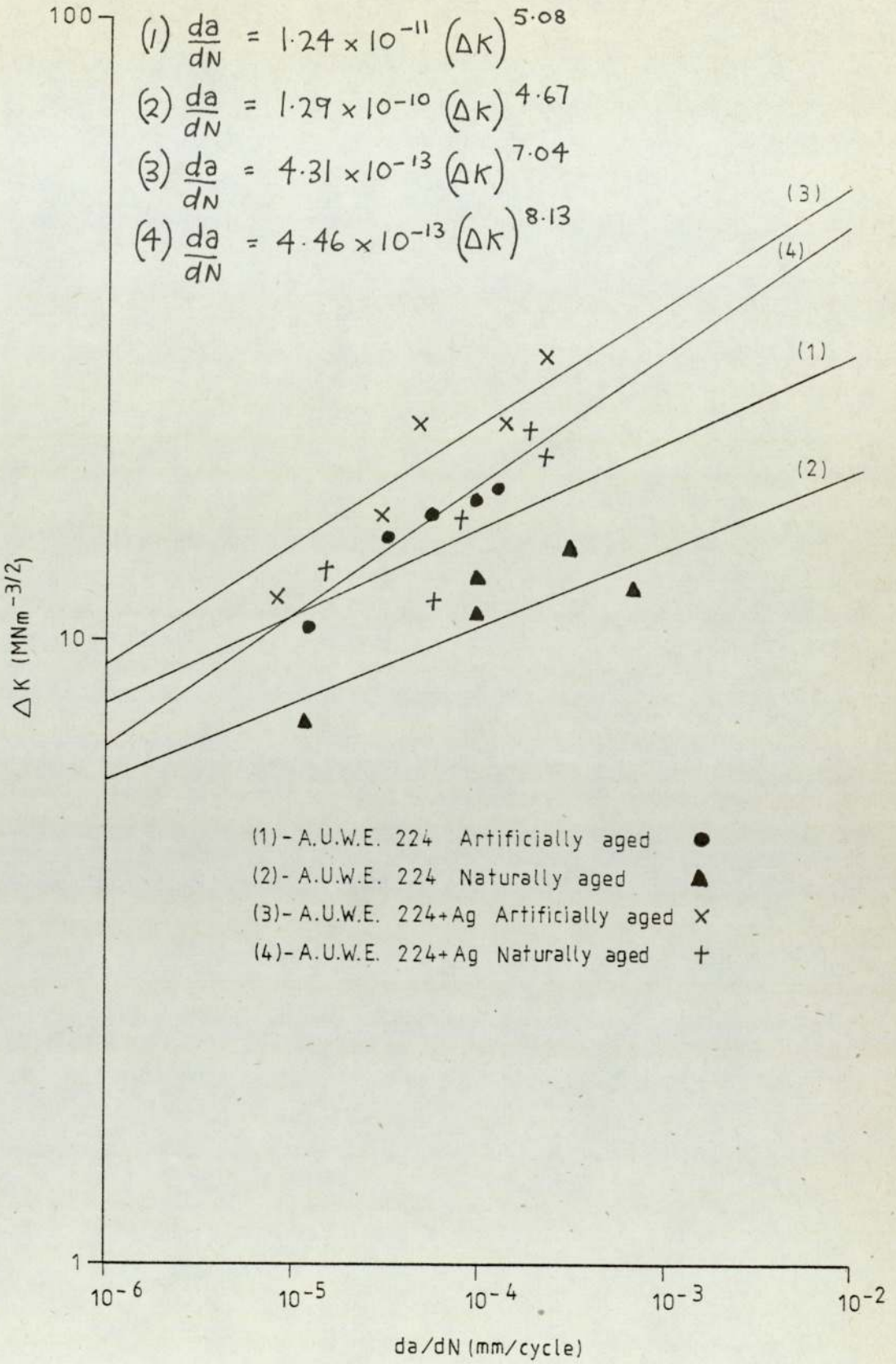

Fig.55. General trend of the fatigue crack propagation results. ((A.U.W.E.) 224 type alloys)

6.2 Compliance data.

6.2.1 Data analysis.

The compliance of all the specimens has been measured but of particular importance was the compliance of the electro-spark machined straight and curved crack fronts in three point bending. This data, together with similar data of S. Crows (113) for compact tension specimens, has been processed using the methods of Collipriest (95) and Ryder et al (96). From Ryder et al:

$$\underbrace{\ln\ln(CEB)}_{y} = e + (v-e)\underbrace{\left\{-\ln\left(1-\frac{a}{w}\right)\right\}^{1/k}}_{x} \quad \cdot \quad (135)$$

we may write $$(y-e) = (v-e)\,x^{1/k} \quad \cdot \quad \cdot \quad \cdot \quad \cdot \quad (136)$$

and by taking logs we obtain

$$\ln(y-e) = \ln(v-e) + \frac{1}{k}\ln(x) \quad \cdot \quad (137)$$

This equation is now in the form of Y = Mx + c (i.e. the equation of a straight line). a/W and CEB results were fed into a computer programme which was designed to calculate the value of 'e' by an iterative procedure. It was possible to determine 'e' in this manner since, at the correct 'e' value the error sum of squares from the linear regression calculation would be at a minimum. Having determined 'e', v and k could now be directly obtained from the relationships:

$$V = \exp(\text{intercept}) + e \quad \text{and} \quad k = \frac{1}{\text{gradient}}$$

According to Ryder et al

$$C_3 = \left[\frac{1}{2}\left(\frac{a}{w}\right)\frac{d(CEB)}{d(a/w)}\right] \quad \cdot \quad \cdot \quad \cdot \quad (138)$$

The derivative of normalised compliance may be given by:

$$\frac{d(CEB)}{d(a/W)} = \left[(v-e)\exp\left(f+\exp(f)\right) x \left\{ \frac{\left[-\ln(1-a/W)\right]^{\left(\frac{1}{k}-1\right)}}{k(1-a/W)} \right\} \right] \quad . \qquad (139)$$

C_3 versus a/W results for both three point bend and compact tension specimens, with straight and curved crack fronts, are shown in figs. 56, 57, 58, and 59 and detailed in tables 7, 8, 9 and 10. In these figures, comparison is shown between the curved crack fronts with and without the applied correction and between polynomial and Ryder's curve fitting procedures.

6.2.2 Curved crack front correction factors.

The effective crack length for the curved crack fronts was calculated according to the following equation, which was derived from Neale's formula for curved crack fronts (see section 3.5):

$$a_{effective} = a_1 + \frac{\left[\frac{(a_2-a_1)}{2} B + \frac{2a_3}{3} \sqrt{\left\{ (a_2-a_1)^2 + B^2 \right\}} \right]}{S} \qquad (140)$$

where the values a_1, a_2, a_3, B and S are illustrated in fig.54. By assuming that the curved crack front was parabolic, S could be determined from the formula (114):

$$S = \int_a^b \sqrt{1 + \left(\frac{dy}{dx}\right)^2}\, dx \qquad (141)$$

The derivation of which is as follows.

Consider a symmetrical parabola given by the formula $Y = Ax^2$

Differentiating with respect to x we obtain:

$$\frac{dy}{dx} = 2Ax \quad . \quad . \quad . \quad . \quad . \quad . \quad . \qquad (142)$$

and therefore:

$$\frac{S}{2} = \int_0^{\frac{B}{2}} \sqrt{\left(1 + 4A^2x^2\right)} dx \quad . \quad . \quad . \qquad (143)$$

where B is the specimen thickness.

If we let $\frac{dy}{dx} = \tan\theta = 2Ax$ . . . . . (144)

then:

$$\frac{S}{2} = \int_0^{\frac{B}{2}} \sqrt{\left(1 + \tan^2\theta\right) dx} \quad . \quad . \quad . \quad (145)$$

$$= \int_0^{\frac{B}{2}} \sqrt{\left(\sec^2\theta\right) dx} \quad . \quad . \quad . \quad . \quad (146)$$

$$= \int_0^{\frac{B}{2}} \left(\sec\theta\right) dx \quad . \quad . \quad . \quad . \quad (147)$$

From the list of standard differentials we obtain:

$$\frac{d}{d\theta} \tan\theta = \sec^2\theta \quad . \quad . \quad . \quad . \quad . \quad (148)$$

$$\frac{d}{d\theta} \sec\theta = \tan\theta \sec\theta \quad . \quad . \quad . \quad . \quad (149)$$

therefore from equation (144) we obtain:

$$2A\,dx = \sec^2\theta\, d\theta \quad . \quad . \quad . \quad . \quad . \quad (150)$$

and

$$dx = \frac{\sec^2\theta\, d\theta}{2A} \quad . \quad . \quad . \quad . \quad . \quad (151)$$

substituting for dx in equation (147) we obtain:

$$\frac{S}{2} = \int_0^{\frac{B}{2}} (\sec\theta \times \sec^2\theta)\, d\theta \times \frac{1}{2A} \quad . \quad . \quad (152)$$

Integrating by parts:

$$\frac{S}{2} = \frac{\sec\theta \times \tan\theta + \ln(\sec\theta + \tan\theta)}{4A} \quad . \quad (153)$$

and as each side of the parabola is symmetric:

$$S = \frac{2Ax\sqrt{1 + 4A^2x^2} + \ln\left[\sqrt{1 + 4A^2x^2} + 2Ax\right]}{2A} \qquad (154)$$

where $A = \frac{4a_3}{B^2}$

6.2.3 Three point bend load point and mouth opening (COD at crack mouth) displacements.

The plastic contribution of the mouth opening displacement (COD at crack mouth) and load point displacement were determined for the majority of the specimens. Where V_{gp} is the plastic mouth opening displacement and q_p is the plastic load point displacement. These plastic displacements could be given by the difference between the total displacements (up to the critical load) and the elastic displacements at the critical load.i.e.

$$V_{gp} = V_{g\ total} - V_{g\ elastic}$$

$$q_p = q_{total} - q_{elastic}$$

where $V_{g\ total}$ was the total mouth opening displacement.

$V_{g\ elastic}$ was the elastic mouth opening displacement.

q_{total} was the total load point displacement.

$q_{elastic}$ was the elastic load point displacement.

The ratio of these two displacements were then expressed in terms of a/W but there was far too much scatter in the results to show a significant trend. For this reason, fig.60 shows the ratio of the total mouth opening displacement to total load point displacement (prior to cracking) as a function of a/W, for the 224 + Ag alloy. As it can be seen from fig.60, the load point displacement is always greater than the mouth opening displacement, although this effect is less pronounced when the a/W values are small.

Table 7. Compliance data for straight crack fronts.

(C.T.S. specimens)

Measured a/W	Measured CEB	Calculated compliance calibration (C_{3c})	Experimental compliance calibration (C_{3e})
0.42	24.34	-	4.81
0.44	25.84	3.37	5.21
0.46	27.09	4.94	5.64
0.48	28.98	6.12	6.12
0.50	33.11	7.13	6.65
0.52	36.00	8.02	7.24
0.54	43.10	8.82	7.91
0.56	49.07	9.51	8.65
0.58	56.30	10.07	9.50
0.60	62.55	10.59	10.45
0.62	71.20	11.05	11.55
0.64	79.79	11.54	12.82
0.66	81.58	12.22	14.30
0.68	99.00	13.23	16.03

e = 0.18

v = 1.4658

k = 2.4033

To obtain a greater range of C_3 values, data generation was used with a/W from 0.2 to 0.9.

Table 8. Compliance data for curved crack fronts.

(C.T.S. specimens)

Measured a/W		Measured CEB	Calculated compliance calibration (C_{3c})	Experimental compliance calibration (C_{3e})
uncorrected	corrected			
0.71	0.605	43.17	11.37	9.92
0.73	0.625	57.56	12.18	10.59
0.75	0.645	70.75	13.00	11.58
0.77	0.665	74.90	13.79	12.73
0.79	0.685	83.90	14.57	14.07
0.81	0.705	91.03	15.32	15.68
0.83	0.725	106.02	16.02	17.63
0.85	0.745	120.38	16.67	20.05
0.87	0.765	131.60	17.24	23.15

e = -500

v = 1.2847

k = 1113.946

To obtain a greater range of C_3 values, data generation was used with a/W from 0.2 to 0.9.

Table 9. Compliance data for straight crack fronts.

(4:1 Span length to width ratio, 3 point bend specimens)

Measured a/W	Measured CEB	Calculated compliance calibration (C_{3c})	Experimental compliance calibration (C_{3e})
0.18	6.02	-	1.78
0.22	7.88	2.20	2.08
0.28	10.28	2.62	2.71
0.38	16.23	3.87	4.00
0.48	28.54	6.37	6.12
0.55	40.70	9.07	8.43
0.59	60.38	10.95	10.66
0.65	89.73	13.94	15.16

e = 0.12

v = 1.4746

k = 2.241

To obtain a greater range of C_3 values, data generation was used with a/W from 0.2 to 0.9.

Table 10. Compliance data for curved crack fronts.

(4:1 Span length to width ratio, 3 point bend specimens)

Measured a/W		Measured CEB	Calculated compliance calibration (C_{3c})	Experimental compliance calibration (C_{3e})
uncorrected	corrected			
0.42	0.35	9.34	4.36	3.59
0.46	0.39	12.04	4.97	4.24
0.50	0.43	17.40	5.50	4.98
0.54	0.47	23.85	6.04	5.83
0.57	0.50	27.38	6.53	6.60
0.63	0.56	36.08	8.07	8.83
0.69	0.62	51.08	10.98	12.26
0.72	0.65	67.82	13.28	14.35

e = 4.0

v = 1.3042

k = 3.3932

To obtain a greater range of C_3 values, data generation was used with a/W from 0.2 to 0.9.

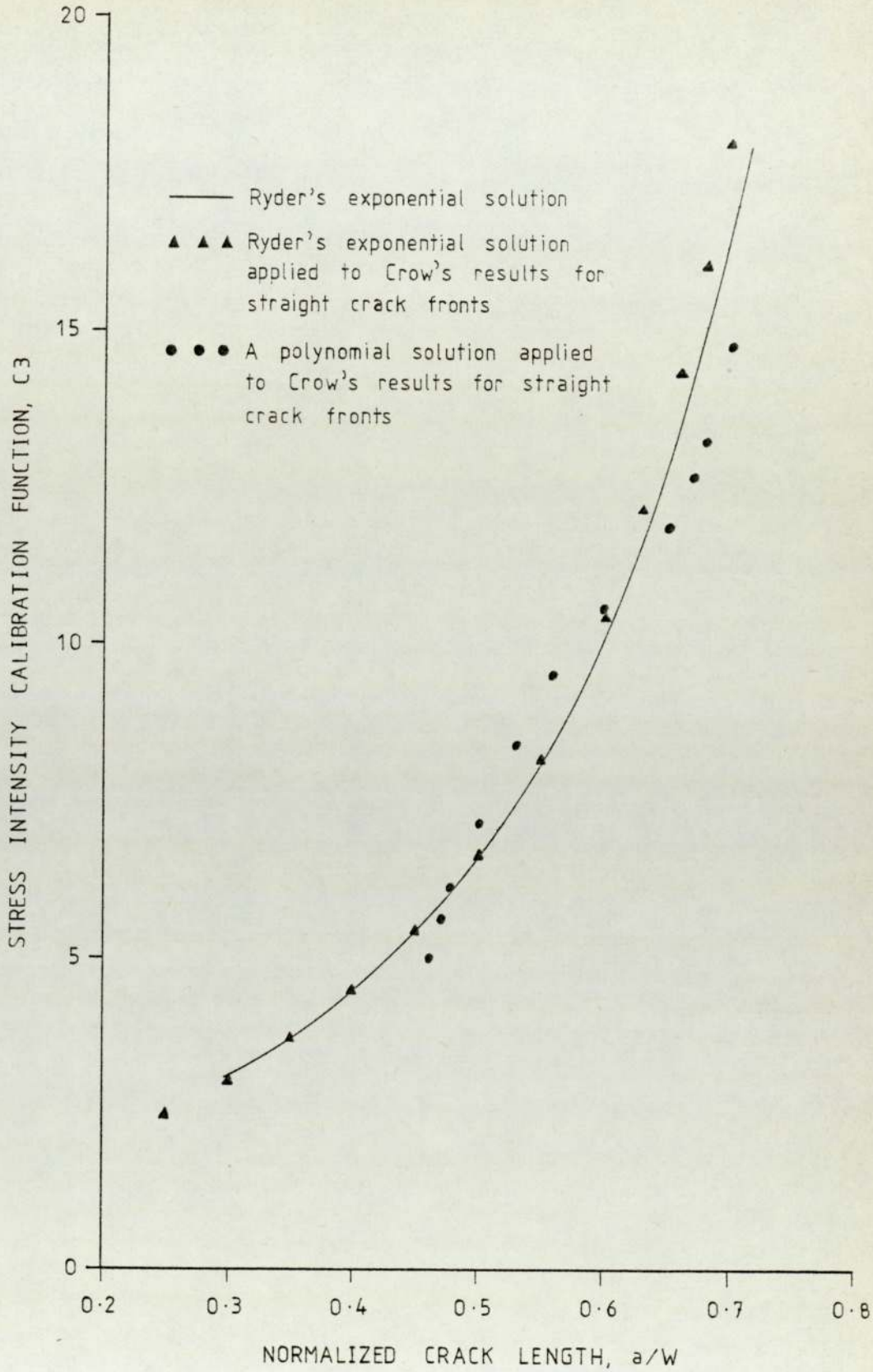

Fig. 56. C_3 versus a/W for straight crack fronts (from Crow's results on compact tension specimens)

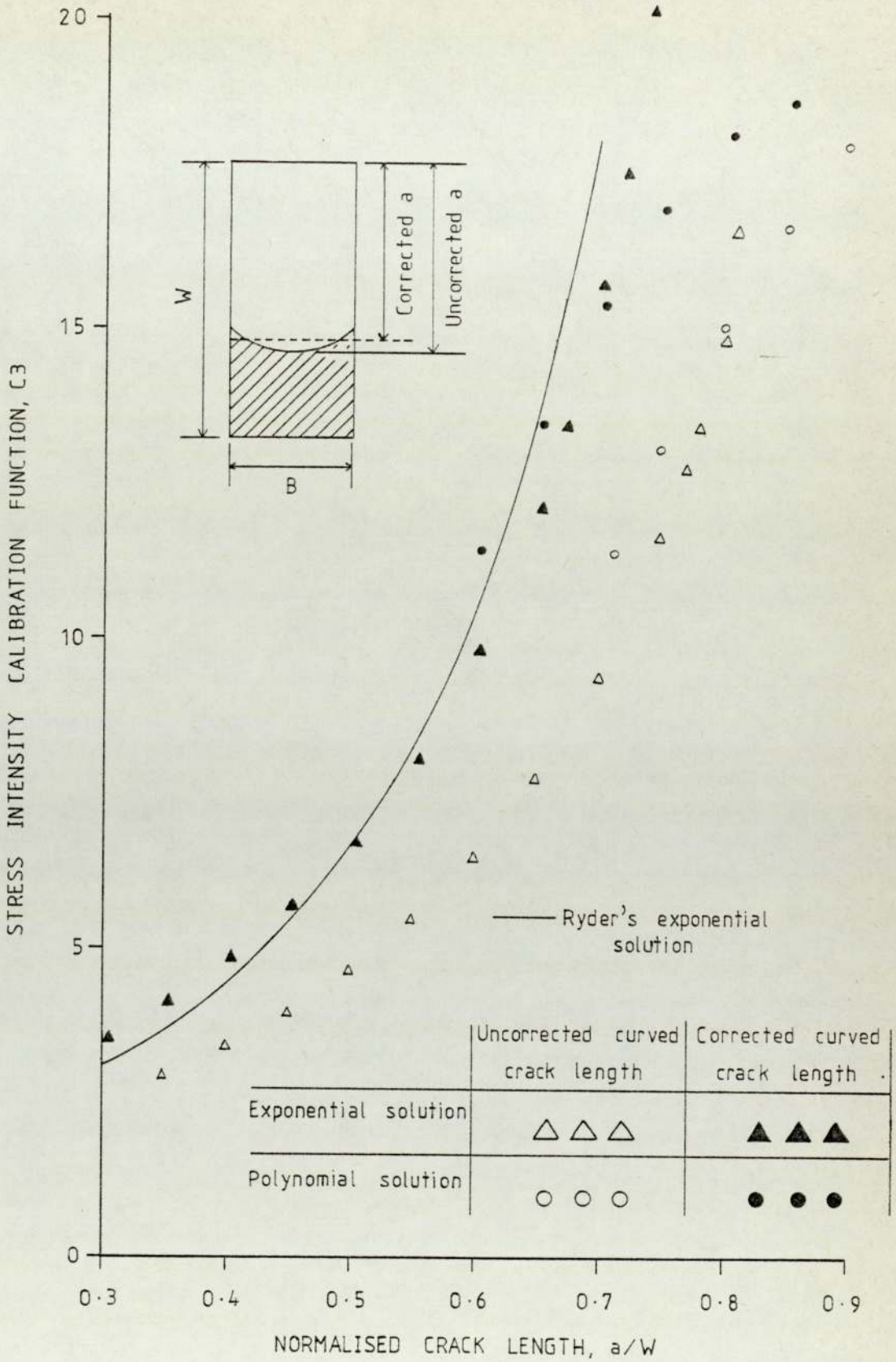

Fig. 57. C_3 versus a/W for curved crack fronts (from Crow's results on compact tension specimens)

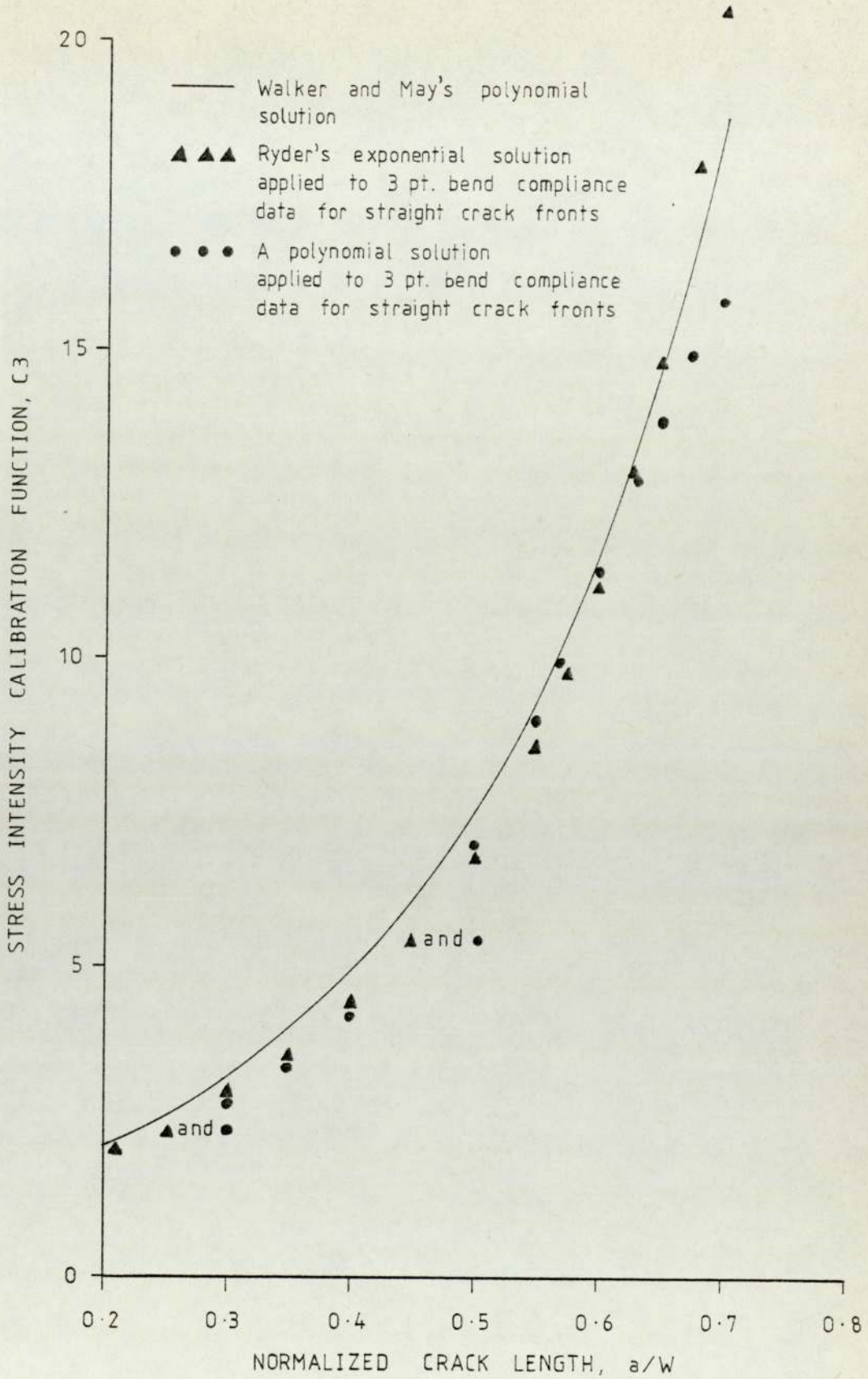

Fig. 58. C_3 versus a/W for straight crack fronts (from three-point bend compliance data)

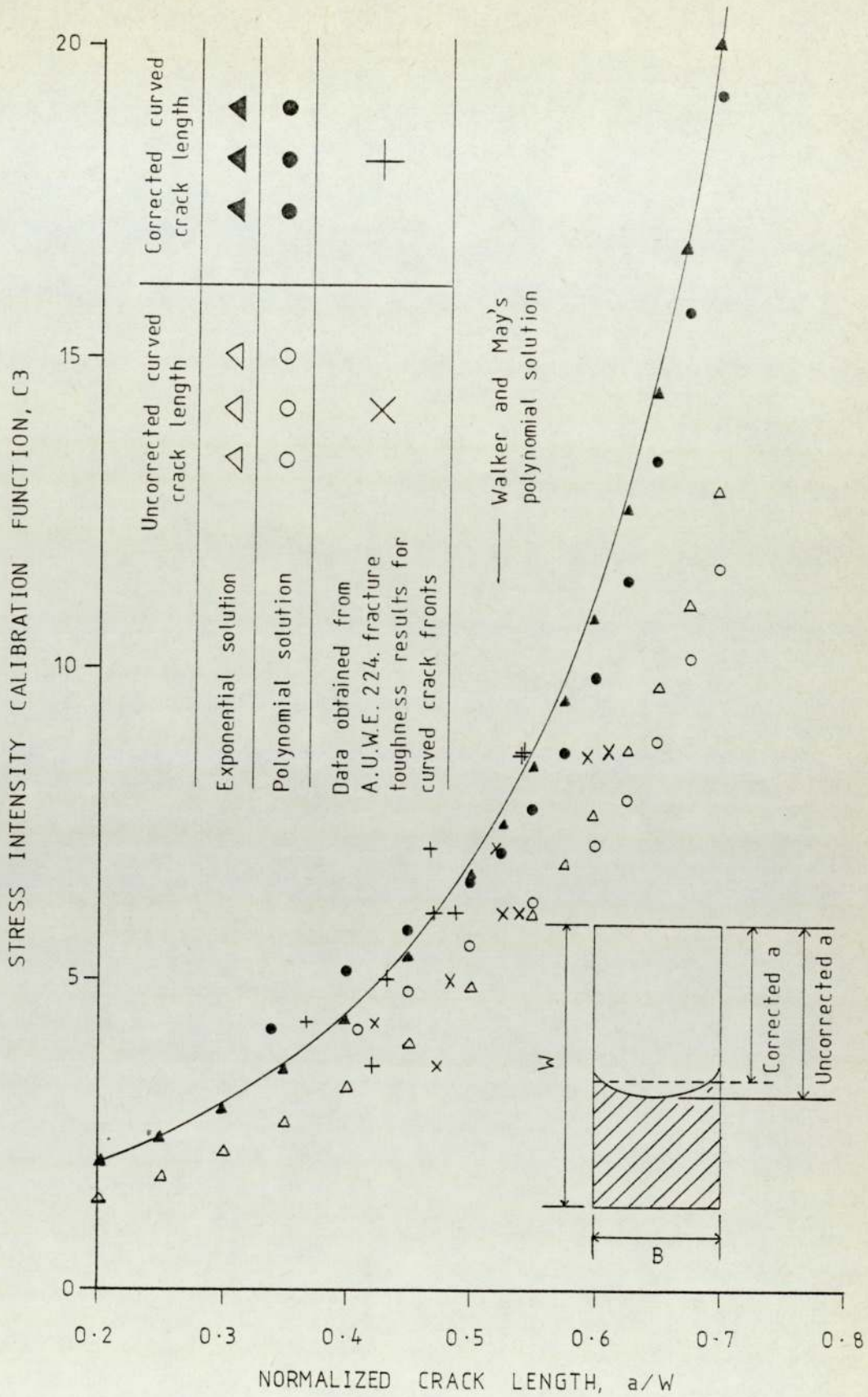

Fig. 59. C_3 versus a/W for curved crack fronts (from three-point bend compliance data)

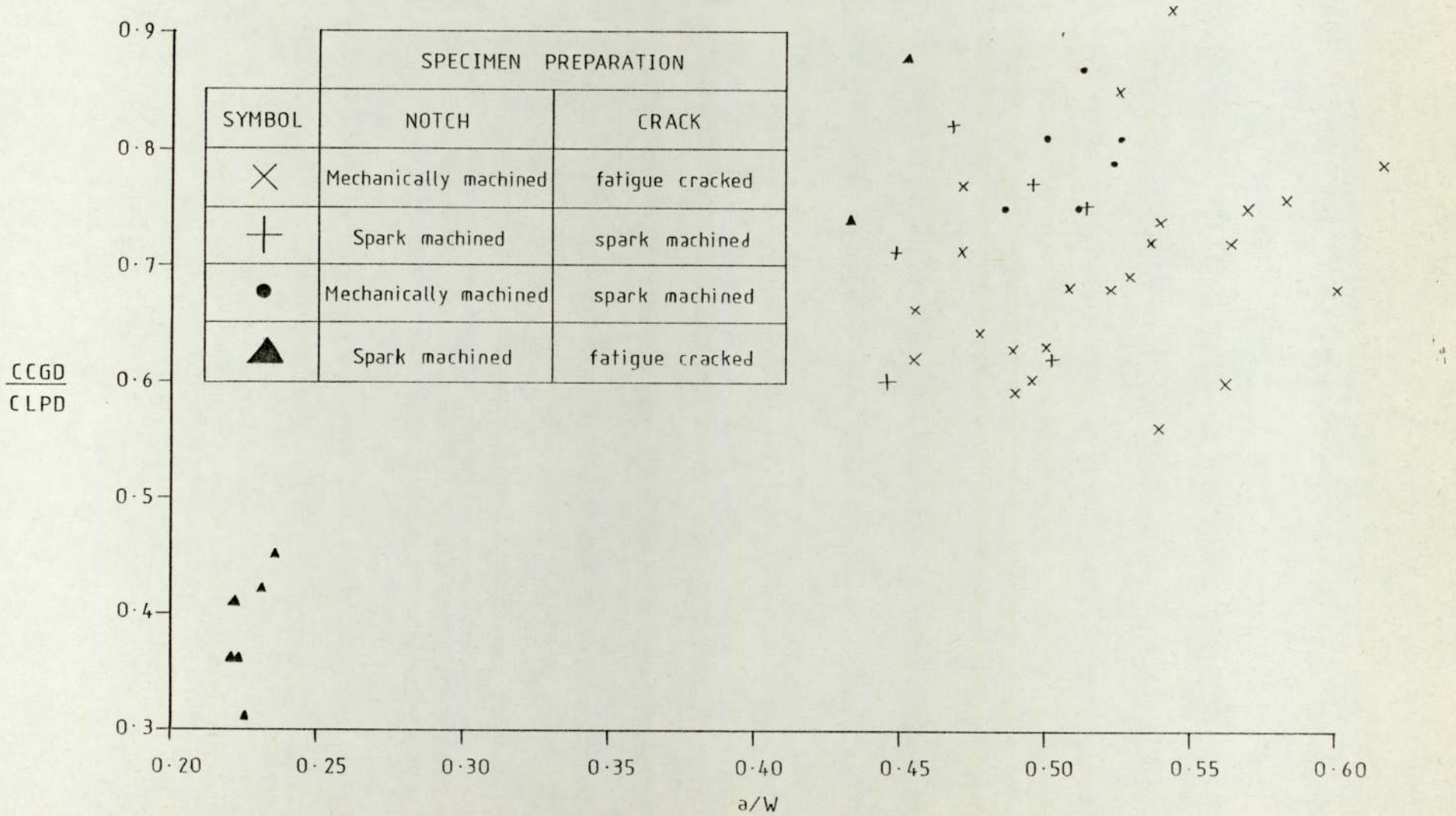

Fig. 60. The relationship between mouth opening and load point displacements for A.U.W.E. 224 Ag.

6.3 Fracture toughness data.

6.3.1 Graphical records.

Three point bend specimens for all the materials were tested to failure in accordance with the details given in the experimental section. A convenient chart speed of 20 mm/min was taken for the load/potential-time records, and a current of 60 amps was applied to the appropriate specimens in order to obtain maximum sensitivity. The clip gauge and transducer magnifications, determined at 10MV/CM, were found to be 550X and 160X respectively.

Initially, some of the load/potential-time records showed a decrease in potential; this has also been observed and commented on by Bachmann and Munz (109). With most of the load-load point displacement (L-LPD) and load-clip gauge displacement (L-CGD) records there was an initial period of 'bedding in'. This was neglected when deciding upon the linear, elastic portion of the graphs. The L-LPD records obtained using the Barnby and Daimalani technique tended to bow during elastic loading. Consequently it was often difficult to decide upon the linear portion of these records. There was far less bowing with the improved rig, but occasionally, the traces did 'jump' but as these jumps were only offsets, they could easily be allowed for. All the records indicated large extents of plasticity since their P_Q:P_{max} ratios and deviations at P_Q and $0.8P_Q$ were often greater than the values recommended in the L.E.F.M. standards. This fact, however, was thought to be the result of large displacement magnifications, since the lack of any visible plastic zone suggests little plastic deformation.

On attainment of the critical load, the records became 'stepped', with these steps becoming more pronounced after reaching the maximum load. This observation could be attributed to initiation and propagation intervals for the crack.

6.3.2 Fracture toughness calculations.

All the data was recorded on data input sheets which were punched and fed into the computer, which used a programme designed to calculate the following:

K_Q L.E.F.M. (i.e. the provisional value of K_{1c}) given by:

$$K_Q \text{ (LEFM)} = \frac{P_Q Y}{BW^{\frac{1}{2}}} \quad . \quad . \quad . \quad . \quad (155)$$

where Y (the compliance function) may be given by (112):

$$Y = 6\left(1.93\left(\frac{a}{w}\right)^{\frac{1}{2}} - 3.07\left(\frac{a}{w}\right)^{\frac{3}{2}} + 14.53\left(\frac{a}{w}\right)^{\frac{5}{2}} - 25.11\left(\frac{a}{w}\right)^{\frac{7}{2}} + 25.80\left(\frac{a}{w}\right)^{\frac{9}{2}}\right) \quad (156)$$

The minimum thickness for L.E.F.M. conditions was calculated according to the recommendations laid down in BS 5447. i.e.

$$B > 4.0\left(\frac{K_{1c}}{\sigma_{ys}}\right)^2 \quad . \quad . \quad . \quad . \quad (157)$$

The maximum fatigue stress intensity K_f was calculated from equation (155) except that the maximum fatigue load, P_f was substituted for P_Q. Critical crack opening displacements were calculated from the equations given in BS DD 19, where, assuming a rotational factor r of 0.45, the COD may be given by:

$$\delta_t = \left[\frac{0.45(w-a)}{0.45W + 0.55a + Z} \times \left(\frac{V_g - \gamma\sigma_y W(1-\nu^2)}{E}\right)\right] \quad (158)$$

for $$V_g \geq \frac{2\gamma\sigma_y W(1-\nu^2)}{E}$$

or $$\delta_t = \left[\frac{0.45(w-a)}{0.45W + 0.55a + Z} \times \left(\frac{V_g^2 E}{4\gamma\sigma_y W(1-\nu^2)}\right)\right] \quad (159)$$

for $$V_g \leq \frac{2\gamma\sigma_y W(1-\nu^2)}{E}$$

Here, z is the height of the clip gauge knife edges above the top faces of the specimen and γ is given by the following expression

$$\gamma = \frac{V_o E}{\sigma_y W(1 - \nu^2)} \quad . \quad . \quad . \quad . \quad . \quad (160)$$

Values of γ are listed in BS DD 19 but they may be represented by the following polynomial equation.

$$\gamma = 1{\cdot}69 - 17{\cdot}05\left(\frac{a}{W}\right) + 88{\cdot}5\left(\frac{a}{W}\right)^2 - 160\left(\frac{a}{W}\right)^3 + 100\left(\frac{a}{W}\right)^4$$

valid for $0.2 \leqslant a/W \leqslant 0.6$ . . . (161)

an alternative method of calculating COD, from plastic crack mouth opening displacement, was also performed using the formula proposed by Dawes (21). For both calculated values of COD, the conversion to K_{1c} was achieved using the expression:

$$K_{1c} = \sqrt{\frac{M.E.\sigma_y \delta}{(1-\nu^2)}} \quad . \quad . \quad . \quad . \quad (162)$$

where provision had been made in the programme to vary the value of M, although M was usually taken as 2.1.

The critical value of J was calculated according to the equation suggested by Rice et al (97) i.e.

$$J = \frac{2U}{B(W - a)} \quad . \quad . \quad . \quad . \quad . \quad (163)$$

Where U was the appropriate energy, equivalent to the difference between the total area under the load-load point displacement record (up to the critical load point) and the area contributed by the un-notched specimen. J_{1c} was then converted to K_{1c} using the expression:

$$K_{1c} = \sqrt{\frac{J_{1c} E}{(1-\nu^2)}} \quad . \quad . \quad . \quad . \quad (164)$$

The plane strain limiting thickness for J was calculated from equation (46).i.e.

$$B = 25.0\left(\frac{J_{1c}}{\sigma_{ys}}\right) \quad . \quad . \quad . \quad . \quad (165)$$

The values for K_Q obtained using the equivalent energy procedure (115 and 116) were calculated from the following expression:

$$K_Q = \frac{P_Q/2 \times Y \times d^{\frac{1}{2}}}{BW^{\frac{1}{2}}} \quad . \quad . \quad . \quad . \quad (166)$$

where d is the ratio of the areas (from the L-LPD record) up to loads of $P_Q/2$ and the critical load, P_c. (see fig.53b).

Where appropriate, the calculations were performed using the corrected crack lengths, details of which are described in section 6.2.2.

6.3.3 The effect of specimen thickness on K.

The fracture toughness data from the 400 mm x 280 mm x 50 mm blocks of 'as cast' A354 and artificially aged 224 alloys is incorporated in the appendix of this thesis and shown graphically in figs.61 and 62, respectively. For the A354 material, each result was plotted individually, the circled points being invalid on account of too much plasticity according to the recommendations laid down in BS 5447 (1). The critical stress intensity for each of the 224 specimens was determined individually by each of five methods, namely: L.E.F.M., COD (Wells), COD (Dawes), J, and equivalent energy. If replication occurred for a specific specimen thickness then the mean was taken accordingly. Whilst the A354 alloy could be showing an upward trend at a thickness of approximately 8 mm, the 224 alloy showed a fairly random distribution.

6.4 Geometrical effects on $K_{(apparent)}$

6.4.1 Comparison of the crack manufacturing methods.

Fracture toughness data obtained from spark machined and fatigue cracked, artificially aged A.U.W.E. 224 + Ag and Alcoa 354 specimens, was fed into an analysis of variance programme (see section 6.7). The results of this analysis are given in table 16 and are illustrated in the histograms of fig 70. From these results, it was decided at this stage that spark machining could be used to simulate both sharp cracks and cracks with different root radii. The manufacturing of cracks by spark machining is discussed in greater detail in section 7.2.

6.4.2 The effect of crack lengths emanating from blunt notches on $K_{(apparent)}$ from J.

Crack lengths from blunt notches, up to the critical value of crack length c_o, were simulated by spark machining. The results of $K_{(apparent)}$ from J (according to equation 164) as a function of $c/(W - a)$ are shown in fig 63. Converted J results were plotted, because the J integral was found to be the most accurate method of determining the fracture toughness. This can be seen from the tables 13 to 16 and figs 69 to 72. The theoretical predictions of c_o, according to Yamamoto and Ao (51) and Smith and Miller (57) are tabulated on this graph, together with the average K_{1c} values for the artificially aged A.U.W.E. 224 and A.U.W.E. 224 + Ag alloys.

6.4.3 The effect of crack root radii on $K_{(apparent)}$ from J.

Crack root radii, as opposed to notch root radii, were produced using spark machining and the results of $K_{(apparent)}$ from J were plotted against $\sqrt{\frac{\rho}{a}}$ in fig 64. The theoretical solution of Spink, Worthington and Heald's (66) for small scale yielding from a crack in an infinite body, is superimposed on this graph. It was realised,

however, that the experimental results plotted in fig 64 were for a condition just before general yielding, which can be seen from a tracing of part of a typical load - load point displacement record shown in fig 64a.

6.4.4 The effect of notch root radii on $K_{(apparent)}$

The data collected from the mechanically machined notches was fed into an analysis of variance programme (see section 6.7) and the results are given in table 14 and illustrated in fig 71. Fig 64b. shows the tracing of a typical load - load point displacement record, together with the corresponding load/potential - time record, for a mechanically machined notch in an artificially aged A.U.W.E. 224 + Ag specimen. From this record it may be seen that the point of deviation of the potential - time trace corresponded to a distinct change in load, just less than the maximum load. As this point was so distinct and consistantly corresponded to initiation (as defined from the potential - time trace) it was decided that the point of initiation for these specimens could be determined without the electric potential apparatus.

6.5 Structural effects on $K_{(apparent)}$

6.5.1 The effect of specimen porosity on $K_{(apparent)}$

A block of as cast KO1 alloy supplied by B.N.F. Metals Technology Centre was machined into seven specimens, each of which contained a different level of porosity. Graphical representation of the $K_{(apparent)}$ results, calculated individually by each of the five available methods, as a function of percentage porosity are shown in fig 65, from which it appears that the effect of porosity is randomly distributed about a mean value. This mean value is approximately 14 $MNm^{-3/2}$, for the $K_{(apparent)}$ from J. The effect of porosity on

$K_{(apparent)}$ has also been examined statistically by comparing the three block thicknesses: 14, 25 and 50 mm, using an analysis of variance programme (see section 6.7).

6.5.2 The effect of aging period on $K_{(apparent)}$

$K_{(apparent)}$ was determined, using the five available methods of calculation, for A.U.W.E. 224 + Ag specimens which had been aged for periods of 1, 3, 6, 12, 48 and 96 hours. The hardness and yield strengths of these specimens are shown in fig 66. These results have been superimposed on the fracture toughness versus time graphs (see figs 67a, b and c) for comparison.

6.6 Critical defect sizes.

Critical defect sizes for elliptical, totally embedded and side cracks (calculated according to equations (24) and (26) respectively) are shown as a function of applied stress in figs 68a and b. The average values of K_{1c} for each of the artificially aged materials, together with their corresponding yield strengths, were substituted in the above equations and are detailed below. The minimum K_{1c} for each material is also given so that a more conservative estimate of critical defect sizes could be obtained.

Alloy	Average K_{1c} (MNm-3/2)	Minimum K_{1c} (MNm-3/2)	σ_{ys} (MNm-2)
Alcoa 354	20	13.3	295
A.U.W.E. 224	26	18.5	420
A.U.W.E. 224 + Ag	17.5	13.0	320

Shape factor = 1.15 (i.e. $\frac{a}{b} = 0.4$)

6.7 Statistical analysis of the fracture toughness data.

The appropriate fracture toughness results incorporated in the appendix of this thesis were rearranged into four separate groups, in order to assess the following:

a) The effect of material, method of test and block size on $K_{(apparent)}$.

b) The effect of material, method of test and notch root radius on $K_{(apparent)}$.

c) The effect of material, method of test and material condition on $K_{(apparent)}$.

d) The effect of material, method of test and method of crack manufacture (i.e. whether spark machined or mechanically machined) on $K_{(apparent)}$.

The results of these four analyses are detailed in tables 13, 14, 15 and 16 and are illustrated in figs 69, 70, 71 and 72. Discussion of these results, in greater detail, is dealt with in the next section.

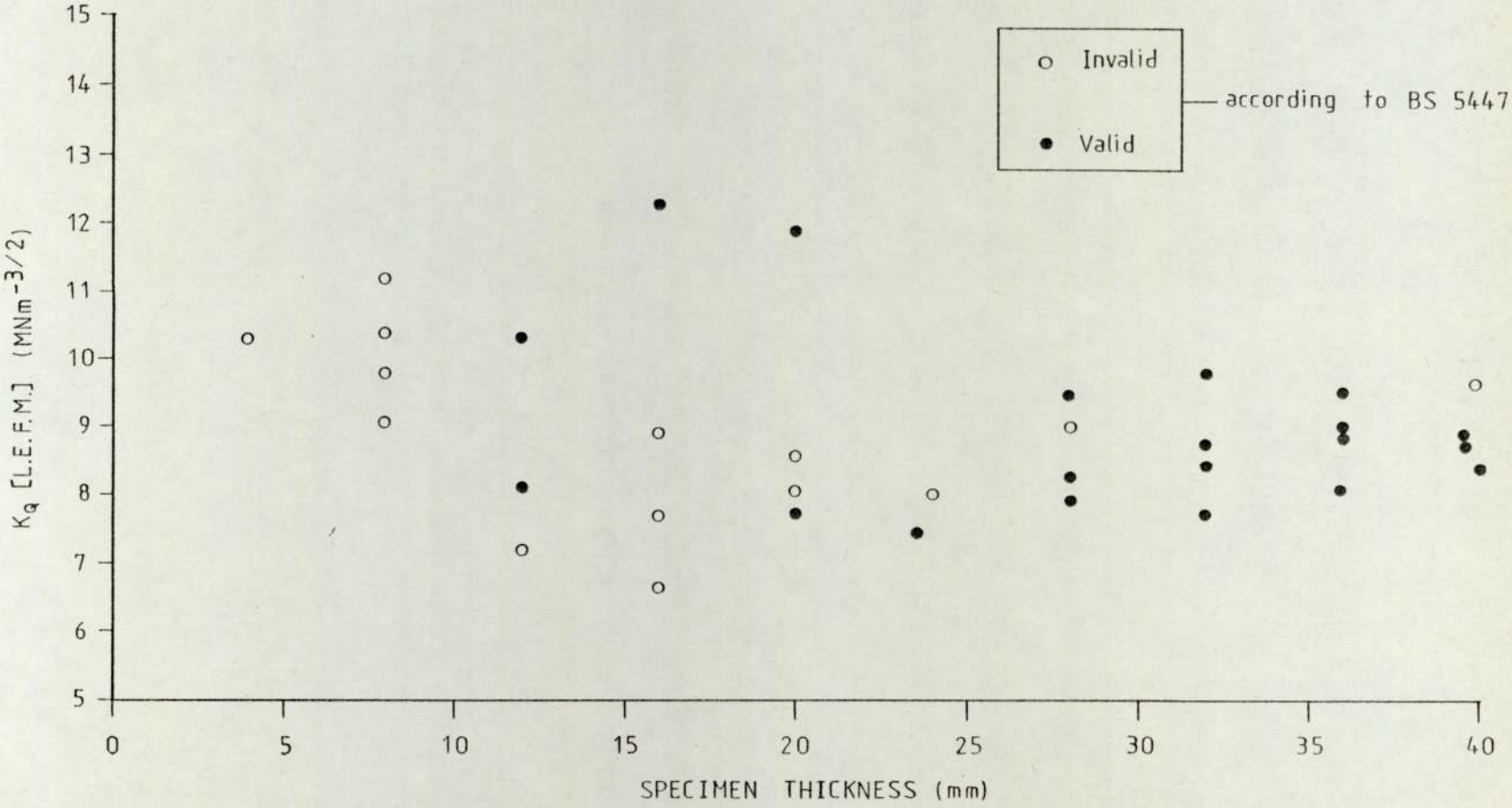

Fig. 61. The effect of specimen thickness on K_Q (L.E.F.M.) for as cast A 354, 280mm blocks

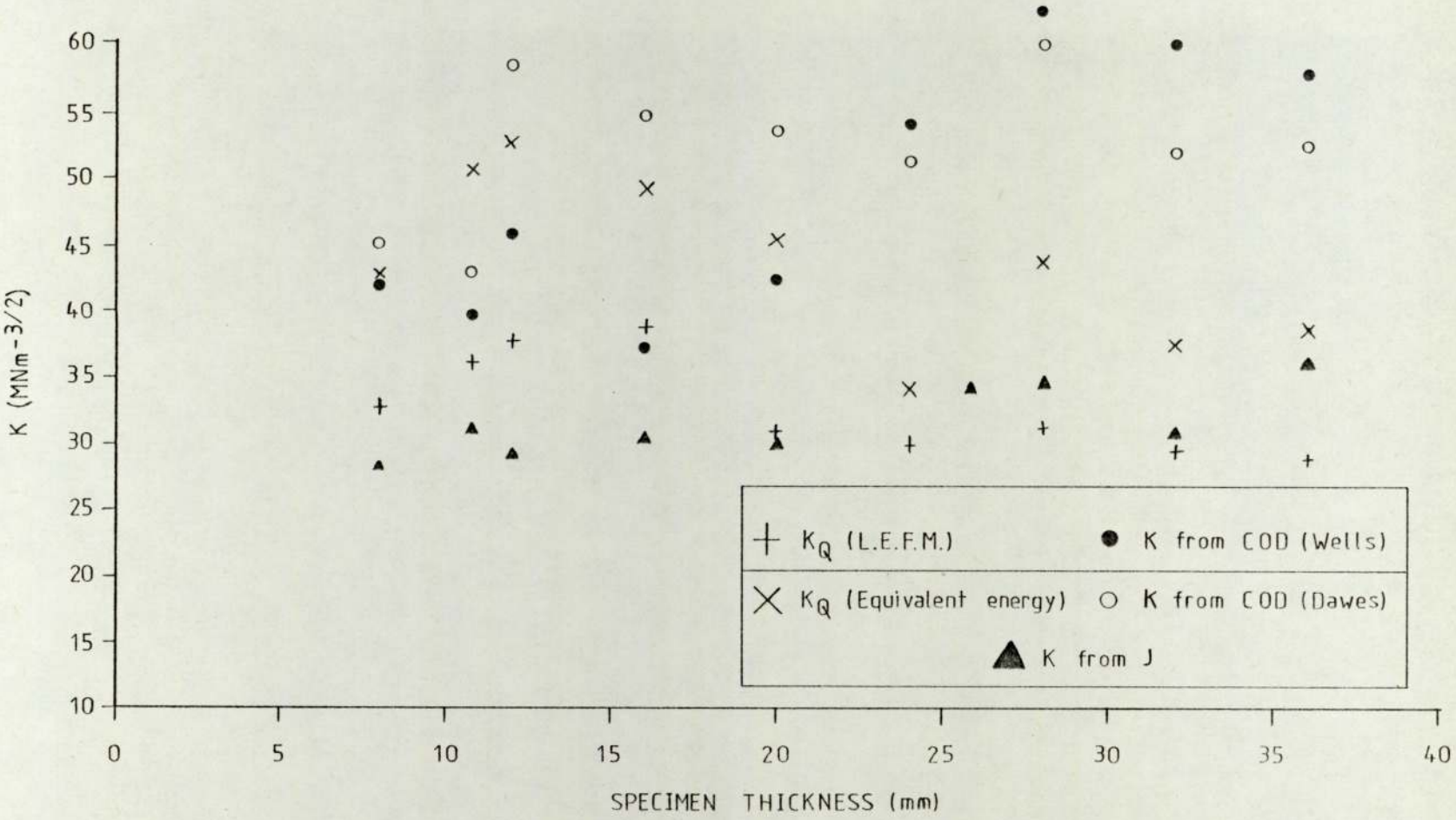

Fig. 62. The effect of specimen thickness on K for A.U.W.E. 224, 280mm x 200mm x 50mm blocks. (Artificially aged condition)

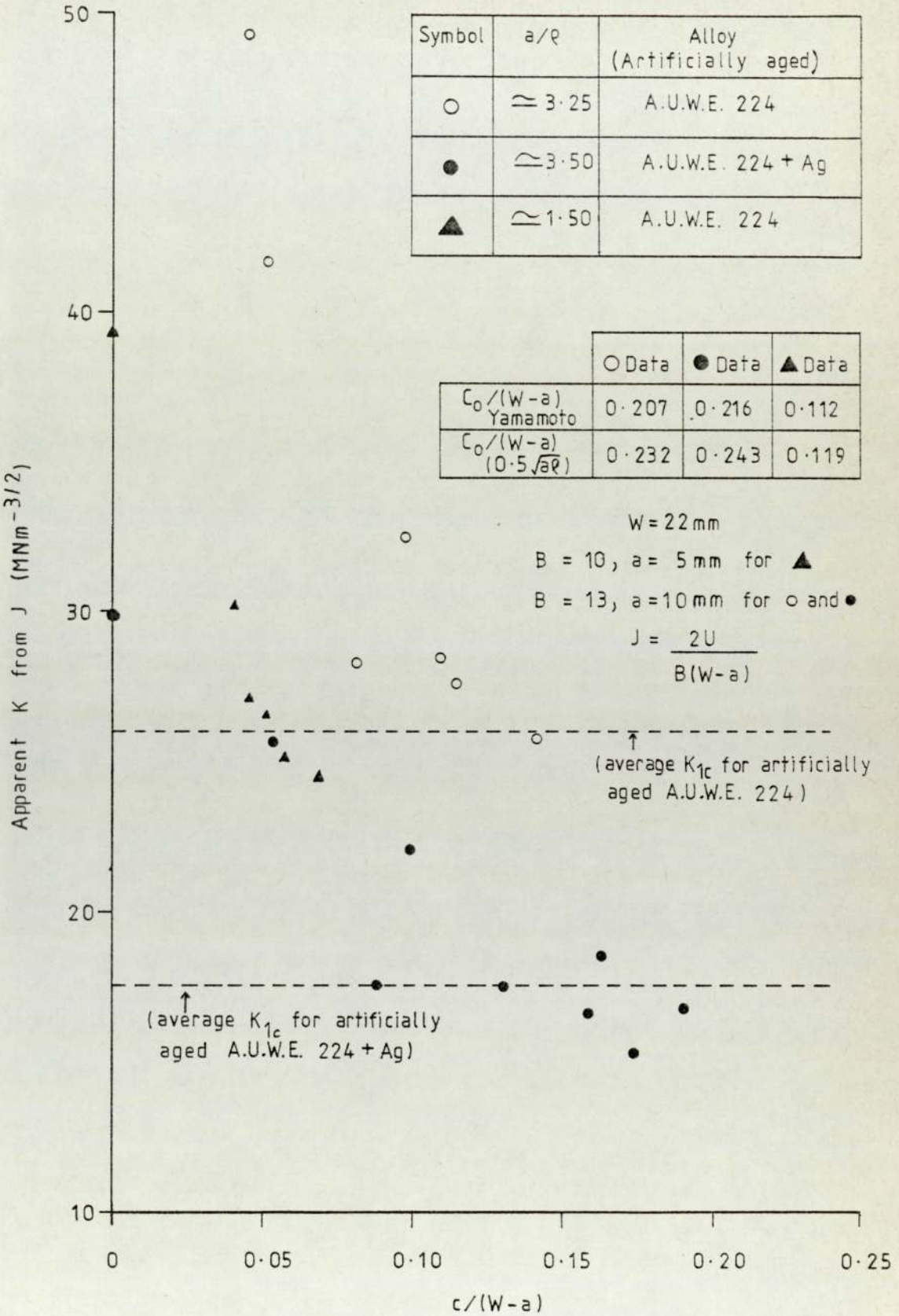

Fig. 63. The effect of short cracks emanating from blunt notches on the apparent K from J.

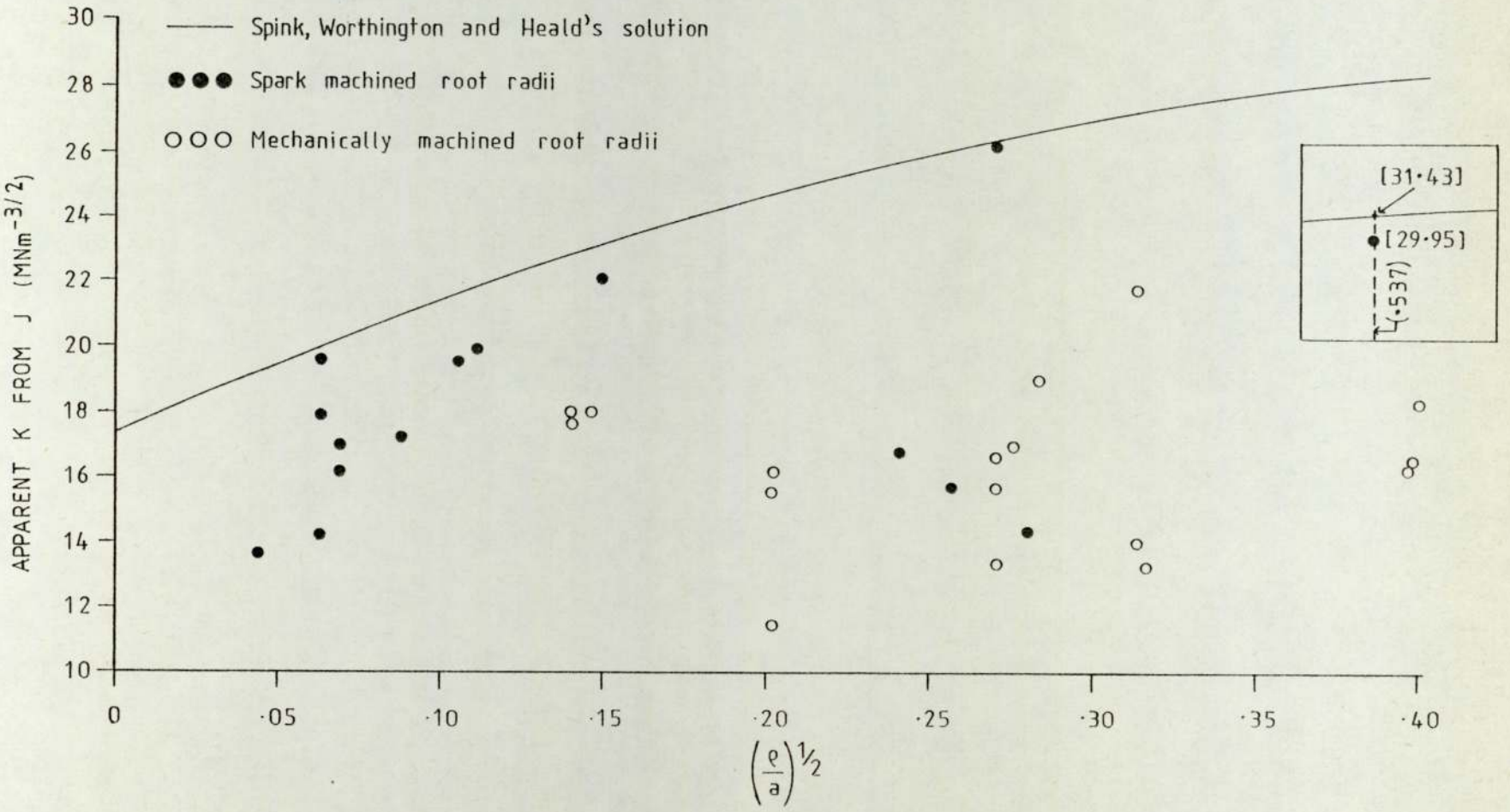

Fig. 64. The effect of crack root radius on $K_{A(\rho)}$ from J for A.U.W.E. 224+Ag alloy (artificially aged)

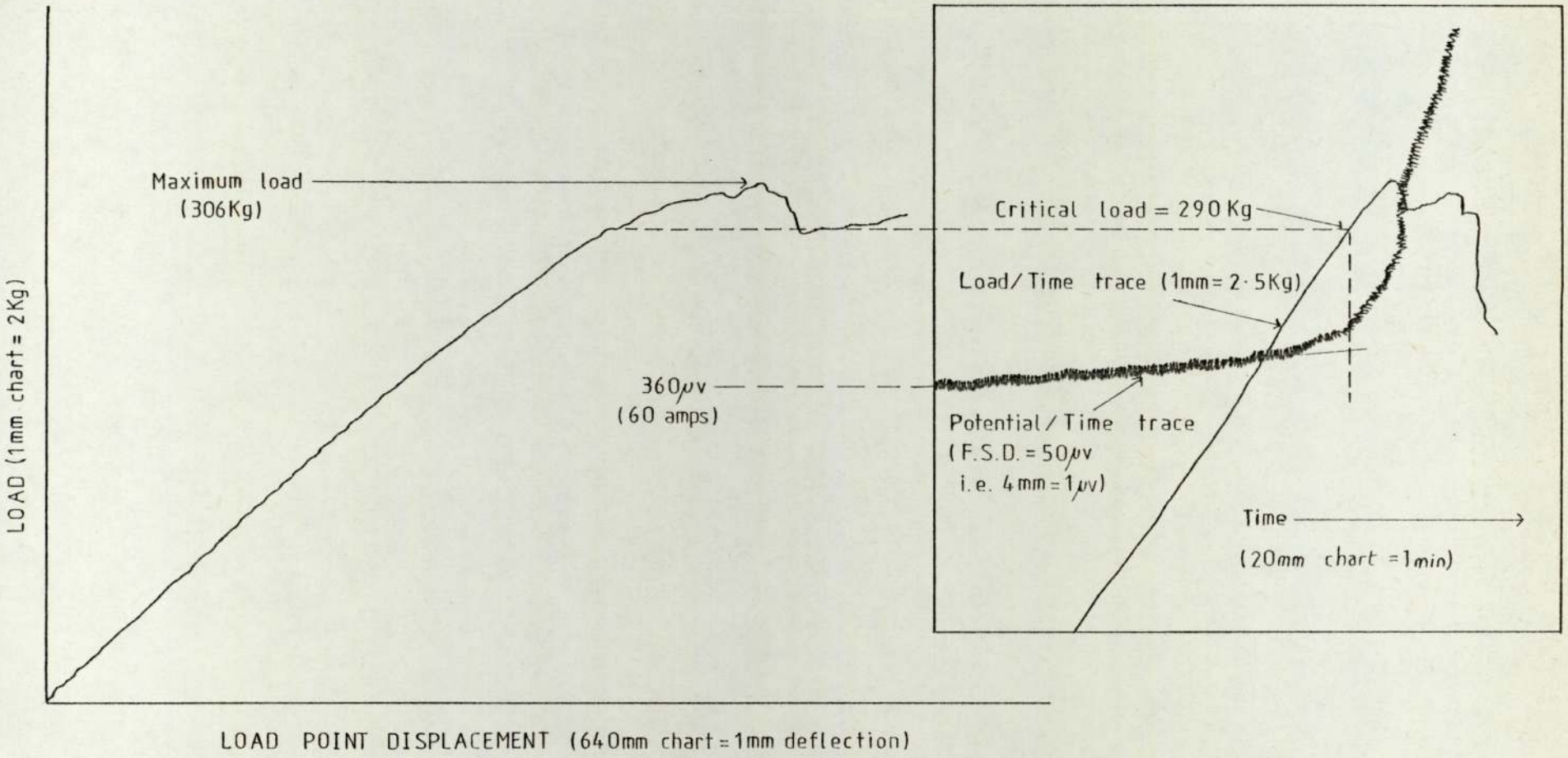

Fig. 64a. Tracings from typical load-load point displacement and time-load/potential records.

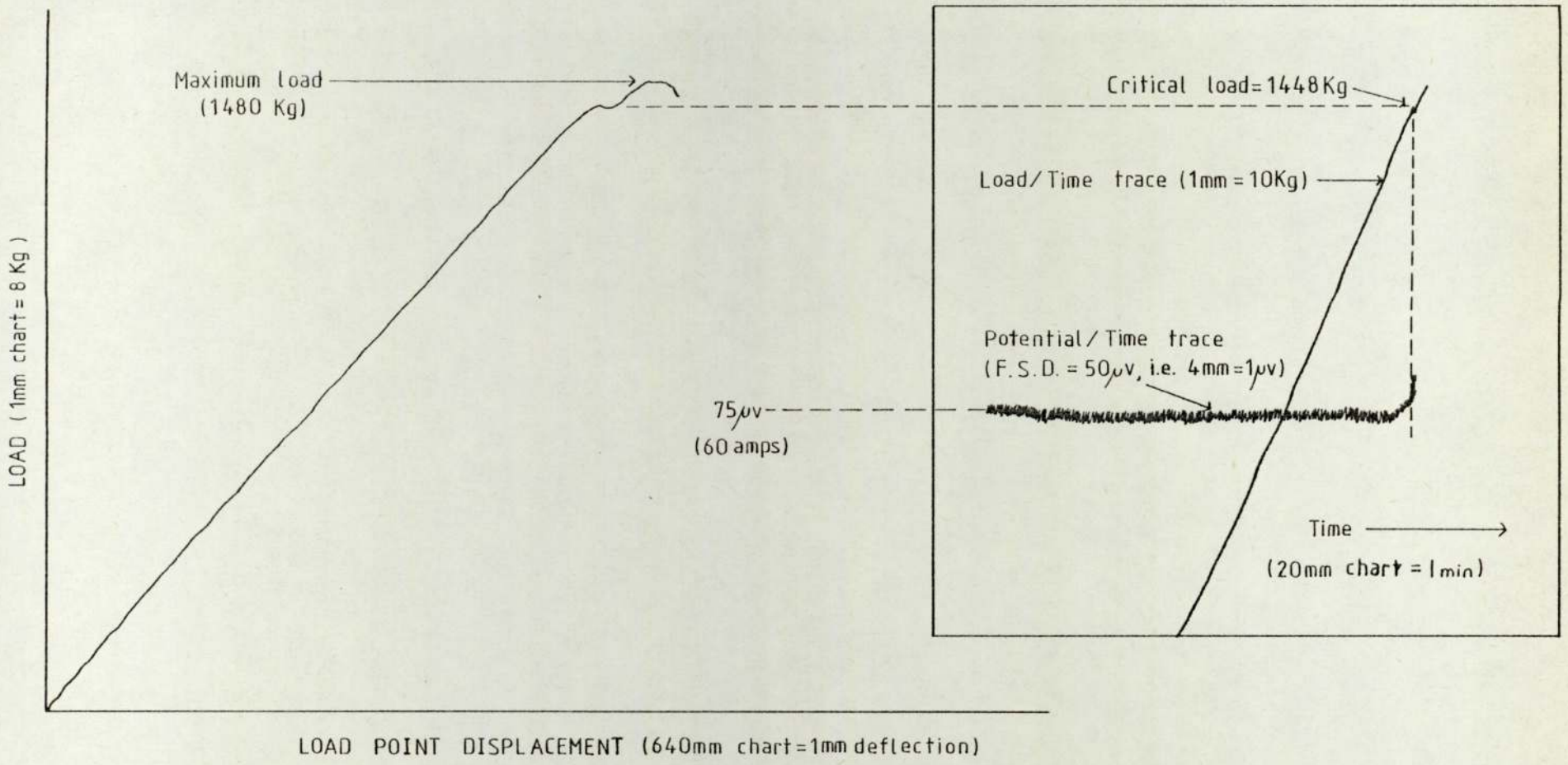

Fig. 64b. Tracings from typical load-load point displacement and time-load/potential records.

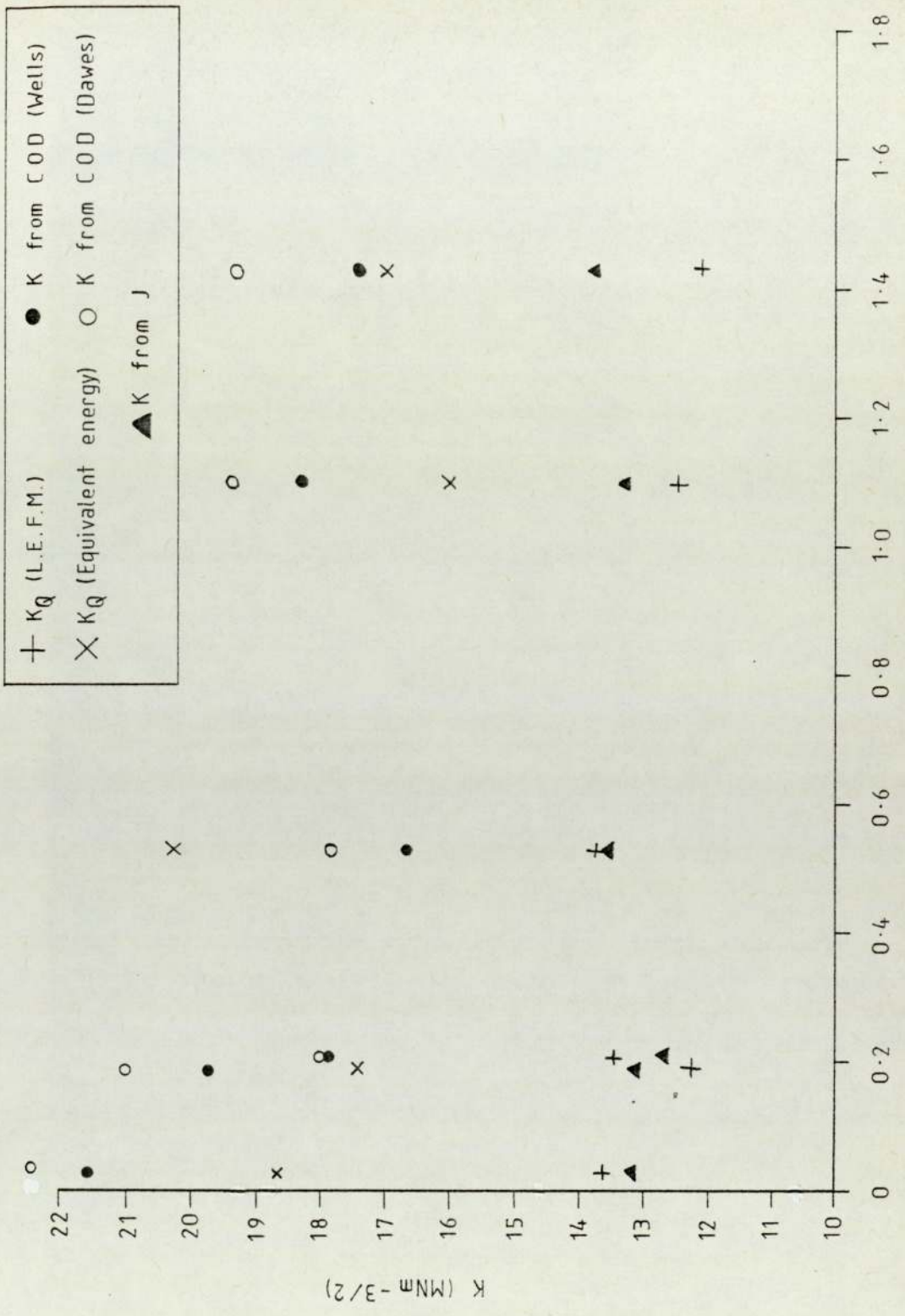

Fig. 65. The effect of specimen porosity on K for as cast KO1 alloy

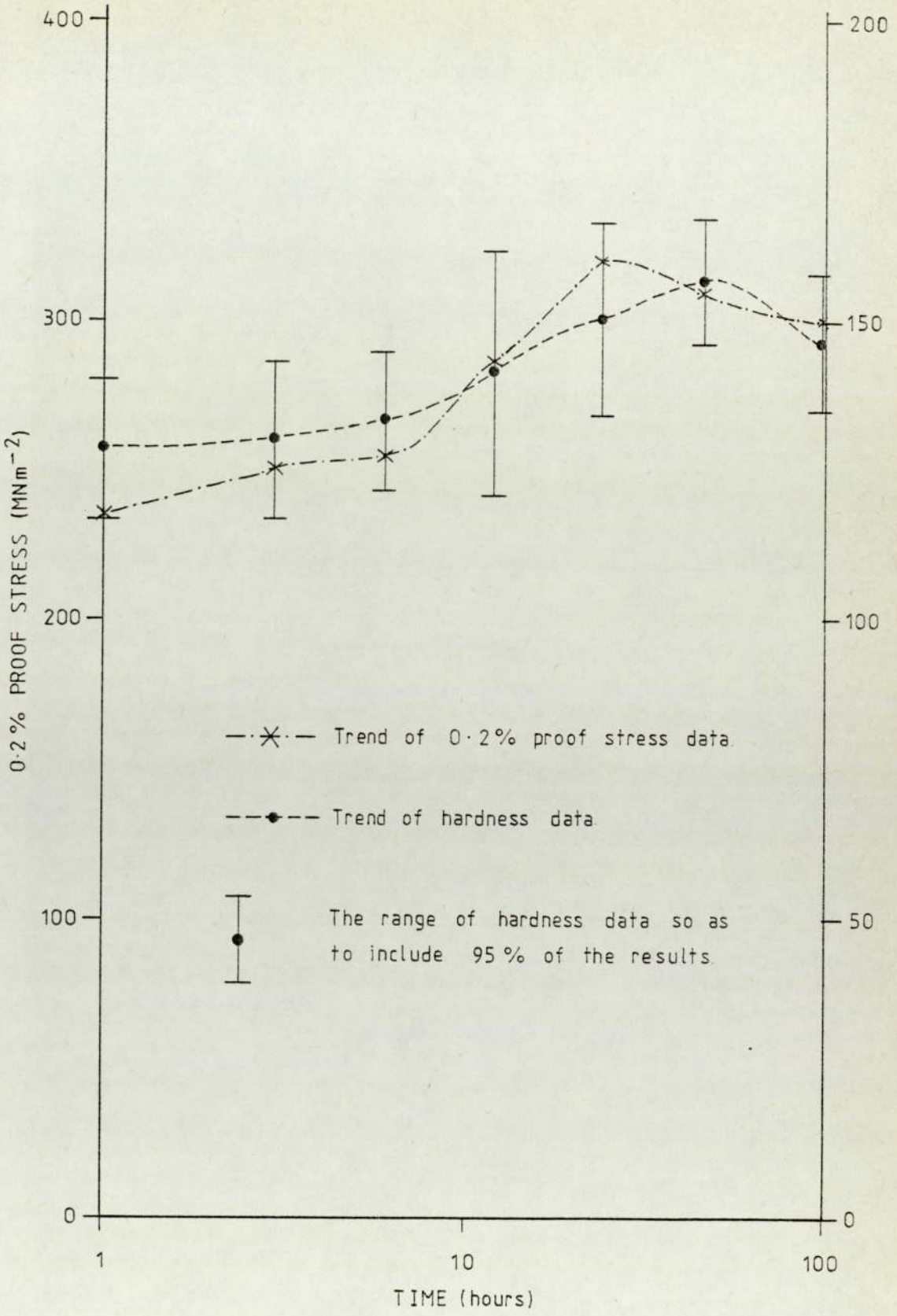

Fig. 66. The effect of aging time on the 0·2% proof stress and hardness of A.U.W.E. 224 + Ag alloy.

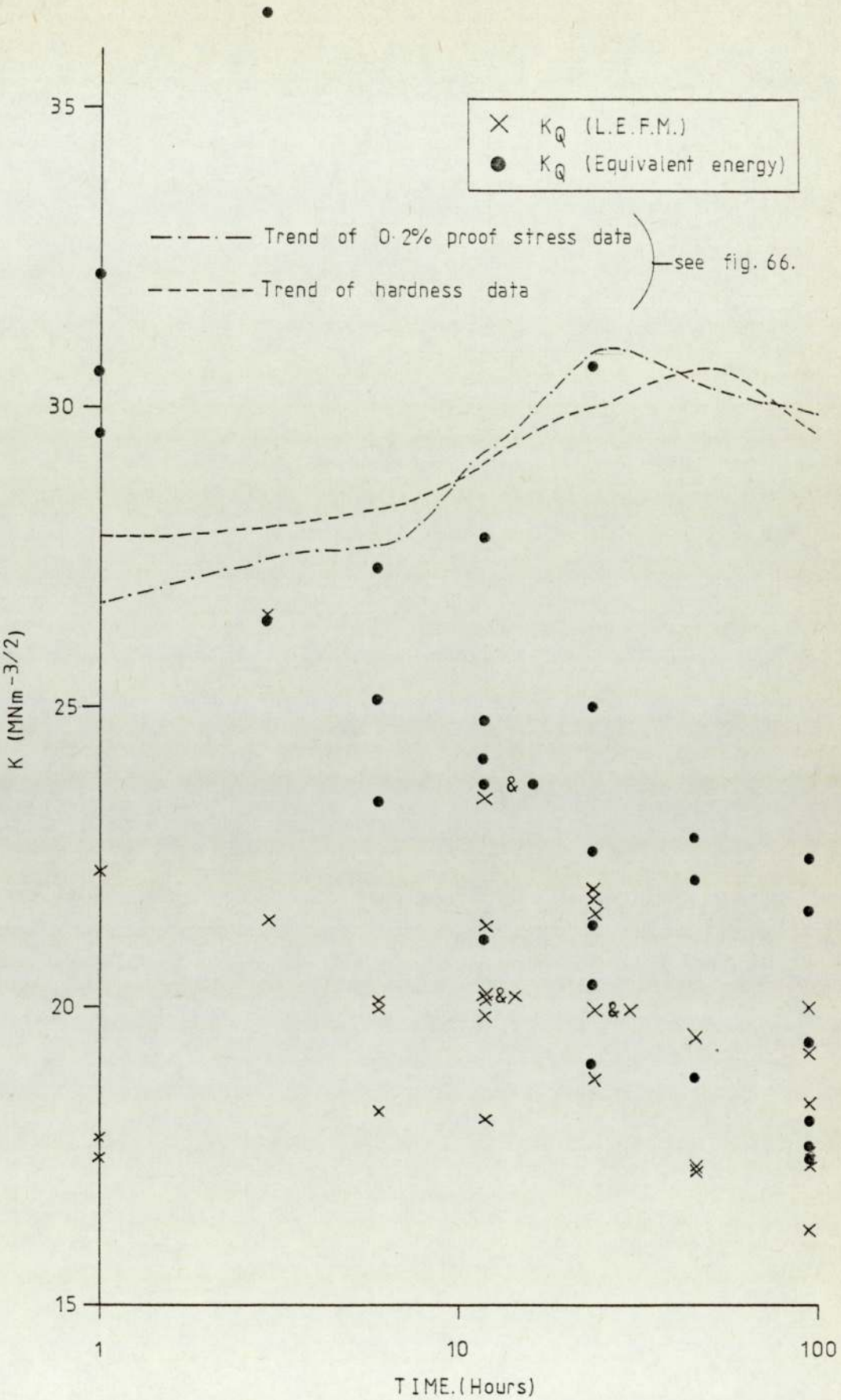

Fig. 67a. The effect of aging time on K (L.E.F.M) and K (Equivalent energy) for A.U.W.E. 224 + Ag alloy

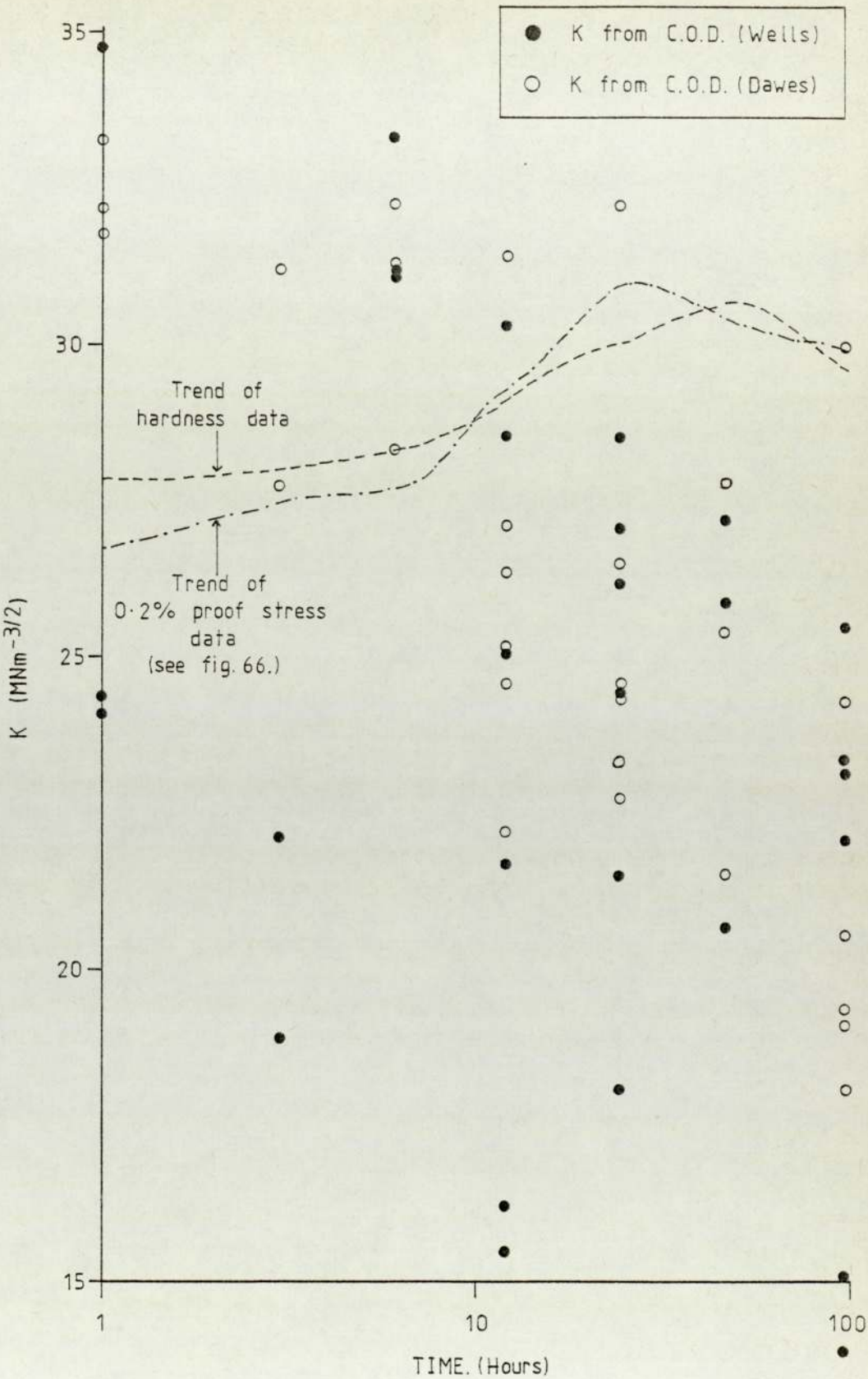

Fig. 67b. The effect of aging time on K from C.O.D. for A.U.W.E. 224 + Ag alloy

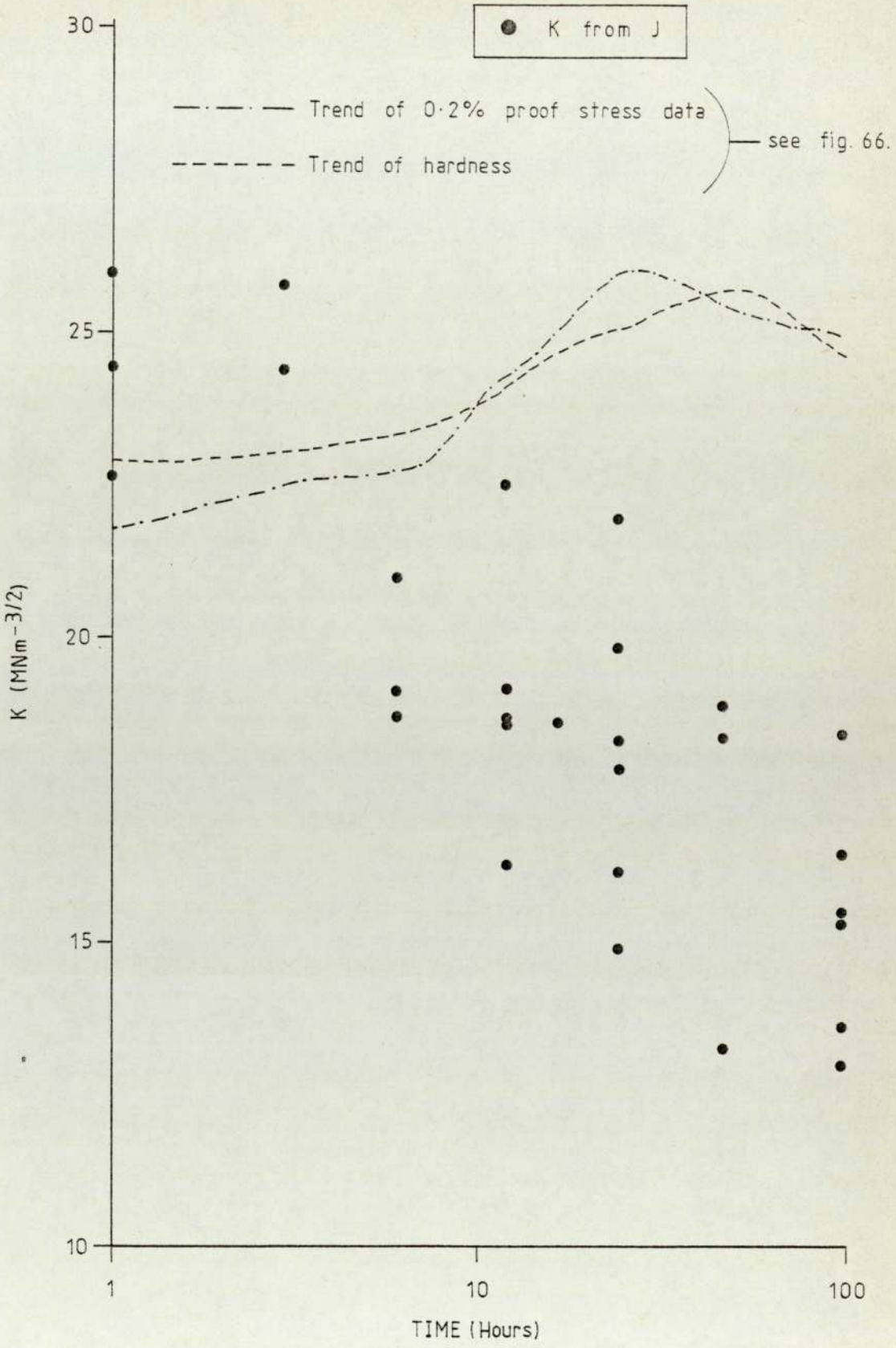

Fig. 67c. The effect of aging time on K from J for A.U.W.E. 224 + Ag alloy

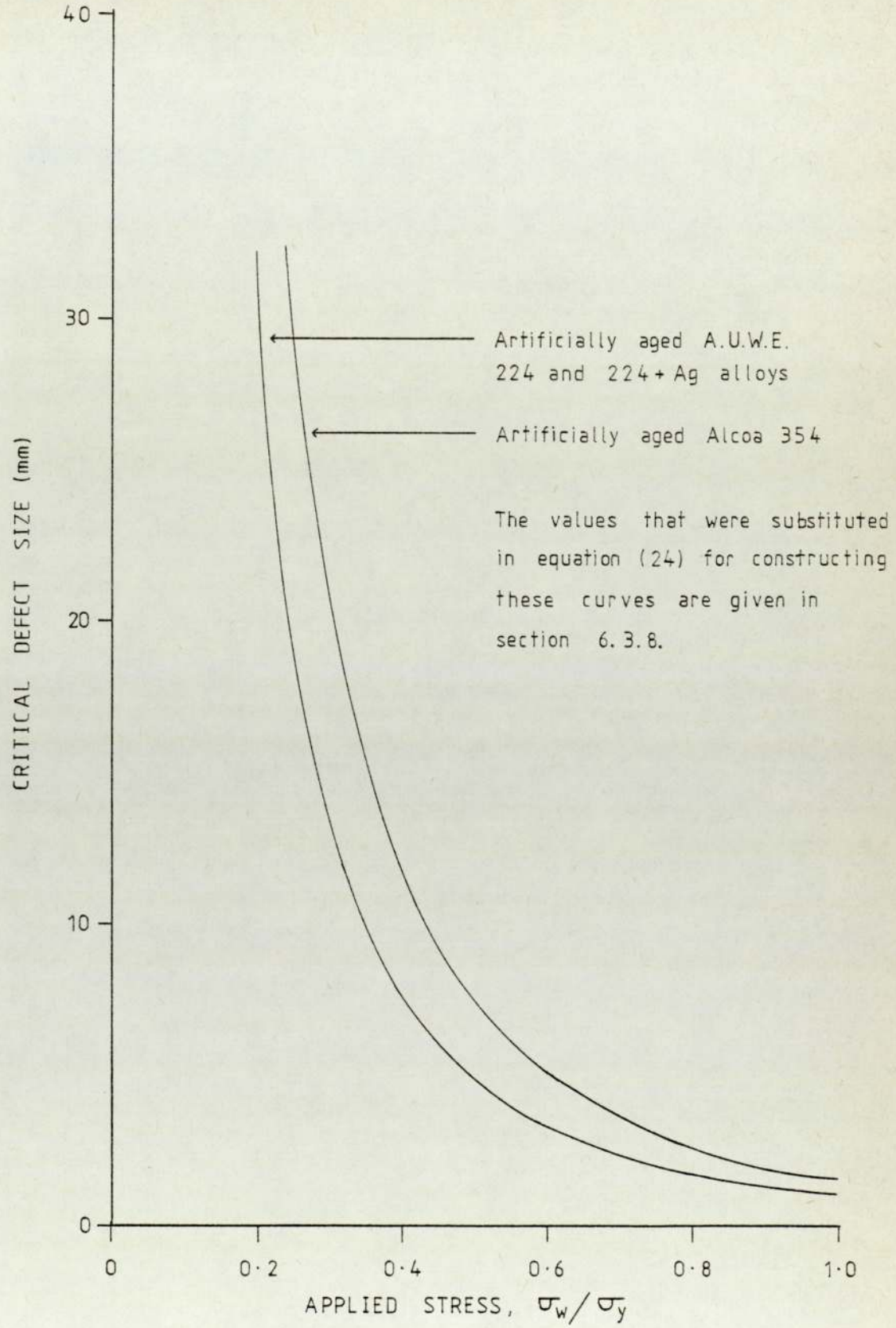

Fig. 68a. Critical defect size as a function of applied stress for totally embedded elliptical defects.

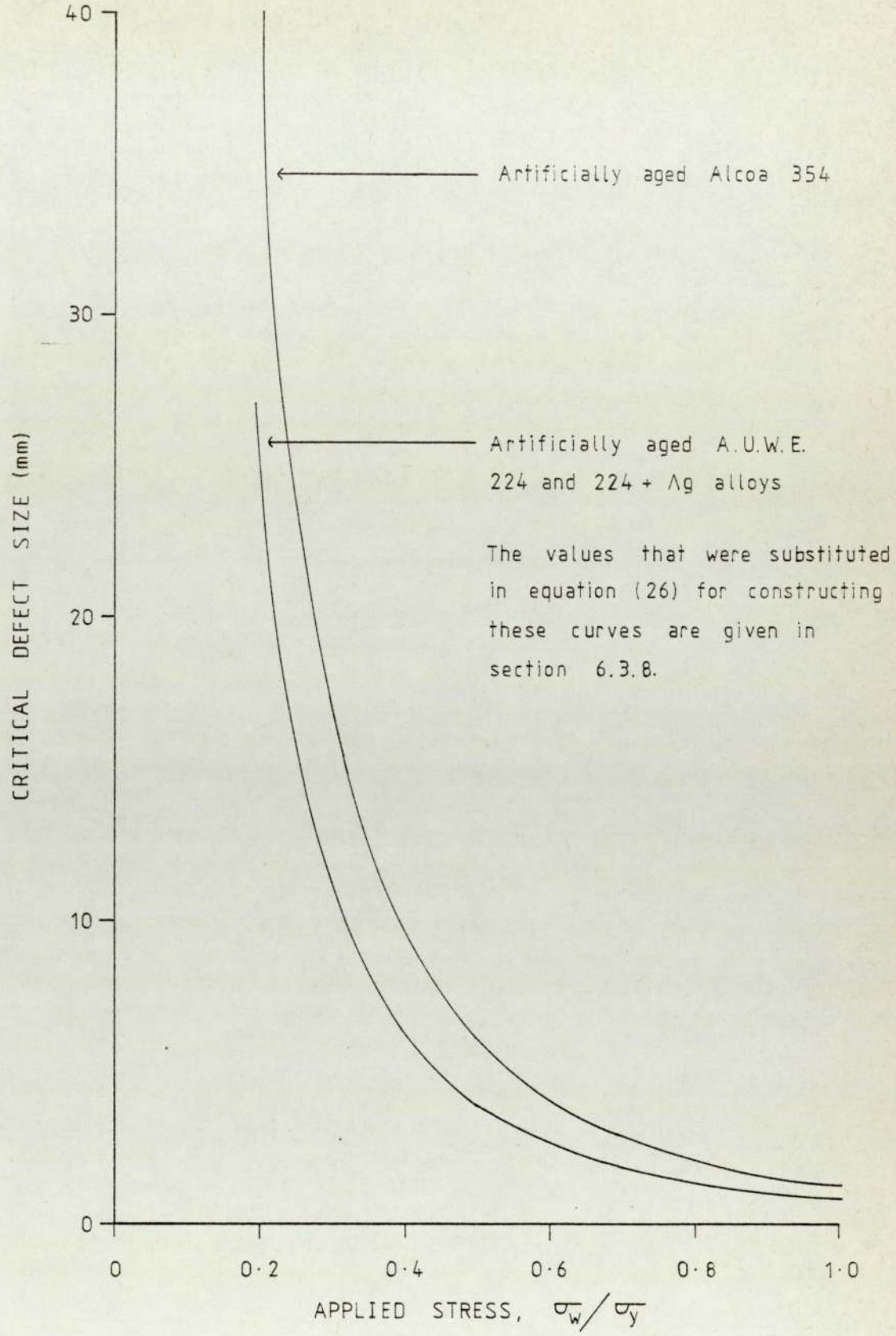

Fig. 68b. Critical defect size as a function of applied stress for elliptical side defects

Table 13. The effects of material, method of test and block size on K.

Model term	Sum of squares	Degrees of freedom	Variance	Variance ratio	Significant at level
A(I)	188.963	2	94.481	9.379	1%
B(J)	554.087	4	138.522	13.750	1%
C(K)	336.400	2	168.200	16.696	1%
AB(IJ)	9468.50	8	1183.562	117.487	1%
AC(IK)	26.288	4	6.572	0.653	-
BC(JK)	117.105	8	14.638	1.453	-
ABC(IJK)	584.450	16	36.528	3.626	1%
Residual	2266.65	225	10.074	-	-
Totals	13542.4	269	50.344	-	-

A-I . . . . 3 Materials

B-J . . . . 5 Test methods

C-K . . . . 3 Block sizes

D-L . . . . 6 Replica's

Table 14. The effects of material, method of test and notch root radius on K.

Model term	Sum of squares	Degrees of freedom	Variance	Variance ratio	Significant at level
A(I)	3598.97	2	1799.487	281.041	1%
B(J)	4245.25	4	1061.313	165.754	1%
C(K)	189.367	2	94.683	14.788	1%
AB(IJ)	1124.10	8	140.513	21.945	1%
AC(IK)	87.978	4	21.995	3.435	5%
BC(JK)	70.259	8	8.782	1.372	-
ABC(IJK)	96.525	16	6.033	0.942	-
Residual	576.263	90	6.403	-	-
Totals	9988.72	134	74.543	-	-

A-I . . . . 3 Materials

B-J . . . . 5 Test methods

C-K . . . . 3 Notch root radii

D-L . . . . 3 Replica's

Table 15. The effects of material, method of test and aging procedure on K.

Model term	Sum of squares	Degrees of freedom	Variance	Variance ratio	Significant at level
A(I)	2327.59	2	1163.791	152.286	1%
B(J)	1582.13	4	395.532	51.757	1%
C(K)	1.683	1	1.683	0.220	-
AB(IJ)	327.114	8	40.889	5.350	1%
AC(IK)	290.155	2	145.078	18.984	1%
BC(JK)	26.596	4	6.649	0.870	-
ABC(IJK)	89.505	8	11.188	1.464	-
Residual	687.794	90	7.642	-	-
Totals	5332.56	119	44.813	-	-

A-I . . . . 3 Materials
B-J . . . . 5 Test methods
C-K . . . . 2 Aging procedures
D-L . . . . 4 Replica's

Table 16. The effects of material, method of test and method of manufacture of crack on K.

Model term	Sum of squares	Degrees of freedom	Variance	Variance ratio	Significant at level
A(I)	61.105	1	61.105	31.083	1%
B(J)	420.539	4	105.135	53.479	1%
C(K)	22.265	1	22.265	11.326	1%
AB(IJ)	26.115	4	6.529	3.321	5%
AC(IK)	65.919	1	65.919	33.531	1%
BC(JK)	0.400	4	0.100	0.051	-
ABC(IJK)	15.806	4	3.951	2.010	-
Residual	78.636	40	1.966	-	-
Totals	690.786	59	11.708	-	-

A-I . . . . 2 Materials

B-J . . . . 5 Test methods

C-K . . . . 2 Methods of crack manufacture

D-L . . . . 3 Replica's

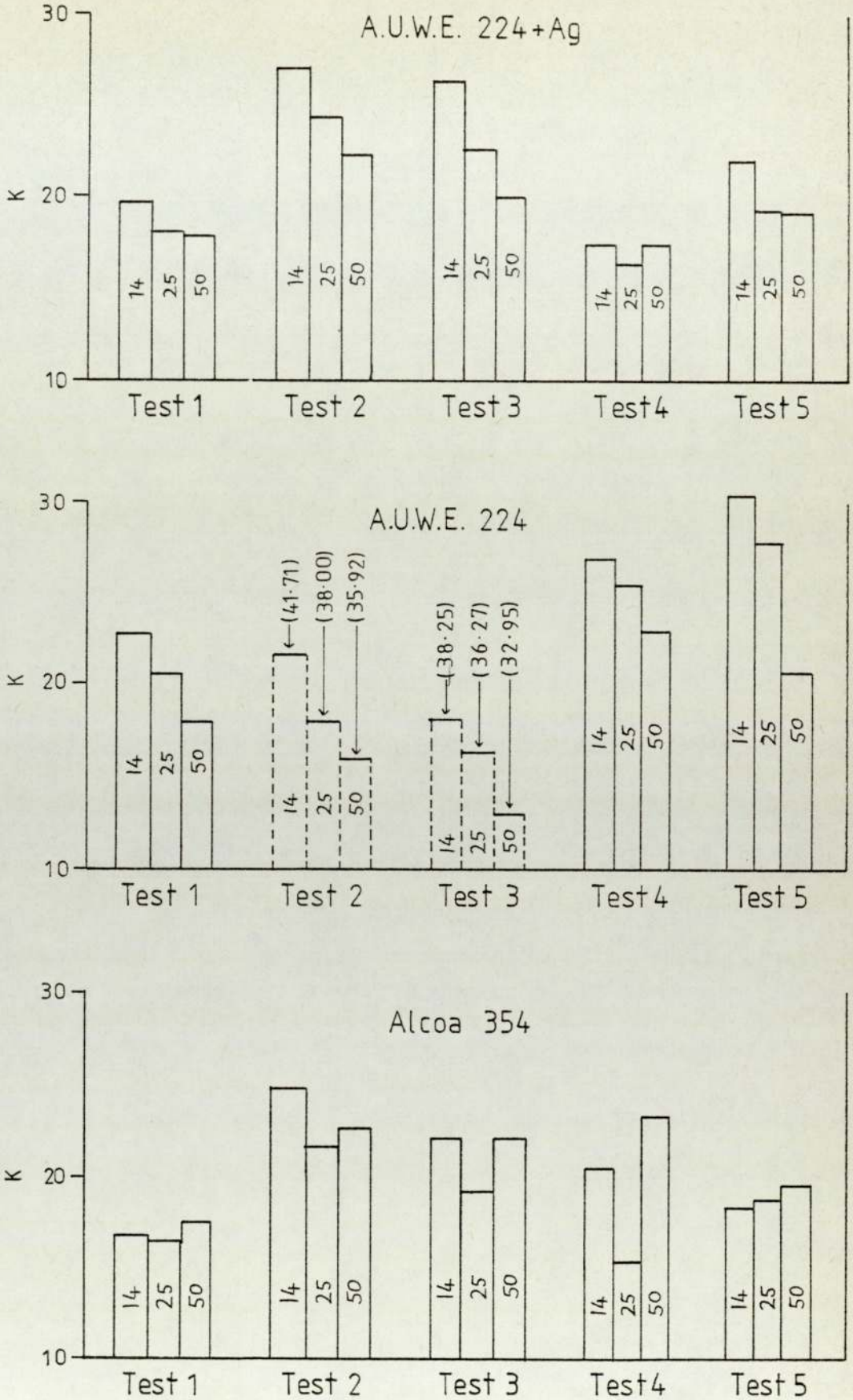

Fig. 69. Histograms for the average effects of block size and method of test on K.

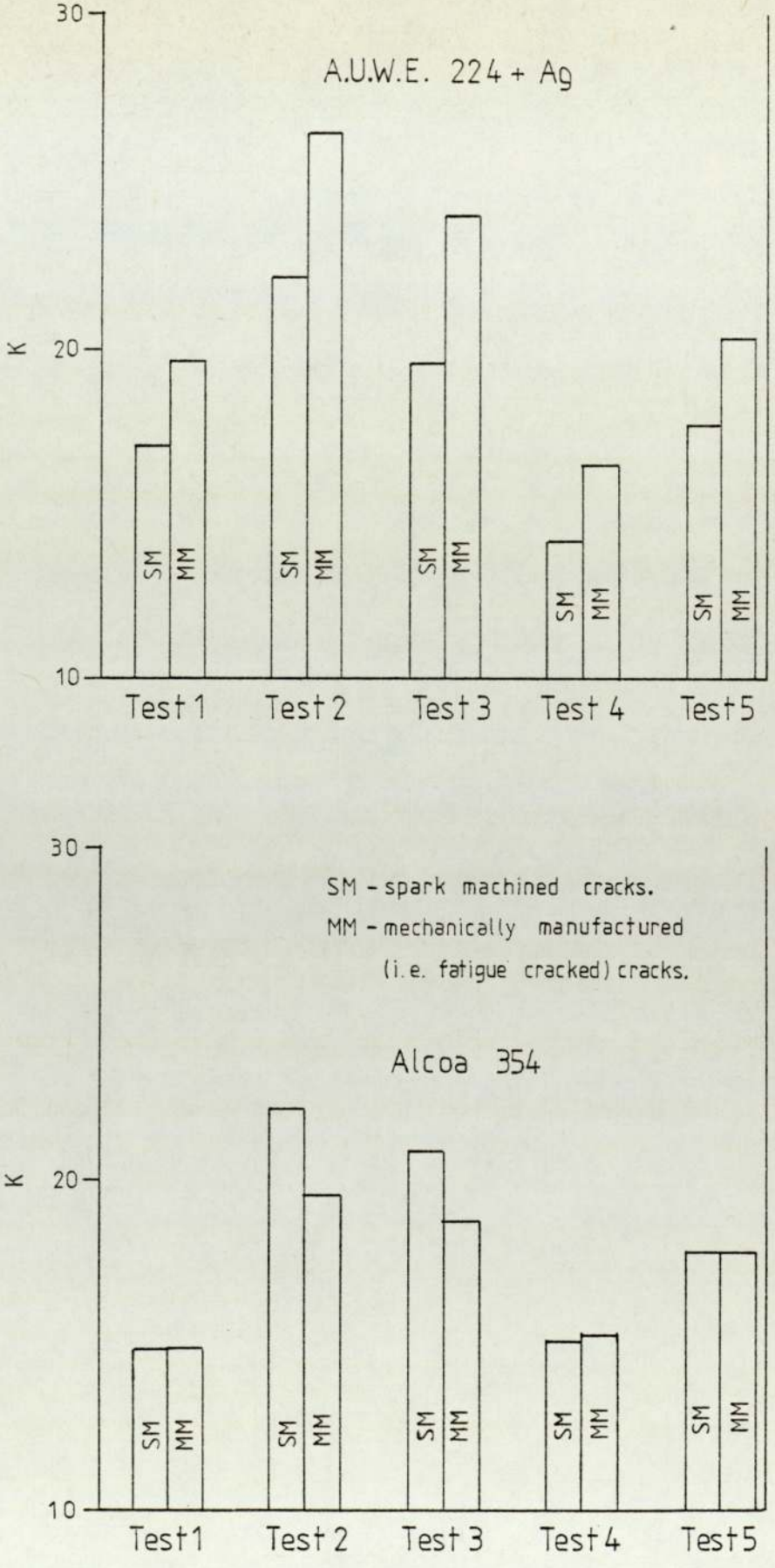

Fig. 70. Histograms for the average effects of crack manufacturing method and test method on K.

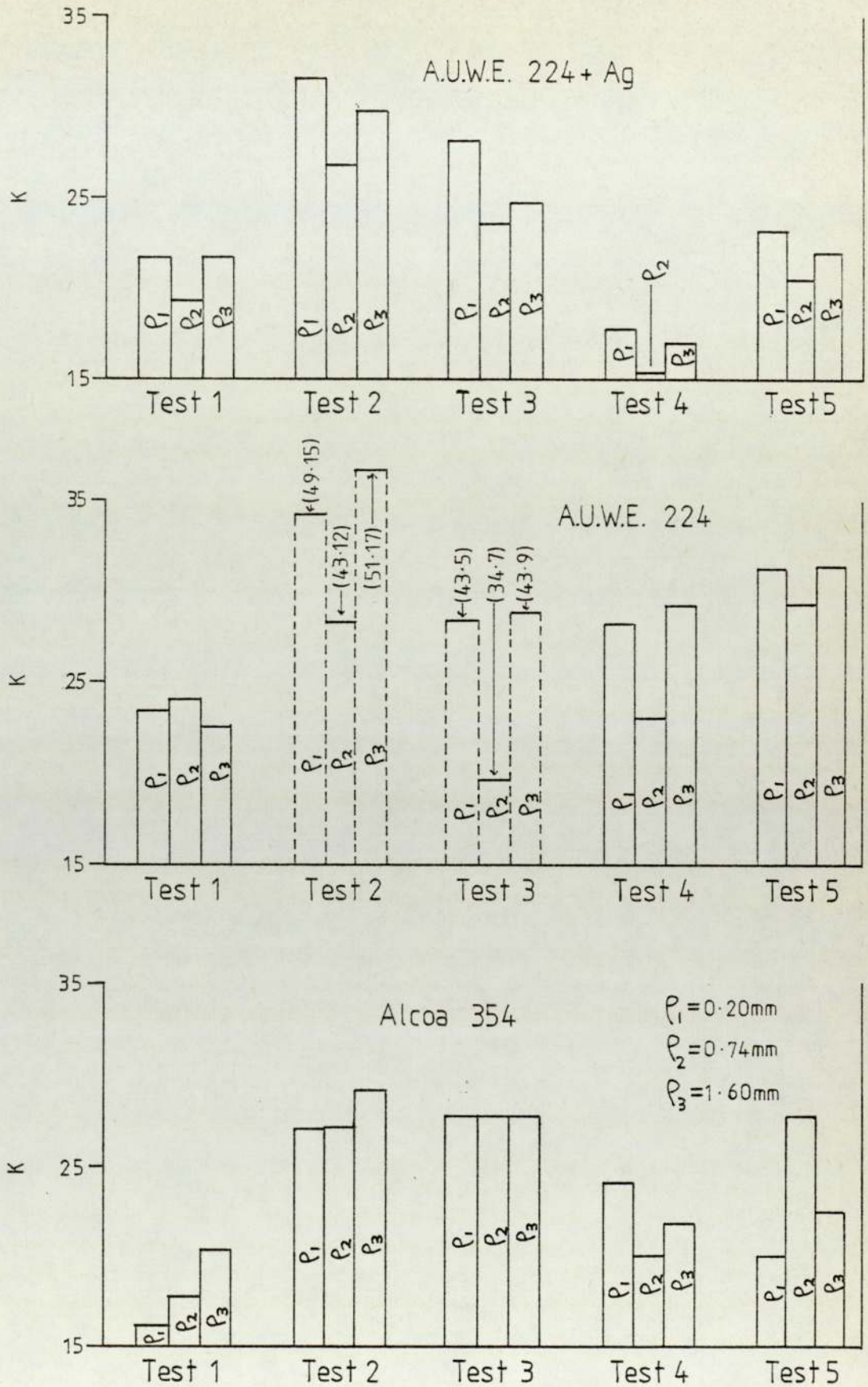

Fig.71. Histograms for the average effects of notch root radius and method of test on K.

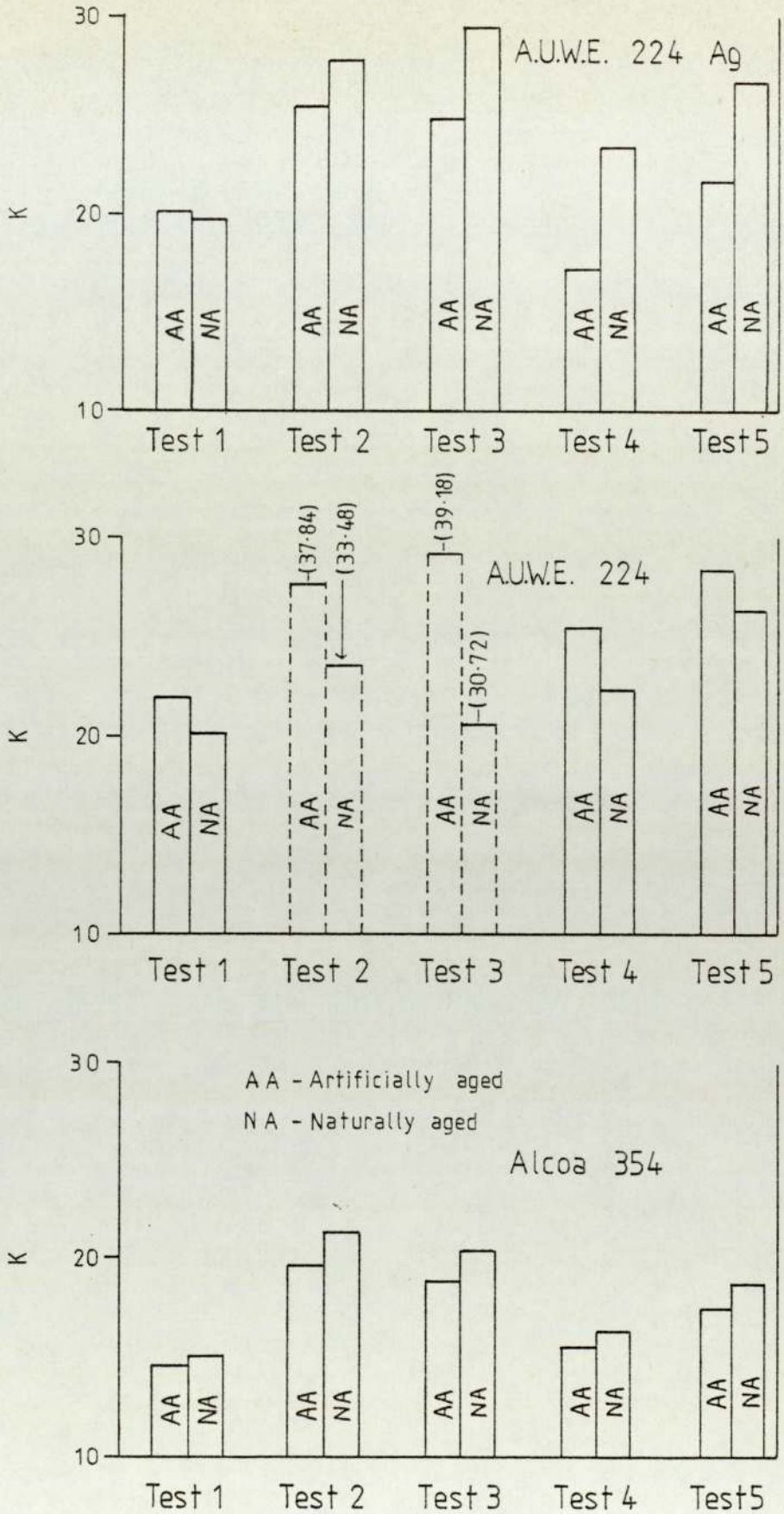

Fig. 72. Histograms for the average effects of material condition and test method on K.

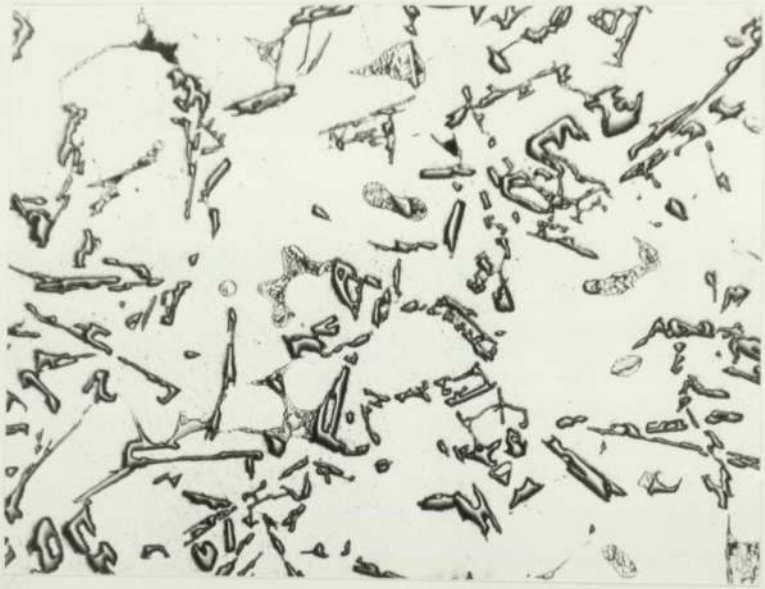

Plate.1. Microstructure of as cast A 354, showing a coarse structure of silicon needles dispersed in a matrix of aluminium. Magnification x 100.

Plate.2. Microstructure of artificially aged A 354 alloy, showing a finer distribution of the silicon needles. Magnification x 100.

Plate.3. Microstructure of naturally aged A 354 alloy, showing a very fine distribution of the silicon needles. Magnification x 100.

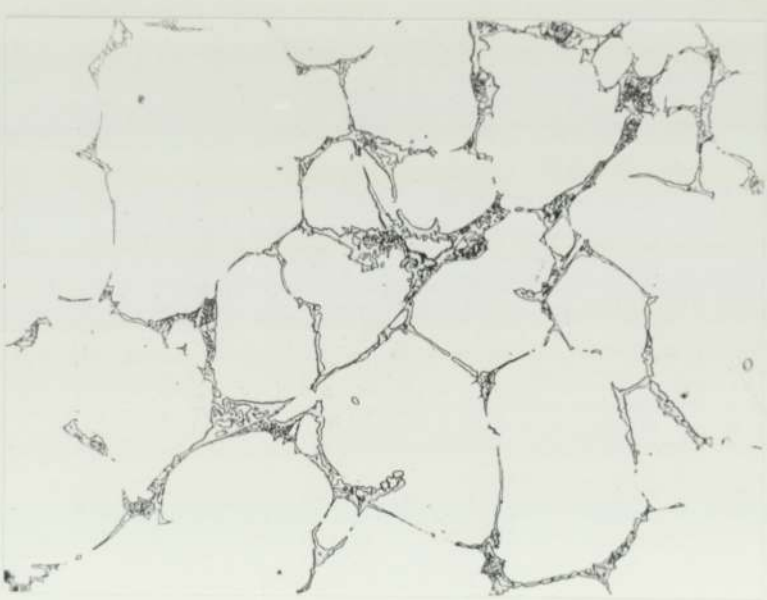

Plate.4. Microstructure of as cast A.U.W.E. 224 alloy showing a coarse dendritic structure. Magnification x 100.

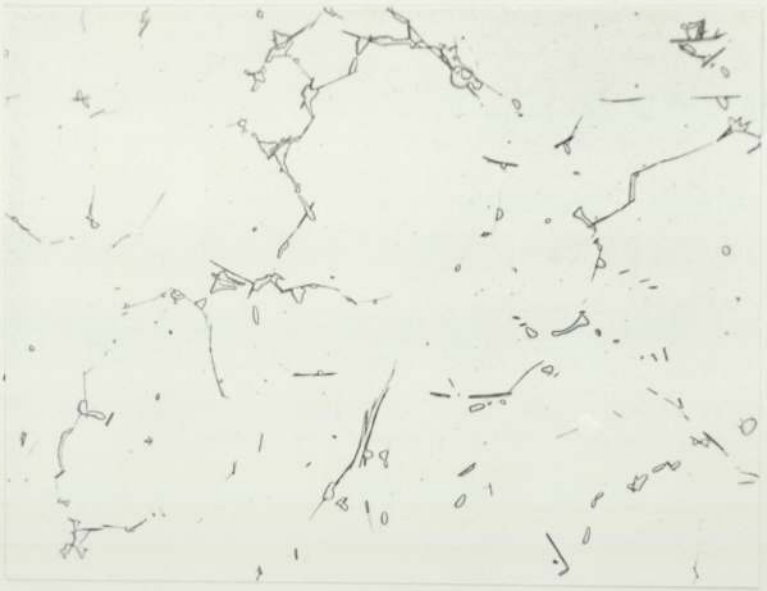

Plate.5. Microstructure of artificially aged
A.U.W.E. 224 alloy.
Magnification x 100.

Plate.6. Microstructure of naturally aged
A.U.W.E. 224 alloy.
Magnification x 100.

Plate.7. Microstructure of as cast A.U.W.E. 224 + Ag alloy, showing a coarse dendritic structure. Magnification x 100.

Plate.8. Microstructure of artificially aged A.U.W.E. 224 + Ag alloy.

Magnification x 100.

Plate.9. Microstructure of naturally aged A.U.W.E. 224 + Ag alloy.

Magnification x 100.

Plate.10. Microstructure of over aged A.U.W.E. 224 + Ag alloy.

Magnification x 100.

Plate.11. Silicon distribution (using micro-probe analysis) across silicon rich needles and an impurity phase. Magnification x 1000.

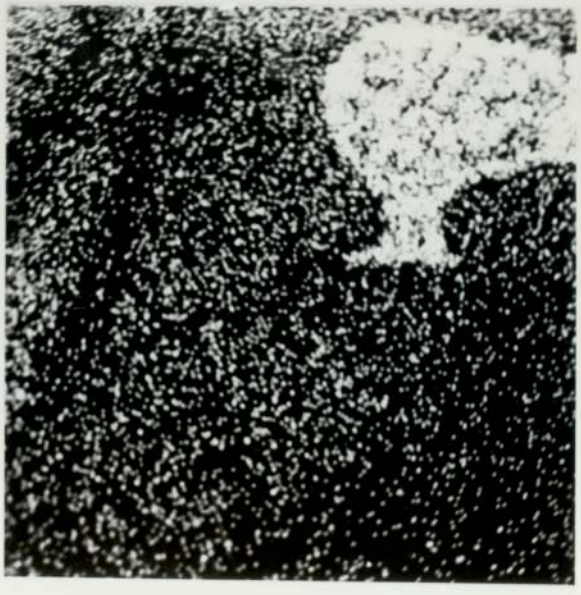

Plate.12. Copper distribution (using micro-probe analysis) across the same area as taken in plate.11. Magnification x 1000.

Plate.13. Iron distribution (using micro-probe analysis) across the same area as taken in Plate.11. Magnification x 1000.

Plate.14. Manganese distribution (using micro-probe analysis) across the same area as taken in Plate.11. Magnification x 1000.

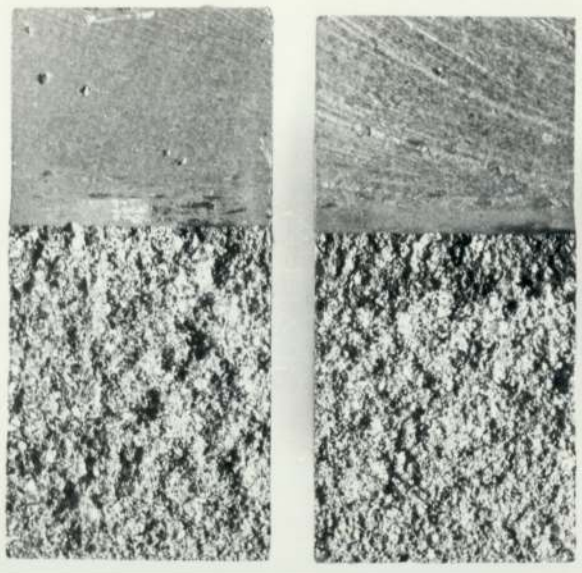

Plate.15. Fracture surface of two machine notched and pre-fatigue cracked specimens. As cast A 354 alloy. Magnification x 3.

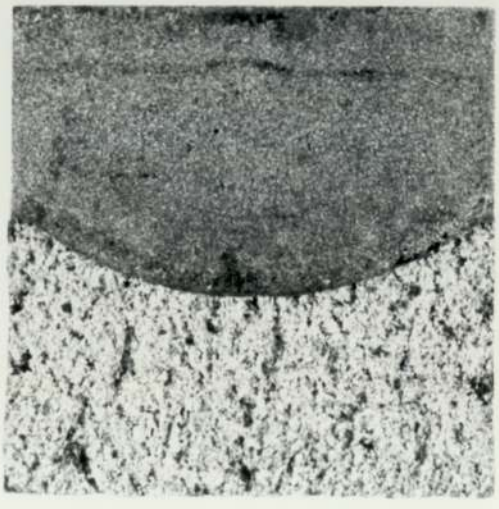

Plate.16. Fracture surface of a spark machined, curved crack front. Artificially aged A.U.W.E. 224 alloy. Magnification x 3.

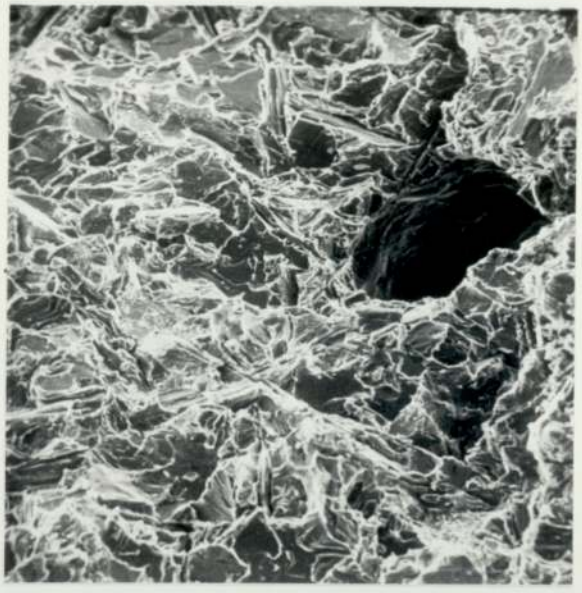

Plate.17. Scanning electron micrograph of the fracture surface of as cast A 354 alloy, showing a region of porosity. Magnification x 60.

Plate.18. Scanning electron micrograph of the fracture surface adjacent to the region of porosity shown in Plate.17. Magnification x 500.

Plate.19. Scanning electron micrograph of the fracture surface of as cast A 354 alloy, showing secondary cracking within a grain. Magnification x 1250.

Plate.20. Scanning electron micrograph of the fracture surface of as cast A 354 alloy, showing secondary cracking as in Plate.19. Magnification x 2500.

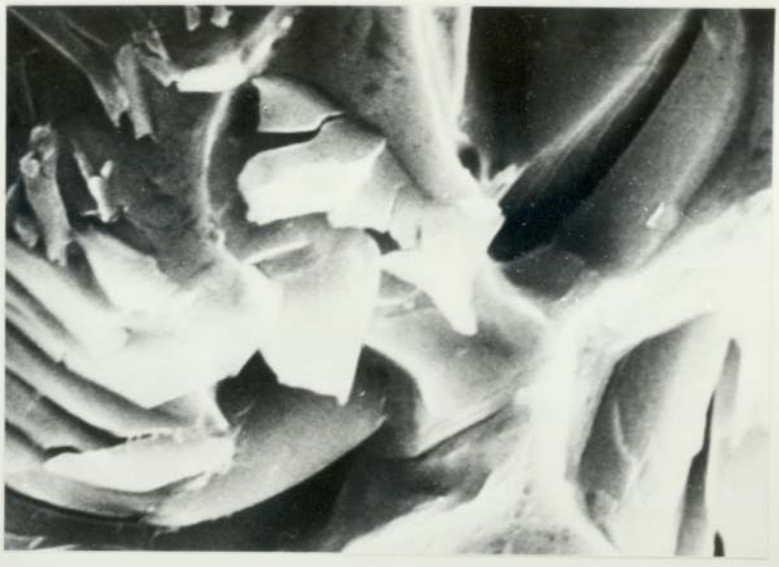

Plate.21. Scanning electron micrograph of the fracture surface of artificially aged A 354 alloy, showing secondary cracking. Magnification x 5000.

Plate.22. Scanning electron micrograph of the fracture surface of artificially aged A 354 alloy, showing a faceted area. Magnification x 7000.

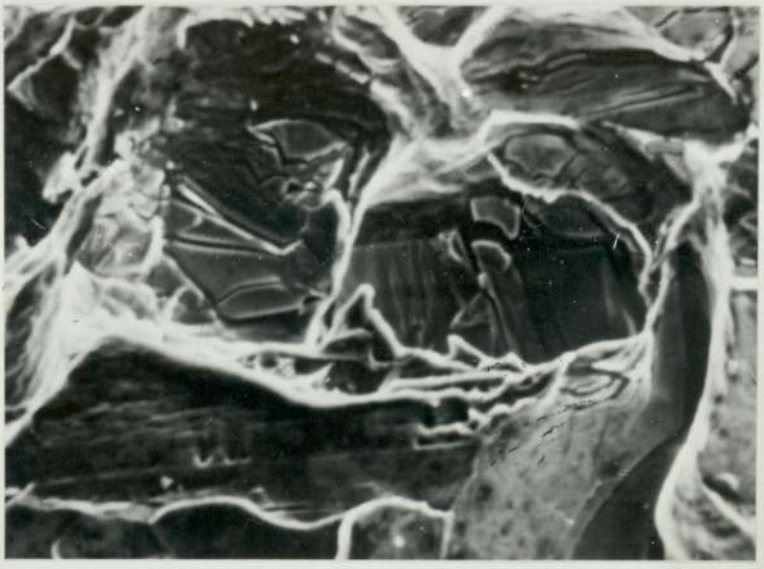

Plate.23. Scanning electron micrograph of the fracture surface of naturally aged A.U.W.E. 224 alloy.
Magnification x 1000.

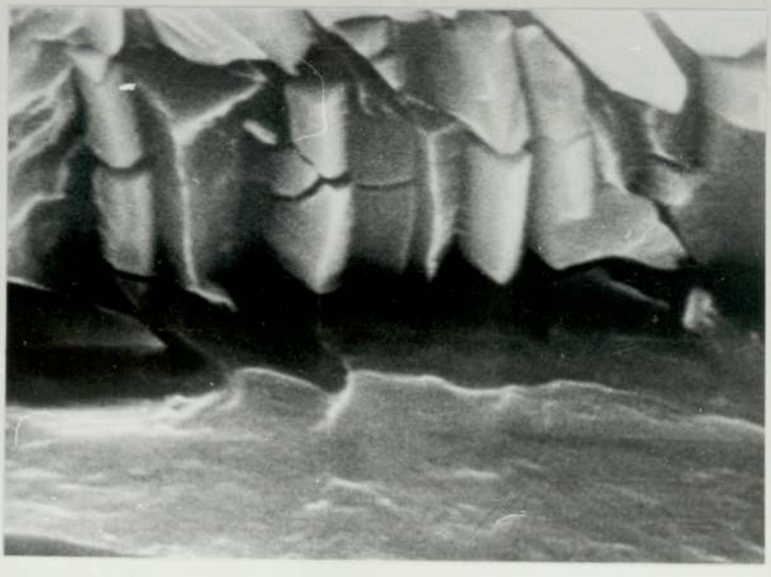

Plate.24. Scanning electron micrograph of the fracture surface of artificially aged A.U.W.E. 224 alloy.
Magnification x 10,000.

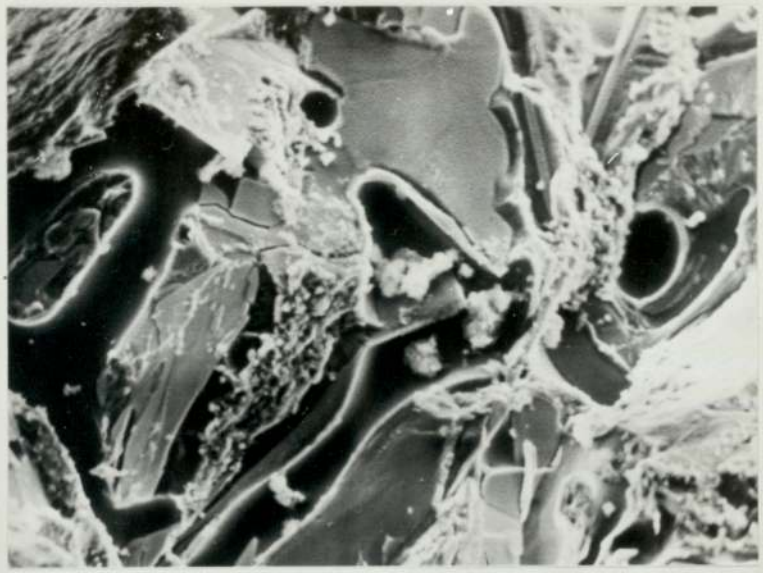

Plate.25. Scanning electron micrograph of the fracture surface of artificially aged A.U.W.E. 224 + Ag alloy, showing an area of impurities. Magnification x 500.

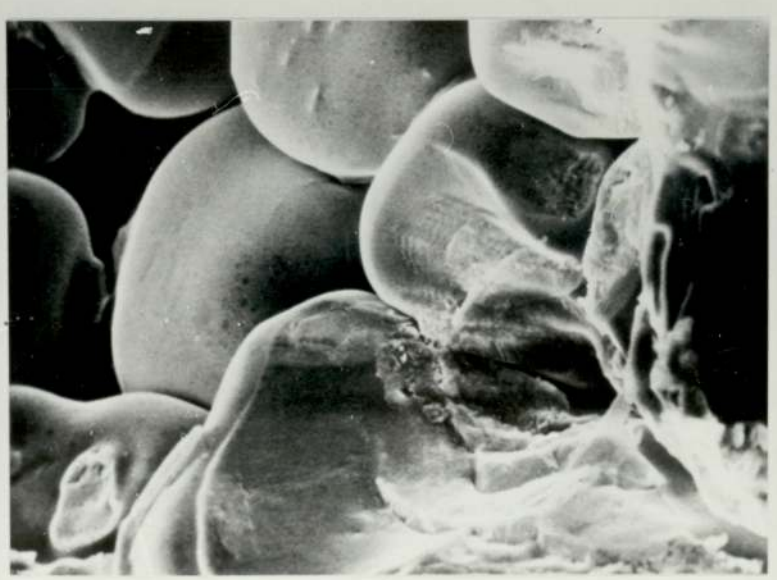

Plate.26. Scanning electron micrograph of the fracture surface of artificially aged A.U.W.E. 224 + Ag alloy, showing an area of inter-dendritic porosity. Magnification x 500.

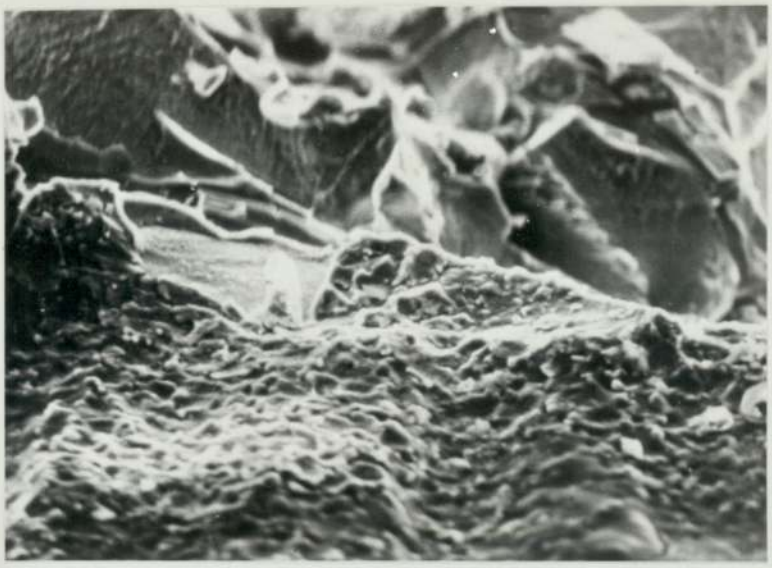

Plate.27. Scanning electron micrograph of the fracture surface at the root of a spark machined notch. Artificially aged A.U.W.E. 224 + Ag alloy. Magnification x 500.

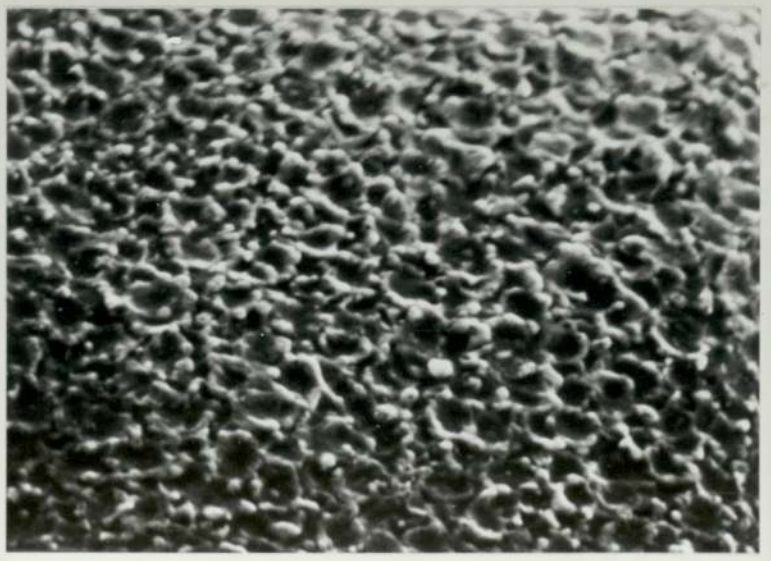

Plate.28. Scanning electron micrograph of the surface of a spark machined notch. Artificially aged A.U.W.E. 224 + Ag alloy. Magnification x 700.

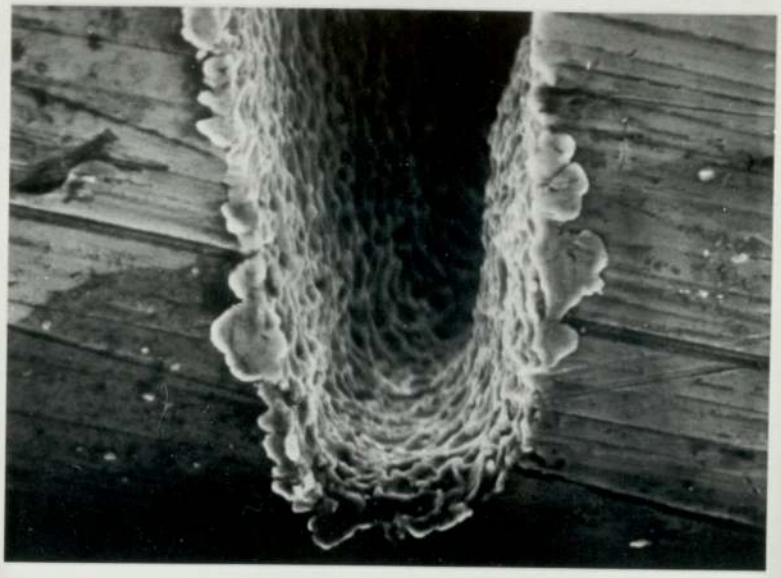

Plate.29. Scanning electron micrograph of the root of a spark machined crack. Artificially aged A.U.W.E. 224 + Ag alloy. Magnification x 750.

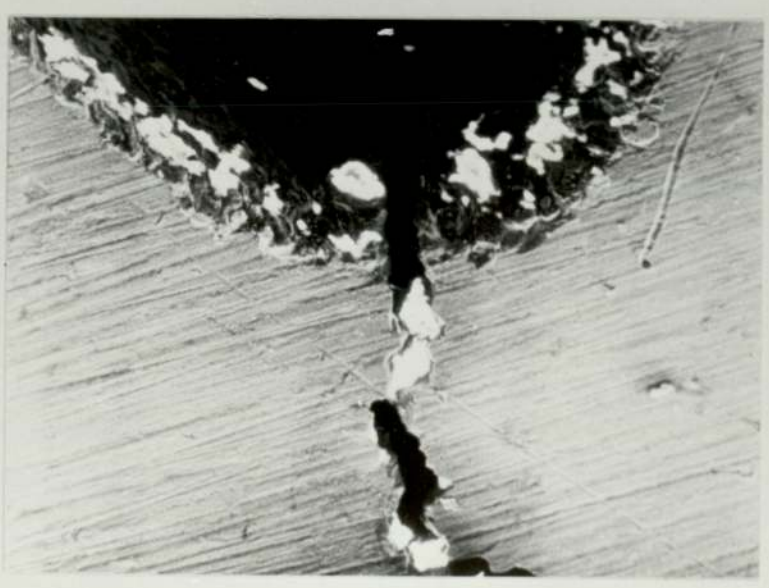

Plate.30. Scanning electron micrograph of a fatigue crack emanating from a spark machined notch. Artificially aged A.U.W.E. 224 + Ag alloy. Magnification x 200.

7. DISCUSSION.

7.1 General.

In this thesis the fracture properties of three high strength aluminium casting alloys have been evaluated in three point bending. A comparison between spark machined cracks and fatigue cracks has been made, together with a proposed experimental procedure for dealing with crack front curvature. The effects of material, material condition and porosity have been discussed, together with the geometrical effects of crack and notch root radius and short cracks emanating from blunt notches. A limited amount of fatigue crack propagation data has also been determined for the A.U.W.E. 224 type alloys.

7.2 The methods of manufacturing cracks and notches.

Owing to the difficulties encountered in producing short fatigue cracks from blunt notches, it was decided to simulate these cracks by spark machining. The major consideration was then that, spark machined cracks should give identical, if not lower values of K_{1c} than equivalent fatigue cracks. In order to assess these spark machined cracks, several specimens have been spark machined cracked and the fracture toughness values obtained from these specimens were directly compared with the values obtained from fatigue cracked specimens.

Examination of the analysis of variance results shown in table 16, together with the histograms constructed from the average values taken from the analysis of variance data shows that spark machined cracks are equivalent to fatigue cracks in Alcoa 354 (see fig 70). The spark machined cracks in the A.U.W.E. 224 + Ag alloy, however, tended to slightly under-estimate the $K_{(apparent)}$ values obtained from the fatigue cracks. It is thought that the difference between the two alloys was because the ΔK's for the fatigue cracked specimens were too high, even though testing had been carried out in accordance with

the recommendations laid down in BS DD3 (8). With reference to the standards it is apparent that the plane strain stress intensity factor, K_f, (corresponding to the maximum force of the fatigue cycle during the final stage of fatigue crack growth rate, i.e. the final 1.25 mm) is the subject of much controversy. For example: BS DD3 suggests that the ratio of the fatigue stress intensity factor to the critical stress intensity factor, should not exceed 0.75, whereas BS 5447 suggests that this K_f/K_{1c} should not exceed 0.7. More recently ASTM E 399-78 (117) states that K_f max must not exceed 60% K_Q. Examination of the results for the artificially aged A.U.W.E. 224 + Ag and Alcoa 354 specimens shows that the K_f/K_{1c} ratio lies typically around a value of 0.6 for both materials. A value of K_f/K_{1c} of 0.6 may not be great enough to cause crack tip blunting in the Alcoa 354 alloy, but some crack tip blunting may have occurred at this value in the A.U.W.E. 224 + Ag alloy. Evidence to support this suggestion can be found by comparing the relative ductilities of these two alloys. From table 6. it can be seen that the typical percentage extensions for artificially aged Alcoa 354 and A.U.W.E. 224 + Ag alloys are 2% and 5% respectively. As these elongations are an indication of ductility and plastic deformation at the crack tip, it is reasonable to assume that more plastic deformation and therefore more crack tip blunting would occur in the A.U.W.E. 224 + Ag alloy than in the Alcoa 354 alloy. It is thought then, that spark machined cracks will give K_{1c} values, providing that the crack root radii can be machined to values of approximately 0.05 mm (see plate 27 and fig. 64). This means that spark machining can be used to simulate sharp cracks.

7.3 Crack front curvature.

If an accurate practical analysis of toughness versus thickness is to be made, it is important to allow for crack front curvature (CFC). Compliance measurements have been carried out on parabolic curved crack fronts, manufactured by spark machining with a parabolic copper former. A typical curved crack fronted specimen is illustrated in plate 16. As there was a great deal of "sinking in" of the rollers during three point bending of these aluminium casting alloys, it was necessary to develop a rig which would measure load point displacements, independent of the effect of the rollers sinking in. This rig is illustrated in fig.50. Load point displacements from this rig, however, were greater than those calculated from theory. The load point displacement at the mid-point of a beam in three point bend may be given by (see section 4.2) the equation:

$$\delta = \frac{PL^3}{4EBW^3}$$

where P is the mid-point load L is the span length
E is Young's modulus B is the specimen thickness
W is the specimen width

Typically the load point displacement rig gave values of load point displacement approximately 1.4 times greater than the theoretical values. An explanation of this difference in the theoretical and measured load point displacements could be that micro yielding had occurred within the specimens during bending, which would tend to increase the measured load point displacements. The values obtained for Young's modulus, substituted to calculate the theoretical load point displacements were determined in uniaxial tension and it has

been assumed that these values will be the same in three point bending.

The Barnby and Daimalani rig (99) used on these aluminium casting alloys, gave load point displacements approximately 20% greater than those obtained from the rig illustrated in fig.50. The difference in the load point displacements obtained from the two rigs was thought to be due to sinking in of the rollers during loading, because of the small specimen size and low yield strengths of these alloys. This would increase the measured load point displacement when using the Barnby and Daimalani rig.

Ryder, Bowie and Pettit's curve fitting procedure (96) was a more satisfactory method of expressing the compliance data and proved to be "easier" to differentiate than the more commonly used polynomial expressions. For example, with Crow's data (113) on curved crack fronts in compact tension specimens (see table 8 and fig.57) the polynomial expression had to be reduced to three terms before the generated d(CEB)/d(a/W) values for stages of a/W produced a smooth curve with no points of maxima or minima. The more terms there are in a polynomial expression, the greater will be the tendency of the differential of the polynomial expression to give points of maxima, minima and inflection.

A comparison between Ryder, Bowie and Pettit's proposed curve fitting procedure applied to compliance data obtained from WOL specimens and Wessel's polynomial expression (73) is shown in fig.40. As there was good agreement between Ryder's curve fitting procedure, applied to his own compliance data and the polynomial solution of Wessel's Ryder's curve fitting procedure was applied to Crow's compliance data for straight crack fronts (see fig.56). A similar exercise has been carried out on three point bend compliance data obtained for straight crack fronts. Here Ryder's curve fitting procedure, applied to three point bend

data was compared with Walker and May's polynomial solution (112). Figs.56 and 58 show that Ryder's curve fitting procedure, applied to experimental compliance data for compact tension and three point bend specimens, agreed favourably with the polynomial expressions of Wessel and Walker and May, respectively. Having established the accuracy of Ryder's procedure, compliance data from curved crack fronted, compact tension and three point bend specimens was processed and the results are shown in figs.57 and 59.

From these results it can be seen that, when the C_3 values for the curved and straight crack fronted specimens are the same, the length of the straight front is equivalent to the length of the "corrected" curved crack front. It is thought that, by measuring the maximum length of a curved crack front, or by adopting the averaging procedure laid down in the standards (1, 2 and 8) an overestimate of the compliance calibration function will be obtained. This suggestion could be supported by considering a typical three point bend specimen of width 22 mm, thickness 22 mm, and maximum curved crack length 12.5 mm (see sketch below):

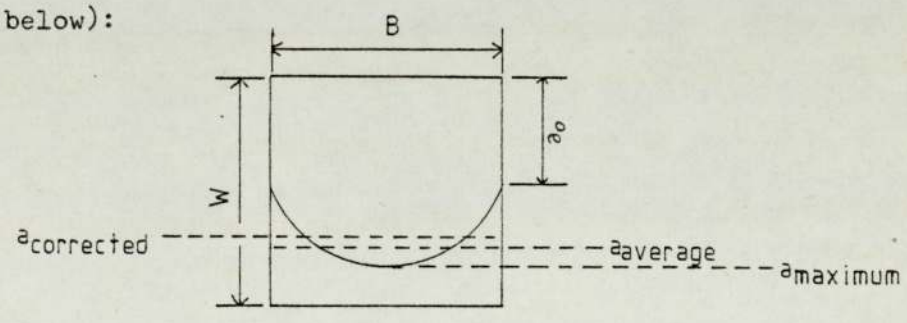

here the values of a, a/W and Y (according to Walker and May) for this specimen can be given as:

	Crack length	a/W	Y
$a_{maximum}$	12.5 mm	.57	13.5
$a_{average}$	11.8 mm	.54	12.1
$a_{corrected}$	11.0 mm	.50	10.6

By assuming that the $a_{corrected}$ was the "correct" value of curved crack length, the compliance calibration functions fot the average and maximum curved crack lengths overestimated this "correct" value by 14 and 27%, respectively. For a symmetric parabolic curved crack front, the averaging procedure laid down in the standards will always give longer crack lengths than the applied correction factor. Consider the parabolic crack front sketched below:

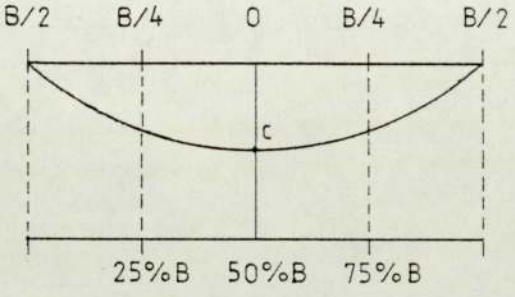

$Y = Ax^2 + c$ (equation of a parabola)

when $x = \frac{B}{2}$, $Y = 0$

therefore $0 = \frac{AB^2}{4} + c$ and $\underline{\underline{A = \frac{-4c}{B^2}}}$

average height of the parabola $= 1/3 \left(c + 2\left(A\left(\frac{B}{4}\right)^2 + c\right)\right)$

$$= 1/3 \left(c + \frac{2AB^2}{16} + 2c \right)$$

$$= c + \frac{AB^2}{24}$$

substitute for A:

average height of parabola $= c - \frac{4c}{B^2} \times \frac{B^2}{24}$

$$= c - \frac{c}{6}$$

$$= \underline{\underline{5/6\ c}}$$

Therefore for a symmetrical, parabolic crack front the average length may be given by:

$$a_{effective} = a_o + 5/6\ (a_{maximum} - a_o)$$

whereas the corrected length would be:

$$a_{effective} = a_o + 2/3\ (a_{maximum} - a_o) \times B/S$$

and as $S \geqslant B$, the corrected curved crack front length is always less than the average curved crack front length (for a parabolic, symmetric, curved crack front).

Although assumptions were made in deriving the length of a curved crack front, S (see section 6.2.2) it is reasonable to suggest, on the basis of compliance data, that a curved crack length may be "corrected" to give an equivalent straight crack front length. Neale (74) has pointed out that the stress intensity varies with position along the curved crack front and will be a maximum at the tip of this curved crack. The maximum stress intensity was thought to determine the event of fracture. The stress intensity along these spark machined curved crack fronts could not be found, but evidence to support the experimental compliance calibrations can be obtained from the fracture loads for curved crack fronted specimens. For example the C_3 values for six individual, curved crack fronted A.U.W.E. 224 specimens, have been determined at fracture using the expression:

$$Y = \frac{K_{1c} \times BW^{\frac{1}{2}}}{P}$$

These C_3 values were then plotted on the C_3 versus a/W graph, shown in fig.59. The C_3 values obtained from the curved crack fronted specimens agreed favourably with the experimental compliance curves, showing the correction procedure for curved crack fronts to be accurate.

7.4 Fracture toughness testing methods.

Five methods of determining the fracture toughnesses of these aluminium casting alloys have been used conjointly, namely:

a) Test 1. The 5% secant, LEFM technique (1, 3 and 8)

b) Test 2. The crack opening displacement (COD) technique detailed in BS Draft for Development 19 (23).

c) Test 3. The crack opening displacement (COD) technique suggested by Dawes (21).

d) Test 4. The J integral technique for single load point displacement records, suggested by Rice et al (97).

e) Test 5. The equivalent energy procedure described by Witt (115).

The results for the fracture toughnesses of the alloys are recorded in the appendix of this thesis. The majority of the K_Q values obtained according to the 5% secant method were not valid K_{1c} values, on account of too much plasticity before fracture. This was shown on the records as:

a) The inelastic deviations at P_Q were greater than 4 times the inelastic deviations at 0.8 P_Q.

b) The $P_{maximum}$: P_Q ratio was greater than 1.1.

The average K_{1c} values obtained for the alloys are given in section 6.6 and have been used to calculate the critical defect sizes.

In order to analyse the 5 available methods collectively, the data was fed into the analysis of variance programme in the following form:

a) K_Q values obtained according to equation 155 where P_Q was the 5% secant load.

b) $K_{(apparent)}$ from COD values obtained from equation 162 where M = 2.1.

c) $K_{(apparent)}$ from J values, according to equation (164)

d) K_Q Equivalent energy values obtained from equation (166)

From the analysis of variance results shown in table 13 and the histograms constructed to illustrate these results (fig.69), it is clear that the method of test has a highly significant effect on the value of $K_{(apparent)}$ obtained. Examination of all these histograms shows that, for the A.U.W.E. 224 type alloys, the COD methods of determining $K_{(apparent)}$ give far higher values than those obtained by the other three methods. The value substituted for M in the conversion equation for COD to $K_{(apparent)}$ for all the alloys was 2.1. As discussed in section 2.4.2.2, the value of M is the subject of much controversy. For example if the value for M had been 1,0, then the converted COD results for the A.U.W.E. 224 type alloys would have produced $K_{(apparent)}$ values of similar magnitudes to those obtained by the other methods. The values of $K_{(apparent)}$ from COD for the artificially aged Alcoa 354 alloy, were similar in magnitude to the $K_{(apparent)}$ obtained by the other methods. This observation tends to suggest that substituting a value of M = 2.1 for the conversion of COD values to $K_{(apparent)}$ values was correct for this alloy.

The difference between the relative magnitudes of the $K_{(apparent)}$ from COD values, for the three alloys can be explained in terms of the differing extents of plastic deformation at the crack tips. The typical percentage elongation for the artificially aged Alcoa 354 alloy was 2%; whereas the typical percentage elongations for the artificially aged A.U.W.E. 224 type alloys were 5%. From these values it is reasonable to suggest that the plastic deformation at the crack tip and therefore COD values were higher for the A.U.W.E. 224 type alloys than the Alcoa 354 alloy. This suggestion is supported by the COD results where, for the artificially aged A.U.W.E. 224 type alloys, the COD's were

typically 2.0 to 3.0 x 10^{-2}mm. The COD's for the artificially aged Alcoa 354 alloy, however, were only typically 0.8 to 1.5 x 10^{-2}mm.

The most reproducible method of determining the K_{1c}'s of these aluminium casting alloys could be found by comparing the standard deviations, about the mean values, for each individual testing method. The J integral technique gave the smallest values of standard deviations about the mean values of $K_{(apparent)}$ from J, out of all the methods. The values of $K_{(apparent)}$ from J, obtained from those specimens designed to determine the fracture toughnesses of these alloys also agreed favourably with the average K_{1c} results shown in section 6.6.

The major source of error in evaluating the J integral was in the determination of the point of initiation. Initiation has been defined as a 1 μ volt change in the total signal level and this could be measured to an accuracy of $\mp$ 2 mm on the potential-time traces. This $\mp$ 2 mm corresponded to a cross head displacement of approximately 0.04 mm (i.e. with a chart speed of 20 mm/minute and a cross head displacement of 0.2 mm/minute). Typically the load point displacements were about 0.35 mm, consequently the error in determining the critical load point displacement (i.e. the load point displacement at initiation) was $0.35 \mp 0.04^{mm}_{\wedge}$ which is about 9%. If we take the simple case where the slope of the linear portion of the load-load point displacement record is at about 45°, then this 9% error in displacement is a maximum error and corresponds to an 18% error in the area determination. This 18% error can be considered to be the error in the J integral, since the errors encountered in

measuring the dimensions of the specimens are negligible in the equation:

$$J = \frac{2U}{B(W-a)}$$

where U is the required area.

In the conversion equation for J to K_{1c} (see equation (164)) the square root of J is taken. The error in K_{1c}, therefore, is equal to the square root of the error in J, which reduces to approximately 4%.

The equivalent energy method for determining K_{1c} values from small scale yielding in non-valid LEFM records has been proposed by Witt (115). The same techniques were used as for the J integral method in which a load-load point displacement record was constructed for the determination of the energy values. As suggested by Merkle and Corten (118) for pure bending and providing a/W is greater than 0.5, the equivalent energy procedure is virtually the same as the J integral method. Evidence to support this suggestion can be found by comparing the histograms constructed for the average values of $K_{(apparent)}$ obtained from these two methods, shown in figs.69 to 72. Here it may be seen that the two methods give similar estimates of $K_{(apparent)}$.

The methods of determining the crack opening displacements were inaccurate for these aluminium casting alloys because of the very small mouth opening displacements (i.e. Vg) and therefore COD's involved.

The accuracy of the potential drop method could be determined in the following manner. Values of crack length were calculated from equation (134) and were found to be within $\pm$ 1 mm of the average crack lengths measured optically after fracture The important factor in this case was, however, the accuracy in determining a change in crack length. As the potential difference calibration curves shown in fig.49 are almost linear over short ranges of a/W, the change in crack length could be calculated to an accuracy corresponding to the sensitivity of the method. It was considered that a change in the total signal level of 1 μ volt, due to an increase in crack length could be reliably detected and this was taken as the initiation condition.

From equation (134) a change of 1 μ volt on a typical total signal level of 360 μ volts, using a current of 60 amps applied along the specimen (see fig.64a) corresponded to an increment in a/W of approximately 0.0025. This represents a crack length increment of 0.06 mm when the width of the specimen is taken as 22 mm.

Typically the mouth opening displacements were within the range 0.14 to 0.18 mm and the magnification used to show these displacements on the load-mouth opening displacement record was about 1000. (i.e. 180 mm chart = 0.18 mm mouth opening displacement). Although the clip gauge could detect a change in the mouth opening displacement of approximately 1 micron, the calibration of the clip gauge was only accurate to 0.02 mm. The accuracy of measurement of the mouth opening displacements was, therefore, approximately 0.16 ± 0.02 mm.

The linear differential core transducer, used for measuring the load point displacements, could detect a change in load point displacement of approximately 2 microns, but the calibration was accurate to about 0.01 mm. Typically the load point displacements were within the range 0.3 to 0.4 mm. Consequently the accuracy of measurement of the load point displacements was about 0.35 ± 0.01 mm.

From the histograms for the average K_Q values, determined by the 5% secant construction, it can be seen that, on average, the invalid K_Q values underestimated the average K_{1c} values recorded in section 6.6. The reason for this was because the 5% secant gave P_Q loads far lower than the actual loads at initiation, as defined by the electrical potential technique.

The combination of test method with: method of crack manufacture, notch root radius, block size and aging treatment had no significant effect on the values of $K_{(apparent)}$ obtained. The combination of material and method of test, however, did have a significant effect on the values of $K_{(apparent)}$ obtained, as shown in table 13, and illustrated in fig.69. This highly significant combination was mainly due to the differing relative magnitudes of the COD values (as previously described in this section) for each of the alloys. Although the combination of the two most highly significant factors would probably be significant in any case.

7.5 Short cracks emanating from blunt notches.

When a sharp crack is very short and emanates from a blunt notch, the stress intensity at the tip of the crack is influenced by the close proximity of the notch. Sharp cracks, simulated by spark machining (see section 7.2), were produced from blunt notches and the results of $K_{(apparent)}$ from J obtained from these cracks are illustrated in fig.63. Originally, these short cracks, emanating from blunt notches, were produced by fatigue cracking, but this proved to be both tedious and inaccurate. The main problem encountered when growing such small fatigue cracks was the effect of crack front bowing. In some cases this was so pronounced that, on breaking open the specimens, there was substantial crack growth in the centre of the specimen but no sign of cracking at the edges.

From the results of c/(W-a) versus $K_{(apparent)}$ from J values, shown in fig.63, it was possible to estimate the values of c_o experimentally. These critical crack lengths were, therefore, obtained from the points where the $K_{(apparent)}$ from J values approached the average K_{1c} values. i.e.

Material (artificially aged)	a/ρ	c_o
A.U.W.E. 224	~ 1.50	$0.25\sqrt{a\rho}$
A.U.W.E. 224	~ 3.25	$0.30\sqrt{a\rho}$
A.U.W.E. 224 + Ag	~ 3.50	$0.35\sqrt{a\rho}$

These estimates of c_o are less than the theoretical predictions of Yamamoto et al (51) and Smith and Miller (57) shown in fig.63. From the results it can be seen that the $K_{(apparent)}$ from J decreases with increase in crack length from the blunt notch. At the condition where c = 0 (i.e. a blunt notch by itself) the concentration of stress can be accommodated by small scale plasticity in a large volume of material.

The energy required to propagate a crack from a blunt notch is, therefore, relatively high and the $K_{(apparent)}$ from J is high. The stress intensity at the tip of a sharp crack emanating from a blunt notch is high; consequently the energy required to propagate a crack is lower than that for a blunt notch, and the $K_{(apparent)}$ decreases.

From Yamamoto's work (51) on sharp cracks emanating from blunt notches, it can be seen that finite element analysis is not applicable for determining the stress intensity at the tip of a crack c = 0. Experimentally, however, it was possible to determine the $K_{(apparent)}$ values for these aluminium casting alloys when c = 0 and these are shown in fig.63.

7.6 Notch and crack root radii.

Crack root radii could be simulated by spark machining as the values of $K_{(apparent)}$ obtained from the spark machined cracked specimens have been shown to be similar to those obtained from fatigue cracked specimens (see section 7.2). The $K_{(apparent)}$ obtained from a spark machined cracked specimen, however, is dependent on the sharpness of the crack tip.

The effect of crack root radius (simulated by spark machining) on $K_{(apparent)}$ from J, for artificially aged A.U.W.E. 224 + Ag alloy is shown in fig.64. From these results it may be seen that the crack root radius has the greatest effect on $K_{(apparent)}$ when the crack tip is very sharp (i.e. up to $\sqrt{\frac{\rho}{a}}$ values of 0.1). The critical value of $\sqrt{\frac{\rho}{a}}$ or the value of $\sqrt{\frac{\rho}{a}}$ when $K_{(apparent)} = K_{1c}$, was approximately 0.05, since, although the average K_{1c} for this alloy was 17.5 $MNm^{-3/2}$ the spark machined cracks tended to give under-estimates of this value. This observation has been previously discussed in section 7.2. If the crack root radii were spark machined to values below the critical root radius, then 'blunting down' to the critical value would occur during

fracture toughness testing. This 'blunting down' is also thought to occur in very sharp fatigue cracks, consequently there is no point in producing fatigue cracks sharper than the value of the critical root radius in fracture toughness testing.

Examination of the load-load point displacement records for these specimens indicates that some degree of yielding has occurred before crack propagation (see fig.64a). The Spink, Worthington and Heald equation (66) for small scale yielding, therefore, could not be directly applied to these results and should only be used as a guide.

Notches of root radii; 0.20, 0.74 and 1.60 mm were mechanically machined into specimens from all three alloys and the values of $K_{(apparent)}$ were determined using all the five available methods. This data was then fed into an analysis of variance programme, the results of which are detailed in table 14 and are illustrated in fig.71. According to these results the notch root radius of a specimen has a significant effect on the value of $K_{(apparent)}$ obtained. Examination of the histograms in fig.71 shows that for the A.U.W.E. 224 type alloys, the 0.74 mm notch root radius tended to give lower estimates of $K_{(apparent)}$ than the other two notch root radii. This observation could be attributed to the different extents of plastic deformation, produced at the notch tips by mechanical machining.

The minimum notch root radius that could be mechanically machined into these specimens was about 0.2 mm. It is thought that, at this value, the cutting tool would cause more plastically deformed material at the notch tip than with a more shallow notch root. In order for a crack to propagate, it would have to overcome this mechanically deformed zone. Consequently the $K_{(apparent)}$ values obtained from the more shallow notch roots were lower than those obtained from the sharp root radii.

Richards and Wood (47) have determined the stress concentration

factors (using two dimensional finite element analysis) for notches in three point bend specimens, of width 22 mm and notch depth 5 mm (see fig.27). From fig.27 the K_T values of 0.74 mm and 0.20 mm notch root radii specimens were estimated as being 3.4 and 6.4 respectively. The value of K_T for the sharper notch (0.20 mm notch root radius) was therefore approximately twice the K_T of the blunter notch (0.76 mm notch root radius). The values of $K_{(apparent)}$ obtained from the 0.76 mm notch root radius specimens were, however, less than those obtained from the 0.20 mm notch root radius specimens, as shown by the average values for $K_{(apparent)}$ in fig.71. It is thought that, with such small values of mechanically machined root radii, the extent of mechanical deformation at the notch tip has more effect on $K_{(apparent)}$ than the stress concentration has. As a notch becomes even more blunt, for example 1.60 mm root radius, the stress concentration at the notch root decreases, consequently the $K_{(apparent)}$ tends to increase. This is shown for the A.U.W.E. 224 type alloys, in the histograms of fig.71.

The histograms for the artificially aged Alcoa 354 alloy shows that on average, $K_{(apparent)}$ is independent of notch root radius, in this alloy. This observation is probably the reason for the significant combination of material and notch root radius shown in table 14. The J integral technique for the Alcoa 354 alloys, however, shows a trend for the effect of notch root radius on $K_{(apparent)}$ similar to that for the A.U.W.E. 224 type alloys. Mechanical machining may not give rise to plastic deformation at the notch tips in the Alcoa 354 alloy, because of the limited amount of ductility. This was thought to be the reason for the similar $K_{(apparent)}$ from COD values, obtained from all three notch root radii, in the Alcoa 354 alloy.

7.7 Dimensional effects on fracture toughness.

The fracture toughness of as cast Alcoa 354 and artificially aged A.U.W.E. 224 alloys has been determined for various specimen thicknesses. The results are detailed in the appendix of this thesis and are illustrated in figs. 61 and 62. The width of these specimens was at least 50 times greater than the plane strain plastic zone sizes, as recommended in the standards (1, 2 and 8). The values for the plane strain plastic zone sizes, together with the minimum specimen thicknesses, are shown below. In order to calculate these values, average values of K_{1c} and typical values of yield strength (obtained from section 6.6) have been substituted into the usual equations (i.e. equations (15b and 16)

Material (artificially aged)	Plane strain plastic zone size (mm)	Minimum thickness (mm)
Alcoa 354	0.26	18.39
A.U.W.E. 224	0.22	15.33
A.U.W.E. 224 + Ag	0.17	11.96

The K_Q results for as cast Alcoa 354 specimens, shown in fig.61 suggests that there may be an upward trend at a thickness of about 8 mm. This, however, was not shown on any of the 'thinner' specimens in the form of shear lips. The experimental value of the minimum specimen thickness proved to be difficult to determine because, at thicknesses less than about 5 mm, the specimens buckled in the three point bend rigs. This means that three point bend tests cannot be used to evaluate the fracture properties of sheet or plate.

Examination of the artificially aged A.U.W.E. 224 alloy results tended to support the findings of the as cast Alcoa 354 alloy, that is, thicknesses above about 4 mm had no effect on K_Q. A less apparent outcome from these A.U.W.E. 224 results was that, out of all the five

available fracture toughness testing methods, the J integral technique was the most accurate. This can be seen from fig.62.

In yielding fracture mechanics, it is the containing of the zone of intense deformation which determines a specimens' thickness requirements. The thickness requirements are therefore very much less than those for LEFM. For example, for the artificially aged 224 + Ag alloy, the minimum thickness requirement, according to BS 5447 (1), was 15.33 mm. The minimum thickness requirement for the J integral method, however, would only be 0.5 mm (equation given below):

$$B_{min} = 25 \times \frac{K_{Ic}\,(1-\nu^2)}{E \quad \sigma_{ys}}$$

As the experimental minimum thickness for the as cast Alcoa 354 and artificially aged A.U.W.E. 224 specimens was less than 4 mm, the thickness of the specimens could be ignored in future analysis.

7.8 Porosity and block sizes.

Porosity was present in all the specimens and can be seen, for example, from the radiographs of the original Alcoa 354 alloy specimens, cast at A.U.W.E. (see fig.44). Although this material was particularly porous, the latter material supplied was considerably sounder. A scanning electron micrograph of an area of dendritic porosity is shown in plate 17, and another area, shown at a higher magnification, in plate 28. In order to determine the extent of porosity, density measurements have been carried out by B.N.F. Technology Centre on specimens taken from various positions within a block of as cast K01 material. From these results, shown graphically in fig.65, it would appear that the extent of porosity, up to approximately 1.5 per cent, has little effect on the value of $K_{(apparent)}$ obtained and the results are scattered about a mean value of about $14 MNm^{-3/2}$. A similar trend of the effect of porosity on the values of $K_{(apparent)}$ could be

seen for the artificially aged Alcoa 354 alloy, shown in the histograms of fig.69. From the analysis of variance results shown in table 13 and illustrated in fig.69, it is clear that the block thickness has a highly significant effect on $K_{(apparent)}$ for the artificially aged A.U.W.E. 224 type alloys. It is proposed that this significance is due to the different porosity levels in the three block thicknesses, despite the fact that these low porosity levels could not be accurately measured using density determinations. The porosity levels in the Alcoa 354 alloy blocks were considerably greater than those of the A.U.W.E. 224 type alloy blocks. It is thought, therefore, that the major effect of porosity occurs at levels less than about 0.05%. This suggestion explains why the values of $K_{(apparent)}$ for the Alcoa 354 alloy, shown in fig.69 are scattered about a mean value of about 20 $MNm^{-3/2}$. In a practical sense, these results show that an improvement in the fracture properties, by porosity control, is not feasible in these aluminium casting alloys, until the porosity level is reduced to less than about 0.05%.

7.9 The effects of material condition on $K_{(apparent)}$.

One of the most important considerations made, when determining the fracture properties of these aluminium casting alloys, was material condition. Solution treated A.U.W.E. 224 + Ag specimens were aged for increasing periods of time. The effects of aging time on the values of $K_{(apparent)}$ determined by the five available methods, are illustrated in figs.67a, b and c. From these graphs and in particular the graph for the J integral results, it is clear that there is a decrease in fracture toughness with increase in aging time. Furthermore this decrease in toughness is gradual until the peak hardness and yield strength is attained, and then the toughness decreases rapidly. This rapid decrease in fracture toughness with the overaged structure could

be attributed to particle rupture at the grain boundaries.

As the aging time was increased, the precipitates, nucleated in the early stages of aging, became more coarse. Maximum hardness and yield strength was, therefore, associated with an optimum small particle size and spacing and a corresponding large number of particles. The majority of particles nucleate and grow at low energy sites within the grains, but some of the particles will form at the grain boundaries. As the aging time is increased these particles at the grain boundaries become coarser and particle rupture occurs more readily. Evidence to support this suggestion can be found by comparing the microstructures for the differently aged conditions of the A.U.W.E. 224 + Ag alloy, shown in plates 8, 9 and 10. Here it can be seen that there was only a slight difference between the naturally and artificially aged conditions. Overaging, however, clearly showed a coarsening of the precipitates at the grain boundaries. Overaging is usually associated with the formation of a denuded zone on each side of the grain boundary. No evidence of these zones (i.e. a ductile fracture appearance) could be seen on the fracture surfaces of the overaged specimens. Evidence of particle rupture or shattering, however, can be seen in plate 24 where this particle was estimated to be about 5 microns across.

From the analysis of variance results shown in table 15, it would appear that there was no significant difference between the naturally and artificially aged conditions. Examination of the histograms for the average values of $K_{(apparent)}$ shown in fig.72, however, suggests that there is an effect of material condition on $K_{(apparent)}$. The values of $K_{(apparent)}$ for the A.U.W.E. 224 + Ag and Alcoa 354 alloys were consistently greater for the naturally aged condition, than they were for the artificially aged condition. This observation, however, was the reverse for the A.U.W.E. 224 alloy. Consequently the overall effect of material condition on the values of $K_{(apparent)}$ taking the

three alloys combined would be insignificant. From the histograms shown in fig.72, it is apparent that the addition of silver to A.U.W.E. 224 greatly reduces the fracture properties of this alloy, particularly for the artificially aged conditions. Evidence to support this observation can be found in section 6.6, where the average values of K_{1c} for the artificially aged A.U.W.E. 224 and 224 + Ag alloys were 26 $MNm^{-3/2}$ and 17.5 $MNm^{-3/2}$ respectively. The mechanisms of failure of all the alloys are discussed in greater detail in the next section.

7.10 The mechanisms of fracture.

The fracture surface of a typical, as cast, Alcoa 354 specimen is shown in plates 17 to 20 inclusive. From these scanning electron micrographs, together with those for the naturally and artificially aged conditions, it can be seen that there was no visible difference between the fracture surfaces, despite the three different material conditions. The mode of failure in the Alcoa 354 alloy was recognised as being inter-granular fracture and the reflective or "bright" appearance, when examined optically (see plate 15) was thought to be due to quasi-cleavage of the silicon particles. Shattering of these silicon particles can be seen in plates 19, 20 and 21.

The mechanism of failure in the A.U.W.E. 224 type alloys was also recognised as being inter-granular fracture. As with the Alcoa 354 alloy, no difference could be seen between the fracture surfaces of the differently heat treated specimens. The reflective or bright appearance of the fracture surfaces in these alloys was thought to be due to a combination of sharply defined grain surfaces, together with particle shattering at the grain boundaries. The extent of particle shattering in these A.U.W.E. 224 type alloys was not as severe as with the Alcoa 354 alloy and a very high magnification was necessary before particle shattering could be clearly seen, as in plate 24.

It is thought that, the greater the amount of precipitate that occurs at the grain boundaries, the more readily particle rupture, and hence inter-granular fracture will occur. This explains the reason for the low fracture toughness value ($\sim$14 $MNm^{-3/2}$) obtained from the overaged specimens.

Porosity and impurity phases within all the alloys provided linkage for crack advance and could be observed on the fracture surfaces. The size of the pores for the A.U.W.E. 224 type alloys was difficult to determine, but for the as cast Alcoa 354 alloy, examination of the radiographs shown in fig.44, together with the pore illustrated in plate 17, suggest a pore size of about 0.5 mm.

7.11 Fatigue crack growth rates for the A.U.W.E. 224 type alloys.

Fatigue crack growth rates for these alloys were difficult to determine accurately because of multi-nucleation of small cracks at the notch roots. This was the main problem encountered when trying to grow predicted fatigue crack lengths from the machined notches.

The appearance of a typical fatigue crack front is illustrated in plate 15 from which it can be seen that the crack fronts were difficult to distinguish with these alloys. Bowing of the fatigue crack fronts was common in most of the specimens. This was thought to be a consequence of thickness, as bowing was more pronounced in the thicker specimens.

Comparison can be made between the fatigue crack growth data obtained for these A.U.W.E. 224 type alloys (shown in fig.55) and their wrought equivalents listed in a paper by Pook (119). For example, the stress required to produce a fatigue crack growth rate of $da/dN = 10^{-6}$ mm/cycle was $\sim$ 2 $MNm^{-3/2}$ for the wrought alloy and $\sim$ 6-9 $MNm^{-3/2}$ for these casting alloys. These observations could be attributed to the extent of porosity which occurred in the casting alloys, as it is

thought that areas of porosity tend to arrest fatigue cracks.

From fig.55, it would appear that the crack growth rates for the naturally and artificially aged conditions, for each alloy, were similar. The stresses required to produce these rates, however, were different. For example, consider the stress required to produce a crack growth rate of $da/dN = 10^{-3}$ mm/cycle. For the A.U.W.E. 224 alloy, this stress was ~ 20 $MNm^{-3/2}$ for the artificially aged condition and about 14 $MNm^{-3/2}$ for the naturally aged condition. Similarly for the A.U.W.E. 224 + Ag alloy, the stresses required to give a crack growth rate of 10^{-3}mm/cycle were ~ 35 $MNm^{-3/2}$ and ~ 30 $MNm^{-3/2}$ for the artificially and naturally aged conditions, respectively. An explanation of these differences between the two alloys and the two conditions could be that the aging precipitate at the grain boundaries was more pronounced in the A.U.W.E. 224 + Ag alloy than in the A.U.W.E. 224 alloy. Furthermore, these precipitates would be coarser in the artificially aged structure than in the naturally aged structure. This can be seen in plates 5, 6, 8 and 9. It is thought that the greater the precipitate at the grain boundaries, the greater will be the restriction to fatigue cracking.

The finite difference procedure for determining the fatigue crack growth data (see fig.55) gave more realistic results than the differentiated polynomial expression for crack length versus number of cycles Curve fitting techniques, for crack length versus number of cycles data, have been discussed by Pook (119). A more accurate approach to this problem could be the fitting of an exponential equation to the results, on a similar basis to that used by Paris (72) but with the inclusion of constants to account for the structural properties. These constants would be necessary, since the relationship between ΔK and da/dN is not entirely geometrical.

7.12 The application of fracture toughness data.

The fracture toughnesses of all the alloys have been evaluated. Examination of the average values of K_{1c} and the typical yield strengths of the alloys, given in section 6.6 suggests that the A.U.W.E. 224 was "tougher" and had a higher yield strength than the A.U.W.E. 224 + Ag alloy. The addition of silver to A.U.W.E. 224, therefore, has a detrimental effect on the toughness, hardness and yield strength. Overaging the A.U.W.E. 224 + Ag alloy greatly reduces its fracture toughness. In service, however, these alloys are generally used in a slightly overaged condition. This ensures that aging will not occur in a structural situation, which could cause a sudden change in yield strength. The extent of this overaging treatment should, therefore, be kept to a minimum.

The as cast structures for all the alloys were coarse (as seen in the microstructures) and the fracture toughness was greatly improved by solution treatment and aging. For example the Alcoa 354 alloy in the as cast condition had a toughness of approximately 10 $MNm^{-3/2}$, whereas in the artificially aged condition the toughness was about 20 $MNm^{-3/2}$. The impurity compounds that were present in these alloys, tended to segregate at the grain boundaries and were thought to contribute to particle rupture and hence grain boundary fracture. A reduction in the impurities would, therefore improve the fracture toughnesses of these alloys.

Critical defect sizes were determined for typical, elliptical, totally embedded and side cracks in infinite body conditions. From the results it can be seen that at an applied stress of about 0.75 x yield stress, the critical defect sizes were approximately 5 mm. It is unlikely, therefore, that the porosity in these alloys will approach the critical size, since the pores size are less than about 0.5 mm. It was realised that these critical defect sizes were determined for an infinite body and that they could be smaller in actual sections.

7.13 Suggestions for further work

1) The fracture properties of these alloys could be determined in a corrosive enviroment, rather than laboratory air. For example, stress corrosion cracking of these alloys in sea water could be investigated by obtaining values for K_{1scc} (the minimum value of K_1 for stress corrosion cracking). Enviromental effects in crack growth have been discussed by Parkins (120).

2) The mechanisms of failure in these alloys has been recognised as being inter-granular fracture. It would be advantageous, therefore, to reduce the amount of precipitate at the grain boundaries and re-distribute this precipitate throughout the grains. Electron microscopy could be used with regard to precipitate growth and to identify any dislocation pile ups if present.

3) The major effect of porosity on the fracture properties of these aluminium casting alloys occurred at levels up to about 0.05%. It would be interesting to determine the effects of very low levels of porosity on the fracture properties. This would mean, however, a more accurate method of determining porosity.

8. CONCLUSIONS

1) Spark machining produced cracks which were equivalent to fatigue cracks and could be used to simulate curved crack fronts, short cracks emanating from blunt notches and crack root radii.

2) The load point displacement rig, developed because of the problems encountered with roller sink in with these alloys, gave accurate and consistent load-load point displacement records.

3) The electrical-potential equipment proved to be satisfactory for measuring fatigue crack propagation rates and detecting crack initiation, in the cracked specimens. The sensitivity of the apparatus was improved by using a relatively high current (60 amps) and no significant specimen heating occurred at this value.

4) Ryder, Bowie and Petitt's curve fitting procedure could be applied to three point bend compliance data. The resulting equations for representing the compliance data were reversible and could be differentiated to yield accurate compliance calibration values.

5) A practical correction factor for curved crack fronts has been determined from compliance data, obtained from curved and straight crack fronts, in both three point bend and compact tension specimens.

6) The method proposed by Rice et al for determining the J integral from single load-load point displacement records gave the most accurate and consistent values of $K_{(apparent)}$ out of the five available testing methods, when compared with the values of K_{1c}.

7) Valid K_{1c}'s were obtained for these aluminium casting alloys at

thicknesses as low as: $B = \left(\frac{K_{Ic}}{\sigma_{ys}}\right)^2$

8) The critical length of a sharp crack emanating from a blunt notch was found experimentally to be approximately 0.25 to $0.35\sqrt{a\rho}$. Cracks which were longer than this critical value would not be influenced by the presence of a blunt notch.

9) The critical value of ρ for the artificially aged A.U.W.E. 224 + Ag alloy was approximately 0.04 mm. Crack root radii which were sharper than this critical value would tend to blunt down to the critical root radius during the fracture toughness test.

10) The mechanism of failure in all these alloys was recognised as being inter-granular fracture. This was also contributed to by particle rupture and particle shattering at the grain boundaries.

11) The addition of silver to the A.U.W.E. 224 alloy greatly reduced the values of fracture toughness, yield strength and hardness of this alloy, particularly for the artificially aged condition.

12) Porosity within these alloys would have to be reduced to a level of less than about 0.05% before an improvement in the fracture properties, by porosity control, could be obtained.

13) The conversion factor, M, used in the equation for COD'S to $K_{(apparent)}$ from COD, was found experimentally to be about 1.0 for the A.U.W.E. 224 type alloys and about 2.0 for the Alcoa 354.

14) For a given applied stress, the fatigue crack propagation rates for the aluminium casting alloys were less than those obtained for their wrought equivalents.

APPENDIX.

Constants used in the calculations given in section 6.3.2.

Cross head speed = 0.2 mm/minute

Poisson's ratio (v) = 0.34

Young's Modulus (E) = 6.9 for A.U.W.E. 224 + Ag

($MNm^{-2} \times 10^4$) 7.0 for A.U.W.E. 224

7.0 for A 354

Knife edge thickness (z) = 1.7 mm

M value used in the conversion = 2.1

of the COD to K.

Explanation of nomenclature.

a) The first two numbers on the top line are the block thickness in mm.

b) The remaining characters on this top line are the specimen's identification.

c) The first character on the bottom line is the method of notch manufacture (i.e. S for spark machining or M for mechanical machining).

d) The second character on the bottom line is the method of crack manufacture (i.e. F for fatigue crack or S for spark machined crack.

e) The third character on the bottom line is the materials condition (i.e. A - artificially aged, N - naturally aged, C - as cast).

f) The fourth and fifth characters on the bottom line (if present) are the aging period in hours.

Table 17. Fracture toughness data for as cast A 354 alloy (block number 1).

Nomenclature	501A MFC	502A MFC	503A MFC	504A MFC	505A MFC	506A MFC	507A MFC	508A MFC	509A MFC	5010A MFC
Specimen width (m x 10-3)	25.01	25.00	24.98	24.99	25.02	25.01	24.99	25.02	25.00	24.97
Specimen breadth (m x 10-3)	40.00	36.00	32.00	28.00	23.95	19.96	15.94	11.96	7.95	3.97
Notch depth (m x 10-3)	10.0	10.0	10.0	10.0	10.0	10.0	10.0	10.0	10.0	10.0
Notch root radius (m x 10-4)	2.0	2.0	2.0	2.0	2.0	2.0	2.0	2.0	2.0	2.0
Crack length (m x 10-3)	13.71	13.69	13.63	13.17	13.35	12.31	13.08	12.24	13.55	13.80
Maximum load (KN)	-	-	-	4.08	-	3.66	-	1.67	1.20	0.60
5 % Secant load (KN)	4.24	4.02	3.17	3.16	-	3.63	1.96	1.33	1.01	0.51
K Fatigue (MNm-3/2)	5.51	5.91	5.09	4.98	6.27	5.89	6.36	5.42	7.77	8.35
K_Q(LEFM) (MNm-3/2)	8.38	8.83	7.70	8.28	-	11.90	8.90*	7.21*	9.80*	10.30*
K_A from COD (Wells) (MNm-3/2)	-	-	-	-	-	-	-	-	-	-
K_A from COD (Dawes) (MNm-3/2)	-	-	-	-	-	-	-	-	-	-
K_A from J (MNm-3/2)	-	-	-	-	-	-	-	-	-	-
K_Q Equivalent energy (MNm-3/2)	-	-	-	-	-	-	-	-	-	-

* Invalid according to BS DD3

Table 18. Fracture toughness data for as cast A 354 alloy (block number 1).

Nomenclature	501B MFC	502B MFC	503B MFC	504B MFC	505B MFC	506B MFC	507B MFC	508B MFC	509B MFC	5010B MFC
Specimen width (m x 10-3)	25.01	24.99	24.97	24.97	24.98	24.98	24.99	24.99	24.98	24.99
Specimen breadth (m x 10-3)	39.50	36.00	31.95	27.95	23.41	19.94	15.95	11.96	7.95	3.94
Notch depth (m x 10-3)	10.0	10.0	10.0	10.0	10.0	10.0	10.0	10.0	10.0	10.0
Notch root radius (m x 10-4)	2.0	2.0	2.0	2.0	2.0	2.0	2.0	2.0	2.0	2.0
Crack length (m x 10-3)	13.63	13.71	13.50	13.50	-	15.81	13.40	-	14.34	-
Maximum load (KN)	-	-	-	-	-	-	2.06	-	1.08	-
5% Secant load (KN)	4.51	4.32	4.04	2.88	-	1.68	1.62	-	.96	-
K Fatigue (MNm-3/2)	5.49	6.13	6.26	4.98	-	8.63	6.64	-	8.12	-
K_Q(LEFM) (MNm-3/2)	8.88	9.50	9.76	7.91	-	8.04*	7.69*	-	10.39*	-
$K_A$from COD (Wells) (MNm-3/2)	-	-	-	-	-	-	-	-	-	-
$K_A$from COD (Dawes) (MNm-3/2)	-	-	-	-	-	-	-	-	-	-
$K_A$from J (MNm-3/2	-	-	-	-	-	-	-	-	-	-
K_QEquivalent energy (MNm-3/2)	-	-	-	-	-	-	-	-	-	-

* Invalid according to BS DD3

Table 19. Fracture toughness data for as cast A 354 alloy (block number 2).

Nomenclature	501A MFC	502A MFC	503A MFC	504A MFC	505A MFC	506A MFC	507A MFC	508A MFC	509A MFC	5010A MFC
Specimen width (m x 10-3)	25.00	25.00	24.99	24.99	24.83	24.98	24.99	24.98	24.98	24.98
Specimen breadth (m x 10-3)	39.90	36.00	32.00	27.95	23.96	19.98	15.95	11.99	8.00	3.92
Notch depth (m x 10-3)	10.0	10.0	10.0	10.0	10.0	10.0	10.0	10.0	10.0	10.0
Notch root radius (m x 10-4)	2.0	2.0	2.0	2.0	2.0	2.0	2.0	2.0	2.0	2.0
Crack length (m x 10-3)	13.83	13.73	13.61	14.66	13.82	14.81	13.22	13.60	12.95	12.62
Maximum load (KN)	-	-	-	-	-	2.41	3.31	2.08	1.25	-
5% Secant load (KN)	4.79	4.08	3.48	2.78	2.40	1.86	2.64	1.59	1.02	-
K Fatigue (MNm-3/2)	6.41	5.91	5.57	6.15	5.40	6.25	6.48	6.49	7.12	8.00
K_Q(LEFM) (MNm-3/2)	9.63*	8.98	8.41	9.00*	8.08*	8.61*	12.26	10.32	9.08*	-
$K_A$from COD (Wells) (MNm-3/2)	-	-	-	-	-	-	-	-	-	-
$K_A$from COD (Dawes) (MNm-3/2)	-	-	-	-	-	-	-	-	-	-
$K_A$from J (MNm-3/2)	-	-	-	-	-	-	-	-	-	-
K_QEquivalent energy (MNm-3/2)	-	-	-	-	-	-	-	-	-	-

* Invalid according to BS DD3

Table 20. Fracture toughness data for as cast A 354 alloy (block number 2).

Nomenclature	501B MFC	502B MFC	503B MFC	504B MFC	505B MFC	506B MFC	507B MFC	508B MFC	509B MFC	5010B MFC
Specimen width (m x 10-3)	25.03	24.97	24.99	24.97	24.98	24.99	24.98	24.97	24.98	24.98
Specimen breadth (m x 10-3)	39.50	39.90	32.00	27.95	23.44	19.92	15.97	11.98	7.98	3.95
Notch depth (m x 10-3)	10.0	10.0	10.0	10.0	10.0	10.0	10.0	10.0	10.0	10.0
Notch root radius (m x 10-4)	2.0	2.0	2.0	2.0	2.0	2.0	2.0	2.0	2.0	2.0
Crack length (m x 10-3)	13.63	13.02	12.77	13.76	13.35	13.76	13.73	13.37	15.38	-
Maximum load (KN)	-	-	4.37	-	-	2.37	1.41	1.60	1.06	-
5% Secant load (KN)	4.41	4.46	4.02	3.33	2.33	1.94	1.34	1.29	0.93	-
K Fatigue (MNm-3/2)	5.69	5.04	5.11	5.40	4.81	5.18	6.94	5.04	9.02	-
K_Q(LEFM) (MNm-3/2)	8.69	8.07	8.73	9.47	7.46	7.74	6.64*	8.12	11.19*	-
K_A from COD (Wells) (MNm-3/2)	-	-	-	-	-	-	-	-	-	-
K_A from COD (Dawes) (MNm-3/2)	-	-	-	-	-	-	-	-	-	-
K_A from J (MNm-3/2)	-	-	-	-	-	-	-	-	-	-
K_Q Equivalent energy (MNm-3/2)	-	-	-	-	-	-	-	-	-	-

* Invalid according to BS DD3

Table 21. Fracture toughness data for artificially aged A.U.W.E. 224 alloy (block number 1).

Nomenclature.	501A MFA24	502A MFA24	503A MFA24	504A MFA24	505A MFA24	506A MFA24	507A MFA24	508A MFA24	509A MFA24	5010A MFA24
Specimen width (m x 10-3)	24.95	24.92	24.99	25.01	25.01	25.02	25.00	25.00	24.98	24.95
Specimen breadth (m x 10-3)	12.04	35.95	32.06	28.00	23.93	19.94	15.96	11.98	7.97	11.77
Notch depth (m x 10-3)	5.00	5.00	5.00	5.00	5.00	5.00	5.00	5.00	5.00	5.00
Notch root radius (m x 10-4)	0.19	2.00	2.00	2.00	1.90	2.10	2.00	1.90	2.00	2.10
Crack length (m x 10-3)	12.46	13.01	10.96	12.00	11.49	11.33	14.40	14.40	12.50	11.50
Maximum load (KN)	12.05	23.05	22.56	17.42	14.28	13.89	9.02	7.02	5.48	10.79
Critical load (KN)	10.47	23.05	22.56	17.42	13.57	13.10	8.51	6.47	4.56	10.43
K Fatigue (MNm-3/2)	18.57	19.16	13.14	14.35	13.80	15.66	19.59	18.83	16.79	15.62
K_Q(LEFM) (MNm-3/2)	29.33	28.54	29.78	31.57	27.74	32.65	34.26	39.91	32.64	46.41
$K_A$from COD (Wells) (MNm-3/2)	55.93	57.15	63.17	59.53	54.88	48.68	45.08	39.50	41.73	36.3
$K_A$from COD (Dawes) (MNm-3/2)	61.76	49.63	57.34	57.02	47.04	47.01	65.31	53.99	45.09	58.08
$K_A$from J (MNm-3/2)	33.19	32.87	33.93	33.91	31.61	27.30	32.15	25.58	28.08	28.5
K_QEquivalent energy (MNm-3/2)	53.86	45.21	40.62	39.85	32.48	38.56	53.75	51.98	42.42	52.37

Table 22. Fracture toughness data for artificially aged A.U.W.E. 224 alloy (block number 1).

Nomenclature.	501B MFA24	502B MFA24	503B MFA24	504B MFA24	505B MFA24	506B MFA24	507B MFA24	508B MFA24	509B MFA24	5010B MFA24
Specimen width (m x 10-3)	24.95	25.00	25.01	24.99	25.02	24.98	24.99	25.00	24.95	24.95
Specimen breadth (m x 10-3)	10.83	35.98	32.02	28.01	24.00	19.96	15.95	11.98	15.96	15.98
Notch depth (m x 10-3)	5.00	5.00	5.00	5.00	5.00	5.00	5.00	5.00	5.00	5.00
Notch root radius (m x 10-4)	2.00	1.90	2.00	2.00	2.00	1.90	1.90	2.10	2.00	2.00
Crack length (m x 10-3)	9.34	11.91	11.66	11.66	11.16	12.03	12.91	13.25	12.50	12.33
Maximum load (KN)	10.40	20.99	19.47	19.23	17.66	15.70	10.91	8.08	13.34	12.00
Critical load (KN)	10.23	20.99	17.65	19.23	17.02	15.38	10.20	7.73	11.78	10.20
K Fatigue (MNm-3/2)	14.98	15.20	14.29	14.22	15.17	12.66	15.94	16.02	23.52	22.99
K_Q(LEFM) (MNm-3/2)	35.82	28.89	29.61	31.18	31.59	29.86	28.24	34.45	49.75	42.11
$K_A$from COD (Wells) (MNm-3/2)	39.65	58.13	56.29	65.57	53.04	35.72	43.19	50.83	29.13	30.11
$K_A$from COD (Dawes) (MNm-3/2)	42.99	54.80	46.40	62.70	55.34	59.97	54.24	59.17	51.73	46.64
$K_A$from J (MNm-3/2)	31.04	39.17	27.81	35.38	36.45	32.68	30.32	28.10	29.64	29.13
K_QEquivalent energy (MNm-3/2)	50.38	32.08	34.13	47.66	40.91	52.22	48.06	52.51	51.32	43.24

Table 23. Fracture toughness data for as cast KO1 alloy.

Nomenclature	A1 MFC	A2 MFC	A3 MFC	B1 MFC	B2 MFC	B3 MFC	C1 MFC			
Specimen width (m x 10-3)	22.05	21.99	21.90	21.97	22.02	21.75	21.95	0.00	0.00	0.00
Specimen breadth (m x 10-3)	12.77	12.80	13.01	12.90	13.04	13.09	13.00	0.00	0.00	0.00
Notch depth (m x 10-3)	5.05	5.15	5.05	5.05	5.15	4.90	5.00	0.00	0.00	0.00
Notch root radius (m x 10-4)	2.00	2.00	2.00	2.00	2.00	2.00	2.00	0.00	0.00	0.00
Crack length (m x 10-3)	11.30	11.35	11.21	11.24	11.66	11.80	11.44	0.00	0.00	0.00
Maximum load (KN)	2.75	2.75	2.69	2.54	2.49	2.51	2.79	0.00	0.00	0.00
Critical load (KN)	2.60	2.65	2.57	2.39	2.34	2.36	2.74	0.00	0.00	0.00
K Fatigue (MNm-3/2)	16.26	16.45	17.23	16.09	16.85	17.67	16.48	0.00	0.00	0.00
K_Q(LEFM) (MNm-3/2)	14.63	12.26	13.46	12.46	12.08	13.68	13.64	0.00	0.00	0.00
$K_A$from COD(Wells) (MNm-3/2)	18.74	19.74	17.86	18.32	17.41	16.62	21.66	0.00	0.00	0.00
$K_A$from COD(Dawes) (MNm-3/2)	19.23	20.98	17.92	19.36	19.31	17.82	22.44	0.00	0.00	0.00
$K_A$from J (MNm-3/2)	10.62	13.10	12.67	13.30	13.73	13.56	13.15	0.00	0.00	0.00
K_QEquivalent energy (MNm-3/2)	22.42	17.38	15.02	15.99	16.97	20.29	18.66	0.00	0.00	0.00

Table 24. Fracture toughness data for A.U.W.E. 224 + Ag alloy.

Nomenclature.	14A1 MFA24	14A2 MFA24	14A3 MFA24	14B1 MFN	14B2 MFN	14B3 MFN	14B4 MFN	14B5 MFA1	14B6 MFA1	14B7 MFA1
Specimen width (m x 10-3)	21.98	22.00	22.00	21.98	21.99	21.98	22.06	22.00	21.98	21.98
Specimen breadth (m x 10-3)	21.99	21.98	21.99	13.05	12.98	13.04	12.98	13.05	12.98	13.04
Notch depth (m x 10-3)	4.90	5.00	4.80	5.60	4.60	5.00	5.06	5.00	4.98	5.05
Notch root radius (m x 10-4)	2.00	2.00	2.00	2.80	1.70	1.30	1.30	1.30	1.10	2.80
Crack length (m x 10-3)	11.54	11.50	11.23	10.00	10.38	11.82	11.00	10.65	10.60	10.98
Maximum load (KN)	6.39	6.08	6.57	5.19	5.18	4.41	4.73	5.57	5.29	5.14
Critical load (KN)	5.96	5.81	6.28	4.41	4.61	4.12	4.31	5.10	5.06	4.90
K Fatigue (MNm-3/2)	14.77	14.65	13.40	13.27	14.04	17.30	13.04	15.52	15.54	16.34
K_Q(LEFM) (MNm-3/2)	20.10	19.52	19.56	17.61	20.00	22.46	19.02	17.77	17.47	22.21
$K_A$from COD (Wells) (MNm-3/2)	27.98	26.22	29.20	28.10	31.15	23.52	27.68	24.12	24.36	34.76
$K_A$from COD (Dawes) (MNm-3/2)	26.59	24.32	26.76	26.18	28.52	29.94	32.45	33.26	32.15	31.77
$K_A$from J (MNm-3/2)	18.41	13.00	19.32	20.43	21.50	26.09	25.53	22.57	24.36	25.89
K_QEquivalent energy (MNm-3/2)	22.98	19.17	22.79	23.11	26.47	29.36	27.69	32.22	29.55	30.16

Table 25. Fracture toughness data for A.U.W.E. 224 + Ag alloy.

Nomenclature.	14B8 MFA3	14B9 MFA3	14B10 MFA12	14B11 MFA12	14B12 MFA12	14B13 MFA24	14B14 MFA24	14B15 MFA24	14B16 MFA96	14B17 MFA96
Specimen width (m x 10-3)	21.98	21.98	22.00	22.01	21.90	22.05	22.05	22.01	22.00	22.00
Specimen breadth (m x 10-3)	12.99	12.98	12.98	12.97	12.98	13.02	13.04	13.06	12.99	12.99
Notch depth (m x 10-3)	5.24	4.72	4.80	4.72	4.20	5.96	5.02	5.00	4.82	4.65
Notch root radius (m x 10-4)	2.40	2.60	2.70	1.50	2.60	2.80	1.50	1.20	2.70	2.40
Crack length (m x 10-3)	11.48	11.28	11.32	11.26	11.80	12.50	12.29	11.69	10.50	10.60
Maximum load (KN)	3.84	4.94	3.73	3.86	3.68	3.57	3.45	4.77	3.53	3.49
Critical load (KN)	3.84	4.51	3.53	3.77	3.51	3.28	3.24	4.59	3.43	3.33
K Fatigue (MNm-3/2)	16.48	15.99	12.60	12.49	13.69	15.02	14.49	13.22	11.18	11.34
K_Q(LEFM) (MNm-3/2)	21.40	26.53	19.83	18.10	21.30	21.91	21.53	21.78	17.59	17.32
K_A from COD (Wells) (MNm-3/2)	22.18	18.91	15.52	16.24	21.70	27.05	18.10	21.51	15.09	13.95
K_A from COD (Dawes) (MNm-3/2)	31.23	27.74	22.26	25.21	24.63	26.53	23.34	32.26	19.16	19.38
K_A from J (MNm-3/2)	24.31	25.71	18.62	18.51	16.22	19.77	18.30	21.90	15.26	12.97
K_Q Equivalent energy (MNm-3/2)	36.64	26.44	21.13	24.76	23.72	25.04	22.60	30.69	19.44	17.48

Table 26. Fracture toughness data for A.U.W.E. 224 + Ag alloy.

Nomenclature.	14B18 MFA96	14C2 SSA24	14C3 SSA24	14C4 SSA24	14C5 SSA24	14C6 SSA24	14C7 SSA24	14C8 SSA24	14D1 SSA24	14D2 SSA24
Specimen width (m x 10-3)	22.00	21.99	22.01	21.99	22.00	21.97	22.04	21.98	22.00	22.03
Specimen breadth (m x 10-3)	12.70	9.98	9.97	9.98	9.98	9.98	9.99	9.96	7.01	6.92
Notch depth (m x 10-3)	5.28	10.15	10.40	10.50	10.00	10.10	10.10	10.05	8.30	8.30
Notch root radius (m x 10-4)	2.70	0.20	0.80	7.60	0.40	1.25	0.40	1.10	2.10	2.10
Crack length (m x 10-3)	10.58	11.95	11.80	10.50	10.90	11.60	11.20	11.55	10.00	10.00
Maximum load (KN)	3.30	2.16	2.49	4.00	2.99	2.92	2.65	2.94	2.50	2.33
Critical load (KN)	3.14	2.10	2.35	4.00	2.86	2.71	2.43	2.55	2.26	2.20
K Fatigue (MNm-3/2)	10.18	0.00	0.00	0.00	0.00	0.00	0.00	0.00	0.00	0.00
K_Q(LEFM) (MNm-3/2)	16.23	16.41	17.30	26.72	18.44	19.27	17.71	19.92	19.60	19.54
$K_A$from COD (Wells) (MNm-3/2)	23.41	23.72	24.65	39.83	25.75	27.75	24.02	26.25	25.28	25.29
$K_A$from COD (Dawes) (MNm-3/2)	30.93	21.03	23.07	29.96	24.41	26.18	20.58	22.02	22.93	21.92
$K_A$from J (MNm-3/2)	13.61	13.65	17.16	26.24	19.37	19.87	14.91	19.54	16.98	16.21
K_QEquivalent energy (MNm-3/2)	18.09	17.87	19.90	26.94	20.97	22.51	17.08	23.51	20.39	19.83

Table 27. Fracture toughness data for A.U.W.E. 224 + Ag alloy.

Nomenclature.	14D3 MFA24	14D4 MFA24	25A1 SSA24	25A2 SSA24	25A3 SSA24	25A4 M-A24	25A5 M-A24	25A6 M-A24	25A7 M-A24	25A8 M-A24
Specimen width (m x 10-3)	22.00	21.96	22.06	22.07	22.04	22.06	22.09	22.05	22.00	22.04
Specimen breadth (m x 10-3)	6.92	6.98	22.10	22.08	22.04	22.04	22.06	21.99	22.04	22.03
Notch depth (m x 10-3)	4.80	4.85	10.30	10.20	10.70	4.90	4.95	4.90	5.00	5.10
Notch root radius (m x 10-4)	2.00	2.00	7.60	7.60	7.60	2.00	2.00	2.00	4.90	5.00
Crack length (m x 10-3)	10.69	10.94	11.10	10.80	11.30	4.90	4.95	4.90	5.00	5.10
Maximum load (KN)	2.51	2.06	5.37	5.55	5.55	14.51	13.96	13.18	13.72	12.63
Critical load (KN)	2.26	1.94	4.90	5.30	5.30	14.12	13.96	13.16	13.72	12.63
K Fatigue (MNm-3/2)	17.70	18.25	0.00	0.00	0.00	0.00	0.00	0.00	0.00	0.00
K_Q(LEFM) (MNm-3/2)	21.36	15.50	17.05	17.04	18.01	21.38	21.21	19.98	20.01	19.62
$K_A$from COD (Wells) (MNm-3/2)	30.03	25.32	22.61	22.02	24.61	30.47	29.95	29.18	30.03	30.57
$K_A$from COD (Dawes) (MNm-3/2)	27.25	25.55	17.86	16.51	19.78	24.95	24.80	22.48	21.73	22.43
$K_A$from J (MNm-3/2)	17.94	14.73	16.39	16.07	14.55	16.24	15.58	11.46	21.79	13.95
K_QEquivalent energy (MNm-3/2)	20.68	19.80	16.46	16.66	18.68	22.30	21.01	18.84	21.40	19.77

Table 28. Fracture toughness data for A.U.W.E. 224 + Ag alloy.

Nomenclature	25A9 M-A24	25A10 SSA24	25A11 M-A24	25A12 M-A24	25B4 SSA24	25B5 S-A24	25B6 SSA24	25B7 SSA24	25B8 SSA24	25B9 SSA24
Specimen width (m x 10-3)	22.09	22.00	21.97	21.98	21.98	22.01	21.99	21.93	22.05	22.09
Specimen breadth (m x 10-3)	22.08	21.99	21.98	21.99	12.88	12.97	10.77	12.98	13.00	13.05
Notch depth (m x 10-3)	5.00	9.95	9.90	9.50	11.25	10.45	10.75	11.50	11.30	10.40
Notch root radius (m x 10-4)	5.00	7.60	7.50	7.60	31.00	31.00	31.00	31.00	31.00	31.00
Crack length (m x 10-3)	5.00	11.85	9.90	9.50	11.85	11.50	10.75	13.50	12.40	12.45
Maximum load (KN)	14.67	4.98	7.37	8.23	3.35	3.31	4.31	2.16	3.02	2.61
Critical load (KN)	14.12	4.20	7.37	8.04	3.33	2.94	4.51	1.89	2.82	2.35
K Fatigue (MNm-3/2)	0.00	0.00	0.00	0.00	0.00	0.00	0.00	0.00	0.00	0.00
K_Q(LEFM) (MNm-3/2)	21.57	16.09	20.62	21.81	20.12	17.45	24.88	16.96	19.15	16.50
$K_A$from COD (Wells) (MNm-3/2)	34.81	21.36	34.04	34.53	33.15	25.60	43.16	24.13	28.16	22.31
$K_A$from COD (Dawes) (MNm-3/2)	28.59	17.63	22.70	23.16	25.94	19.70	33.49	16.76	22.42	18.02
$K_A$from J (MNm-3/2)	13.32	14.23	16.98	19.03	25.41	17.29	29.95	16.56	21.92	15.26
K_QEquivalent energy (MNm-3/2)	21.79	15.47	22.02	22.06	21.76	17.80	25.11	17.33	20.07	16.12

Table 29. Fracture toughness data for A.U.W.E. 224 + Ag alloy.

Nomenclature.	25B10 SSA24	25B11 SSA24	25B12 SSA24	25C1 SFA6	25C2 SFA6	25C3 SFA6	25C4 SFA12	25C5 SFA12	25C6 SFA12	25C7 MFA24
Specimen width (m x 10-3)	22.06	21.99	22.01	22.01	22.03	21.99	22.01	21.99	22.01	21.04
Specimen breadth (m x 10-3)	13.03	13.01	13.05	10.00	10.02	9.98	9.97	9.98	9.99	9.99
Notch depth (m x 10-3)	10.75	11.40	11.40	4.60	4.65	4.60	4.90	4.80	4.90	5.00
Notch root radius (m x 10-4)	31.00	31.00	31.00	2.00	2.00	2.00	2.00	2.00	2.00	2.00
Crack length (m x 10-3)	12.55	13.15	12.80	10.30	9.82	9.86	11.30	11.04	10.90	9.90
Maximum load (KN)	2.43	2.22	2.47	4.45	4.47	4.06	3.49	3.73	3.77	3.33
Critical load (KN)	2.29	2.16	2.26	3.80	3.88	3.86	3.14	3.59	3.39	3.10
K Fatigue (MNm-3/2)	0.00	0.00	0.00	23.17	21.64	20.69	22.33	20.06	19.61	22.57
K_Q(LEFM) (MNm-3/2)	15.88	15.64	15.24	19.94	20.01	18.24	20.16	20.93	23.49	19.90
$K_A$from COD (Wells) (MNm-3/2)	24.65	25.29	25.68	33.27	31.07	31.30	25.07	28.53	30.34	28.54
$K_A$from COD (Dawes) (MNm-3/2)	18.93	20.56	20.29	31.35	28.31	32.24	27.18	31.40	26.36	24.61
$K_A$from J (MNm-3/2)	16.37	18.18	17.30	19.06	20.95	18.65	19.01	22.48	18.63	17.77
K_QEquivalent energy (MNm-3/2)	14.51	15.91	17.34	27.36	23.46	25.10	24.12	27.78	23.69	21.37

Table 30. Fracture toughness data for A.U.W.E. 224 + Ag alloy.

Nomenclature.	25C8 MFA24	25C9 MFA24	25C10 MFA48	25C11 MFA96	25C12 SSA24	25C13 SSA24	25C14 SSA24	25C15 SFA48	25C16 SFA48	25C17 SFA96
Specimen width (m x 10-3)	22.01	22.00	21.97	22.00	22.03	22.00	21.99	22.02	22.00	22.02
Specimen breadth (m x 10-3)	9.97	9.97	9.90	9.92	9.98	9.99	9.99	8.90	9.32	9.99
Notch depth (m x 10-3)	5.00	5.00	4.75	5.00	10.50	10.45	9.70	4.90	4.90	5.10
Notch root radius (m x 10-4)	2.00	2.00	2.00	2.00	2.50	2.60	2.50	2.00	2.00	2.00
Crack length (m x 10-3)	10.37	9.70	11.68	10.82	11.50	11.80	11.70	10.50	10.90	11.26
Maximum load (KN)	3.06	3.73	2.33	3.00	2.26	2.47	2.22	3.14	3.02	2.88
Critical load (KN)	2.88	3.38	2.21	2.64	2.11	2.36	2.00	2.79	2.86	2.79
K Fatigue (MNm-3/2)	22.14	20.26	19.02	15.32	0.00	0.00	0.00	19.27	16.49	19.15
K_Q(LEFM) (MNm-3/2)	18.73	19.96	17.33	18.34	16.63	18.66	15.92	19.50	17.25	19.23
$K_A$from COD (Wells) (MNm-3/2)	26.23	24.49	20.73	23.11	20.77	24.64	20.55	25.94	27.22	25.49
$K_A$from COD (Dawes) (MNm-3/2)	22.76	24.36	21.56	20.61	17.93	22.12	18.59	25.48	27.80	24.33
$K_A$from J (MNm-3/2)	14.84	16.07	13.26	15.45	14.02	16.63	11.56	18.27	18.81	18.37
K_QEquivalent energy (MNm-3/2)	19.00	20.34	18.79	17.64	16.42	20.26	16.14	22.17	22.82	22.45

Table 31. Fracture toughness data for A.U.W.E 224 + Ag alloy.

Nomenclature.	25C18 SFA96	25C19 S-A24	25D1 SFA24	25D2 MFA24	25D3 MFA24	25D4 MFA24	501A SFA24	502A SFA24	503A SFA24	504A MFA24
Specimen width (m x 10-3)	22.00	21.97	21.99	22.00	22.01	22.02	44.20	44.14	44.15	44.14
Specimen breadth (m x 10-3)	9.98	9.98	7.00	6.98	6.98	7.01	44.16	44.16	44.11	44.17
Notch depth (m x 10-3)	5.00	11.75	4.70	4.70	4.75	4.95	17.50	19.00	21.00	20.00
Notch root radius (m x 10-4)	2.00	2.60	2.00	2.00	2.00	2.00	2.00	5.00	5.00	2.00
Crack length (m x 10-3)	11.09	11.75	10.75	10.75	10.33	10.10	26.08	23.61	26.93	24.96
Maximum load (KN)	3.04	3.04	2.16	1.96	2.20	1.96	10.90	16.24	12.40	13.73
Critical load (KN)	2.94	3.00	1.84	1.95	1.96	1.86	10.43	15.69	11.34	12.94
K Fatigue (MNm-3/2)	19.48	0.00	18.55	18.12	16.57	15.98	15.56	10.23	13.45	10.82
K_Q(LEFM) (MNm-3/2)	19.99	23.99	16.87	18.79	18.06	15.89	15.93	20.34	18.66	17.60
$K_A$from COD (Wells) (MNm-3/2)	22.11	34.95	21.92	22.75	24.93	22.45	23.81	23.06	20.84	22.85
K_A from COD (Dawes) (MNm-3/2)	18.03	27.36	24.73	20.97	21.85	20.96	21.21	21.83	23.16	22.80
$K_A$from J (MNm-3/2)	16.40	22.06	16.87	20.58	14.16	15.28	17.08	17.69	18.25	16.96
K_QEquivalent energy (MNm-3/2)	21.58	24.01	20.38	18.85	18.41	17.94	16.68	20.58	20.32	19.19

Table 32. Fracture toughness data for A.U.W.E. 224 + Ag alloy.

Nomenclature	505A MFA24	506A MFA24	501B S-A24	502B S-A24	503B S-A24	504B M-A24	505B M-A24	506B M-A24	507B M-A24	508B M-A24
Specimen width (m x 10-3)	44.12	44.10	22.10	22.09	22.08	22.05	22.04	22.02	22.10	22.03
Specimen breadth (m x 10-3)	44.09	44.10	22.09	22.08	22.07	22.03	22.08	22.02	22.10	22.05
Notch depth (m x 10-3)	20.00	20.00	9.20	11.00	12.35	10.05	10.00	9.80	10.15	10.00
Notch root radius (m x 10-4)	2.00	2.00	7.20	7.20	7.20	2.00	2.00	2.10	7.40	7.40
Crack length (m x 10-3)	26.82	25.67	9.20	11.00	12.35	10.05	10.00	9.80	10.15	10.00
Maximum load (KN)	12.40	11.53	7.28	5.84	4.59	8.16	7.81	8.87	6.63	8.08
Critical load (KN)	11.53	11.30	6.71	5.81	4.47	8.08	7.22	8.59	6.63	7.77
K Fatigue (MNm-3/2)	13.03	12.11	0.00	0.00	0.00	0.00	0.00	0.00	0.00	0.00
K_Q(LEFM) (MNm-3/2)	19.31	15.74	16.87	17.64	17.20	22.10	19.25	23.46	18.42	21.40
$K_A$from COD (Wells) (MNm-3/2)	22.00	21.16	28.90	27.86	27.74	34.01	28.13	32.21	26.76	29.54
$K_A$from COD (Dawes) (MNm-3/2)	20.86	22.64	20.19	23.81	22.40	31.82	24.72	27.48	23.51	26.21
$K_A$from J (MNm-3/2)	17.44	16.67	14.36	15.71	16.78	17.95	17.67	18.02	15.70	16.72
K_QEquivalent energy (MNm-3/2)	20.12	18.42	17.01	20.29	18.89	24.23	21.35	23.91	19.94	22.49

Table 33. Fracture toughness data for A.U.W.E. 224 + Ag alloy.

Nomenclature.	509B M-A24	5010B M-A24	5011B M-A24	5012B M-A24						
Specimen width (m x 10-3)	22.06	22.04	22.08	22.09	0.00	0.00	0.00	0.00	0.00	0.00
Specimen breadth (m x 10-3)	22.09	22.01	22.08	22.09	0.00	0.00	0.00	0.00	0.00	0.00
Notch depth (m x 10-3)	10.00	10.15	10.05	10.20	0.00	0.00	0.00	0.00	0.00	0.00
Notch root radius (m x 10-4)	7.40	16.00	16.00	16.00	0.00	0.00	0.00	0.00	0.00	0.00
Crack length (m x 10-3)	10.00	10.15	10.05	10.20	0.00	0.00	0.00	0.00	0.00	0.00
Maximum load (KN)	6.55	6.86	9.22	7.22	0.00	0.00	0.00	0.00	0.00	0.00
Critical load (KN)	6.43	6.75	8.90	7.06	0.00	0.00	0.00	0.00	0.00	0.00
K Fatigue (MNm-3/2)	0.00	0.00	0.00	0.00	0.00	0.00	0.00	0.00	0.00	0.00
K_Q (LEFM) (MNm-3/2)	18.01	19.39	25.18	20.26	0.00	0.00	0.00	0.00	0.00	0.00
K_A from COD (Wells) (MNm-3/2)	24.25	27.42	33.32	28.38	0.00	0.00	0.00	0.00	0.00	0.00
K_A from COD (Dawes) (MNm-3/2)	20.75	22.73	28.04	23.44	0.00	0.00	0.00	0.00	0.00	0.00
K_A from J (MNm-3/2)	13.41	16.62	18.27	16.30	0.00	0.00	0.00	0.00	0.00	0.00
K_Q Equivalent energy (MNm-3/2)	19.02	19.44	25.50	21.21	0.00	0.00	0.00	0.00	0.00	0.00

Table 34. Fracture toughness data for A.U.W.E. 224 alloy.

Nomenclature.	14A1 MFA24	14A2 MFA24	14A3 MFA24	14B1 M-A24	14B2 M-A24	14B3 M-A24	14B4 MSA24	14B5 MSA24	14B6 MSA24	14B7 MSA24
Specimen width (m x 10-3)	21.96	21.94	21.97	22.01	22.01	22.00	22.00	22.01	22.00	21.98
Specimen breadth (m x 10-3)	21.97	21.97	21.99	13.00	12.98	12.99	13.02	13.01	12.92	13.00
Notch depth (m x 10-3)	4.90	4.95	4.95	10.10	10.10	10.10	9.96	10.05	9.95	9.97
Notch root radius (m x 10-4)	2.10	2.00	2.00	30.50	30.50	30.50	30.50	30.50	30.50	31.00
Crack length (m x 10-3)	13.14	11.95	11.85	10.10	10.10	10.40	10.50	10.70	10.95	11.17
Maximum load (KN)	6.65	7.45	7.94	10.04	8.83	8.43	7.73	6.98	5.57	5.57
Critical load (KN)	6.51	7.14	7.84	10.04	8.83	8.43	7.57	6.83	5.06	5.45
K Fatigue (MNm-3/2)	19.20	15.82	15.52	0.00	0.00	0.00	0.00	0.00	0.00	0.00
K_Q(LEFM) (MNm-3/2)	24.84	21.39	21.57	27.17	24.74	23.61	24.66	27.26	27.60	26.63
$K_A$from COD (Wells) (MNm-3/2)	43.58	38.32	43.74	104.48	97.58	104.40	79.01	63.03	42.75	48.79
$K_A$from COD (Dawes) (MNm-3/2)	40.88	30.60	42.15	91.43	86.69	91.27	65.07	50.03	33.19	40.19
$K_A$from J (MNm-3/2)	33.04	23.97	31.89	71.24	63.10	67.27	49.13	41.43	28.16	32.66
K_QEquivalent energy (MNm-3/2)	35.47	30.86	28.37	65.67	60.80	61.20	47.94	40.89	30.03	33.15

Table 35. Fracture toughness data for A.U.W.E. 224 alloy.

Nomenclature	14B8 MSA24	14B9 MSA24	14B10 MSA24	14C1 SSA24	14C2 M-A24	14C3 SSA24	14C4 MFA24	14C5 MFA24	14C6 MFA24	14C7 MSA24
Specimen width (m x 10-3)	21.98	22.00	22.00	22.00	22.00	22.00	21.99	21.99	21.98	21.99
Specimen breadth (m x 10-3)	13.01	13.00	12.99	9.98	10.01	9.99	9.98	9.99	10.00	9.97
Notch depth (m x 10-3)	9.20	10.00	10.00	4.90	4.90	4.70	5.10	5.00	5.10	4.95
Notch root radius (m x 10-4)	30.40	30.40	30.50	32.80	33.00	32.50	2.00	2.00	2.00	32.50
Crack length (m x 10-3)	11.03	11.35	11.40	5.80	4.90	5.41	12.90	12.39	12.46	5.75
Maximum load (KN)	5.00	5.49	5.18	8.32	13.72	9.57	3.61	3.35	3.51	9.02
Critical load (KN)	4.88	4.90	4.90	7.97	13.72	9.38	3.37	3.25	3.18	9.02
K Fatigue (MNm-3/2)	0.00	0.00	0.00	0.00	0.00	0.00	18.28	17.67	17.88	0.00
K_Q(LEFM) (MNm-3/2)	25.95	27.13	27.35	27.12	26.88	23.64	23.30	25.53	23.63	26.71
$K_A$from COD (Wells) (MNm-3/2)	42.78	43.92	43.26	44.42	101.69	68.79	48.37	42.61	39.69	62.27
$K_A$from COD (Dawes) (MNm-3/2)	34.30	33.02	34.74	35.50	87.66	57.43	45.08	37.97	34.86	51.31
$K_A$from J (MNm-3/2)	25.62	28.25	27.48	26.53	39.04	30.09	34.04	30.18	26.75	26.91
K_QEquivalent energy (MNm-3/2)	28.64	30.18	28.50	30.65	51.93	38.84	39.02	30.96	31.14	37.26

Table 36. Fracture toughness data for A.U.W.E. 224 alloy.

Nomenclature.	14C8 MSA24	14C9 MSA24	14D1 MFA24	14D2 MFA24	14D3 MFA24	14D4 MFA24	25A4 MFA24	25A5 MFA24	25A6 MFA24	25A7* SSA24
Specimen width (m x 10-3)	21.99	22.00	22.00	21.99	21.98	21.99	21.96	22.00	22.01	22.00
Specimen breadth (m x 10-3)	10.01	9.98	6.98	6.99	6.98	6.99	21.99	22.00	22.00	22.01
Notch depth (m x 10-3)	5.00	5.00	5.10	5.21	5.00	5.00	5.00	5.00	5.00	7.57
Notch root radius (m x 10-4)	32.00	32.30	2.00	2.10	2.10	2.10	2.00	2.00	2.00	5.00
Crack length (m x 10-3)	6.00	6.20	10.69	12.49	12.69	12.35	12.27	10.15	11.81	8.08
Maximum load (KN)	8.19	7.84	3.13	2.31	2.37	2.43	7.84	10.47	7.92	12.79
Critical load (KN)	7.81	6.96	2.90	1.98	1.98	1.95	7.49	9.61	7.53	12.49
K Fatigue (MNm-3/2)	0.00	0.00	14.61	19.21	19.94	18.78	21.45	15.58	19.83	0.00
K_Q(LEFM) (MNm-3/2)	26.33	23.49	25.00	20.37	22.35	21.05	23.84	25.25	22.98	18.42
$K_A$from COD (Wells) (MNm-3/2)	45.97	41.21	43.50	36.85	37.96	33.80	43.02	37.71	39.17	56.63
$K_A$from COD (Dawes) (MNm-3/2)	39.05	36.77	53.08	33.18	33.43	30.44	39.40	34.90	36.34	46.74
$K_A$from J (MNm-3/2)	25.03	24.34	27.44	24.47	24.73	22.80	30.39	26.70	27.20	29.82
K_QEquivalent energy (MNm-3/2)	31.19	27.79	31.86	27.99	28.88	26.20	35.11	27.11	26.74	34.46

* Curved crack front specimens

Table 37. Fracture toughness data for A.U.W.E. 224 alloy.

Nomenclature.	25A8* SSA24	25A9* SSA24	25A10* SSA24	25A11* SSA24	25A12* SSA24	25B2 SSA24	25B3 SSA24	25B4 MFA24	25B5 MFA24	25B6 MFA24
Specimen width (m x 10-3)	21.99	21.99	22.00	21.99	22.01	22.02	22.00	22.02	21.99	22.00
Specimen breadth (m x 10-3)	21.99	22.01	21.99	22.00	21.96	12.99	12.99	12.99	12.99	12.99
Notch depth (m x 10-3)	8.75	9.88	10.33	9.70	9.02	9.85	9.85	5.10	5.05	5.00
Notch root radius (m x 10-4)	5.00	5.00	7.50	5.00	5.00	32.50	32.50	2.00	1.90	2.00
Crack length (m x 10-3)	9.25	10.27	10.70	10.26	9.50	10.85	10.75	12.68	12.28	12.90
Maximum load (KN)	12.45	10.59	9.92	9.41	10.67	6.08	4.86	4.12	4.20	4.12
Critical load (KN)	11.92	10.48	9.39	9.17	10.47	6.08	4.61	3.84	3.88	3.78
K Fatigue (MNm-3/2)	0.00	0.00	0.00	0.00	0.00	0.00	0.00	22.85	21.48	23.76
K_Q(LEFM) (MNm-3/2)	25.73	24.74	26.39	16.67	24.53	19.63	21.78	16.93	22.49	22.87
$K_A$from COD (Wells) (MNm-3/2)	37.38	51.51	45.16	46.32	42.34	69.84	41.27	48.18	37.70	35.96
$K_A$from COD (Dawes) (MNm-3/2)	38.01	45.12	35.38	44.77	22.16	79.33	31.45	45.02	34.29	35.47
$K_A$from J (MNm-3/2)	25.13	31.31	29.76	30.64	27.46	42.97	23.62	31.91	27.21	27.70
K_QEquivalent energy (MNm-3/2)	31.36	34.78	29.47	31.81	28.20	42.95	27.31	34.21	29.23	32.65

* Curved crack front specimens

Table 38. Fracture toughness data for A.U.W.E. 224 alloy.

Nomenclature.	25B7 SSA24	25B8 SSA24	25B9 SSA24	25B10 SSA24	25B11 SSA24	25B12 SSA24	25C4 SSA24	25C5 SSA24	25C6 SSA24	25C7 MFA24
Specimen width (m x 10-3)	22.01	21.97	21.96	22.01	21.98	21.99	21.99	21.98	21.99	21.99
Specimen breadth (m x 10-3)	13.01	13.01	13.01	13.03	13.00	13.01	9.99	9.98	9.98	9.98
Notch depth (m x 10-3)	10.30	10.30	10.30	10.00	10.05	9.90	9.45	9.30	9.60	5.00
Notch root radius (m x 10-4)	3.00	3.00	32.50	32.50	32.50	32.50	5.00	5.00	5.00	2.00
Crack length (m x 10-3)	11.95	12.30	12.15	11.70	11.65	11.90	9.95	9.85	10.00	12.44
Maximum load (KN)	4.45	4.22	4.10	4.17	4.12	3.73	4.41	4.55	4.75	3.43
Critical load (KN)	4.39	4.02	4.08	3.90	3.71	3.57	4.41	4.50	4.70	3.24
K Fatigue (MNm-3/2)	0.00	0.00	0.00	0.00	0.00	0.00	0.00	0.00	0.00	18.75
K_Q(LEFM) (MNm-3/2)	24.36	23.38	23.64	22.30	20.55	21.13	20.42	19.82	21.01	24.67
$K_A$from COD (Wells) (MNm-3/2)	46.47	43.66	42.16	38.45	39.68	37.01	52.84	51.94	56.23	42.24
$K_A$from COD (Dawes) (MNm-3/2)	35.91	35.44	34.79	30.73	33.75	29.45	48.26	44.37	48.50	48.17
$K_A$from J (MNm-3/2)	31.62	29.17	29.15	23.52	27.07	23.10	31.30	32.33	34.02	28.87
K_QEquivalent energy (MNm-3/2)	30.08	30.88	29.04	25.94	25.86	26.79	35.65	35.88	37.74	33.11

Table 39. Fracture toughness data for A.U.W.E. 224 alloy.

Nomenclature.	25C8 MFA24	25C9 MFA24	25C10 MFA24	25C11 MFN	25C12 MFN	25C13 MFN	25C14 MFN	25D1 MFA24	25D2 MFA24	25D3 MFA24
Specimen width (m x 10-3)	22.00	21.98	21.99	21.98	21.98	21.98	21.99	22.00	21.98	21.96
Specimen breadth (m x 10-3)	10.00	10.01	9.95	9.97	9.97	9.97	9.97	7.03	6.98	7.01
Notch depth (m x 10-3)	5.00	5.00	5.04	5.03	5.10	5.02	5.00	4.98	5.10	4.80
Notch root radius (m x 10-4)	2.10	2.10	2.30	2.00	2.00	2.00	2.10	2.10	1.90	2.00
Crack length (m x 10-3)	12.30	12.52	13.25	12,02	12.28	11.67	12.30	12.10	11.55	12.55
Maximum load (KN)	3.16	3.00	2.48	2.92	2.71	3.33	2.84	2.04	2.23	1.79
Critical load (KN)	2.97	2.65	2.29	2.73	2.55	2.92	2.73	1.73	1.91	1.70
K Fatigue (MNm-3/2)	19.13	19.85	22.56	17.56	19.16	16.62	19.21	26.35	24.42	19.42
K_Q(LEFM) (MNm-3/2)	21.23	21.85	19.98	20.41	22.22	18.37	19.47	19.86	17.28	18.11
$K_A$from COD (Wells) (MNm-3/2)	38.09	34.12	36.93	31.77	30.90	35.09	36.16	29.62	36.24	36.32
$K_A$from COD (Dawes) (MNm-3/2)	47.40	29.21	31.94	27.69	29.45	31.70	34.05	24.60	30.02	37.86
$K_A$from J (MNm-3/2)	25.71	22.62	24.45	22.23	20.30	22.81	23.94	19.59	21.53	24.61
K_QEquivalent energy (MNm-3/2)	29.09	26.05	25.61	26.26	24.65	27.15	28.06	21.94	22.97	27.01

Table 40. Fracture toughness data for A.U.W.E. 224 alloy.

Nomenclature.	25D4 MFA24	501A SFA24	502A SFA24	503A SFA24	504A MFA24	505A MFA24	506A MFA24	501B* SSA24	502B* SSA24	504B M-A24
Specimen width (m x 10-3)	21.98	43.95	43.96	44.00	43.95	43.92	43.95	22.02	22.02	22.01
Specimen breadth (m x 10-3)	7.00	43.98	43.99	43.97	43.91	43.98	43.97	22.02	22.02	22.02
Notch depth (m x 10-3)	4.75	19.45	20.80	22.00	20.00	20.00	20.00	12.15	11.80	9.95
Notch root radius (m x 10-4)	1.90	5.00	5.00	5.00	1.90	1.90	1.90	5.00	5.00	1.90
Crack length (m x 10-3)	11.50	21.45	20.35	20.97	25.93	24.23	22.61	11.96	11.65	9.95
Maximum load (KN)	2.16	21.97	19.30	18.99	13.33	15.69	18.83	5.61	6.41	9.96
Critical load (KN)	1.90	19.14	17.57	16.08	13.06	15.46	17.80	5.32	6.00	9.96
K Fatigue (MNm-3/2)	16.44	0.00	0.00	0.00	15.43	13.42	11.82	0.00	0.00	0.00
K_Q (LEFM) (MNm-3/2)	14.89	21.21	18.01	17.19	18.28	16.96	16.37	19.43	19.33	22.19
K_A from COD (Wells) (MNm-3/2)	41.30	29.96	35.62	28.09	34.55	42.47	44.86	31.37	33.16	52.42
K_A from COD (Dawes) (MNm-3/2)	35.80	26.11	25.86	22.77	45.68	38.03	39.28	25.36	28.87	47.29
K_A from J (MNm-3/2)	23.89	18.59	22.12	19.71	24.00	27.23	26.04	20.50	22.97	30.86
K_Q Equivalent energy (MNm-3/2)	24.60	22.01	17.62	16.97	21.07	22.32	23.77	20.43	23.00	31.18

Table 41. Fracture toughness data for A.U.W.E. 224 alloy.

Nomenclature.	505B M-A24	506B M-A24	507B M-A24	508B M-A24	509B M-A24	5010B M-A24	5011B M-A24	5012B M-A24		
Specimen width (m x 10-3)	22.02	22.00	22.01	22.02	22.02	22.02	22.02	22.02	0.00	0.00
Specimen breadth (m x 10-3)	22.02	22.01	22.00	22.00	22.01	21.99	22.02	22.01	0.00	0.00
Notch depth (m x 10-3)	10.05	10.10	10.15	10.15	10.15	10.10	10.10	10.10	0.00	0.00
Notch root radius (m x 10-4)	2.10	1.90	7.50	7.50	7.50	16.00	16.00	16.00	0.00	0.00
Crack length (m x 10-3)	10.05	10.10	10.15	10.15	10.15	10.10	10.10	10.10	0.00	0.00
Maximum load (KN)	10.28	8.87	9.10	8.87	9.41	9.18	10.43	9.89	0.00	0.00
Critical load (KN)	10.28	8.87	9.90	8.87	9.41	9.18	10.43	9.89	0.00	0.00
K Fatigue (MNm-3/2)	0.00	0.00	0.00	0.00	0.00	0.00	0.00	0.00	0.00	0.00
K_Q(LEFM) (MNm-3/2)	24.49	23.14	23.98	23.73	23.72	20.66	23.54	23.55	0.00	0.00
$K_A$from COD (Wells) (MNm-3/2)	51.99	43.03	40.20	43.40	46.06	51.77	51.77	51.77	0.00	0.00
$K_A$from COD (Dawes) (MNm-3/2)	44.91	38.20	29.97	39.45	41.60	46.66	42.03	43.03	0.00	0.00
$K_A$from J (MNm-3/2)	31.03	22.58	17.06	24.66	27.57	27.88	30.30	28.98	0.00	0.00
K_QEquivalent energy (MNm-3/2)	33.43	28.69	28.41	29.17	30.43	30.77	32.71	31.95	0.00	0.00

Table 42. Fracture toughness data for Alcoa 354 alloy.

Nomenclature.	14A1 MFA8	14A2 MFA8	14A3 MFA8	14A4 SFA8	14B1 M-A8	14B2 M-A8	14B3 M-A8	14B4 M-A8	14B5 MFA8	14B7 MFA8
Specimen width (m x 10-3)	21.99	21.99	21.97	21.99	21.94	21.99	21.91	21.93	21.96	21.94
Specimen breadth (m x 10-3)	21.99	21.98	21.97	21.99	12.94	12.97	12.94	12.97	12.98	12.96
Notch depth (m x 10-3)	5.00	4.96	5.00	5.50	9.90	9.90	9.85	9.85	10.00	10.00
Notch root radius (m x 10-4)	1.80	1.80	1.80	4.00	32.00	31.90	32.00	32.00	31.80	31.80
Crack length (m x 10-3)	10.82	11.06	11.39	12.05	9.90	9.90	9.85	9.85	11.73	11.77
Maximum load (KN)	5.53	5.56	6.00	4.75	13.34	13.18	12.32	11.29	6.28	6.90
Critical load (KN)	5.34	5.38	5.69	4.71	13.34	13.18	12.32	11.29	5.41	6.75
K Fatigue (MNm-3/2)	12.65	16.36	14.47	19.03	0.00	0.00	0.00	0.00	14.77	17.42
K_Q(LEFM) (MNm-3/2)	15.19	16.00	16.51	17.84	52.31	47.34	48.01	42.62	34.42	34.77
$K_A$from COD (Wells) (MNm-3/2)	22.61	21.35	20.59	21.89	58.80	48.35	44.60	44.96	26.36	24.71
$K_A$from COD (Dawes) (MNm-3/2)	21.58	21.95	24.25	20.90	69.20	68.23	63.30	58.79	38.59	44.69
$K_A$from J (MNm-3/2)	19.88	24.21	25.09	18.84	52.87	50.58	32.54	30.85	25.68	28.09
K_cEquivalent energy (MNm-3/2)	17.24	17.80	19.75	17.58	70.66	65.03	61.80	58.63	42.00	44.52

Table 43. Fracture toughness data for Alcoa 354 alloy.

Nomenclature	14B8 MFA8	14B9 MFA8	14B10 SFA8	14C1 SFA8	14C3 SFA8	14C4 MFA8	14C5 MFA8	14C6 MFA8	14C7 MFA8	14C8 MFA8
Specimen width (m x 10-3)	21.93	22.00	21.93	21.95	21.95	21.91	21.98	21.92	22.03	22.00
Specimen breadth (m x 10-3)	12.94	12.92	12.95	10.00	10.00	9.93	9.95	9.92	9.46	9.96
Notch depth (m x 10-3)	9.95	9.95	9.90	5.45	5.50	4.94	4.92	4.94	5.00	4.95
Notch root radius (m x 10-4)	32.00	32.00	32.00	4.20	4.00	1.80	1.80	1.80	63.50	63.50
Crack length (m x 10-3)	11.84	13.58	12.72	12.36	12.37	8.70	10.66	11.15	9.24	9.66
Maximum load (KN)	6.44	5.34	5.34	2.13	2.20	3.37	2.82	2.98	4.07	3.68
Critical load (KN)	6.16	5.08	5.34	2.02	1.88	3.17	2.31	2.79	3.92	3.33
K Fatigue (MNm-3/2)	17.63	21.72	18.88	15.88	15.91	10.60	12.28	13.29	12.99	13.06
K_Q(LEFM) (MNm-3/2)	35.89	40.09	38.63	18.81	17.78	14.65	15.29	19.83	20.94	19.96
$K_A$from COD (Wells) (MNm-3/2)	24.26	23.18	24.62	24.19	19.33	20.77	16.97	23.27	27.46	25.12
$K_A$from COD (Dawes) (MNm-3/2)	41.67	45.07	40.71	18.42	18.03	29.66	20.18	22.74	28.25	22.14
$K_A$from J (MNm-3/2)	24.96	26.09	20.96	16.41	16.50	16.89	14.40	21.26	23.39	24.37
K_QEquivalent energy (MNm-3/2)	41.11	46.52	44.50	19.59	16.95	18.14	17.14	21.04	24.67	23.41

Table 44. Fracture toughness data for Alcoa 354 alloy.

Nomenclature.	14D1 SFA8	14D2 SFA8	25A1 S-A8	25A2 S-A8	25A3 S-A8	25A4 M-A8	25A5 M-A8	25A6 M-A8	25A7 M-A8	25A8 M-A8
Specimen width (m x 10-3)	21.96	21.98	21.98	21.99	22.03	21.97	21.97	22.01	22.01	21.99
Specimen breadth (m x 10-3)	7.02	7.04	21.98	22.01	22.02	21.99	22.03	22.01	22.02	22.02
Notch depth (m x 10-3)	5.50	5.55	6.00	6.00	5.95	4.98	5.02	5.06	4.90	5.03
Notch root radius (m x 10-4)	4.20	4.40	4.00	4.00	3.60	2.10	1.90	2.00	4.80	5.20
Crack length (m x 10-3)	11.23	11.27	6.00	6.00	5.95	4.98	5.02	5.06	4.90	5.03
Maximum load (KN)	1.81	1.88	11.53	11.29	10.82	13.80	13.33	15.14	15.14	13.53
Critical load (KN)	1.66	1.68	11.53	11.29	10.82	13.80	13.33	15.14	15.14	13.53
K Fatigue (MNm-3/2)	16.83	16.84	0.00	0.00	0.00	0.00	0.00	0.00	0.00	0.00
K_Q(LEFM) (MNm-3/2)	17.04	18.32	19.37	18.10	17.02	19.12	18.53	21.31	20.02	19.99
$K_A$from COD (Wells) (MNm-3/2)	23.45	21.30	30.92	30.93	30.60	34.72	34.21	34.67	34.80	34.49
$K_A$from COD (Dawes) (MNm-3/2)	20.78	19.61	26.32	26.83	28.00	56.07	31.08	31.06	29.97	23.58
$K_A$from J (MNm-3/2)	16.09	16.79	19.71	22.72	16.33	24.04	24.74	19.80	21.64	24.09
K_QEquivalent energy (MNm-3/2)	18.70	18.71	21.23	19.89	20.48	20.91	22.07	24.42	22.23	20.96

Table 45. Fracture toughness data for Alcoa 354 alloy.

Nomenclature.	25A9 M-A8	25A10 M-A8	25A11 M-A8	25A12 M-A8	25B1 SFA8	25B2 SFA8	25B4 MFA8	25B5 MFA8	25B6 MFA8	25B7 MFA8
Specimen width (m x 10-3)	21.96	21.91	21.89	21.95	21.99	21.94	21.95	21.95	21.86	21.95
Specimen breadth (m x 10-3)	21.97	21.95	21.84	21.98	13.02	12.99	13.00	13.01	12.99	12.96
Notch depth (m x 10-3)	5.02	5.05	5.10	5.16	5.60	5.60	4.95	4.98	4.95	5.10
Notch root radius (m x 10-4)	5.20	7.60	8.00	8.00	4.00	4.00	2.00	2.00	1.90	8.00
Crack length (m x 10-3)	5.02	5.06	5.10	5.16	11.78	12.14	9.57	9.28	9.79	9.52
Maximum load (KN)	15.77	13.57	13.96	14.51	2.92	3.14	4.08	3.96	4.26	3.92
Critical load (KN)	15.77	13.57	13.96	14.51	2.84	3.00	3.41	3.43	3.77	3.41
K Fatigue (MNm-3/2)	0.00	0.00	0.00	0.00	11.08	11.80	11.75	11.30	12.20	11.71
K_Q(LEFM) (MNm-3/2)	22.37	19.98	21.05	21.84	16.52	17.87	15.65	14.88	15.96	14.83
$K_A$from COD (Wells) (MNm-3/2)	36.44	34.95	33.80	33.54	23.49	20.79	21.02	19.67	20.22	20.18
$K_A$from COD (Dawes) (MNm-3/2)	30.80	29.76	27.69	25.75	22.68	22.38	18.14	17.64	20.99	18.78
$K_A$from J (MNm-3/2)	25.54	25.70	20.82	28.40	17.57	17.97	14.78	14.23	15.75	16.56
K_QEquivalent energy (MNm-3/2)	22.56	21.84	23.11	22.96	19.67	22.12	16.01	15.19	21.15	18.91

Table 46. Fracture toughness data for Alcoa 354 alloy.

Nomenclature.	25B8 MFA8	25B9 MFA8	25B10 MSA8	25B12 MSA8	25C2 MSA8	25C3 SSA8	25C4 SSA8	25C5 MSA8	25C6 MSA8	25C7 MFA8
Specimen width (m x 10-3)	21.87	21.87	21.90	21.82	21.96	22.02	21.83	21.99	21.95	21.83
Specimen breadth (m x 10-3)	12.97	12.93	12.96	12.95	9.98	10.00	9.97	9.97	9.97	9.97
Notch depth (m x 10-3)	5.14	5.06	4.95	4.85	7.85	8.65	8.40	8.40	8.30	5.37
Notch root radius (m x 10-4)	8.00	8.00	63.50	63.50	4.80	5.00	5.00	5.00	5.00	1.90
Crack length (m x 10-3)	10.10	10.30	5.80	6.30	9.40	10.10	9.20	9.60	9.45	10.24
Maximum load (KN)	3.96	3.71	6.67	6.04	3.18	2.75	3.00	2.88	3.02	2.69
Critical load (KN)	3.24	3.14	6.67	6.00	2.80	2.47	2.73	2.55	2.75	2.32
K Fatigue (MNm-3/2)	12.73	13.12	0.00	0.00	0.00	0.00	0.00	0.00	0.00	10.40
K_Q(LEFM) (MNm-3/2)	16.96	15.60	19.06	17.67	15.88	13.59	13.94	14.50	15.54	14.52
$K_A$from COD (Wells) (MNm-3/2)	19.33	18.67	34.33	31.99	22.29	19.75	22.46	20.61	23.51	19.45
$K_A$from COD (Dawes) (MNm-3/2)	16.04	17.66	23.67	27.39	20.48	20.75	21.78	19.10	21.17	18.26
$K_A$from J (MNm-3/2)	14.22	13.25	24.48	19.14	15.88	14.71	15.87	13.87	15.38	14.93
K_QEquivalent energy (MNm-3/2)	18.41	17.59	20.09	19.56	16.66	16.57	18.10	16.65	19.46	15.79

Table 47. Fracture toughness data for Alcoa 354 alloy.

Nomenclature	25C8 MFA8	25C9 MFA8	25C10 MFA8	25C11 MFN	25C12 MFN	25C13 MFN	25C14 MFN	25D1 MFA8	25D2 MFA8	25D3 S-A8
Specimen width (m x 10-3)	21.95	21.98	21.91	21.92	21.94	21.97	21.99	22.02	21.95	21.94
Specimen breadth (m x 10-3)	9.97	9.99	9.92	9.97	9.97	9.96	9.94	6.97	6.96	6.97
Notch depth (m x 10-3)	5.27	5.33	5.24	5.14	4.96	4.98	5.08	5.19	5.04	13.10
Notch root radius (m x 10-4)	2.00	2.00	2.10	1.90	2.00	2.10	2.00	1.90	1.90	4.20
Crack length (m x 10-3)	10.72	10.60	10.63	10.36	10.41	10.35	9.48	10.42	10.96	13.10
Maximum load (KN)	2.77	2.96	2.88	2.94	3.06	2.80	3.06	2.08	2.00	1.16
Critical load (KN)	2.41	2.55	2.47	2.75	2.58	2.63	2.63	1.72	1.92	1.07
K Fatigue (MNm-3/2)	11.01	10.76	10.96	11.81	11.88	11.76	10.46	16.90	18.39	0.00
K_Q(LEFM) (MNm-3/2)	14.13	15.43	15.31	16.17	15.59	14.98	13.73	16.71	16.95	14.42
$K_A$from COD (Wells) (MNm-3/2)	18.89	19.95	20.21	22.76	20.24	20.18	22.33	19.73	24.63	24.38
$K_A$from COD (Dawes) (MNm-3/2)	17.38	19.38	20.45	21.22	20.25	21.71	18.66	17.25	23.74	21.46
$K_A$from J (MNm-3/2)	14.84	15.53	16.35	17.20	16.04	16.72	15.32	14.71	17.55	16.24
K_QEquivalent energy (MNm-3/2)	18.39	18.22	17.90	19.73	18.55	19.42	16.72	17.29	21.42	16.33

Table 48. Fracture toughness data for Alcoa 354 alloy.

Nomenclature	25D4 S-A8	501A SFA8	502A SFA8	503A SFA8	504A MFA8	505A MFA8	506A MFA8	501B SFA8	502B SFA8	503B SFA8
Specimen width (m x 10-3)	21.95	43.92	44.01	44.05	44.11	44.05	44.20	22.01	22.01	22.01
Specimen breadth (m x 10-3)	6.98	44.01	44.02	43.98	44.15	44.05	44.20	22.04	22.00	22.00
Notch depth (m x 10-3)	13.10	17.60	17.60	17.60	20.00	19.90	20.10	4.70	4.65	4.60
Notch root radius (m x 10-4)	4.40	5.00	4.60	4.60	2.00	1.90	2.00	3.20	4.60	4.60
Crack length (m x 10-3)	13.10	23.18	25.57	24.83	28.34	31.16	25.00	11.31	11.01	13.15
Maximum load (KN)	1.24	12.55	10.43	11.53	9.26	9.10	15.22	5.45	5.88	4.12
Critical load (KN)	1.14	12.35	10.19	10.75	9.41	9.02	15.06	5.30	5.41	4.11
K Fatigue (MNm-3/2)	0.00	7.44	8.96	8.42	11.30	14.82	8.42	16.26	16.20	21.89
K_Q(LEFM) (MNm-3/2)	15.39	16.87	14.30	15.11	16.83	22.66	18.77	15.99	17.44	17.92
$K_A$from COD (Wells) (MNm-3/2)	26.43	23.31	19.50	20.43	23.46	18.35	27.37	22.52	24.73	22.00
$K_A$from COD (Dawes) (MNm-3/2)	21.97	18.21	12.83	18.21	24.56	23.19	28.73	21.15	26.57	22.38
$K_A$from J (MNm-3/2)	17.66	25.09	26.28	21.55	22.31	21.10	26.74	19.25	21.71	20.57
K_QEquivalent energy (MNm-3/2)	17.46	18.11	15.95	15.64	19.70	23.35	21.41	19.02	20.52	20.59

Table 49. Fracture toughness data for Alcoa 354 alloy.

Nomenclature.	504B M-A8	505B M-A8	506B M-A8	507B M-A8	508B M-A8	509B M-A8	5010B M-A8	5011B M-A8	5012B M-A8	
Specimen width (m x 10-3)	21.98	21.96	21.96	21.97	22.04	21.99	21.96	22.00	21.96	0.00
Specimen breadth (m x 10-3)	21.99	21.95	21.96	22.00	22.06	22.02	21.95	22.00	21.96	0.00
Notch depth (m x 10-3)	10.00	9.95	9.80	9.95	10.15	10.00	10.00	10.05	10.00	0.00
Notch root radius (m x 10-4)	1.90	2.00	2.00	6.10	6.10	6.10	15.80	15.80	16.00	0.00
Crack length (m x 10-3)	10.00	9.95	9.80	9.95	10.15	10.00	10.00	10.05	10.00	0.00
Maximum load (KN)	6.47	6.35	6.83	7.06	7.06	6.56	7.25	7.60	7.73	0.00
Critical load (KN)	6.47	6.35	6.75	7.06	7.06	6.50	7.25	7.60	7.73	0.00
K Fatigue (MNm-3/2)	0.00	0.00	0.00	0.00	0.00	0.00	0.00	0.00	0.00	0.00
K_Q(LEFM) (MNm-3/2)	16.34	15.39	16.81	18.43	17.43	17.13	19.50	20.77	20.51	0.00
$K_A$from COD (Wells) (MNm-3/2)	27.07	26.28	27.35	28.62	26.94	25.64	27.78	29.82	29.93	0.00
$K_A$from COD (Dawes) (MNm-3/2)	27.08	27.56	28.63	29.56	27.80	26.32	27.18	27.43	28.87	0.00
$K_A$from J (MNm-3/2)	25.83	25.55	20.86	20.54	18.21	21.41	21.58	19.79	23.80	0.00
K_QEquivalent energy (MNm-3/2)	19.64	18.74	21.48	22.43	21.88	20.87	21.48	22.23	22.88	0.00

ACKNOWLEDGEMENTS

The author wishes to thank Professor J.T. Barnby for his guidance and supervision of this work. My thanks are also given to the Admiralty Underwater Weapons Establishment for their sponsorship, financial support and supplying the materials.

I should also like to thank my colleagues and the technicians in the Department of Metallurgy and Materials for their help where appropriate and to my wife for her support and assistance in Typing this thesis.

GENERAL REFERENCE SECTION.

(1) BS 5447:1977 'Methods of test for Plane Strain Fracture toughness (K_{1c}) of Metallic Materials' British Standards.

(2) E 399-74 (1975) Annual A.S.T.M. Standards part 10, 561-580.

(3) Griffith, A.A. 'The phenomenon of rupture and flow in solids' Phil. Trans. Roy. Soc. (A221) 163.

(4) Irwin, G.R. 'Fracture dynamics', in Fracturing of metals A S M Cleveland, 1948.

(5) Orowan, E. 'Fracture and strength of solids', Rep. Prog. Phys. 1949 (12), 185.

(6) Irwin, G.R. 'Analysis of stresses and strains near the end of a crack traversing a plate', J. Appl. Mech, 1957 (24), 109.

(7) Westergaard, H.M. 'Bearing pressures and cracks', J. Appl. Mech. 1939, (61) A49.

(8) BS. Draft for Development 3: 1971 'Methods for Plane Strain Fracture Toughness (K_{1c}) Testing'. British Standards.

(9) Irwin, G.R. 'Seventh Sagamore Ordinance Materials Research Conference', 1960.

(10) Barnby, J.T. 'Toughness and Critical size', Fracture mechanics series 3, Non Destructive Testing, 1972 (5) 32-37.

(11) Vitvitskii, P.M. and Leonov, M. Ya. Vses Inst Nauchn-Tekhn. Inform. Akad. Nauk. SSSR Pt. 1 (1960) 14.

(12) Bilby, B.A. Cottrell, A.H. and Swinden, K.H. 'The spread of yield from a notch', Proc. Roy. Soc. 1963 (A272) 304-314.

(13) Dugdale, D.S. 'Yielding of steel sheets containing slits', Jnl. Mech. Phys. Solids 1960 (8) 100-104.

(14) Barenblatt, G.I. 'The mathematical theory of equilibrium cracks in brittle fracture', Advances in Applied Mechanics 1962 (7) 55.

(15) Wells, A.A. 'Unstable crack propagation in metals: cleavage and fast fracture', Crack Propagation Symposium, Cranfield, 1961.

(16) Hahn, G.T. and Rosenfield, A.R. 'Sources of fracture toughness: the relationship between K_{1c} and the ordinary tensile properties of metals', Applications Related Phenomena in Titanium Alloys ASTM STP 432, 1968, 5-32.

(17) Hayes, D.J. and Turner, C.E. 'An application of Finite Element Techniques to Post Yield Analysis of Proposed Standard Three-Point Bend Fracture Test Pieces', Int. J. Fracture. 1974, (10) 17.

(18) Wells, A.A. 'The mechanics of the fracture transition in yielding materials' N D A C S S, CODA panel report 1970, p.46.

(19) Rice, J.R. 'Crack tip plasticity and fracture initiation criteria' Third International Congress on Fracture, Munich 1973, paper 441.

(20) Wells, A.A. and Burdekin, F.M. Int. J. Fracture Mech. 1971, (7) p.242.

(21) Dawes, M.G. 'Elastic Plastic Fracture Toughness based on the COD and J contour integral concepts', Research report 54/1978/E. The Welding Institute, January 1978.

(22) Smith, R.F. and Knott, J.F. Practical Application of Fracture Mechanics to Pressure Vessel Technology, Inst. Mech. Engrs., London, 1971, 65.

(23) BS. Draft for Development 19: 1972 'Methods for Crack Opening Displacement (COD) Testing'. British Standards.

(24) Rice, J.R. 'A path independent integral and the approximate analysis of strain concentration by notches and cracks', Jnl. Appl. Mech. 1968 (June), 379-386.

(25) Rice, J.R. in fracture. H. Liebowitz, Ed., (2) Academic Press, New York, 1968, pp.191-311.

(26) Hutchinson, J.W. J. Mech. Phys. Solids. 1968, (16) 13.

(27) Rice, J.R. and Rosengren, G.F. J. Mech. Phys. Solids. 1968, (16) 1.

(28) Hayes, D.J. 'Origins of the stress intensity factor approach to fracture' Jnl. Strain Analysis 1975, (10) No.4, 198-200.

(29) Landes, J.D. and Begley, J.A. ASTM STP 514, Philadelphia, 1972, 24.

(30) Begley, J.A. and Landes, J.D. ASTM STP 514, Philadelphia, 1972, pp.1-20.

(31) Irwin, G.R. and Kies, J.A. Welding Research Supplement. 1954, (19) pp.193-198.

(32) Krafft, J.M., Sullivan, A.M. and Boyle, R.W. in proceedings Crack Propagation Symposium, College of Aeronautics, (1) Cranfield, England, pp.8-26.

(33) 'Fracture Toughness Evaluation by R-curve methods' ASTM STP 527, 1973.

(34) 'Recommended Practice for R-Curve Determination', ASTM Annual Book of Standards part 10, Philadelphia, 1975.

(35) Heyer, R.H. and McCabe, D.E. 'Plane Stress Fracture Toughness Testing using a Crack Line Loaded Specimen' Engg. Fracture Mech. 1972, (4) p.393.

(36) Heyer, R.H. and McCabe, D.E. 'Crack Growth Resistance in Plane Stress Fracture Testing' Engg. Fracture Mech. (4) 1972, pp.413-430.

(37) Judy, R.W. and Goode, R.J. 'Fracture extension resistance (R-curve) characteristics for three high strength steels' ASTM STP 527, 48-61.

(38) Neale, B.K. 'The influence of crack shape on fracture toughness testing', Int. J. Fracture. 1976, (12) pp.499-502.

(39) Forsythe, G.E. and Wasow, W.R. 'Finite Difference Methods for Partial Differential Equations' New York, John Wiley and Sons, Inc., 1960.

(40) Crandall, S.H. 'Engineering Analysis', New York, McGraw-Hill 1956.

(41) Desai, C.S. and Abel, J.F. 'Introduction to the Finite Element Method', Von Nostrand Reinhold Company, New York, 1972.

(42) Zienkiewicz, O.C. 'The Finite Element Method in Engineering Science', McGraw-Hill, London, 1971.

(43) Peterson, R.E. 'Stress concentration design factors': charts and relations useful in making strength calculations for machine parts and structural elements. New York, Wiley, 1974.

(44) Faupel, J.H. 'Engineering Design', a synthesis of stress analysis and materials engineering, Wiley, 1965.

(45) Leven, M.M. and Frocht, M.M. 'Stress-Concentration Factors for Single Notch in Flat Bar in Pure and Central Bending', J. Appl. Mech. (19) 1952, pp.560-561.

(46) Neuber, H. 'Theory of notch stresses', Springer, Berlin, 1958.

(47) Richards, T.H. and Wood, P.C. 'Stress Concentration Factors for Some Blunt Notched Three Point Bend Fracture Specimens', a report on work carried out for the Procurement Executive of the Ministry of Defence under Contract No. AT/2097/028. Department of Mechanical Engineering, University of Aston in Birmingham, 1978.

(48) Brown, W.F. and Srawley, J.E. Plane strain crack toughness testing, 1967 (ASTM STP 410, Philadelphia).

(49) Cartwright, D.J. and Rooke, D.P. 'Evaluation of Stress Intensity Factors', Jnl. Strain Analysis. (10) No.4, October 1975, 217-224.

(50) Rooke, D.P. and Cartwright, D.J. 'Compedium of stress intensity factors', Her Majesty's Stationery Office, 1975.

(51) Yamamoto, Y. and Ao, K. 'Stress Intensity Factors for Cracks in Notch Bend Specimens for Three Point Bending', Int. J. Fracture. (12) 1976, pp.495-497.

(52) Yamamoto, Y., Sumi, Y. and Ao, K. 'Stress Intensity Factors of Cracks Emanating from Semi-Elliptical Side Notches in Plates', Int. J. Fracture. (10) 1974, pp.593-595.

(53) Yamamoto, Y. and Tokuda, N. Int. J. Num. Methods Engg. 1973, (6) 427-439.

(54) Benthem, J.P. and Koiter, W.T. Methods of Analysis and Solutions of Crack Problems, Noordhoff International Publishing, Leyden (1973), 131-178.

(55) Jergeus, H.A. 'A simple formula for the stress intensity factors of cracks in side notches', Int. J. Fracture. 1978, (14) pp.R113-R116.

(56) Smith, R.A., Jerram, K. and Miller, K.J. 'Experimental and Theoretical Fatigue-Crack Propagation Lives of Variously Notched Plates', Jnl. Strain Analysis. 1974, (9) pp.61-66.

(57) Smith, R.A. and Miller, K.J. 'Fatigue cracks at notches'. Int. J. Mech. Science. 1977, (19) pp.11-22.

(58) Smith, R.A. Fracture Mechanics in Engineering Practice, 1976, annual conference of the stress analysis group of the Institute of Physics, Sheffield, Editor: P. Stanley.

(59) Novak, S.R. and Barsom, J.M. 'Brittle Fracture (K_{1c}) Behaviour of Cracks Emanating from Notches' ASTM STP 601 1976, pp.409-447.

(60) Irwin, G.R. 'Structural Mechanics', Pergamon, New York, (1960), 557-594.

(61) Hasebe, N. and Kutanda, Y. 'Calculation of Stress Intensity Factor from Stress Concentration Factor', Engg. Fracture Mech. 1978, (10) pp.215-221.

(62) Smith, E. Proc. Roy. Soc. London. A299 455.

(63) Vitek, V. 'Yielding from a Crack with Finite Root-Radius Loaded in Uniform Tension', J. Mech. Phys. Solids. 1976, (24) pp.67-76.

(64) Vitek, V. 'Yielding on Inclined Planes at the Tip of a Crack Loaded in Uniform Tension', J. Mech. Phys. Solids. 1976, (24) pp.263-275.

(65) Heald, P.T., Spink, G.M. and Worthington, P.J. 'Post Yield Fracture Mechanics', Mat. Sci. Eng. 1972, (10) 129-138.

(66) Spink, G.M., Worthington, P.J. and Heald, P.T. 'The Effect of Notch Acuity on Fracture Toughness Testing', Mat. Sci. Eng. 1973, (11) 113-117.

(67) Pickens, J.R. and Gurland, J. 'The Fracture Toughness of WC-Co Alloys Measured on Single-edge Notched Beam Specimens Pre-cracked by Electron Discharge Machining', Mat. Sci. Eng. 1978, (33) pp.135-142.

(68) Chermant, J.L., Deschanvres, A. and Iost, A. in Fracture Mechanics of Ceramics, Vol.7, Plenum Press, New York 1974, p.346.

(69) Tada, H., Paris P. and Irwin, G. 'The stress analysis of cracks handbook', D E L Research Corporation, Hellertown, Pennsylvania, 1973.

(70) Swedlow, J.L. and Ritter, M.A. 'Toward Assessing the Effects of Crack Front Curvature (CFC) ASTM STP 513, 1972, pp.78-89.

(71) Burck, L.H. 'Fatigue Growth of Surface Cracks in Bending', Engg. Fracture Mech. 1977, (9) pp.389-395

(72) Paris, P.C. and Erdogam, F. 'A critical analysis of crack propagation laws', Trans. ASME. series D, 1963, (85) 528-534.

(73) Wessel, E.T. 'State of the art of the WOL specimen for K_{1c} fracture toughness testing', Engg. Fracture Mech. 1968, (1) pp.77-103.

(74) Neale, B.K. 'An investigation into the effect of thickness on the fracture behaviour of compact tension specimens', Int. J. Fracture. (14) 1978, pp.203-212.

(75) Edelson, B.I. and Baldwin, W.M, Jr., 'The effect of second phases on the mechanical properties of alloys', Trans. ASM 1962, (55) 230.

(76) Mulherin, J.H. and Rosenthal, H. 'Influence of none equilibrium second-phase particles formed during solidification upon the mechanical behaviour of aluminium alloy', Met. Trans. (2) 1971, 427.

(77) Low, J.R. Jr., Van stone, R.H. and Merchant, R.H. NASA TR No. 2, NASA Grant NGR-39-087-003 (1972).

(78) Karl-Heinz-Schwalbe, 'On the Influence of Microstructure on Crack Propagation Mechanics and Fracture Toughness of Metallic Materials', Engg. Fracture Mech. 1977 (9) pp.795-832.

(79) Thompson, D.S. and Zinkham, R.E. 'The effect of alloying and processing on the fracture characteristics of aluminium sheet', Engg. Fracture Mech. 1975, (7) p.389.

(80) Saunders, D.S. 'The Fracture Toughness of an Aluminium casting alloy', Conference of the Australia fracture group 1974, Editor:- Leicester, R.H. pp.23-30.

(81) Austen, P.R. and Williamson, H.M. 'Fracture behaviour of Al-Mg. 7 weight per cent Si alloys', Conference of the Australia fracture group 1974, Editor:- Leicester, R.H. pp.16-22.

(82) Hahn, G.T. and Rosenfield, A.R. 'Experimental determination of plastic constraint ahead of a sharp crack under plane strain conditions', Trans. ASM 1966, (59) p.909.

(83) Wilshaw, T.R., Rau, C.A. and Tetelman, A.S. 'A general model to predict the elastic-plastic stress distribution and fracture strength of notched bars in plane strain bending', Engg. Fracture Mech. 1968, (1) 191.

(84) Die-Cast Metals; Light Metals and Alloys (Including Electrical Conductors) Annual book of ASTM Standards, 1978, Part 7.

(85) Kaufman, J.G., Nelson, F.G., Jr. and Marshall Holt. 'Fracture Toughness of Aluminium Alloy Plate Determined with Center-Notch Tension, Single Edge Notch Tension and Notch Bend Tests', Engg. Fracture Mech. 1968, (1) pp. 259-274.

(86) Kaufman, J.G. and Marshall Holt. 'Fracture Characteristics of Aluminium Alloys', Alcoa Research Laboratories, Tech. Paper No. 18, Pittsburgh, Penn. 1965.

(87) Nelson, F.G. and Kaufman, J.G. 'Fracture toughness of plain and weded 3" thick aluminium alloy plate', ASTM STP 536, 1973, pp. 350-376.

(88) Liebowitz, H. (Editor), 'Fracture Mechanics of Aircraft Structures' AGARDograph No.176, 1974, pp. 555-576.

(89) Nock, J.A. Jr. and Hunsicker, H.Y. 'High-Strength Aluminium Alloys' Journ. of Metals 1963 (15) No.3, pp. 216-224.

(90) Kaufman, J.G. and Hunsicker, H.Y. 'Fracture Toughness Testing at Alcoa Research Laboratories' ASTM STP 381, Philadelphia 1964, pp. 290-308.

(91) Irwin, G.R. and Kies, J.A. 'Critical energy rate analysis of fracture strength', Weld. J (Res.suppl.) 1954 (33) 193s-198s.

(92) Bonesteel, R.M., Piper, D.E. and Davinroy, A.T. 'Compliance and K, Calibration of Double Cantilever Beam (DCB) Specimens', Engg. Fracture Mech. 1978, (10) pp.425-428.

(93) Wilson, W.K. 'Analytical determination of stress intensity factors for the Manjoine Brittle fracture test specimen', report No. WERL-0029-3. Westinghouse Research Laboratories, Aug. 1965.

(94) Wilson, W.K. 'Optimization of WOL brittle fracture test specimens', Report No.66-1B4-BTLRF-R1. Westinghouse Research Laboratories, Jan. 1966.

(95) Collipriest, J.E. Jr. and Thatcher, C.S. 'Cyclic crack growth in aluminium alloy 7074 T851', Rockwell International Space Division, Report No. SD73-SH-0070, Aug. 1973.

(96) Ryder, J.T., Bowie, G.E. and Pettit, D.E. 'Recent Considerations in Experimental Compliance Calibration of the WOL Specimens', Engg. Fracture Mech. 1977, (9) pp.901-923.

(97) Rice, J.R., Paris, P.C. and Merkle, J.G. 'Some Further Results of J-Integral Analysis and Estimates', ASTM STP 536, 1973, pp.231 -245.

(98) Ryder, G.H. 'Strength of Materials', McMillan and Co., Ltd., London 1969, p.203.

(99) Barnby, J.T. and Daimalani, 'Assessment of the fracture toughness of cast steels', Part 1, Low alloy steels, Journ. Mat. Sci. 1976 (11) pp.1979-1988.

(100) Wells,A.A. 'The Status of COD in Fracture Mechanics', Canadian Congress of Applied Mechanics, Calgary, 1971.

(101) Ingham, T., Egan, G.R., Elliot, D. and Harrison, T.C, ' The effect of geometry on the interpretation of COD test data' Paper C54/71. I. Mech. E. conference on Practical Application of Fracture Mechanics to Pressure Vessel Technology, London, May 1971.

(102) Sumpter, J.D.G. and Turner, C.E. 'A method for determination of J_c', ASTM STP 601 1976 pp. 3-18.

(103) Dawes, M.G. 'The application of fracture mechanics to brittle fracture in steel weld metals', Ph.D thesis (CNAA), The Welding Institute, December 1976.

(104) Johnson, H.H. 'Calibrating the electric potential method for stidying slow crack growth', Mat. Res. Std. 1965 (5) p. 442.

(105) Cooke, R.J. and Robinson, J.L. 'Some further considerations of the Potential Drop Method for measuring crack lengths', Research report. Department of Physical Metallurgy and Science of Materials, University of Birmingham.

(106) Gilbey, D.M. and Pearson, S., 'Measurement of the length of a central or edge crack in a sheet of metal by an electrical resistance method', R.A.E. Technical Report, No.66402, 1966.

(107) Ritchie, R.O., 'Crack growth monitoring, some considerations on the electrical potential method', Department of Metallurgy and Materials Science, University of Cambridge.

(108) Ritchie, R.O., Garrett, C.G. and Knott, J.F., 'Crack growth monitoring. Optimisation of the electrical potential technique using an analogue method', Int. Journ. Fracture Mech. 1971, (7) pp.462-467.

(109) Bachmann, V. and Munz, D. 'Unusual Potential Drop during the Application of the Electrical Potential Method in a Fracture Mechanics Test', Journ. of Test Eval. 1976, (4) pp.252-260.

(110) Pisarski, H.G. 'A review of ductile crack initiation and crack growth measurements method', The welding Institute, Research Bulletin, April 1978, pp.97-101.

(111) Swinyard, G. 'Foundry Behaviour of High Strength Aluminium Alloy', Admiralty Underwater Weapons Establishment, Portland, May 1974.

(112) Walker, E.F. and May, M.J. 'Compliance functions for various types of test specimen geometry', BISRA Report, No.MG/E/307/67.

(113) Crow, S.E. 'Compliance Calibration of Notched Bodies', Undergraduate project, Department of Metallurgy and Materials, University of Aston in Birmingham, 1978.

(114) Sokolnikoff, I.S. and Redheffer, R.M. Mathematics of Physics and Modern Engineering. (second edition) Mc Graw-Hill 1968.

(115) Witt, F.J. 'Equivalent energy procedures for predicting gross plastic fracture', Oak Ridge National Laboratory, Paper ORNL-TM-3172.

(116) Buchalet, C. and Mager, T.R. 'Experimental verification of lower bound K_{1c} values utilising the equivalent energy concept', ASTM STP 536, pp. 281-296.

(117) E 399-78 (1978) Annual A.S.T.M. Standards, part 10, 512-533.

(118) Merkle, J.G. and Corten, H.T. 'A J Integral Analysis for the Compact Specimen, Considering Axial force as Well as Bending Effects', Journ. Press. Vess. Tech. 1974 (96) pp. 286-292.

(119) Pook, L.P. 'Analysis and Application of Fatigue Crack Growth Data' Jnl. Strain Analysis. 1975 (10) pp. 242-250.

(120) Parkins, R.N. 'Enviromental Effects In Crack Growth' Jnl. Strain Analysis. 1975 (10) pp. 251-257.